HIGH MOMENTUM JET QUENCHING IN $\sqrt{s_{\mathrm{NN}}} = 62.4$ GeV Cu+Cu AND Au+Au COLLISIONS

Dissertation
presented for the degree of
Doctor of Philosophy in Physics
by
Truls Martin Larsen
November 7, 2007

NIELS BOHR INSTITUTE
FACULTY OF SCIENCE – UNIVERSITY OF COPENHAGEN

ii

High Momentum Jet Quenching in $\sqrt{s_{\mathrm{NN}}} = 62.4$ GeV Cu+Cu and Au+Au Collisions

by Truls Martin Larsen
Supervisor Prof. Dr. Sc. Jens Jørgen Gaardhøje November 7, 2007

Prof. Dr. Birger B. Back
Argonne National Laboratory, University of Chicago, USA

Prof. Dr. Thomas Døssing
University of Copenhagen, Denmark

Prof. Dr. Hans–Åke Gustafsson
University of Lund, Sweden

NIELS BOHR INSTITUTE
FACULTY OF SCIENCE – UNIVERSITY OF COPENHAGEN

Acknowledgements

There are a number of people who deserve a big "Thank You!". They have helped me with everything from details of computer programming and the data analysis to discussions of the physics of the BRAHMS results:

Jens Jørgen Gaarhøje (my supervisor), Flemming Videbæk (BRAHMS spokesperson), Christian Holm Christensen, Cătălin Ristea, Ian Bearden, Stephen J. Sanders, Michael Murray, and the rest of the BRAHMS collaboration.

A general thanks goes to the HEHI group, with whom I have written this thesis, for giving me the opportunity to write a Ph.D., and sending me around the world to interesting conferences and meetings.

A special thanks goes to Rodolphe Marie and Anders Mikkelsen who helped me through a dark week in September 2007.

Truls Martin Larsen
NBI Copenhagen Denmark, October 2007.

Contents

Chapter 1

Introduction

All matter around us is made up of electrons, neutrons and protons. The protons and neutrons are themselves made up of 3 so–called quarks, held together in a bound state by the strong nuclear force, described by QCD (Quantum ChromoDynamics). It confines the smallest building blocks in nature, the quarks and gluons, within "colourless" hadrons, like protons and neutrons. The quarks and gluons posses a peculiar charge, termed "colour", which has 3 values: "red", "green", "blue". QED (Quantum ElectroDynamics) describes electro–magnetic interactions (behaviour of particles with electric charges and magnetic fields), where the force carrier is the neutral, massless photon. In contrast to QED, the force carriers in QCD, the gluons, also carry the colour charge.

The potential between two "colour" charges, separated by a distance r, is phenomenologically known to be of the form:

$$V_{qq}(r) = \frac{A(r)}{r} + ar \tag{1.1}$$

where $A(r)$ is function which goes like $1/\log(r)$ and a is the string tension constant. This rather peculiar form, compared to the electromagnetic and gravitational force, gives rise to some interesting effects in relation to the freedom of quarks inside a hadron. The linear term of the potential ensures that no lone quark exists, since when two quarks are pulled far apart, the energy stored in the potential is enough to create a new quark and anti–quark pair. Eventually the potential breaks down and new hadrons are formed. This is why quarks are in bound "colourless" states. At very short distances they will repel each other as the $A(r)/r$ term of the equation plays the dominant role. The only way quarks can be "free" is if they are all in short distances from one another, called "asymptotic freedom". It was proposed by T. D. Lee in [1, 2] to search for this "asymptotic freedom" of quarks and gluons in heavy ion collisions, where one could create QGP (Quark Gluon Plasma).

The RHIC (Relativistic Heavy Ion Collider) has been operational since summer of 2000, and has now collided heavy ions, e.g. Au+Au, up to $\sqrt{s_{\mathrm{NN}}} = 200$ GeV. The matter created at the RHIC top energy has revealed a large amount of new phenomena, warranting a new name, sQGP (strongly interacting quark gluon plasma, described in section 3.4). Though the matter is extremely short lived (only a few tens of fm/c) and small $\lesssim 10 - 100$ fm, it has higher energy density than any other human created matter, perhaps up to ~ 50 times the energy density of a proton.

This extremely dense and hot matter has high opacity. High momentum partons loose large amounts of energy as they traverse the created matter, and are even absorbed (hight p_{T} suppression). This has been shown in jet measurements (shown in section 2.3), where only one of the jets in back–to–back pairs escape the created medium. Testing of scaling variables between nucleon–nucleon and nucleus–nucleus collisions, also show that nucleon–nucleon collisions produce more high momentum particles, scaled and compared to nucleus–nucleus collisions.

Suppression of high momentum particles was not observed at lower energy heavy ion facilities, like the SPS (Super Proton Synchrotron). This suggests that jet suppression, also called high p_{T} suppression, develops at collisions energies between $\sqrt{s_{\mathrm{NN}}} = 17.3$ GeV and 200 GeV.

This work presents a systematic study of high p_{T} suppression in Cu+Cu and Au+Au collisions at intermediate energy, $\sqrt{s_{\mathrm{NN}}} = 62.4$ GeV. A systematic investigation of the onset of suppression as a function of the collision energy, and the geometries will be presented. Traditional studies of high p_{T} suppression have focused on unidentified charged hadrons. In this work the first studies of identified particles, $\pi^{\pm}$, $K^{\pm}$, p and $\bar{p}$, at this collision energy, as a function of geometry (two colliding systems), centrality and rapidity are presented.

Chapter 2

Heavy ion collisions at RHIC

The motivation for the studies of ultra relativistic heavy ion collisions in experiments, at the AGS (Alternating Gradient Synchrotron), SPS (Super Proton Synchrotron) and RHIC (Relativistic Heavy Ion Collider) has been to create in the laboratory and understand the properties of the QGP. This is believed to be the matter the universe consisted of in the first micro seconds after the Big Bang. Through the study of this matter one also hopes to get a better understanding and/or theoretical description of the creation of mass, the strong nuclear force and QCD.

At the RHIC, four experiments study the properties of this matter at a center of mass collision energy ~ 12 times higher than at the SPS. The four experiments constructed along the accelerator beam line were BRAHMS (Broad RAnge Hadron Magnetic Spectrometer), PHENIX (Pioneering High Energy Nuclear Interaction eXperiment), PHOBOS (in memory of a previously rejected proposal called M.A.R.S., Phobos is a Mars moon), and STAR (Solenoidal Tracker At RHIC). All experiments were designed with different physics ideas in mind, though they all shared some capabilities, such as measuring multiplicity and charged hadron spectra at midrapidity. The experimental program of these experiments has resulted in a wealth of new results and discoveries.

2.1   Heavy ion collisions, geometry, and evolution

Heavy ion collisions can range from head–on (central) collisions to barely overlapping (peripheral) collisions. Thus the volume of the produced matter can be studied by varying the collision centrality. A head–on collisions will produce an azimuthally symmetric shape, while a semi peripheral collisions could look like the illustration in figure 2.1. The figure shows a semi peripheral collision from different angles. The impact parameter $\vec{b}$ is always perpendicular to the nuclei's velocities $\vec{v}$. The velocity vector, $\vec{v}$, together with the interaction point constitutes the "beam axis". The beam axis and $\vec{b}$ defines the "reaction plane". The right part of figure 2.1 is a view down on the reaction plane.

There are also several other important kinetic variables used in describing heavy ion collisions. For a particle with mass m_0 escaping the collision at an angle θ relative to the beam axis, with momentum p, we define transverse momentum p_{T}, longitudinal momentum p_{L}, pseudorapidity η, and rapidity y as:
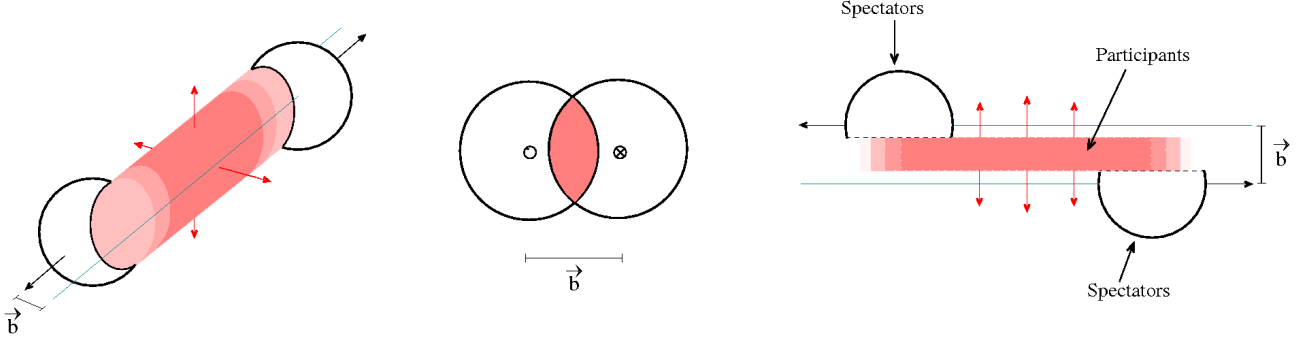
Figure 2.1: The figure shows a schematic view of a mid central heavy ions collision. To the left a 3D perspective view is seen, in the middle a view along the beam axis and to the right a view perpendicular to the beam axis and the impact parameter $\vec{b}$, which is also the reaction plane of the collisions. The experimental measurement of the reaction plane is often called the event plane. The figure is from [3].

$$p_{\mathrm{L}} = |\vec{p}| \cdot |\cos\theta| \tag{2.1}$$

$$p_{\mathrm{T}} = |\vec{p}| \cdot |\sin\theta| \tag{2.2}$$

$$y = \frac{1}{2}\ln\frac{E + p_{\mathrm{L}}}{E - p_{\mathrm{L}}} \tag{2.3}$$

$$y \xrightarrow{m \ll p} \eta = \frac{1}{2}\ln\frac{p + p_{\mathrm{L}}}{p - p_{\mathrm{L}}} = \tanh^{-1}(\cos\theta) \tag{2.4}$$

where $E^2 = m_0^2 + p^2$ ($c \equiv 1$ in all formulas used in this work). The rapidity is additive under a Lorentz boost. The pseudorapidity is used instead of rapidity when measuring unidentified charged hadrons, since it does not involve the particle's mass. The beam particles, in the approximation of $p \ll m \Rightarrow E \approx p_{\mathrm{L}}$, have $y = \ln(2p_{\mathrm{L}}/m_0)$.

A schematic overview of how a heavy ion collision is expected to evolve at the RHIC is shown in figure 2.2. The collision is illustrated from pre–collision to kinetic freeze–out. The evolution of a collision is divided into two states: initial and final. The two top illustrations represent the initial state, and the rest correspond to the final state. The initial state lasts from pre–collision until, and including, the hard scattering of the incident partons. The final state starts when the initial state ends. Matter is created and evolves through thermalisation and expansion, until the particles chemically and then kinematically freeze out. Different observations are attributed to the initial or final state, and also to different stages of the evolution of either state.

In the initial state the incident partons pass through the the "cold" nuclear matter of the other nucleus, and go through incoherent hard scatterings, where jets are produced. The particles created from these jets, will be in investigated in this work. After the nuclei have passed each other, they break up into fragments and between them a hot, dense, matter is created. The created matter is highly unthermalised at this stage in the final state. It may have a spatially anisotropic azimuthal shape, depending on the centrality of the collision. Any spatial anisotropy of the created matter transforms
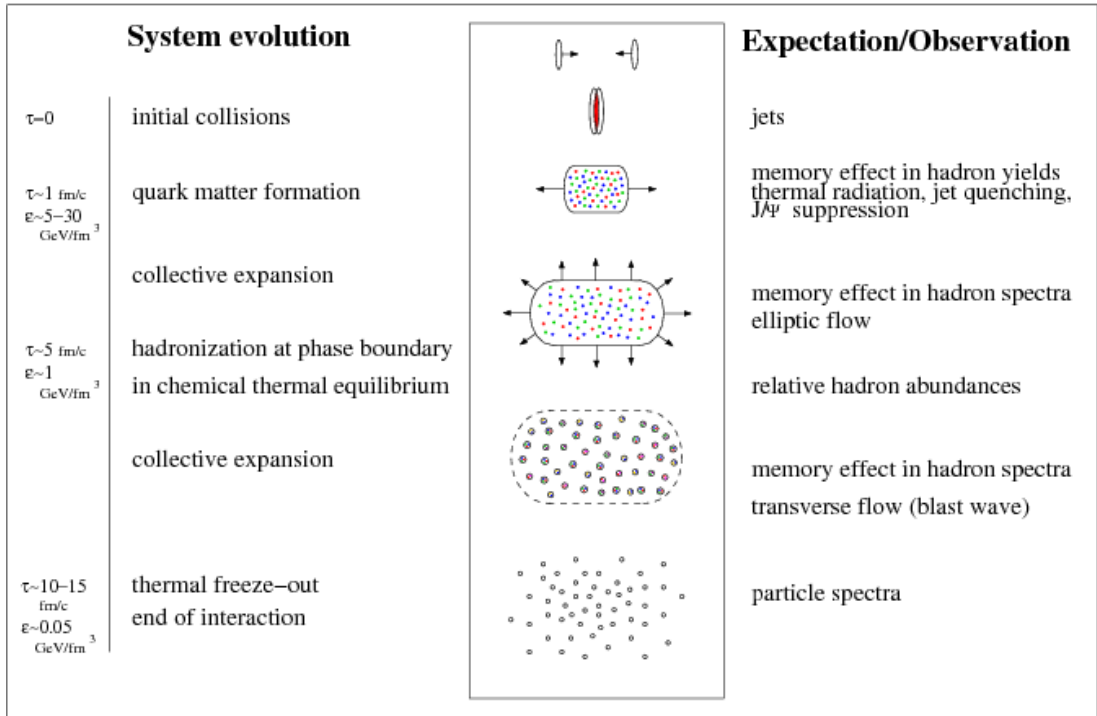
Figure 2.2: The figure shows a schematic overview of a heavy ions collision at the RHIC. The figure is taken from [3].

into a parton momentum anisotropy as the created matter thermalises[1] and expands. If the thermalisation process is fast, the azimuthal momentum anisotropy becomes large, and if thermalisation is slow, azimuthal momentum anisotropy becomes small or vanishes. The created matter expands until chemical freeze–out, where all the hadrons are created.

The hard partons, created in the initial state, have to travel though the expanding matter before they can escape the "fireball". After the chemical freeze–out, the matter consists of hadrons and leptons, They react kinematically with each other until the temperature and energy density drops even further. When the energy density and temperature is low enough, they stop interacting, called the kinetic freeze–out. The particles then fly out to the surrounding detectors where the particle spectra are measured.

The main observations obtained by the experiments will be discussed in the following sections.

2.2 Main results from the first RHIC years

A wealth of measurements have been published by the RHIC experiments. These include measurements of the initial energy density, the freeze–out temperature, the system size, elliptic flow, and back–to–back jet correlations. Many of these measurements are now understood, but some still pose

---

[1]Global thermalisation is not necessary, but local thermalisation should occur.

	$\sqrt{s_{\mathrm{NN}}}$ [GeV]	$\langle R \rangle$ [fm]	$\langle N_{\mathrm{part}} \rangle$	ϵ_{Bj} GeV/fm^3	Experiment
^{16}O+^{27}Al	19.4	3.0	39	1.0	NA35
^{16}O+^{63}Cu	19.4	3.0	50	1.5	NA35
^{16}O+^{107}Ag	19.4	3.0	58	1.9	NA35
^{16}O+^{197}Au	19.4	3.0	69	2.3	NA35
^{32}S+^{32}S	19.4	3.8	58	1.3	NA35
^{32}S+^{63}Cu	19.4	3.8	82	1.7	NA35
^{32}S+^{107}Ag	19.4	3.8	95	2.1	NA35
^{32}S+^{197}Au	19.4	3.8	113	2.6	NA35
^{207}Pb+^{207}Pb	17.3	6.6	390	3.2	NA49
^{197}Au+^{197}Au	62.4	6.0	337	3.7	BRAHMS
^{197}Au+^{197}Au	130	6.0	344	4.4	BRAHMS
^{197}Au+^{197}Au	200	6.0	353	5.0	BRAHMS

Table 2.1: The table shows the calculated initial energy densities, using Bjorken's hydrodynamical formula in equation 2.5 [8]. All energy densities were calculated using a formation time $\tau_0 = 1$ fm/c. The data from NA35 is taken from [9], data from NA49 is taken from [10].

questions. Overview articles were published by all four RHIC experiments in [4, 5, 6, 7]. The following paragraphs will give a brief overview of the measurements and results and their interpretations.

Initial energy density
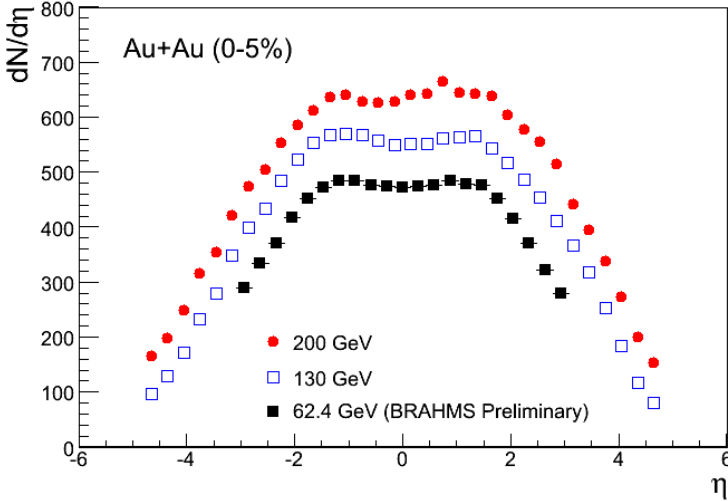
Figure 2.3: The figure shows the measured charged particle multiplicity in 0–5% central Au+Au collisions. The multiplicity, measured by the BRAHMS experiment, is shown for the 3 collision energies studied at the RHIC.

Bjorken's hydrodynamical model [8] proposed a way to estimate the initial energy density in a heavy ion collision, the energy density once the system has thermalised in the final state. In the model he assumed that particle production around midrapidity[2] is uniform in the longitudinal direction and Lorentz boost invariant, with no transverse expansion in both nucleon–nucleon and nucleus–nucleus collisions, and that the baryons from the colliding nuclei should also be found to be within 2-3 units of rapidity from the beam rapidity (forward rapidity). The last assumption is also called "transparency", as the net baryon density at midrapidity should be 0. With these assumption the initial energy density would be proportional to the particles' transverse energy

---

[2]A particle emitted perpendicular to the beam axis in a collider, $p_{\mathrm{L}} = 0$, has rapidity $y = 0$, called midrapidity.

rapidity distribution, with the following formula:

$$\epsilon_{\mathrm{Bj}} = \frac{\langle E \rangle}{V} = \frac{\langle m_{\mathrm{T}} \rangle}{\pi R^2 \tau_0} \frac{dN}{dy} \qquad (2.5)$$

where $m_{\mathrm{T}} = \sqrt{p_{\mathrm{T}}^2 + m_0^2}$ is the transverse mass of the emitted particles, R is the radius of the smallest of the two colliding nuclei and dN/dy is the rapidity density of particles. The assumption that the net baryon density at midrapidity is 0 is not true at SPS but nearly fulfilled at RHIC energies. In the article [11] published by BRAHMS, the net proton density (hyperons also contribute to the net baryon density) at midrapidity is measured to be 6.3, which is low compared to SPS ~ 25. Equation 2.5 is thus probably a reasonable estimation of the initial energy density at the RHIC. It is though questionable if Bjorken "transparency" is fulfilled at the SPS, and if equation 2.5 is valid.

At the SPS initial energy densities were estimated from the experimental results, using equation 2.5, for a variety of different collision systems as shown in table 2.1. The estimates was made using a formation time $\tau_0 = 1$ fm/c. The calculated energy densities in table 2.1, ranging from 1.0-3.2 GeV/fm^3, are very high compared to that of nuclear matter (~ 0.17 GeV/fm^3). If the created matter consists of hadrons, they will overlap in space, thus making it likely that the matter is a dense gas of hadrons and the constituents of the hadrons, the quarks and gluons. The same estimates from Au+Au collisions at $\sqrt{s_{\mathrm{NN}}} = 62.4$ GeV, 130 GeV and 200 GeV are also given in table 2.1. The formation time was assuming to be $\tau_0 \leq 1$ fm/c. The charged particle multiplicity, shown in figure 2.3, is 2/3 of the total multiplicity. (One assumes that neutral, positive and negative particles are produced with the same abundance.) Au+Au collisions at $\sqrt{s_{\mathrm{NN}}} = 62.4$ GeV and 200 GeV then have $dN/dy \approx 690$ and 950 at midrapidity, respectively. This indicates an energy density of $\epsilon_{62.4} > 3.7$GeV/fm^3 and $\epsilon_{200} > 5$ GeV/fm^3. Both the RHIC intermediate and top energy collisions is consistent with a matter consisting only of quarks and gluons.

Freeze–out temperature

By investigating the slope of particle spectra, typically $p_{\mathrm{T}} < 2$ GeV/c, one obtains insight into the thermal and collective aspects of a collisions. The random (thermal) effects are typically interpreted as the kinetic freeze–out temperature, T_{fo}, and the collective effect as the radial flow velocity, β_{T}. The results are obtained by performing simultaneous statistical hydrodynamics–inspired fits to the m_{T} spectra of pions, kaons and (anti-) protons. This is refered to as "Blast wave" fits [12]. STAR has measured the temperatures and collective flow velocities in Au+Aucollisions at $\sqrt{s_{\mathrm{NN}}} = 200$ GeV, as shown in the left panel of figure 2.4. The chemical freeze–out temperature, T_{ch}, is obtained through a model fit to measured particle ratios. The particle ratios are calculated as the ratio of integrated identified particle spectra. Like and unlike particle ratios has been made for a big number of particles at the RHIC. Using a grand canonical ensemble [13, 14], the ratios are fitted, shown as solid lines in the right panel of figure 2.4. The model assumes that the matter is in thermal and chemical equilibrium. The fit gives the chemical freeze–out temperature, the baryon chemical potential, and the non–equilibrium parameter, γ_s for particles containing one or more s or $\bar{s}$ quarks. This statistical model does a very good job of reproducing the particle ratios measured by STAR.

The chemical freeze–out temperature is shown as the solid, yellow line on the right panel of figure 2.4, $T_{ch} = 163 \pm 5$MeV. The left panel also reveals a decreasing kinetic freeze–out temperature for more
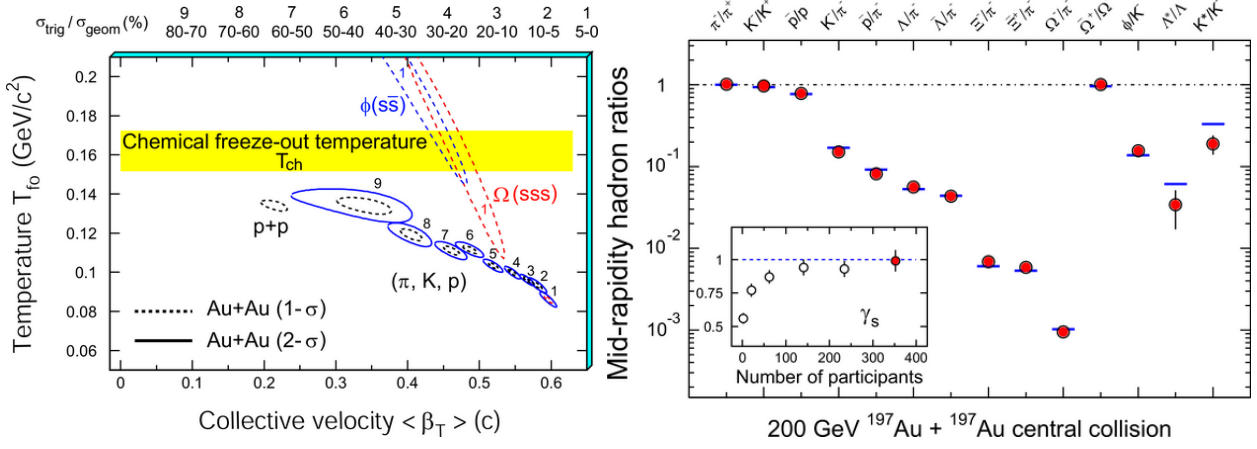
Figure 2.4: The left panel shows the kinematic freeze–out temperature for a range of collisions centralities, numbered from 1 (central) to 9 (peripheral). The dashed and solid lines indicate the 1 and 2 standard deviations contours, respectively. Kinetic freeze–out in $p + p$ collisions is also indicated. The right panel shows like– and unlike– particle ratios. The solid lines are model fits [13, 14] to the data. The model reproduces the data very well. Both figures are from STAR [7].

central collisions with an increased collective flow velocity. These results indicate that the increase in expansion velocity happens after the chemical freeze–out. The ϕ and Ω shows a much higher kinetic freeze–out temperature, compared to the one from $\pi^\pm$, $K^\pm$, p and $\bar{p}$ spectra. The figure also indicates that their flow velocity is accumulated before chemical freeze–out occurs.

System size

The system size, the radius of the created matter before it freezes out, can be determined by doing a HBT (Hanburry–Brown–Twiss [15, 16]) pion interferometry measurement. This measurement could reveal the geometry of the matter at freeze–out, but also reveal information of on how long the created matter emits particles. If the matter is in a very mixed state and the transition from QGP to a hadronic phase is of first order, the duration of particle emission should be long and/or the source size large.

Experimentally, the correlation function C(q) is defined as:

$$C(q) = \frac{\sigma d^6\sigma}{d^3p_1 d^3p_2} \bigg/ \left(\frac{d^3\sigma}{d^3p_1} \cdot \frac{d^3\sigma}{d^3p_2} \right) \tag{2.6}$$

where $q = |\vec{p}_1 - \vec{p}_2|$, $d^3\sigma/d^3p$ is the single–particle cross section and $d^6\sigma/d^3p_1 d^3p_2$ is the two–particle cross section. The numerator is determined directly from data, while the denominator is constructed using a standard event–mixing technique.

The distribution of the pion pairs' momentum difference, q, is fitted with a 3D gaussian (Bertch–Pratt parametrisation [17, 18]):

$$C(\vec{q}) = 1 + \lambda e^{-(R_{side}^2 q_{side}^2 + R_{out}^2 q_{out}^2 + R_{long}^2 q_{long}^2)} \tag{2.7}$$
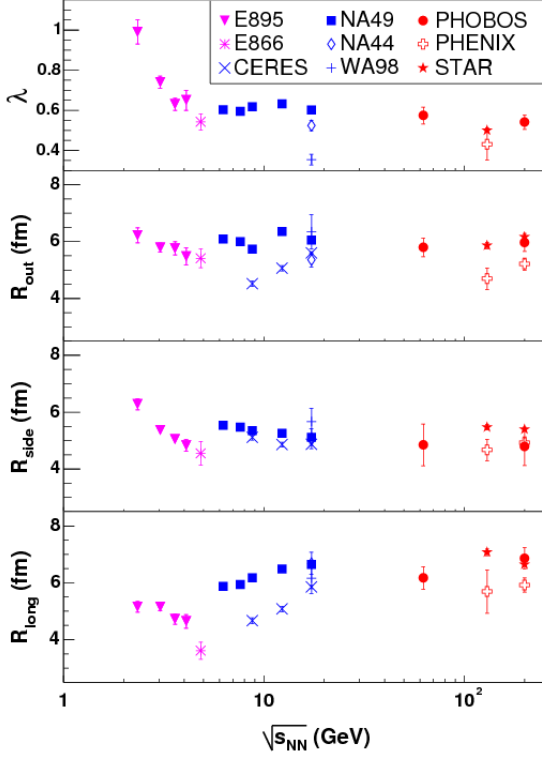
Figure 2.5: The figure shows HBT radii as a function of collision energy, with no significantly change over 2 orders of magnitude in collision energy. The figure is made by PHOBOS [19].
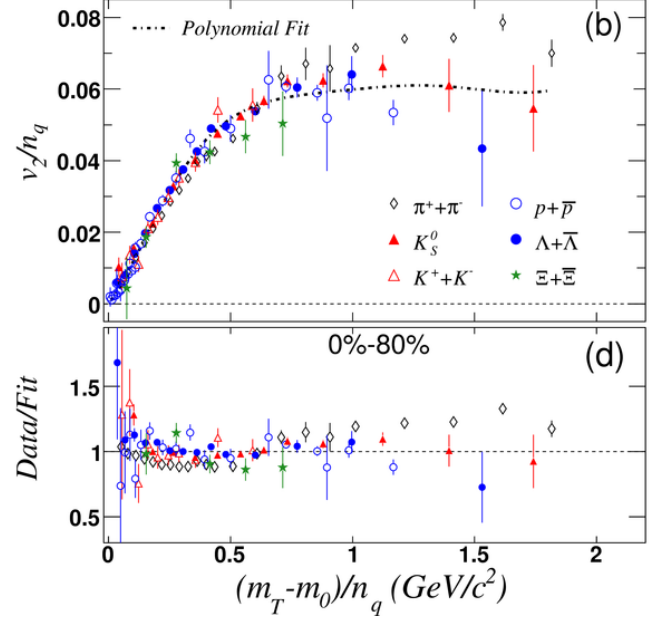
Figure 2.6: The figure shows quark scaled identified particle flow v_2/n_q as a function of $m_T - m_0)/n_q$, where n_q is the number of valence quarks in the particle, for Au+Au collisions at $\sqrt{s_{NN}} = 62.4$ GeV at mid-rapidity. Except for the pions they all show the same behaviour. Pions are thought to deviate since a substantial number of these are decay products from resonance particles at $p_T < 1.5$ GeV/c. This is further discussed by STAR [20], where the figure is taken from.

where λ represents the correlation strength, $\vec{q}$ is the pion pairs momentum difference and R is the radius. q_{long} is parallel to the beam axis, q_{out} is parallel to the mean transverse momentum of the pion pairs $(\vec{k_T} = 0.5(\vec{p_{T1}} + \vec{p_{T2}}))$ and q_{side} is perpendicular to q_{long} and q_{out}.

Measurements of these radii are similar to what was measured at the SPS, small radii, as shown in figure 2.5. The small radii have excluded many hydrodynamical models. Remarkably the radii do not change significantly from $\sqrt{s_{NN}} = 2$ GeV to $\sqrt{s_{NN}} = 200$ GeV. Though there are systematic deviations between the experiments, one cannot see any sharp discontinuities. A sharp discontinuity has been thought of as a QGP formation signature, if there is a first order transition between hadronic phase and the QGP. This is referred to as the "HBT puzzle".

Elliptic flow

Non–central heavy ion collisions will have an elliptical/"almond" shape in the overlapping region of the two nuclei, as shown in figure 2.1. This can cause a collective anisotropic flow of particles in the

azimuthal plane in the initial part of the collisions. This spatial anisotropy translates into momentum anisotropy. During the thermalisation, the partons go through multiple scatterings. The flow can be quenched by the multiple scatterings. A long thermalisation process could therefore quench the flow. Thus remaining elliptic flow, after freeze–out, will be a signature of early thermalisation.

The azimuthal distribution of particles can be decomposed into a Fourier expansion:

$$\frac{d^3 n}{p_{\mathrm{T}} dp_{\mathrm{T}} dy d\phi} = \frac{d^2 n}{2\pi p_{\mathrm{T}} dp_{\mathrm{T}} dy} \left(1 + 2 \sum_n v_n \cos(n\phi')) \right) \tag{2.8}$$

where ϕ' is the azimuthal angle of the particle relative to the reaction plane azimuthal angle. STAR has made such measurements in $\sqrt{s_{\mathrm{NN}}} = 62.4$ GeV Au+Au collisions, for a number of particles species, which is shown in figure 2.6. The elliptic flow is very large, suggesting that the created matter is thermalising very fast, even at this intermediate collision energy.

2.3 Jet suppression in $\sqrt{s_{\mathrm{NN}}} = 200$ GeV collisions at RHIC
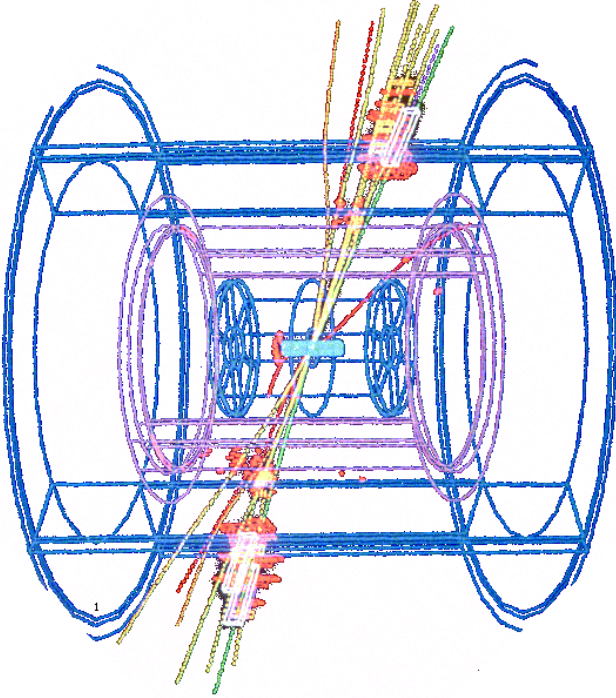
Figure 2.7: The figure shows a jet event from a $p + \bar{p}$ collision recorded with the UA2 detector. Two high p_{T} partons are produced azimuthally back–to–back, which then fragments into jets, visible as the coloured lines.

$p + \bar{p}$ (and also $p + p$) collisions produce jets as shown in figure 2.7. This jet event was recorded with the UA2 detector. Jets has also been searched for in the heavy ion collisions at RHIC. A jet is correlated p_{T} particles arising from the fragmentation of a high momentum parton. These leading high momentum partons originate from the initial hard scatterings of the incident partons. From momentum and energy conservations these partons must be produced in pairs, back–to–back. Measuring these can therefore reveal information about the matter that forms after the initial scatterings. Since the leading parton must traverse through this matter.

Figure 2.8 shows the correlation between triggering on a high p_{T} hadron and the azimuthal distribution, $\Delta\phi$, of the other hadrons from the same collision relative to the trigger particle. The peak around $\Delta\phi = 0$ shows that the trigger particle is accompanied by lower momentum fragments from the leading parton. From energy and momentum conservation one expects to see a peak $\Delta\phi = \pi$ radians away from the trigger hadron. This peak is clearly seen for $p+p$ and d+Au collisions. Amazingly there is no peak at all for central Au+Au

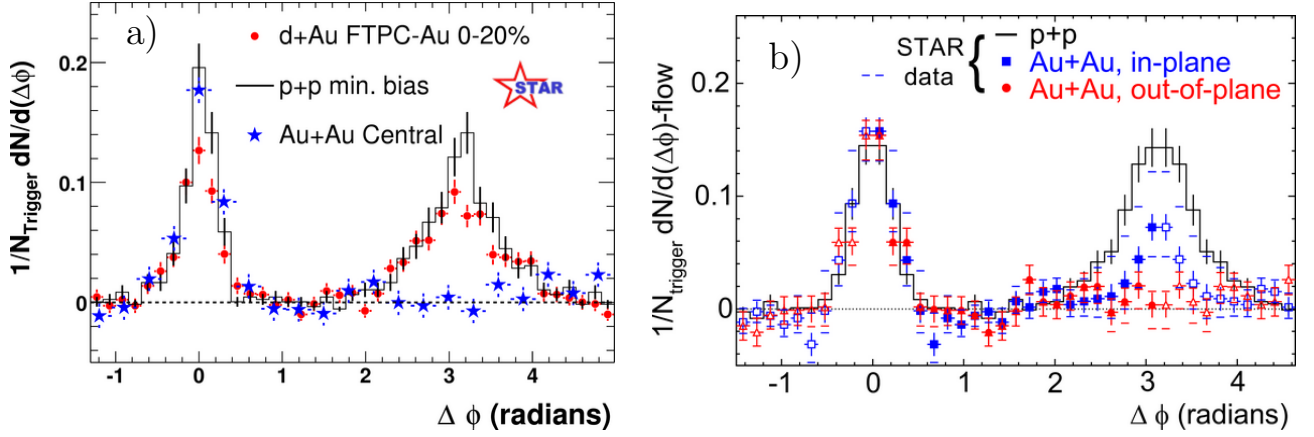Figure 2.8: The figure shows the azimuthal distribution of particles relative to the azimuthal angle of the high momentum trigger particle. The peak seen at $\Delta\phi = \pi$ radians away from the trigger particle represents the back–to–back nature of jets. Figure a) shows back–to–back correlation for $p+p$, central $d+$Au and central Au+Au collisions at $\sqrt{s_{\mathrm{NN}}} = 200$ GeV. Figure b) show two distributions in Au+Au mid–central collisions $(20\% - 60\%)$. One where the trigger particle is emitted in the event plane and the other when the trigger particle is emitted perpendicular to the event plane. In–plane jets show full suppression of the away–side jet, while only a little suppression is seen in out–of–plane jets. The flow contribution, see section 2.2, is subtracted from the distributions. The figures are made by STAR [7].

collisions. This means, in central Au+Au collisions, that one of the partons from the initial hard scattering loses all it momentum as it traverses the matter created in the collision. This then leads to a flat distribution of hadrons in the opposite direction of the high p_{T} trigger hadron. The figure also shows that the suppression of the away–side jet depends on the path length. When the leading parton is emitted in the reaction plane, having the shortest possible distance to travel before escaping the created matter, the away–side jet is visible. When the leading parton is emitted perpendicular to the reaction plane, having the longest possible distance to travel trough the created matter, the away–side jet disappears all together.

PHENIX has also studied the p_{T} dependence of the shape of the away–side jet, as shown in figure 2.9. They have studied the distribution by combining different p_{T} regions for the trigger particle and the away–side particles. The figure also shows a comparison of Au+Au and Cu+Cu collisions at $\sqrt{s_{\mathrm{NN}}} = 62.4$ GeV and 200 GeV. The away–side peak is suppressed at $\Delta\phi = \pi$ in central collisions, left and middle vertical row of panels of figure 2.9. No suppression is seen in peripheral collisions, right vertical row of panels. There are two indicated regions called "HR" (head–region) and "SR" (shoulder–region) in the left panels. In central collisions the away–side yield is enhanced in SR, $\Delta\phi = \pi \pm 1.1$, and suppressed in the HR, when the away–side momentum region is $p_{\mathrm{T}} < 3$ GeV/c. As the leading parton on the away–side propagates through the matter it generates a "Mach shock–wave" [21], which results in two smaller jets on the away–side. According to [22], the observed behaviour reflects the competition between matter induced modifications and jet fragmentation. These observations excludes other explanations, such as Gluon Čherenkov radiation and large angle gluon radiation.

The middle and right panel also reveal that the jet suppression has little dependence on the system
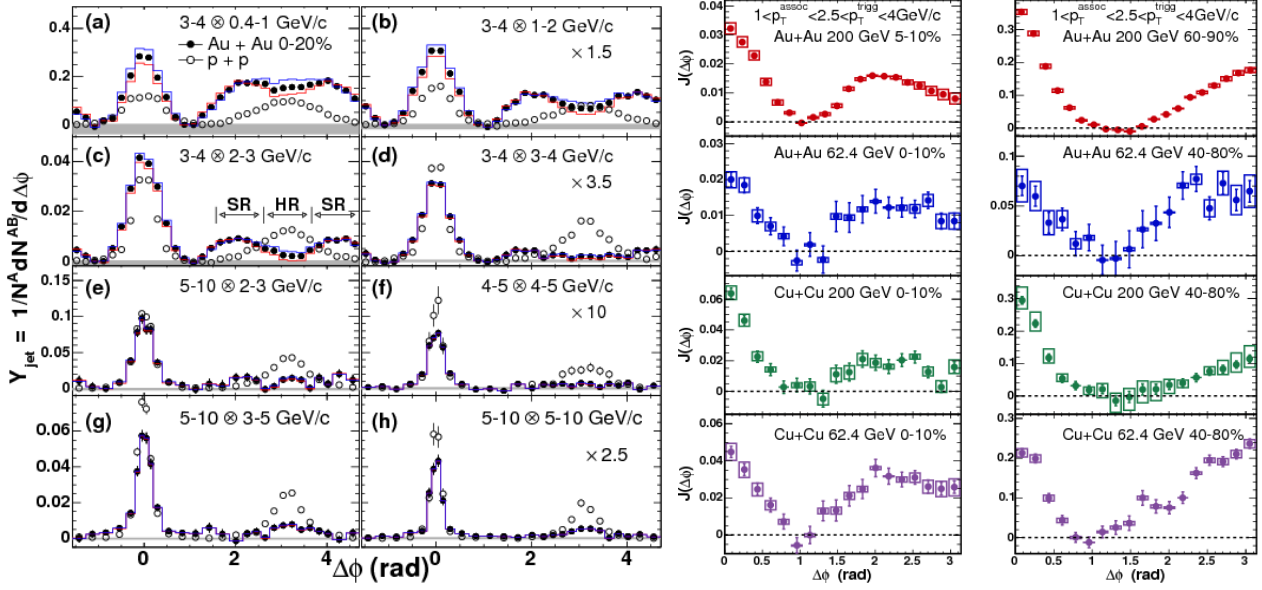
Figure 2.9: The figure shows azimuthal distribution of particles relative to the trigger particle, the "jet associated partner yield", see [22, 23] for a thorough description of Y_{jet} and $J(\Delta\phi)$. Different combinations of p_T regions for the trigger particle and for the away–side particles in minimum bias $p + p$ collisions and 0–20% central Au+Au collisions at $\sqrt{s_{NN}} = 200$ GeV are shown in the left panel. The away–side particles in $p+p$ collisions are seen for all combinations of p_T regions. Au+Au collisions only show high abundance of away–side particles when triggering in the 3-4 GeV/c momentum region and away–side particles having lower momentum. With the high momentum trigger region, 5-10 GeV/c, there are very few away–side particles. The middle panel show central collisions in Cu+Cu and Au+Au collisions at $\sqrt{s_{NN}} = 62.4$ GeV and 200 GeV, with the trigger particle's momentum range of 2.5-4 GeV/c and the associated particles in the 1-2.5 GeV/c momentum range. Panel (b), (d), (f), and (h) are scaled as indicated, for clarity. The right panel show the same as the middle panel except these are peripheral collisions. The peripheral collisions show an away–side peak at $\Delta\phi = \pi$, while the central have a local minimum there. Central collisions show a peak at $\Delta\phi \approx \pi - 1$. Elliptic flow has been subtracted from the distribution. The figures are made by PHENIX [22, 23].

size or collision energy. PHENIX argue in [23] that the observed behaviour indicate that the speed of sound in the created matter is between that expected in a hadron gas and QGP [24]. Also the data disfavours a first order transition of the created matter, which would cause a second away–side peak. This peak is not seen.

The jets in heavy ion collisions are clearly affected by the matter they traverse, as compared to $p + p$ collisions. This can be utilised by looking at the scaling behaviour of the transverse momentum spectra in heavy ion collisions relative to $p+p$ collisions. Measurements of high p_T particle suppression is further investigated in chapter 4. Scaling behaviour of high momentum particles, as a function of specie and energy will be investigated in this thesis.

Chapter 3

The physics behind relativistic heavy ion collisions

As shown in section 2.3, high momentum partons interact with the created matter in heavy ion collisions. pQCD (perturbative Quantum Chromo Dynamics) calculations for particles with $p_{\mathrm{T}} > 2$ GeV/c in nucleon–nucleon collisions, on a range of collision energies, have been able to reproduce the observed spectra [25]. Therefore the same calculations have been performed using particles in heavy ion collisions with the inclusion of matter, which the high momentum parton must traverse before being observed. This modification to the calculations are associated with initial and final state effects of a heavy ion collision. If one can disentangle the initial and final state effects through experimental observation, new knowledge about the QGP will appear. Unfortunately these two effects, are competing effects and experimental disentangling of these have so far been difficult.

A short overview will be given of the different initial and final state effects, and how they affect the experimental observables.

3.1 Elementary collisions

To understand the parton structure function of a proton, in the QCD parton model [26, 27], one can scatter a lepton (i.e. an electron) on a proton, as shown in figure 3.1. The kinematic variables in this interactions is:

- $q = k - k'$ is the four–momentum transfer, where k and k' is the momentum of a lepton, with mass m_l, before and after the interaction.

- p is the momentum of a proton, with mass 'M, before the interaction.

- W is the mass of the recoiling system of hadrons after the interaction.

- $x = Q^2/(2M\nu)$ (Bjorken scaling variable), where $\nu = q \cdot p/M$ is the lepton's energy loss, and Q^2 is the transverse squared momentum transfered by the virtual photon.

If the lepton's momentum loss and the transverse energy transfer is large, the proton is decomposed into it's constituent partons, (anti–) quarks and gluons. The interaction between the lepton and the
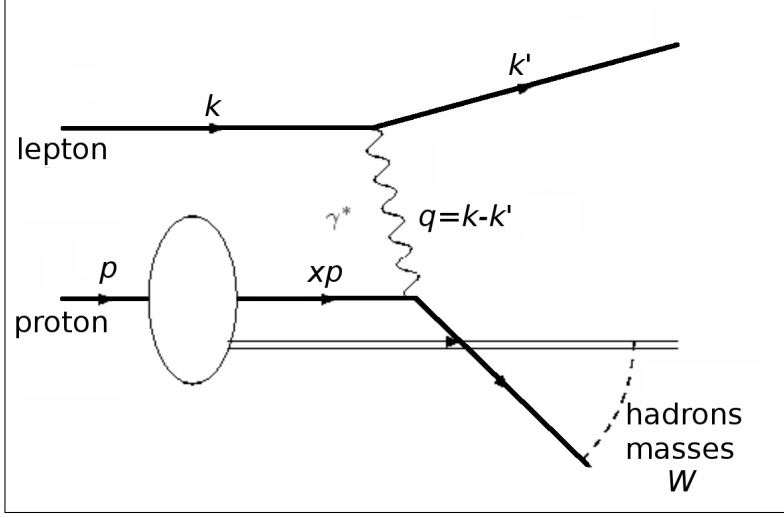
Figure 3.1: The figure shows a schematic view of a deep inelastic scattering of a lepton on a proton, through the exchange of a virtual photon γ^*. The lepton's and proton's initial momenta are k and p, respectively. After the scattering, their momenta are k'. xp is the momentum of the parton scattering with the virtual photon γ^*. The figure is taken from [28].

proton will be incoherent, and a differential cross–section for an unpolarised interaction can be written as [27]:

$$\frac{d^2\sigma}{dE'd\Omega} = \frac{4\alpha E'^2}{Q^4}\left(W_2(\nu, Q^2)\cos^2\frac{\theta}{2} + 2W_1(\nu, Q^2)\sin^2\frac{\theta}{2}\right) \tag{3.1}$$

where Ω is the solid angle, θ the lepton scattering angle, $E' = \sqrt{m_l^2 + k'^2}$. The functions, $W_{1,2}$, are called the dimensional structure functions of the proton. They contain the vertex of the recoiling hadrons, which are non–perturbative. The corresponding deep inelastic scattering of a spin $\frac{1}{2}$ object is shown in figure 3.1, where the lepton exchanges a virtual photon with a parton in the proton. This can be written as:

$$\frac{d^2\sigma}{dE'd\Omega} = \frac{4\alpha E'^2}{Q^4}\left(\cos^2\frac{\theta}{2} + \frac{Q^2}{4M^2}\sin^2\frac{\theta}{2}\right)\delta\left(\nu - \frac{Q^2}{2M}\right) \tag{3.2}$$

Equation 3.1 and 3.2 are very similar and from a comparison one can extract a functional form of the proton's dimensional structure functions W_1 and W_2:

$$W_1(\nu, Q^2) \equiv \frac{Q^2}{4M^2}\delta\left(\nu - \frac{Q^2}{2M}\right) \tag{3.3}$$

$$W_1(\nu, Q^2) \equiv \delta\left(\nu - \frac{Q^2}{2M}\right) \tag{3.4}$$

W_1 and W_2 can also be written as dimensionless quantities [27, 29]:

$$F_1(x, Q^2) \equiv MW_1(\nu, Q^2) \tag{3.5}$$

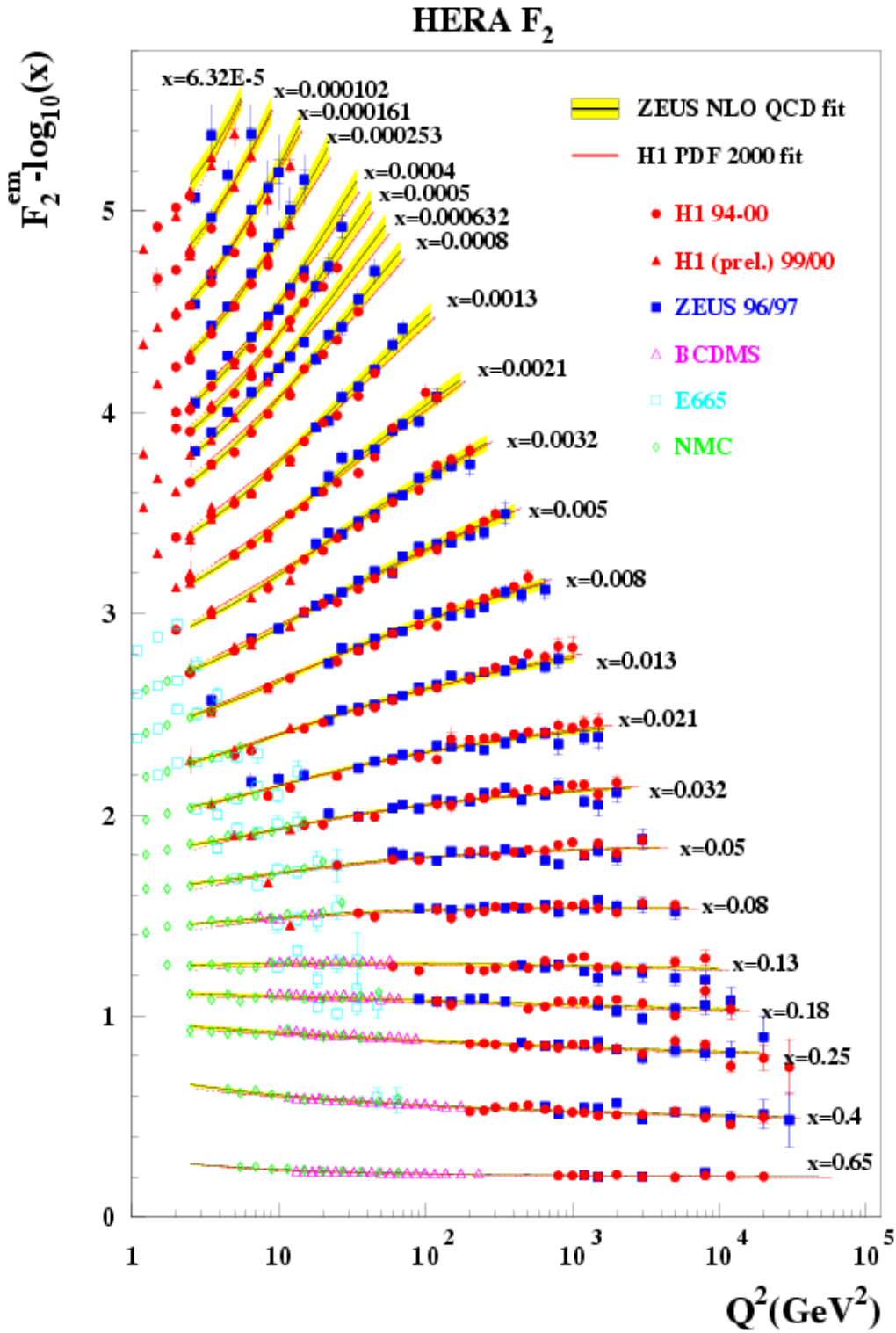$$F_2(x, Q^2) \equiv \nu W_2(\nu, Q^2) \tag{3.6}$$

Figure 3.2: The figure shows the structure functions measured by the ZEUS and the H1 experiment at HERA. pQCD calculations/fits are shown as the solid lines. pQCD have increasing difficulty describing the lower-x data. The figure is from [30].

where F_1 and F_2 are called structure functions. Measurements of F_2 can be seen in figure 3.2. The figure shows that pQCD is able to describe this data. F_1 and F_2 are independent of Q^2 when ignoring logarithmic effects from the strong interaction (high momentum transfers Q^2), and reduces to:

$$F_2(x) = 2xF_1(x) = \sum_i e_i^2 x \left(q_i(x) + \bar{q}_i(x) \right) \tag{3.7}$$

where i is the sum over flavours, $\bar{q}_i(x)$ and $q_i(x)$ are the anti–quark and quark number density, and e_i is the (anti–) quark fraction of the proton's electric charge. $f(x) = q(x) + \bar{q}(x)$ is called the parton distribution functions. It is interpreted as the probability of finding a parton with momentum faction x within the nucleon. The lepton is acting as a probe into the proton.

The cross–section for inclusive hadron production in a $p + p$ collision is more complicated than $e + p$ collisions. Since both reaction partner contains partons, the cross–section is written in terms of the parton distribution function $f(x, Q^2)$, $p + p \rightarrow h + X$ [25]:

$$\frac{d\sigma^{pp}}{dy d^2 p_{\mathrm{T}}} = K \sum_{abcd} \int_0^1 \int_{x_a^{min}}^1 \int_{x_b^{min}}^1 f_a(x_a, Q_b^2) \cdot f_b(x_b, Q_b^2) \cdot \frac{d\sigma^{ab \rightarrow cd}}{d\hat{t}} \cdot \frac{D_{h/c}^0(z_c, Q_c^2)}{\pi z_c^2} dx_b dx_a dz_c \tag{3.8}$$

where K is a phenomenological factor, which is used to correct for higher order QCD corrections in jet production, when performing pQCD calculations. Typical values for K are $1 - 4$. The sum is over hard scatterings $a + b \rightarrow c + d$. $d\sigma^{ab \rightarrow cd)}/d\hat{t}$ is the hard parton–parton cross–section to produce the outgoing partons c and d, with $\hat{t} \equiv (p_a - p_c)^2$ the invariant momentum transfer from parton a to parton c (Mandelstam variable). $d\sigma(ab \rightarrow cd)/d\hat{t}$ can be calculated in leading order or next to leading order pQCD. $D_{h/c}^0(z_c, Q_c^2)$ is the fragmentation function, the probability that parton c fragments into a hadron with momentum fraction $z_c = p_h/p_c$, which is the momentum fraction of the final, observable hadron.

Quark and gluon fragmentation functions are not equal. As an example, the coupled differential equations for photon production is given by [25]:

$$\frac{dD_{\gamma/q_i}(z_\gamma, Q^2)}{d\hat{t}} = \frac{e_i^2 \alpha}{2\pi} \frac{1 + (1 - z_\gamma)^2}{z_\gamma} + \frac{\alpha_s(Q^2)}{2\pi} \int_{z_\gamma}^1 \left(D_{\gamma/q_i}(z, Q^2) P_{qq}(\frac{z_\gamma}{z}) + D_{\gamma/g}(z, Q^2) P_{gq}(\frac{z_\gamma}{z}) \right) \frac{dz}{z} \tag{3.9}$$

$$\frac{dD_{\gamma/g}(z_\gamma, Q^2)}{d\hat{t}} = \frac{\alpha_s(Q^2)}{2\pi} \int_{z_\gamma}^1 \frac{1}{z} \sum_{i=0}^{2f} \left(D_{\gamma/q_i}(z, Q^2) P_{gq}(\frac{z_\gamma}{z}) + D_{\gamma/g}(z, Q^2) P_{gg}(\frac{z_\gamma}{z}) \right) dz \tag{3.10}$$

where where e_i is the factional charge of quark i, f is the number of quark flavours, α_s is the strong coupling constant, α is the QED coupling constant, and the functions P_{qq}, P_{gg}, and P_{gq} are splitting functions [29]. For hadronic end products the equations become more complicated, see e.g. [31] for the calculation of pion and kaon fragmentation functions.

A simple set of fragmentation functions can be used when single particle cross–sections and two particle correlations are considered [25]. They do not give an adequate description if all the hadronisation processes, from all the partons, are considered at once. Perturbative techniques are good at

describing experimental measurements for high z_c. Fragmentation functions are compared to $e^+ + e^-$ annihilation processes, to confirm their accuracy. The many fragmentation processes in a $p+p$ collisions makes the cross–section drastically change from $e + p$ collisions, as the set of fragmentation functions needed to describe all possible processes increases drastically. Equation 3.8 factorises soft and hard scattering, where the soft term is represented in the parton distribution functions. These cannot be calculated by QCD, as these partons are confined inside the nucleon and in a non–perturbative state. This also contributes to the abrupt change in cross–section for $p + p$ compared to $e + p$ collisions. The parton distribution functions have to be determined experimentally.

The following section will describe the relation between the measurement of high $p_{\rm T}$ particles in $p + p$ collisions and A+B collisions, and the theoretical argument how it can be done.

3.2 R_{AA}, R_{cp}, and number of binary collisions

Nuclear modification factor, R_{AA}

To be able to compare heavy ion collisions with nucleon–nucleon collisions, one has to understand the scaling behaviour between these two systems. The cross–section for hard scattering in a $p + p$ collision determined from "leading logarithm" pQCD can be written as [5, 25]:

$$\frac{d^3\sigma}{dx_a dx_b d\cos\theta^*} = \frac{1}{s} \sum_{ab} f_a(x_a) f_b(x_a) \frac{\pi \alpha_s^2(Q^2)}{2x_a x_b} \Sigma^{ab}(\cos\theta^*) \tag{3.11}$$

$$\alpha_s^2(Q^2) = \frac{\alpha_0}{1 + \frac{\alpha_0}{12\pi}(11 n_c - 2n_f) \log \frac{Q^2}{\Lambda^2}} \tag{3.12}$$

where $\alpha_s^2(Q^2)$ is the "running" strong coupling "constant" at four–momentum transfer Q^2, where Λ is a scale constant and $\Lambda \ll Q$, n_c is the number of colour charges (3) and n_f is the number of quark flavours. The sum in the cross–section equation is over the parton reactions $a + b \to c + d$. θ^* is the scattering angle in the parton–parton center of mass system, and s is the collision energy ($\sqrt{s_{\rm NN}}$) squared. The equation gives the $p_{\rm T}$ spectrum of the outgoing parton c. The hard scattering generates a parton with high momentum.

Since the hard scattering is point–like and the total cross–section factorises as shown in eq. 3.11, a $p+A$ collision should have a cross–section proportional to the number of possible point–like encounters. For $A + B$ colliding at impact parameter b, the cross–section should be proportional to the nuclear overlap function, $T_{AB}(b)$. If this scaling is true, the relationship between cross–sections for collisions of $A + B$ collision and $p + p$ is:

$$\frac{d^2 N_{AB}}{dp_{\rm T} dy}\bigg|_b = T_{AB}(b) \frac{d^2 \sigma_{pp}}{dp_{\rm T} dy} \tag{3.13}$$

If there are any initial or final state effects, induced by the created matter, this scaling might not be correct. Therefore studying the ratio of the right hand side to the left hand side can reveal

information about the created matter. The nuclear modification factor, R_{AB} is defined as:

$$R_{AB} = \frac{\frac{dN^2_{AB}}{dp_{\mathrm{T}} dy}}{\langle N^{AB}_{\mathrm{coll}}\rangle \cdot \frac{dN^2_{pp}}{dp_{\mathrm{T}} dy}} \tag{3.14}$$

where $\langle N^{AB}_{\mathrm{coll}}\rangle = \langle T_{AB}\rangle \cdot d^2 N_{pp}/d^2\sigma_{pp}$, is the average number of incoherent binary collisions for a given centrality in an $A + B$ collision. (If the collision is symmetric, R_{AA} will be written instead of R_{AB}.) Studying this distribution can reveal the underlying physics in heavy ion collisions. The low p_{T} part of the nuclear modification factor tells about the bulk properties and is expected to scale with the number of participants, $\langle N_{\mathrm{part}}\rangle$ and not $\langle N_{\mathrm{coll}}\rangle$. The high p_{T} part can be used for tomography of the matter created in the collision (see section 3.3.4). Alternatively, if $R_{AB} = 1$, nuclear collisions are just a superposition of $p + p$ collisions.

Central–to–peripheral ratio, R_{cp}

If $p+p$ collision distributions are not available, a different ratio can be constructed, called the central–to–peripheral ratio, R_{cp}. This ratio uses the peripheral collisions to construct the reference spectrum. The spectrum in the numerator and the denominator are both scaled with their corresponding number of incoherent binary collisions. The R_{cp} is thus defined as:

$$R_{cp} = \frac{\langle N^{peri}_{\mathrm{part}}\rangle \cdot \frac{dN^2_{cent}}{dp_{\mathrm{T}} dy}}{\langle N^{cent}_{\mathrm{coll}}\rangle \cdot \frac{dN^2_{peri}}{dp_{\mathrm{T}} dy}} \tag{3.15}$$

where $\langle N^{cent}_{\mathrm{coll}}\rangle$ and $\langle N^{peri}_{\mathrm{coll}}\rangle$ are the average number of incoherent binary collisions in the central and peripheral centrality bins, respectively.

The number of participants and binary collisions

The number of binary collisions that occur when colliding heavy ions is calculated using a so–called Glauber model [32]. There are two common methods: Monte Carlo simulation, and Optical model calculation. The BRAHMS collaboration uses an optical Glauber model, together with the Hijing (Heavy Ion Jet INteraction Generator [33]) event generator, to perform this calculation. A Wood–Saxon number density profile is used to describe the density of nucleons in a nucleus:

$$\rho(r) = \frac{\rho_0}{1 + e^{\frac{r-r_0}{c}}},$$
$$\text{with } {}^{197}\mathrm{Au}: c = 0.535 \pm 0.027 \text{ fm}, r_0 = 6.38 \pm 0.06 \text{ fm}, \rho_0 = 0.169 \text{ fm}^3 \tag{3.16}$$
$${}^{63}\mathrm{Cu}: c = 0.586 \pm 0.018 \text{ fm}, r_0 = 4.214 \pm 0.026 \text{ fm}, \rho_0 = 0.169 \text{ fm}^3$$

where r is the distance from the center of th nucleus. Integration of this density profile gives the number of nucleons in the nucleus: $4\pi \int \rho(r) r^2 dr = 63$ and 197 for Cu and Au, respectively. The

constants for the Wood–Saxon potential are taken from [34], and were obtained from the results of measurements scattering electrons on heavy ions.

The nuclear overlap function, T_{AB}, for the two colliding nuclei is:

$$T_{AB}(b) = \frac{1}{N} \int \rho_1(\vec{s}, z_1) \cdot \rho_2(\vec{s} - \vec{b}, z_2) d^2 s dz_1 dz_2 \qquad (3.17)$$

where $\vec{s}$ is a vector perpendicular to the beam axis, z_1 and z_2 are coordinates along the Z axis, and $N = \int T_{AB}(b) d^2 b$ is a normalisation constant.

The probability for n interactions in a collision with impact parameter b can then be calculated from the nuclear overlap function and the $p + p$ cross–section:

$$P(n, b) = \binom{AB}{n} (\sigma_{pp} T_{AB}(b))^n \cdot (1 - \sigma_{pp} T_{AB}(b))^{AB-n} \qquad (3.18)$$

where A and B is the number of nucleons in each of the nuclei and σ_{pp} is the cross–section for a $p + p$ collision. For $p + p$ collisions at $\sqrt{s_{\mathrm{NN}}} = 62.4$ GeV one measures $\sigma_{pp} = 36 \pm 1$ mb. This assumes that $p + p$ and $p + \bar{p}$ cross–sections are the same, as described in [35].

The number of incoherent binary collisions, $\langle N_{\mathrm{coll}} \rangle$ and the number of participants $\langle N_{\mathrm{part}} \rangle(b)$ is then given as:

$$\langle N_{\mathrm{coll}} \rangle(b) = \sigma_{pp} \cdot A \cdot B \cdot T_{AB}(b) \qquad (3.19)$$

$$\langle N_{\mathrm{part}} \rangle(b) = 2A \int T_{AB}(\vec{s}) \left(1 - \left(1 - \sigma_{pp} \cdot T_{AB}(\vec{s} - \vec{b}) \right)^{AB} \right) d^2 s \qquad (3.20)$$

The $\langle N_{\mathrm{coll}} \rangle$ and $\langle N_{\mathrm{part}} \rangle$ are shown in table 6.1 and 8.1. These calculations were inspired by [36].

3.3 Nuclear modifications

There are several models that try to explain a deviation from 1 of R_{AB} at high momentum and at low and high collision energies. The lowest momentum part of the R_{AB} is believed to scale with the number of participants in the incident nuclei. These particles do not originate from the initial hard scatterings, but are produced at the later times, in the hadronic expansion phase up to freeze–out. The low momentum part of the R_{AB} should saturate at $R_{AB}(p_{\mathrm{T}} < 0.2) \approx \langle N_{\mathrm{part}} \rangle / (2 \langle N_{\mathrm{coll}} \rangle)$, as can be seen in figure 3.3. With increasing p_{T}, the initial hard scatterings of the incident partons becomes more important and dominates the particle production at $p_{\mathrm{T}} > 4$ GeV/c. The following section gives a brief description of of initial and final state effects.

3.3.1 "Cronin" Enhancement from multiple scattering or recombination

In the mid 70s it was discovered by Cronin et al. [38, 39] at FERMILAB that high p_{T} particle production in p+A collisions at $\sqrt{s_{\mathrm{NN}}} = 21$ GeV is enhanced beyond the simple binary collision scaling
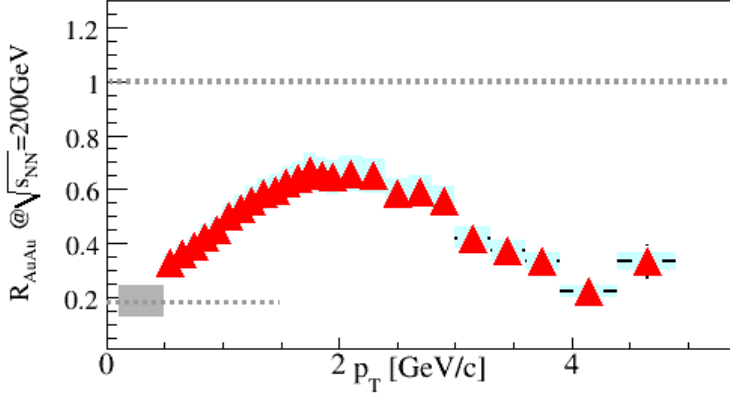
Figure 3.3: The figure shows the nuclear modification factor for 0–10% central Au+Au collisions at $\sqrt{s_{\mathrm{NN}}} = 200$ GeV. The low p_{T} region approaches the scaling with $\langle N_{\mathrm{part}} \rangle$, denoted by the lower dotted line. The data are measured by the BRAHMS experiment [37].

of $p + p$ collisions. This enhancement is commonly referred to as the Cronin effect. Traditionally this effect was parametrised as:

$$E\frac{d^3\sigma^{pA}}{dp^3} = E\frac{d^3\sigma^{pp}}{dp^3}\langle N_{\mathrm{coll}}\rangle^{\alpha(p_{\mathrm{T}})} \tag{3.21}$$

where $\langle N_{\mathrm{coll}}\rangle$ is the number of incoherent binary collisions, and $\alpha(p_{\mathrm{T}})$ is a fit parameter. $\alpha(p_{\mathrm{T}}) > 1$ means enhancement. The effect on the R_{AA} can be seen in the left panel of figure 4.1, where the R_{AA} value exceeds 1 for $p_{\mathrm{T}} \gtrsim 3$) GeV/c. This means that the high p_{T} regions of the spectra show an increase compared to binary scaling. The effect has two possible explanations: multiple scattering and/or parton recombination in the created matter as it thermalises.

The incident partons carry large longitudinal momenta, and small transverse momenta. As the partons travel through the nuclear matter in the initial phase of the collision, they will undergo multiple soft scatterings. This transfers some of their longitudinal momenta into the transverse direction. Finally, the partons undergo hard parton–parton scatterings. The shift in momenta results in a p_{T} broadening of the incident partons which finally leads to an enhancement of $1 < p_{\mathrm{T}} < 4$ GeV/c particles. X. N. Wang [40] describes this as a lowering of the cross–section for hard scattering (e.g. forward), thereby making it more likely that the parton will acquire its transverse momentum component from two successive scatterings.

Parton recombination can also produce the "Cronin" enhancement [41]. However, as opposed to multiple scattering, this is a final state effect. This model is more applicable for higher energy collisions, such as those at the RHIC energies. With much higher multiplicity and temperature, these collisions have a bigger fraction of the particles produced at moderate p_{T}. R. C. Hwa and C. B. Yang suggest in [41] that these particles come from thermalised partons and that they are produced through parton recombination/coalescence. Jets could also contribute to the production of the moderate p_{T} particles. The "Cronin" effect should become negligible at very high p_{T}, as seen for $R_{d\mathrm{Au}}$ in figure 4.4, and also be strongly reduced with increasing rapidity, as the BRAHMS measurements in [42] indicates.

3.3.2 Nuclear shadowing

Nuclear shadowing is a phenomenon arising from the difference of the parton structure function of a "free" nucleon and of a nucleon bound inside a nucleus. This was first observed in deep inelastic scattering by the EMC (European Muon Collaboration) [43]. Shadowing is manifested as a depletion of low-x partons (x is the fraction of the nucleon momentum carried by the parton) in the bound nucleon, as compared to a free nucleon.

The nucleons inside the nucleus are tightly bound, making their wave functions act coherently and cause interesting effects to the parton structure function of a nucleon in a nucleus. This phenomenon was observed in the following way. The differential cross–section for a one–photon scattering from a lepton on a nucleus can be written as:

$$\frac{d\sigma_{1\gamma}^2}{dxdQ^2} = \frac{F_2(x, Q^2)}{xQ^4} \cdot k(x, Q^2) \tag{3.22}$$

where $-Q^2$ is the four momentum of the virtual photon exchange between the lepton and the target. $k(x, Q^2)$ is independent of the nuclear mass [44, 45]. The ratio of the measured cross–sections for a nucleon[1] and a nucleus is shown in figure 3.4. This ratio is the same as F_2^A/F_2^N.

The top panel show a schematic drawing of the ratio of the structure functions, F_2^A/F_2^D, along with data in the bottom panel. The shadowing region is $x < 0.05$. When probing the nucleus from a high momentum reference frame, the parton wave functions are overlapping with partons from other nucleons in the nucleus. The overlap will increase with the momentum of the reference frame, or with decreasing x, as the probe "sees" increasing number of gluons. Thus partons from different nucleons can fuse and enhance the number of high-x partons and reducing the number of low-x partons. At low enough x the gluon density will saturate, as described in section 3.3.3.

Three other regions are denoted in the top panel in figure 3.4, "enhancement, "EMC effect" and "Fermi smearing". Due to momentum conservation in the nucleon, for $0.07 < x < 0.15$ the ratio slightly exceeds 1, as the total momentum must add up to the nucleon momentum. This enhancement is called anti–shadowing. The next range, $0.15 < x < 0.8$, show again a depletion in the structure function for a nucleon in a nucleus compared to the free nucleon. This region, discovered by the EMC collaboration [43], has most of the nucleons momentum in the valence quarks. The valence quarks' wave functions could be distorted from the neighbouring nucleons, thus showing the depletion. This is the EMC effect. The highest part of the distribution, $x > 0.8$, again exceeds 1. This is possible because the kinematic limit in a nucleus is $x = A$. A parton can get $x > 1$ if it is a high-x parton which receives an additional "kick" from a parton from a different nucleon, e.g. caused by the "Fermi" motion of the nucleons. The region is called Fermi–smearing. A theoretical and experimental review on shadowing can be found in [47].

3.3.3 Saturation

D. Kharzeev and M. Nardi gives an overview of the saturation phenomena in [48]. This occurs when the number of partons in a nucleus, viewed from a high momentum reference frame, try to fill up a bigger area than the size of the nucleus. The nucleus is high Lorentz contracted, and all the parton

---

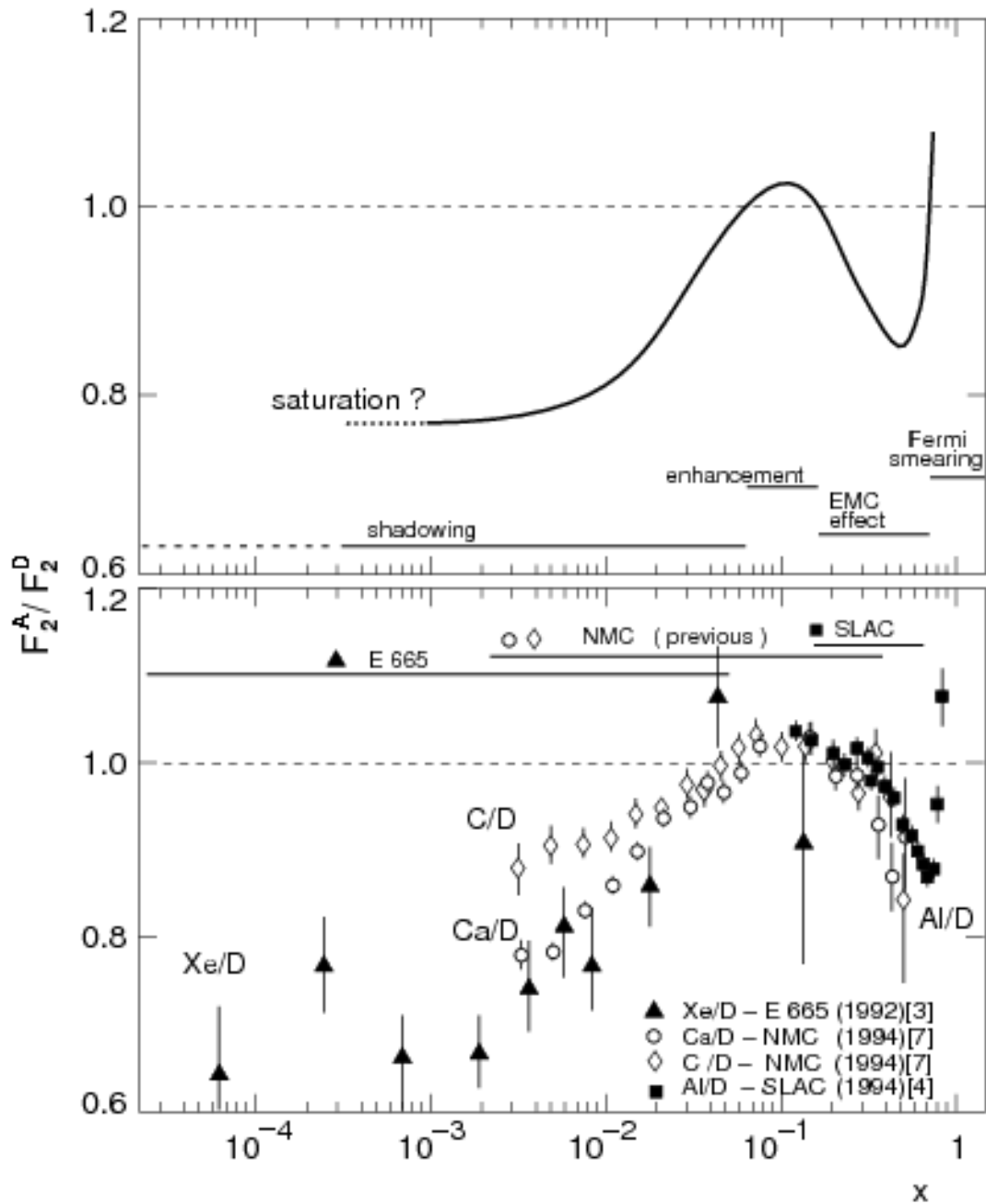[1]The reference, or free nucleon, structure function is deuterium.

Figure 3.4: The top panel show as schematic drawing of the ratio of parton structure function in a large nucleus compared to a deuteron. Also denoted under the graph are four x-regions. $x < 0.07$ is the shadowing region, $0.07 < x < 0.15$ is the anti–shadowing or enhancement region, $0.15 < x < 0.8$ is the EMC effect region, and $x > 0.8$ is the Fermi–smearing region. The bottom panel shows measurements from several experiments. The figure is from [46].

are confined in a thin sheet. If a parton has a transverse momentum Q it will occupy a space of π/Q^2, derived from Heisenberg's uncertainty principle. This makes it possible to calculate the "maximum" number of partons inside the nucleus. The partons cross–section is $\sigma \sim \alpha_s(Q^2)\frac{\pi}{Q^2}$. The transverse area of the nucleus is $S_A \sim \pi R_A^2$, so the "maximum" number of partons in this area is:

$$N_A \sim \frac{S_A}{\sigma} \sim \frac{Q^2 R_A^2}{\alpha_s(Q^2)} \tag{3.23}$$

If the number of partons becomes $> N_A$, they will overlap in space, and will interact with each other. Solving equation 3.23 for Q gives the saturation scale:

$$Q_s \sim \alpha_s(Q^2)\frac{N_A}{R_A^2} \sim A^{1/3} \tag{3.24}$$

With x being the fraction of the nucleus momentum carried by a parton, decreasing x increases the number of partons. Using an empirical parameter λ the saturation scale should go as $Q_s \sim A^{1/3}x^{-\lambda}$. In [49], fits to data from HERA were performed, scattering virtual photons on protons, resulting in $\lambda \approx 0.3$. This approach gives a good description at midrapidity.

D. Kharzeev and M. Nardi then calculates the number of partons produced in a heavy ion collision:

$$\frac{d^2N}{d^2bd\eta} = k \cdot \frac{n_c^2 - 1}{4\pi^2 n_c} \cdot \frac{1}{\alpha_s} \cdot Q^2 \tag{3.25}$$

where η is the pseudorapidity and k is the "partition liberation" coefficient accounting for the transformation of virtual photons in the initial state to the on–shell partons in the final state. They find that $k = 1.23 \pm 0.20$ from comparison to RHIC data, which is close to unity. Saturation plays an important role in the CGC (Colour Glass Condensate) theory which is described in section 3.4.

3.3.4 Jet quenching

Jets are created from high momentum partons originating from initial hard scatterings in a nucleon–nucleon or nucleus–nucleus collision. High momentum partons moving through a QGP will loose energy through colour interactions with the constituents of the matter [50, 51, 52]. The interactions are multiple elastic scatterings and gluon radiation. The energy loss, ΔE, in the limit of an optically thick QGP, was found to increase quadratically with distance, L, travelled:

$$\Delta E \approx \frac{\alpha_s}{2}\frac{\mu^2}{\lambda}L^2 \tag{3.26}$$

where μ^2 is the Debye screening mass for colour electric fields in the plasma and λ is the gluon mean free path length. This calculation has been improved in [53, 54, 55]. The authors introduced finite opacity [53, 54] and a opacity expansion [55]. This changes the quadratic path length behaviour, in particular for collision energies below the RHIC maximum energy ($\sqrt{s_{\mathrm{NN}}} = 200$ GeV). The energy loss
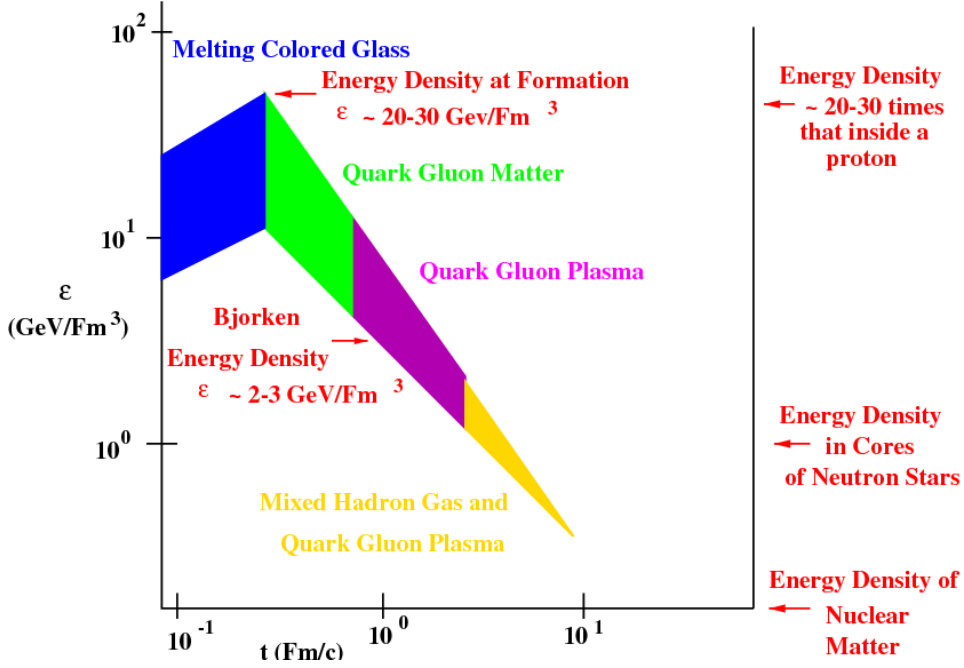
Figure 3.5: The figure shows the evolution of two colliding nuclei described by the CGC. This is equivalent of two sheets of glass colliding, which then melts creating a volume of high energy density. The created matter then cools down and goes through the phases described by the different colours in the figure. The figure is from [57].

is still larger than the energy loss in hadronic matter. Calculations in [56] also show that the energy loss depends on the density of the matter. The energy loss leads to a suppression of high momentum particles relative to $\langle N_{\text{coll}}^{AB} \rangle$ scaled nucleon–nucleon collision, where no matter is created. High p_{T} particles can therefore be used for tomographic measurements of the created matter. If the initial parton momentum distribution is known, measuring the produced particles momentum distribution will reveal information on the length travelled by the parton in the created medium and/or how much of it's momentum dissipated into the QGP.

3.4   The CGC and the sQGP

The Colour Glass Condensate

The CGC is a theoretical QCD description of the partonic matter in a nucleon in a high momentum reference frame. QCD evolution equations describe the gluon density measured in deep inelastic scattering. Traditionally these equations are linear [58, 59], which becomes a problem with decreasing x, resulting in the "infrared problem". This means that the gluon density and cross–section diverge (increase at low-x). This is physically impossible, the gluon density must saturate. DGLAP [60, 61, 29] equations were developed to solve the "infrared problem". The explanation to saturation, in the CGC theory using the DGLAP evolution equations, is gluon fusion or recombination. Since the the number

of gluons is saturated, they will act highly coherently like a condensate. In a high momentum reference frame the time scales are Lorentz dilated. The low-x gluons are generated from gluons with large x, which are Lorentz time–dilated. This causes the evolution of the gluons to appear slow from a non–dilated reference frame, e.g. the lab frame. This is reminiscent of the property of ordinary glass, and is called colour glass since it contains colour charges.

The CGC describes the partition functions for $x \lesssim 10^{-2}$ gluons. The CGC also calculates the saturation scale, Q_s, in momentum transfer between the gluons. For momentum transfers $\lesssim Q_s$, the production of gluons saturates at a density of $\sim 1/\alpha_s$.

By using the CGC theory, the initial condition/state of the colliding nucleus is known, and even better it is described by QCD. Illustrated in figure 3.5 is the evolution of a heavy ion collision if the incident nucleus is described by the CGC theory.

The strongly interacting quark gluon plasma, sQGP

Before the RHIC started colliding heavy ions, it was expected that $\sqrt{s_{\mathrm{NN}}} = 200$ GeV collisions would create a weakly interacting quark gluon plasma. The quarks would be asymptotically free, and the strong coupling constant, $\alpha_s \ll 1$, This would make it possible to perform perturbative calculations to describe the QGP, and being simpler in it's structure than the QCD "vacuum". The first 4 years of RHIC measurements revealed results that could not only be described by pQCD, though the high momentum measurements could. Thus the created matter was given an new name: sQGP. In [57] M. Gyulassy and L. McLerran argue that there are 3 criteria for the formation of sQGP:

1. Matter at energy densities so large that the simple degrees of freedom are quarks and gluons. This energy density is that predicted by lattice gauge theory for the existence of a QGP in thermal systems, and is about 2 GeV/fm^3 .

2. The matter must be to a good approximation thermalised.

3. The properties of the matter [...] while it is hot and dense must follow from QCD computations based on hydrodynamics, lattice gauge theory results, and perturbative QCD for hard processes such as jets.

They conclude in this article: "All of the above are satisfied from the published data at RHIC... This leads us to conclude that the matter produced at RHIC is a strongly coupled quark–gluon plasma (sQGP) contrary to original expectations that were based on weakly coupled plasma estimates." From the results presented in chapter 2, these criterias indeed appear to be met. Measurements of energy density, from Bjorken estimation indicates $\epsilon_{Bj} > 5$ GeV/fm^3 as discussed in section 2.2, and high degree of thermalisation, as deduced from the v_2 azimuthal anisotropy discussed in section 2.2, consolidate the first two points.

Whether or not the third point is met, the most rigorous of the three, is still under discussion. Point number 3 clearly dictates that all measurements should be reproduced by calculations.

In [62] E. Shuryak argues that the created matter is strongly coupled since the viscosity to entropy ratio is the lowest ever observed, $\eta/s \sim 10^{-1}$, making it an "ideal fluid" and not a gas. The observed large elliptic flow at the RHIC con only be explained by a strongly coupled matter. The same hydrodynamic behaviour has been observed in super–cooled Li^6 atoms, which behaves like a strongly

coupled Fermi or Bose gas. The plasma's constituents can also be bound at temperatures above the critical temperature, T_c, even for large bound states as the ρ, ω, ϕ meson (it could also contain coloured, bound quasi–particles). This is confirmed by measurements. This is not possible in a deconfined, weakly interacting QGP, where these particles should not exist.

J. L. Nagle discusses in [63] whether this matter is strongly interaction or strongly coupled. A plasma's coupling is given as: $\Gamma = \langle E_p \rangle / \langle E_k \rangle$, where E_p is the potential energy from the $1/r$ term in equation 1.1, and E_k is the kinetic energy. Electromagnetic plasmas with $\Gamma \ll 1$, behave as a gas. $\Gamma \gg 1$ is characteristic of a plasma that is strongly coupled and which behaves like a low viscosity liquid, a "near perfect liquid". Calculation of Γ in RHIC top energy collisions [64], resulted in $\Gamma \simeq 1.5 - 5$ with a plasma temperature of $T = 200$ MeV.

What empirically confirms the plasma to be strongly interacting is that it is strongly bound through a large α_s. This is a result of the interpretation of the suppression of jets and high p_T particles. By calculating the jet quenching with leading order pQCD, as in [56], and making it reproduce R_{AA}, they calculate the gluons rapidity density to be $dN/dy \sim 1000$. But as J. L. Nagle say: "However another approach is to say you know the color charge density and can then infer the coupling strength. This then implies that the coupling strength is much larger than predicted from the effectively leading order perturbative calculation — which may be consistent with the sQGP description."

3.5   The transfragmentation region

R. C. Hwa and C. B. Yang [65, 66] have done calculations on parton recombination in heavy ion collisions, in what they refer to as the transfragmentation region (TFR). The region is defined as $0.6 < x_\text{F} < 1.2$ or roughly $\eta' = \eta - y_{beam} > 0$, where $x_\text{F} = 2p_\text{L}/\sqrt{s_\text{NN}}$ is called Feynman-x. The calculation were inspired by the multiplicity measurement published by PHOBOS [67] for a range energies. As can be seen in figure 3.6, the multiplicity extends to $\eta' > 0$. Momentum conservation forbids particle production in this region in $p + p$ collisions (kinematic limit), e.g. an elastic collision where the protons are deflected to $+\eta$ and $-\eta$.

Any single parton must satisfy $x < 1$ (x being the fraction of the nucleons momentum carried by the parton), thus production of a hadron with $x_\text{F} > 1$ is impossible through parton fragmentation, thus severely suppressing any jet structure at high x_F. Through parton recombination, between constituents from two different nucleons, a hadron can get $x_\text{F} > 1$, as the momentum fractions are additive. This leads to interesting effects in the particle production as a function of p_T. They consider the production of protons and pions, and find that it is rather easy to find three nucleons each contributing with a quark with $x \sim 1/3$, thus forming a proton at $x \sim 1$. It is much more difficult to create at pion at the same x_F. The anti–quark in the pion with $x \sim 1/3$ has to come from the quark sea or from a high-x gluon converted to $q+\bar{q}$. The $\bar{q}$ with $x \sim 1/3$ the needs to combine with a quark with $x \sim 2/3$ to create the $x \sim 1$ pion. The production of $x_\text{F} \sim 1$ pions is therefore suppressed. The author argue that such a particle production should give a large p/π^+ ratio, but also, based on the same argumentation give a large Λ/K^+ ratio.

The recombination formula for proton production in an $A + B$ collisions considering 3 nucleons in
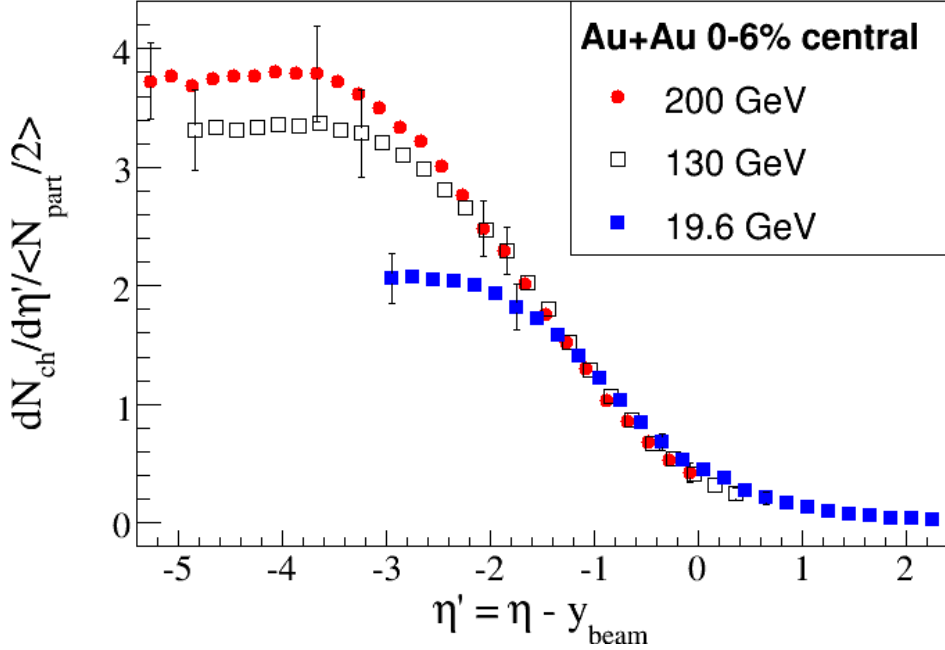
Figure 3.6: The figure shows the participant scaled particle pseudorapidity density shifted with the beam rapidity, y_{beam}. The $\sqrt{s_{NN}} = 62.4$ GeV and 130 GeV extend out to $\eta' > 0$. This region is the transfragmentation region in [65]. The figure is made by PHOBOS [67].

A in a longitudinal tube at distance s from the center of A:

$$H_p^{(3)B}(x_{\text{F}}) \equiv x\frac{dN_p^{(3)B}}{dx} = \int \frac{F_{uud}^{(3)B}(x_1, x_2, x_3)R_p(x_1, x_2, x_3, x_{\text{F}})}{x_1 x_2 x_3}dx_1 dx_1 dx_3 \tag{3.27}$$

where R_p is the proton recombination function studied in [68, 69, 70, 71], and $F_{uud}^{(3)B}(x_1, x_2, x_3)$ is the 3-quark distribution. In p+B collisions all three quark would come from the projectile p, and $\sum_i x_i < 1$. In the TFR in an $A + B$ collision, with $x \gtrsim 1$, the quarks must come from different nucleons, which means it should factorise as:

$$F_{uud}^{(3)B}(x_1, x_2, x_3) = F_{\bar{\nu}}^u(x_1) \cdot F_{\bar{\nu}}^u(x_2) \cdot F_{\bar{\nu}}^d(x_3) \tag{3.28}$$

where $\bar{\nu} = 2\langle N_{\text{coll}}^{AB}\rangle/\langle N_{\text{part}}^{AB}\rangle$ is the average number of wounded nucleons, The authors argue that a proton's maximum value is 3, since each x_i is independent of the others. The corresponding formula for pion production is:

$$H_\pi^{(2)B}(x_{\text{F}}) \equiv x\frac{dN_\pi^{(2)B}}{dx} = \int \frac{F_{q\bar{q}}^{(2)B}(x_1, x_2)R_\pi(x_1, x_2, x)}{x_1 x_2}dx_1 dx_2 \tag{3.29}$$

$$F_{q\bar{q}}^{(2)B}(x_1, x_2) = F_{\bar{\nu}}^q(x_1) \cdot F_{\bar{\nu}}^{\bar{q}}(x_2) \tag{3.30}$$

To get the total production of protons and pions, the sum must be made over the overlapping region of the $A + B$ collisions at impact parameter b:

$$H_p^{AB}(x_{\mathrm{F}}, b) = \int \frac{(\sigma \cdot T_A(s))^3 \, H_P^{(3)B}(x_{\mathrm{F}}, b, s)}{3! \cdot \sigma} d^2 s \tag{3.31}$$

$$H_\pi^{AB}(x_{\mathrm{F}}, b) = \int \frac{(\sigma \cdot T_A(s))^2 \, H_\pi^{(2)B}(x_{\mathrm{F}}, b, s)}{3! \cdot \sigma} d^2 s \tag{3.32}$$

where σ is the inelastic nucleon–nucleon cross section, and $T_A(s)$ is the thickness function normalised to A. The authors expect the $H_\pi^{(2)B}(a, b, s)$ to be suppressed compared to $H_P^{(3)B}(a, b, s)$, since the $F_\nu^{\bar{q}}(x_2)$ is severely damped at large x_2.

Since $|\vec{s} - \vec{b}|$ can be as large as the radius of the nucleus, the number of collisions the partons encounters can have large fluctuation, which will lead to momentum degradation of the produced particles. Momentum degradation is incorporate in their model with a free parameter $0 < \kappa < 1$ in the recombination function R, such that it should be written as $R(x_{\mathrm{F}}, \kappa)$ and $H_p^{AB}(x_{\mathrm{F}}, b, \kappa)$. Decreasing the value κ increases the momentum degradation, lowering the production at a given x. Note that proton production in equation 3.31 is integrated over R_p^3 and pion production is integrated over R_π^2, thus the value of the p/π ratio is sensitive to this parameter.

In [66], R. C. Hwa and C. B. Yang investigate regeneration of soft partons from the initial nuclear matter effects. They modify the 3-quark distribution function F, considering that the initial nucleus consists, in addition to the valence quarks, sea–quarks, strange quarks and gluons. This changes $F_\nu^{\bar{q}}$ and increases the production of pions (and even more for $\bar{p}$ as it only contains $\bar{q}$), though the effect on $F_\nu^{\bar{q}}$ is very small. Thus there is very little effect on the proton production. The differential inclusive hadron p_{T} production, dN_h, taking momentum degradation and soft parton regeneration into account, can be written as:

$$\frac{x_{\mathrm{F}}}{p_{\mathrm{T}}} \frac{dN_h}{dx_{\mathrm{F}} dp_{\mathrm{T}}} = H_h^{AB}(x_{\mathrm{F}}, \kappa) V_h(p_{\mathrm{T}}) \tag{3.33}$$

$$V_p(p_{\mathrm{T}}) = c_\pi^2 \cdot F_\nu^q(x_1) F_\nu^{\bar{q}}(x_2) \cdot e^{-p_{\mathrm{T}}/T} \tag{3.34}$$

$$V_\pi(p_{\mathrm{T}}) = c_p^3 p_{\mathrm{T}} \cdot F_\nu^u(x_1) F_\nu^u(x_2) F_\nu^d(x_3) \cdot e^{-p_{\mathrm{T}}/T} \tag{3.35}$$

where T is a free parameter assuming local thermal equilibrium of partons in a co–moving frame whose velocity in the center–of–mass system corresponds to the x_{F}.

From equation 3.34 and 3.35, the p/π^+ ratio should have an approximate linear p_{T} dependence, and should exceed 1 for $p_{\mathrm{T}} > 1$ GeV/c. The $0.6 < x_{\mathrm{F}} < 1.2$ region is accessible to BRAHMS in $\sqrt{s_{\mathrm{NN}}} = 62.4$ GeV collisions.

Chapter 4

Review of nuclear modification factors at SPS and RHIC

To investigate the suppression of jets in heavy ion collisions, a direct comparisons is made with the production of high p_{T} particles in elementary reactions, such as $p+p$, where no QGP matter is expected to be created. A comparison between central to peripheral heavy ion collisions can also be made, R_{cp}. Both of these comparisons are made using p_{T} spectra.

A vast number of results have been published at SPS and now at RHIC energies. The following sections gives an overview of these results and addresses the suppression seen at RHIC top energy collisions. Particle spectra for $\pi^{\pm}$, $K^{\pm}$, p and $\bar{p}$ for $\sqrt{s_{\mathrm{NN}}} = 62.4$ GeV have been published by PHOBOS [72] and STAR [73] ($\pi^{\pm}$, p, and $\bar{p}$). R_{AA} for pions have also been published by STAR [73], using the pion parametrisation for $p + p$ collisions suggested by D. d'Enterria in [74]. These results will be discussed in more detail in chapter 7. The $\sqrt{s_{\mathrm{NN}}} = 17.3$ GeV to 200 GeV results will be discussed here for later reference.

4.1   Nuclear modification factors at SPS

Lower energy heavy ion collision studies have been performed at the SPS. These experiments used a fixed target, which means they could not make $p + p$ collisions as their reference in the nuclear modification factor. In addition to R_{cp} measurements, a $p + p$ parametrisations [74] was used to construct R_{AA}.

Nuclear modification factors from the SPS are shown in figure 4.1. As can be seen in the figure, there is an increase in the number of high p_{T} pions (π^0 or $\pi^{\pm}$) in heavy ion collisions. Such an increase was first reported in proton–nucleus collisions in the mid 70's at the FERMILAB, ranging from $\sqrt{s_{\mathrm{NN}}} = 19.4$ GeV to 27.4 GeV, for inclusive charged hadrons at midrapidity [38, 39]. This effect has since been called "Cronin" enhancement. Figure 4.1 shows that the enhancement appears in a range of collision systems in the energy range $\sqrt{s_{\mathrm{NN}}} = 17.3$ GeV to 31 GeV. Both central Pb+Pb and minimum bias $\alpha + \alpha$ collisions shows the same enhancement, indicating that the enhancement is due to initial state and not final state effects, as the created matter is $\alpha + \alpha$ is very small. Alternatively it could be interpreted as an initial state effects, due to multiple scattering in $\alpha + \alpha$ and to final state parton recombination in Pb+Pb collisions, as discussed in section 3.3.1. R. C. Hwa and C. B.
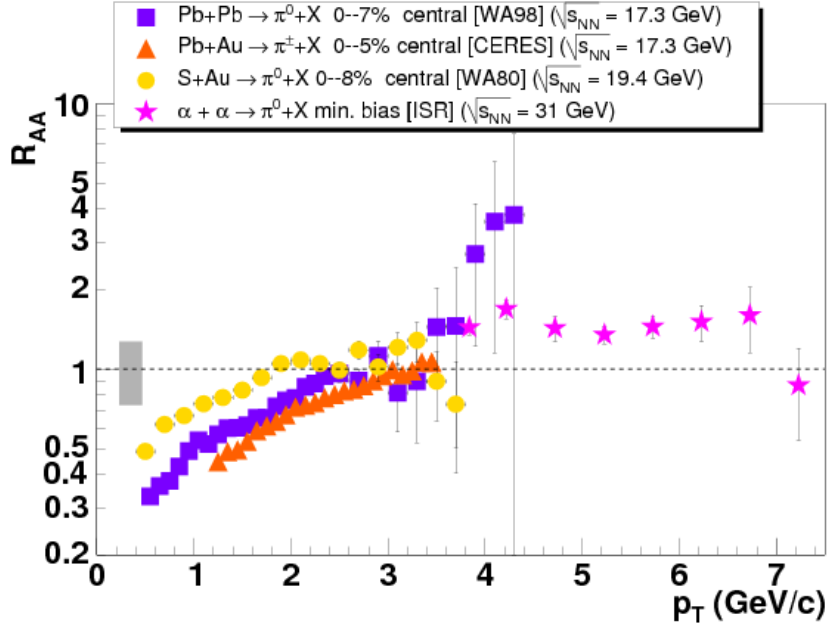
Figure 4.1: The figure shows "Cronin" enhancement of the nuclear modification factors for pions (π^0 and $\pi^{\pm}$) at SPS energies. Notice the logarithmic scale for R_{AA}. The data in the figure is from [75, 76, 77].
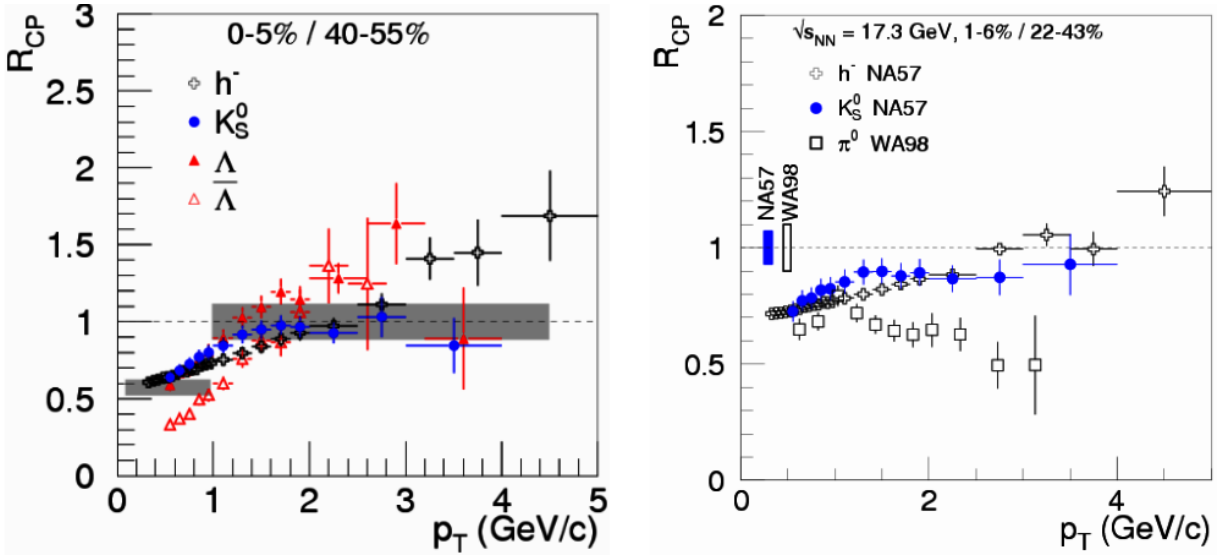

Figure 4.2: The figure shows the R_{cp} for h^-, π^0, K_S^0, Λ and $\bar{\Lambda}$ measured by the NA57 and the WA98 experiment. The peripheral spectra in the right panel correspond to 40–55% centrality, and in the right panel 22–43% centrality. The figure is from [78].

Yang state in [41] that this explanation should only be applicable to higher collision energies, thus disfavouring the explanation of a final state effect in Pb+Pb collisions at $\sqrt{s_{\mathrm{NN}}} = 17.3$ GeV.

Figure 4.2 shows the central to peripheral ratio of p_{T} spectra for ^{207}Pb+^{207}Pb at $\sqrt{s_{\mathrm{NN}}} = 17.3$ GeV for various particle species. The negative charged hadrons in the left panel show a different p_{T} dependence compared to π^0. K_S^0 show similarities to the h^-, reaching scaling at $p_{\mathrm{T}} < 2$ GeV/c, while h^-, Λ, and $\bar{\Lambda}$ is enhanced above 2 GeV/c. The R_{cp}, except for the π^0, at this energy have a p_{T} dependence very similar to the R_{AA}.

New analysis of the SPS data has been done, which has spurred a debate about the enhancement. The p_{T} spectra from $p + p$ collisions used in the denominator, in figure 4.1, depends on how the parametrisation is done, see discussion in [74]. WA98 measured p+Pb and p+C collisions which they used instead of the $p + p$ parametrisation as the denominator [79]. These proton–nucleus collisions go through very few hard scatterings, but more than $p+p$, so the p_{T} spectra are scaled with $\langle N_{\mathrm{coll}}^{p+\mathrm{Pb}} \rangle$ and $\langle N_{\mathrm{coll}}^{p+\mathrm{C}} \rangle$. The created partons/particles are not affected by any dense hot matter which is created in the heavy ion collisions, though they are affected by the "cold" nuclear matter from the nucleus. This R_{AA} show high p_{T} suppression of π^0 in figure 4.3. The suppression is stronger when p+Pb spectra is used as the reference, as compared to the p+C, right and left side of figure 4.3, respectively. If the asymmetric collisions have an enhanced number of high p_{T} particles relative to $p+p$ collisions, as seen by the Cronin collaboration [38, 39], a ratio below 1 in the R_{AA} for Pb+Pb collisions is caused by the p+C (or p+Pb) spectra. The same enhancement is even seen in d+Au collisions, in figure 4.4, at RHIC energies.
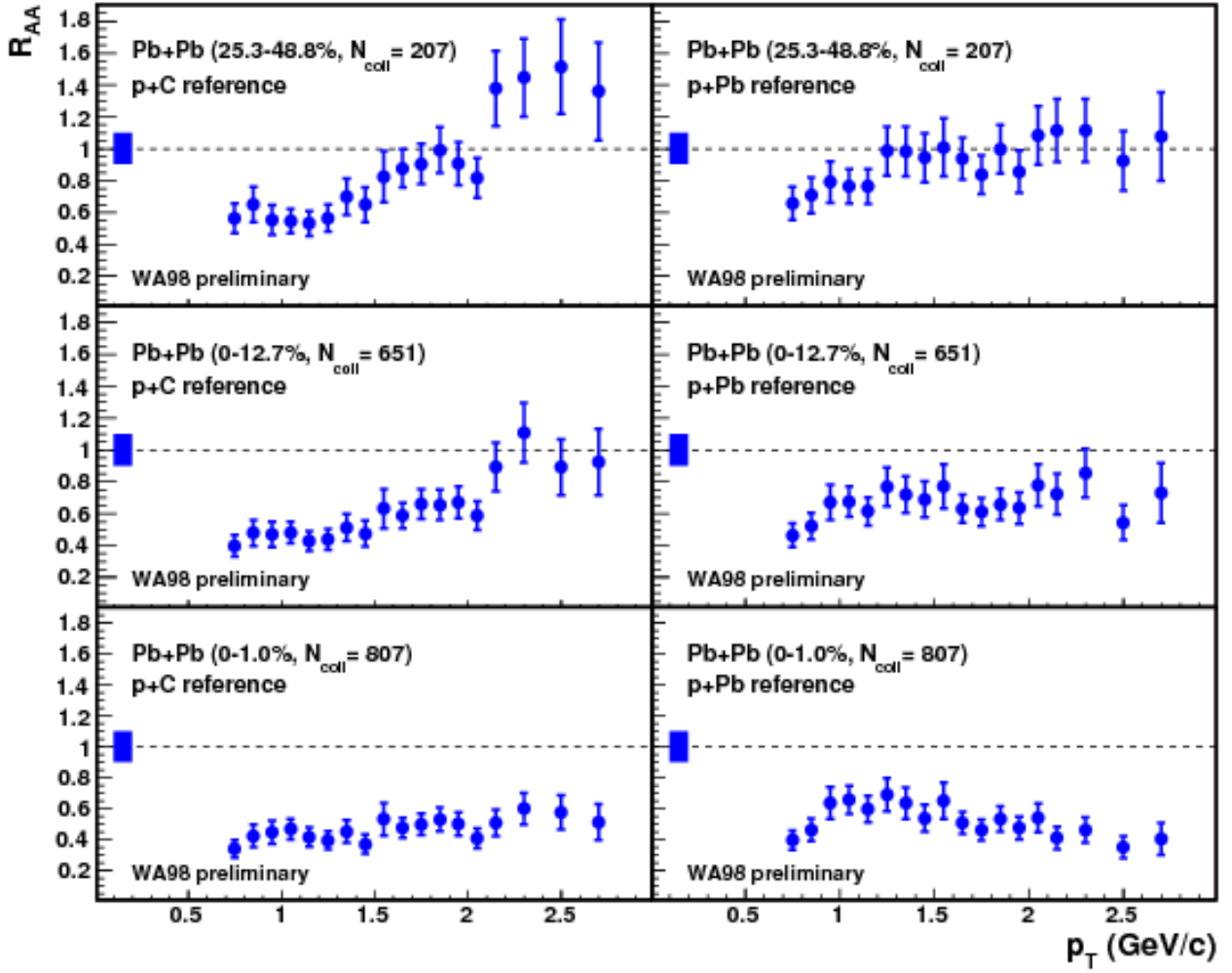
Figure 4.3: The figure shows a special R_{AA} at $\sqrt{s_{\mathrm{NN}}} = 17.3$ GeV, where the reference spectra for the nuclear modification factor is p+C on the left side and p+Pb on the right side. The p_{T} spectra in p+C and p+Pb collisions are scaled with $\langle N_{\mathrm{coll}}^{p\mathrm{C}} \rangle$ and $\langle N_{\mathrm{coll}}^{p\mathrm{Pb}} \rangle$, respectively. Using p+Pb spectra gives as stronger suppression than using p+C spectra as reference. The figure is made by WA98 [79].

4.2 Nuclear modification factors at RHIC

The "Cronin" enhancement seen at the SPS is also present at midrapidity in d+Au collisions at RHIC top energy. Figure 4.4 show the R_{AB} measured by STAR. A strong enhancement is see above 2 GeV/c, caused by either p_{T} broadening in the initial state or parton recombination in the final state. In these collisions there is no large volume of created matter to suppress the high p_{T} particles, as compared to central Au+Au collisions.

BRAHMS has collected two very high statistics data sets of Au+Au and Cu+Cu collisions at $\sqrt{s_{\mathrm{NN}}} = 200$ GeV. The R_{AA} for charged hadrons and identified particles in Au+Au collisions measured by BRAHMS as a function of rapidity are shown in figure 4.5 and 4.6, and utilises the data set taken in 2004. The published results in [37] have used the data taken in 2001. The 2004 data set has more than an order of magnitude more data, and can therefore extend to higher p_{T}.
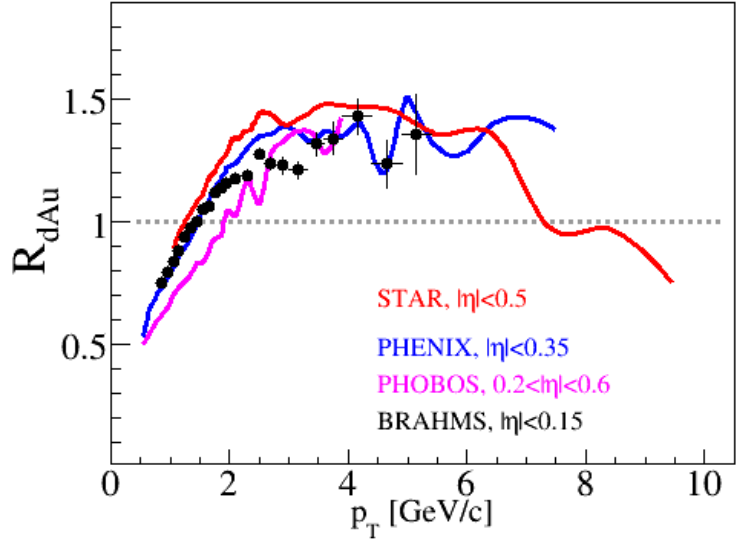

Figure 4.4: The figure shows the nuclear modification factor for inclusive charged hadrons in minimum bias d+Au $\sqrt{s_{\mathrm{NN}}} = 200$ GeV collisions at midrapidity at RHIC. The black points are the BRAHMS results with statistical uncertainties, while the lines are from STAR, PHENIX, and PHOBOS, shown without any uncertainties. The data show very good agreement and is from [37, 80, 81, 82].
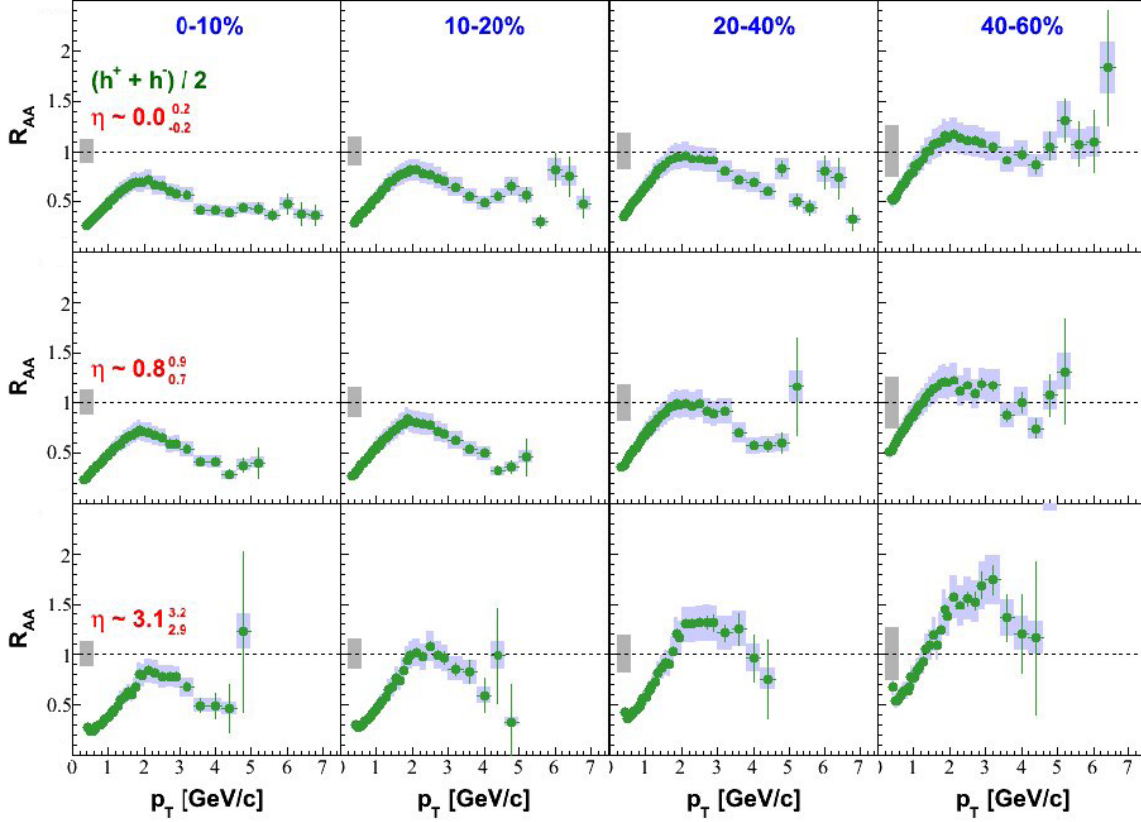
The charged hadron results from BRAHMS at $\sqrt{s_{\mathrm{NN}}} = 200$ GeV are shown in figure 4.5 for 5 different pseudorapidity bins. The results for charged hadrons from the RHIC in Au+Au collisions, show the opposite behaviour compared to SPS. The most remarkable feature for these nuclear modification factors is that they seem to be more or less pseudorapidity independent, for central collisions. The suppression has neither any charge dependence. $\eta = 3.5$ is not inside the fragmentation region for $\sqrt{s_{\mathrm{NN}}} = 200$ GeV collisions [11], where the physics should be different. This is an indication that the same created matter is is seen from $\eta = 0 - 3.5$.

The big difference in the R_{AA}, between SPS and RHIC, is another strong indication that the matter created in Au+Au collisions at $\sqrt{s_{\mathrm{NN}}} = 200$ GeV differs from Pb+Pb collisions at $\sqrt{s_{\mathrm{NN}}} = 17.4$ GeV. Suppression of the high p_{T} particles is the dominant effect in the $\sqrt{s_{\mathrm{NN}}} = 200$ GeV results, possibly due to the creation of sQGP.

Figure 4.5: The figure show the nuclear modification factor for unidentified hadrons in Au+Au collisions at $\sqrt{s_{\mathrm{NN}}} = 200$ GeV measured by BRAHMS. The top row of panels shows the distribution of particles in η-p_{T} space. The second row of panels shows the invariant p_{T} spectra. The solid lines in each panel under the markers is the $p + p$ results. The R_{AA} for the 0–10% most central collisions is shown in the third row of panels. The bottom row shows the central, 0–10% centrality, to peripheral, 40–60% centrality, ratio. The 2 ratios show no dependence on the pseudorapidity. The figure is from [83].

4.2.1 R_{AA} for light quark particles at the RHIC

This section will present R_{AA} for particles containing u, $\bar{u}$, d $\bar{d}$ quarks. These quarks have the lowest mass. The nuclear modification factors for pions and (anti-) protons are shown in figure 4.6 for Au+Au collisions. The pions are the most suppressed particles, without any apparent rapidity dependence. The protons show enhancement at all rapidities, but the anti–protons indicate more enhancement at $y \sim 3.1$ than at midrapidity. This is not due to parton recombination as proposed by R. C. Hwa and C. B. Yang discussed in section 3.5, as these particles have an $x_{\mathrm{F}} < 0.45$.

PHENIX has done an extensive study of the π^0, shown in figure 4.7, extending out to 13 GeV/c. High p_{T} π^0 measurements behave the same way as the charged hadrons, and are suppressed by a factor of ~ 5. At all centralities a saturation of the suppression occurs at ~ 4 GeV/c, with most central collisions being most suppressed. The 70–80% and 80–92% centrality bins does show any suppression.
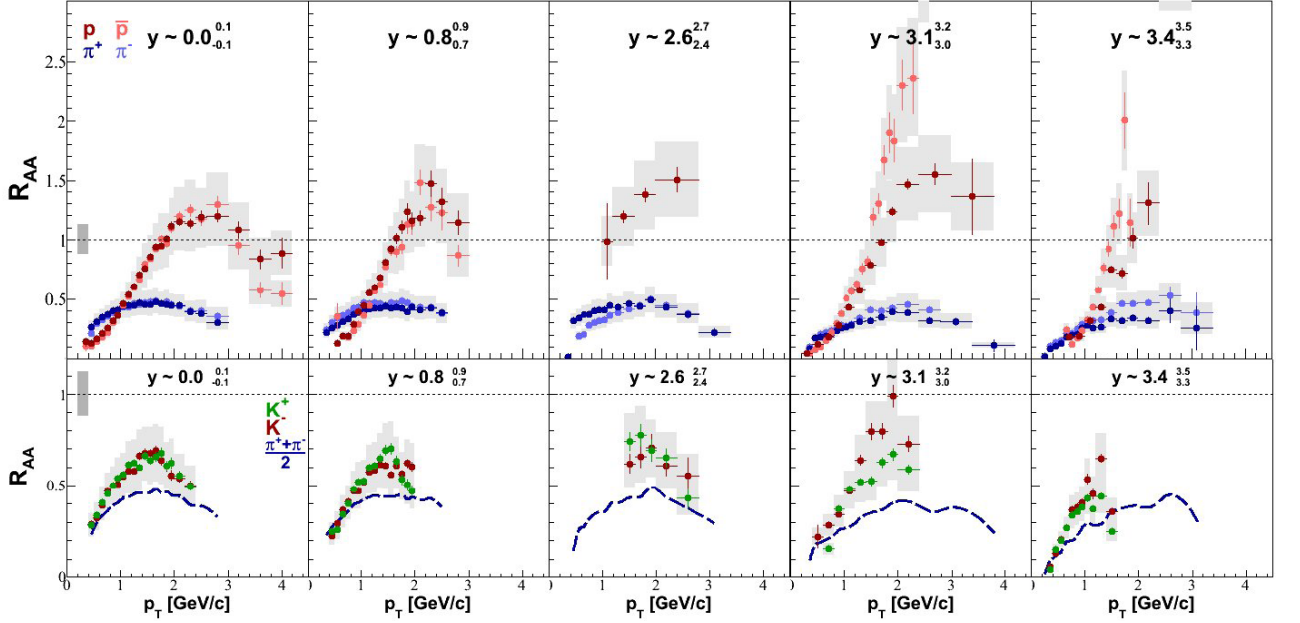
Figure 4.6: The figure shows the nuclear modification factor for pion, kaons, proton and their antiparticles for centrality 0–10% in Au+Au collisions at $\sqrt{s_{\mathrm{NN}}} = 200$ GeV. measured by BRAHMS. The protons show enhancement at all rapidities, the kaons are suppressed by a factor of ~ 1.5, and the pions are suppressed by a factor of ~ 5. The figure also shows that the R_{AA} does not depend on the particle's charge or rapidity in the range $0 < y < 3.4$, though there is an indication that this is not true for anti–protons. Anti–protons show increasing enhancement with rapidity. The figure is from [83].

The "minimum bias" sample, 0–92%, is very similar to the 20–30% central collisions. The figure shows that the R_{AA} has a clear dependence on the size of the created matter.

Figure 4.8 investigates the dependence on the created matter's size further. The left panel shows how the average R_{AA}, for $5 < p_{\mathrm{T}} < 8$ GeV/c, behaves as a function of the particles emission angle relative to the reaction plane, $\Delta\phi$. Even for relatively central collisions, 10–20%, a $\Delta\phi$ dependence is seen. For the in–plane π^0s, $\Delta\phi < 10°$, $R_{AA} \sim 0.4$ and ~ 0.25 for π^0 emitted out–of–plane. Minor changes of the parton path length in the dense matter, changes its momentum. The in–plane R_{AA} shows a strong dependence on the collision centrality. In–plane π^0s in 50–60% central collisions shows no suppression. In 60–70% central collisions, enhancement is seen for emission angle $\Delta\phi < 25°$. The out–of–plane π^0s are suppressed between $0.3 < R_{AA} < 0.6$, with a weaker dependence on the collision centrality compared to the in–plane π^0s.
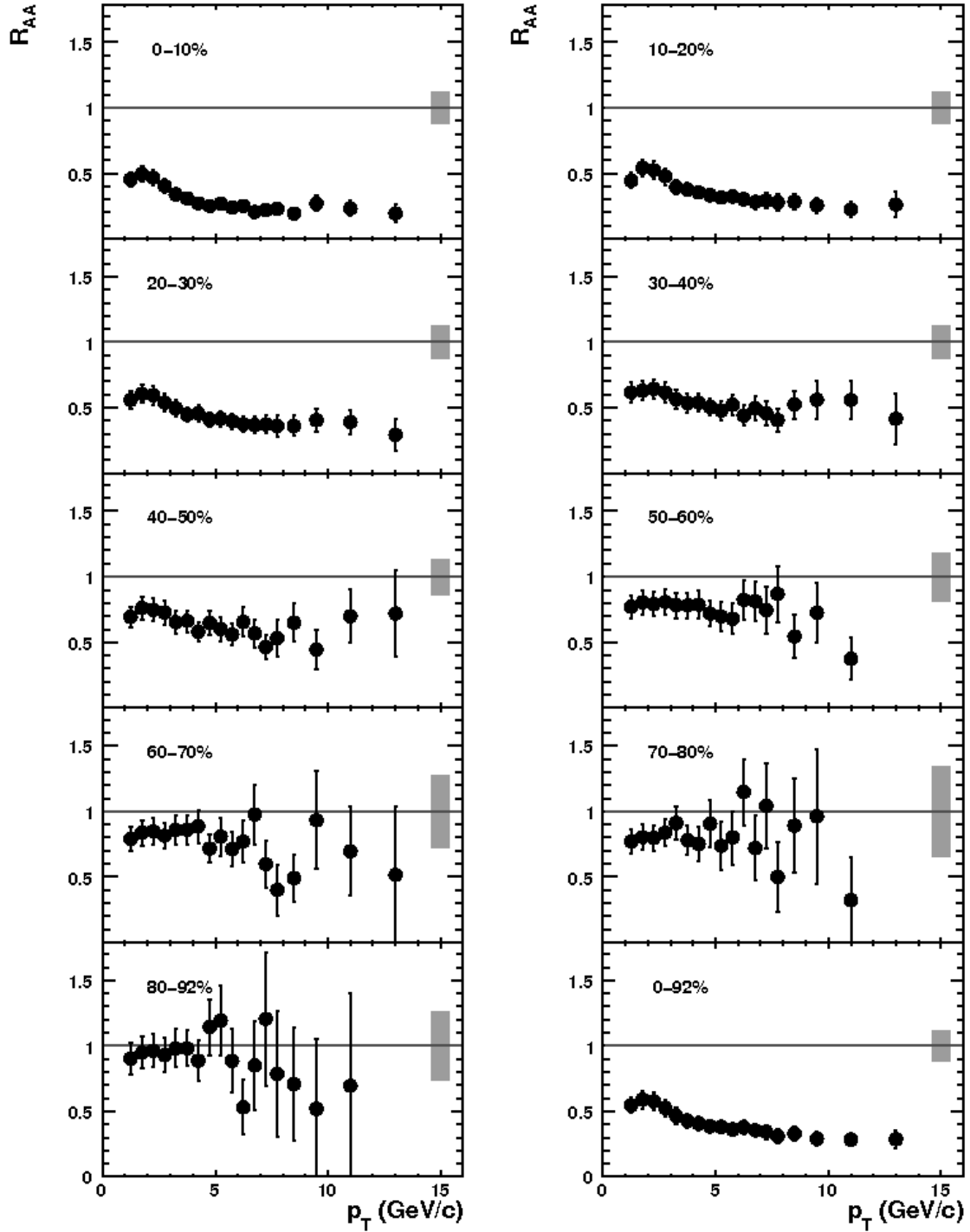
Figure 4.7: The figure shows the R_{AA} for π^0 as a function of centrality. The most central collisions, 0–10%, show a suppression of ~ 5 for $p_{\mathrm{T}} > 4$ GeV/c. As the collisions become more peripheral the suppression decreases. The most peripheral collisions, 80–92%, show no suppression. The "minimum bias" sample, 0–92%, is very similar to the 20–30% centrality bin. The figures are made by PHENIX [84].
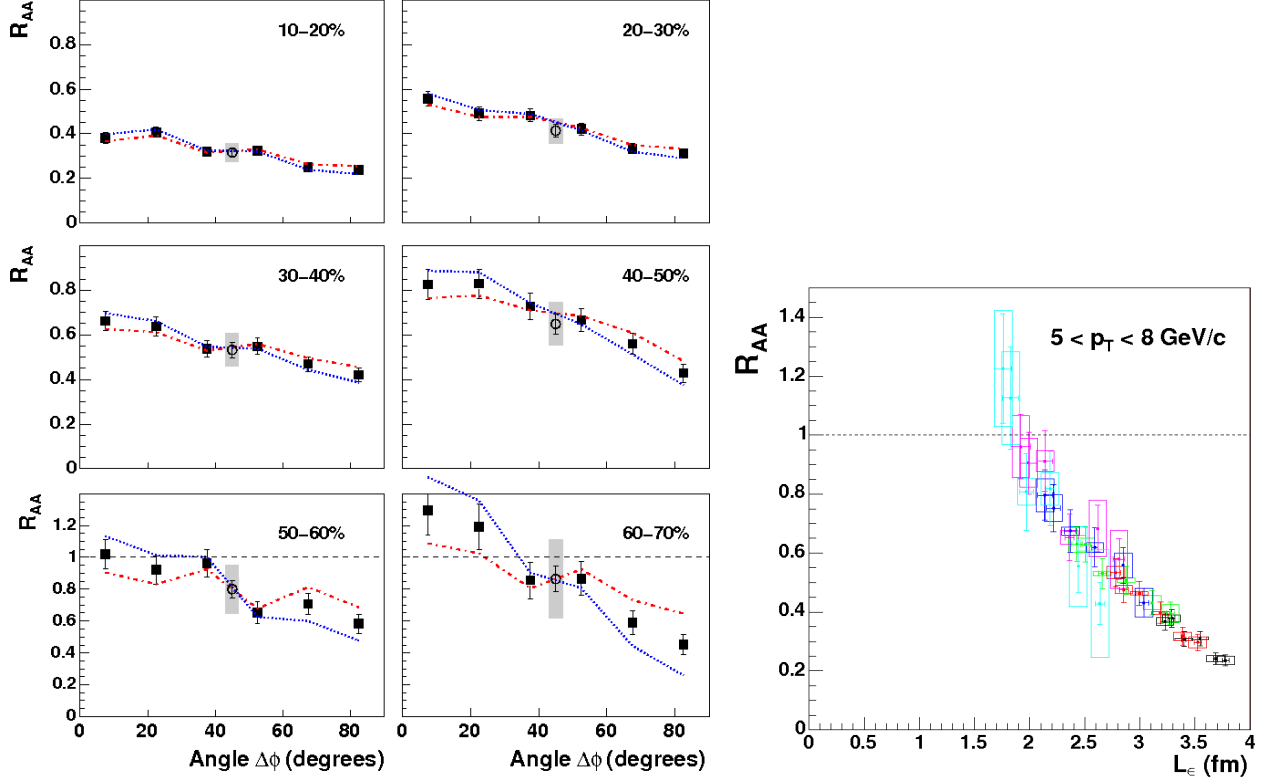
Figure 4.8: The left panel shows the integrated R_{AA} for $5 < p_{\mathrm{T}} < 8$ GeV/c as a function of the particle emission angle relative to the reaction plane. With $\Delta\phi = 0°$ the distance the particle must travel is the short ellipse radius, while at $90°$, the particle travels along the long radius of the ellipse. Increasing suppression is seen as the particles is emitted further and further away from the reaction plane, for all centralities. The right panel shows the average R_{AA} between $5 < p_{\mathrm{T}} < 8$ GeV/c as a function of path length. The colours denote different centrality bins: cyan 60–70%, mauve 50–60%, blue 40–50%, green 30–40%, red 20–30%, black 10–20%. Within each centrality group, the six different data points correspond to the same $\Delta\phi$ points in the to left panel and is directly related to particle emission angle relative to the reaction plane, $\Delta\phi$. L_ϵ is defined as the distance from the center of the collision volume to the outer edge of the elliptical collisions geometry. All figures are from the PHENIX experiment [84].

This strong path length dependence is further investigated in the right panel of figure 4.8. It shows the average R_{AA}, for $5 < p_{\mathrm{T}} < 8$ GeV/c, as a function of the path lengths the parton have to travel in the created matter. The path length is calculated as the distance from the center of the collision to the outer edge, using the $\Delta\phi$ angle. The shape of the transverse collision zone is estimated to be an ellipse with a sharp outer edge. From this calculation, each of the $\Delta\phi$–points in the left panel are transformed over to an in–matter path length, L_ϵ. R_{AA} as a function of this in–matter path length is plotted in the right panel of figure 4.8.

Suppression by a factor of ~ 5 have an average calculated path length in the created matter of
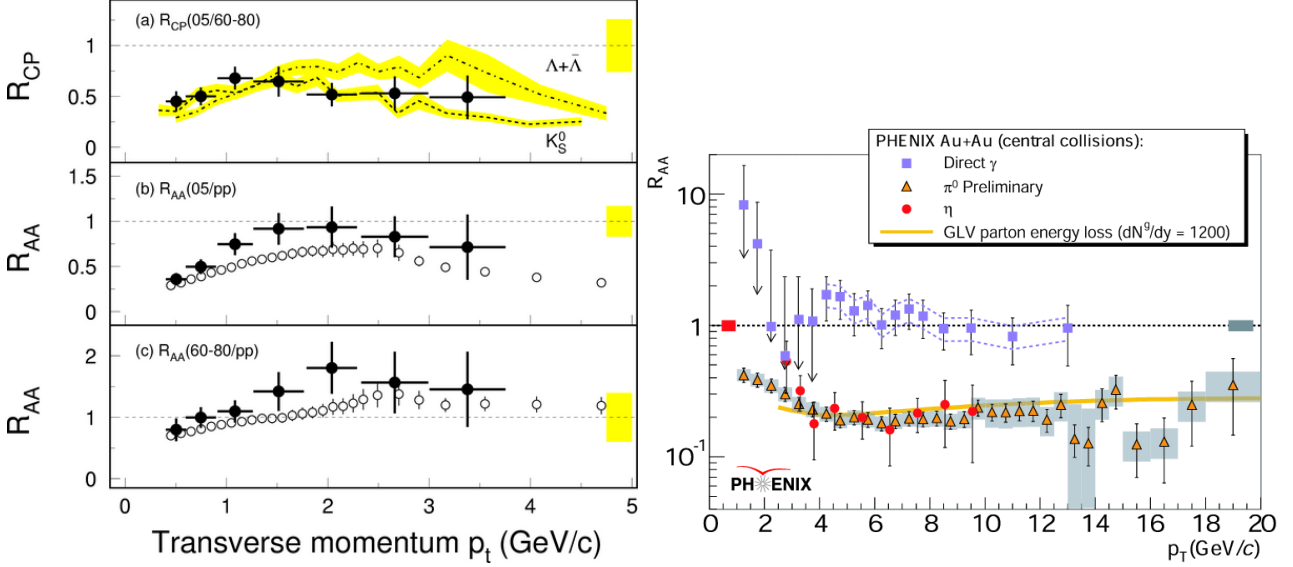
Figure 4.9: The left panel shows R_{AA} and R_{cp} for the ϕ meson, black points, compared to the K_S^0, dashed line, and the Λ, dot–dashed line. The open circles are charged hadrons. The right panel shows that the η has the same amount of suppression as π^0. Also shown in the figure is direct γ measurements, which show scaling behaviour relative to $p+p$, indicating that enhancement and suppression cancels. The left panel is made by STAR [85], and the right by PHENIX, an updated version of [86].

$3.5-4$ fm. As the path length decreases, so does the suppression. At ~ 2 fm the suppression and enhancement are equal, and there is an indication that for shorter path lengths enhancement takes over. This could be further addresses by adding measurements from the much smaller Cu+Cucollisions at the same energy. Through more measurements of shorter and longer path lengths, and with reduced uncertainties, it should be possible to determine the functional relation between R_{AA} and L_ϵ.

The ϕ meson, with a mass of 1.019 GeV/c^2, show neither enhancement of suppression in central collisions, as shown by black points in the middle, left panel of figure 4.9. It's more suppressed than protons, but much less than pions. This is very different compared to the η (547.3 MeV/c^2) in the right panel. The suppression of the η is equally strong compared to π^0, though being much heavier.

An interesting feature of particles containing u, $\bar{u}$, d $\bar{d}$ valence quarks, is the relative behaviour of the mesons to baryons. Both pions and kaons shows suppression, while the (anti-) protons show enhancement. There is no indication of any charge dependence for mesons. Neither is there any charge dependence for (anti-) protons at midrapidity. There is no trivial mass dependence of the suppression of the mesons. Protons and antiprotons are the only non–strange baryon measured at RHIC, but the protons show similar behaviour to the ϕ, with approximately the same mass.

4.2.2 R_{AA} for heavy quark particles at the RHIC

The STAR and the PHENIX experiment have measured the nuclear modification factor for other particle species than discussed so far. They have capabilities to measure strongly decaying particles containing the s, $\bar{s}$, c, $\bar{c}$, b, and $\bar{b}$ quarks. Already presented is the weakly decaying $K^\pm$ (494 MeV/c^2),
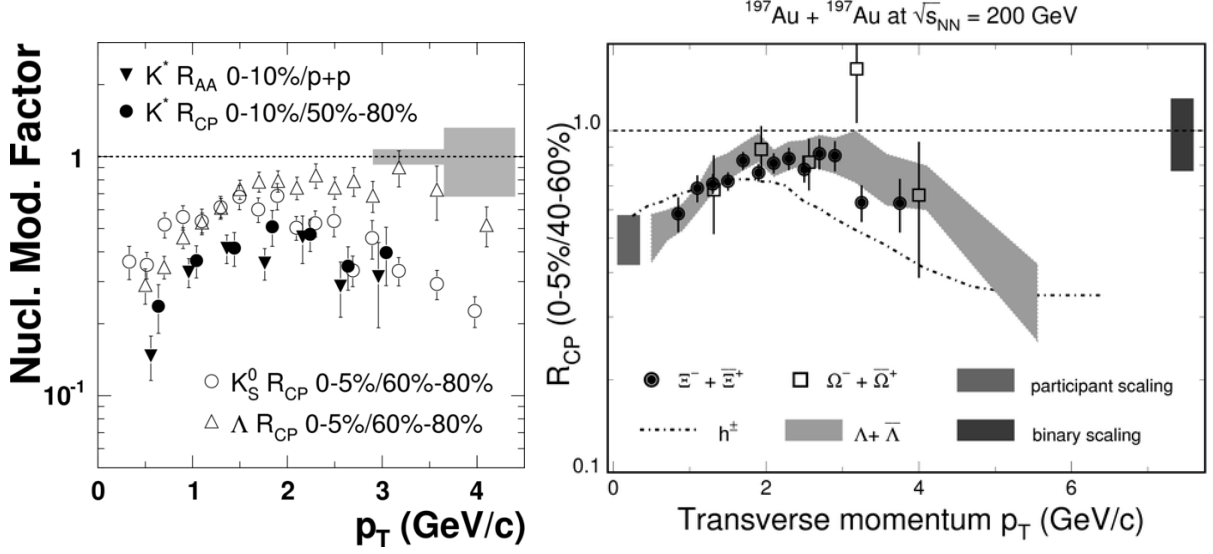
Figure 4.10: The figure shows the nuclear modification factor for particles containing the strange quark s. The left panel shows the R_{AA} and R_{cp} for the $K(892)^*$ particle and the R_{cp} for the K_S^0 and the λ (1116 MeV/c^2). The R_{cp} for the hyperons is shown on the right. The K^* and K_S^0 show the same amount of suppression. The R_{cp} for Ξ (1321 MeV/c^2), Ω (1672 MeV/c^2) and λ is shown in the right panel. The charged hadrons are shown for comparison in the right panel. Both panels have a logarithmic scale. The figure are made by STAR [87, 88].

measured by BRAHMS [83], figure 4.6. The charged kaons are not as suppressed as the pions, having an R_{AA} value between the protons and the pions. The R_{AA} for K^* (892 MeV/c^2)[87] is shown in the left panel of figure 4.10. It is suppressed by the same amount as the $K^{\pm}$. The R_{cp} for K^* and K_S^0 (498 MeV/c^2) shows the same p_{T} dependence, also being very similar to the $K^{\pm}$. In the right panel the hyperons R_{cp} [88], Ξ^-, $\bar{\Xi}^+$, Ω^-, $\bar{\Omega}^+$, Λ, and $\bar{\Lambda}$ is also shown. The Ξ (1321 MeV/c^2) and Λ (1116 MeV/c^2) shows the same p_{T} behaviour, both being a little suppressed. The statistics for the Ω (1672 MeV/c^2) is to poor to conclude if they show any enhancement or suppression. No R_{AA} measurements are available for the hyperons. No R_{AA} measurements are available for K_S^0, K_L^0, λ, Ξ, or Ω.

The J/ψ ($c\bar{c}$ meson) nuclear modification factor has been measured by PHENIX [89] and is shown in the left panel of figure 4.11. The heavy J/ψ, (3097 MeV/c^2), shows suppression comparable to pions. All the charm quarks have to be produced in initial hard parton scattering, or gluon fusion, due to its large mass. The distance between the c and the $\bar{c}$ is large. If the created matter contains colour charges, Debye screening can break the binding of the pair. J/ψ suppression has been believed to be a QGP signature, but the production of J/ψ is approximately the same at the RHIC and the SPS.

Strong suppression is seen in single–electron R_{AA} [90] in the right panel of figure 4.11. These electrons should come from semi–leptonic D (1.87 GeV/c^2) or B (5.28 GeV/c^2) meson decays. They are clearly more suppressed than the J/ψ, despite being heavier and with a smaller separation between the two quarks. The bottom black dotted line is a calculation assuming only charm quark, D, decays. Indicating that the predominant production of single non–photonic electrons are from D mesons.
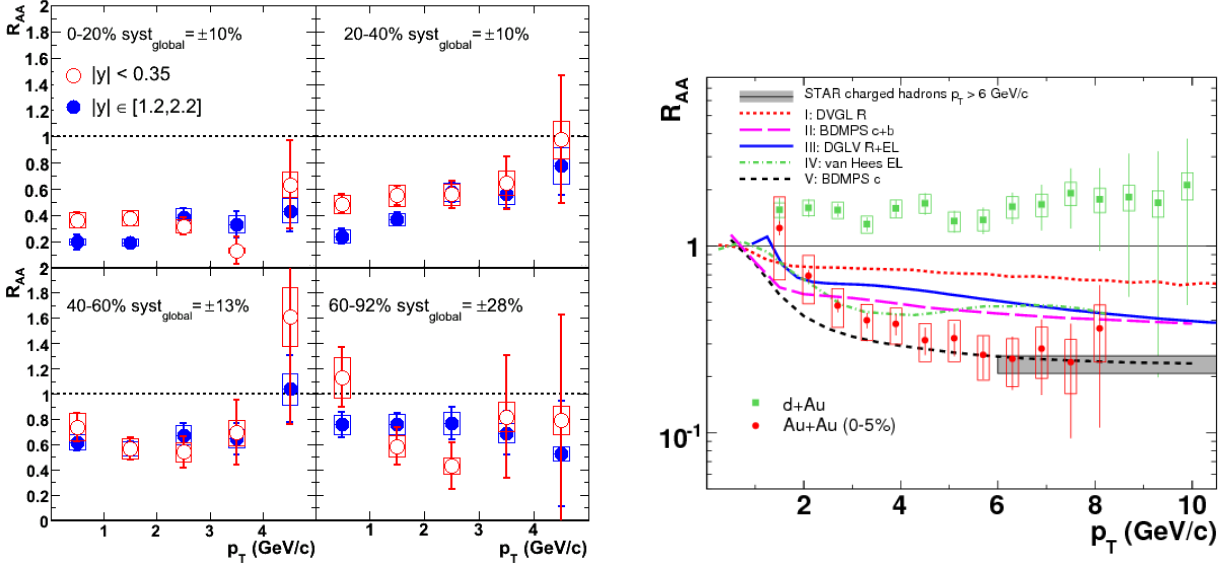
Figure 4.11: The left panel shows the R_{AA} for the J/ψ meson as a function of centrality for two rapidity bins, at mid- and forward rapidity. The right panel shows single electron measurements, which should come from a b or c quark decay. The R_{AA} saturates at 4 GeV/c, suppressed by a factor ~ 5. The left panel is made by PHENIX [89], and the right by STAR [90].

The shown figures seem to suggest that the amount of suppression depends on the mass, if one disregards particles with charm quarks. All the kaon types loose equal amounts of energy as they traverse the created matter, which is intermediate between that for pions and protons. These measurements points to a created matter imposing a high energy loss on any parton traversing it, and is an important piece in the puzzle of understanding the top energy RHIC collisions.

Chapter 5

The RHIC accelerator and the BRAHMS experiment

Figure 5.1: Aerial overview of Brookhaven National Laboratory.

The Relativistic Heavy Ion Collider, RHIC, is located at Brookhaven National Laboratory in the USA, the home of the AGS accelerator [91]. BNL has been doing heavy ion research since 1970. At that time the main machine was the Tandem Van de Graaff.

The heavy ions start their journey at the Tandem van de Graaff, and are further accelerated in the Booster and finally the AGS, before they enter the RHIC ring with a momentum of ~ 10 GeV/c per nucleon. The Tandem Van de Graaff accelerates the ions up to ~ 1 AMeV/c. Protons start their journey in the LINAC (Linear Accelerator), which gives them a momentum of 200 MeV/c. The Booster is a synchrotron machine where the both protons and heavier ions are further accelerated, and the beam is intensified, before the last electrons are stripped from heavy ions. The AGS accelerates anything from protons to gold ions up to 10 GeV/c pr nucleon, before sending them into the RHIC ring. More details can be found at [92].

Run	System	$\sqrt{s_{\mathrm{NN}}}$	Time
I	Au+Au	130 GeV	Summer 2000
IIa	Au+Au	200 GeV	Autumn 2001
IIb	$p + p$	200 GeV	Autumn 2001
IIIa	d+Au	200 GeV	Winter 2003
IIIb	$p + p$	200 GeV	Spring 2003
IVa	Au+Au	200 GeV	Winter 2004
IVb	Au+Au	62.4 GeV	Spring 2004
IVc	$p + p$	200 GeV	Spring 2004
Va	Cu+Cu	200 GeV	Winter 2005
Vb	Cu+Cu	62.4 GeV	Spring 2005
Vc	$p + p$	200 GeV	Spring 2005
VI	$p + p$	62.4 GeV	Spring 2006

Table 5.1: BRAHMS data taking at the RHIC.

In the RHIC (a collider ~ 1.2 km in diameter) the ions can be accelerated up to 100 AGeV/c. Polarised protons can be accelerated up to 250 GeV/c. The RHIC utilises super conducting magnets for bending the ions around the RHIC and the RHIC has collided ions with a center of mass energy of 20, 62, 4, 130 and 200 A GeV, as of summer 2006. An overview of the RHIC experimental facility can be seen in fig. 5.1.

The operations of the RHIC started in the summer of 2000. Until summer 2005 there were 4 active experiments at the RHIC: BRAHMS, PHOBOS, PHENIX and STAR. PHOBOS finished it's experimental program in the summer of 2005 and BRAHMS completed it's measurement program in summer of 2006. In table 5.1 is a summary of the running periods at the RHIC where BRAHMS took data.

The design of BRAHMS [93] was based on the idea used by an AGS experiment, [94, 95], which utilises movable, small solid angle spectrometers. In addition there is a set of detectors for measuring the global characteristics of the collisions. The BRAHMS design is described in the following chapters.

5.1 The BRAHMS detector

The BRAHMS experiment is shown in figure 5.2. It was designed to measure and identify particles from low to high p_{T} from mid to forward rapidities in the range $-0.2 < \eta < 3.9$. None of the other RHIC experiments can measure particles at BRAHMS' most forward region. At the intermediate RHIC energies, measurements can be carried out in the fragmentation region of the two colliding nuclei. The total acceptance of BRAHMS is shown in figure 5.3.

To categorise the collisions, a set of global detectors, described in section 5.2, are positioned close to the interaction point. These detector gives information on the point of interaction, the centrality of the collision and the interaction plane. The description given below is for the setup used in the three last running periods: 2004, 2005 and 2006. For a description of the setup in the previous runs see [3, 96, 97, 98]. More technical details on the individual detectors can be found in [93, 99].
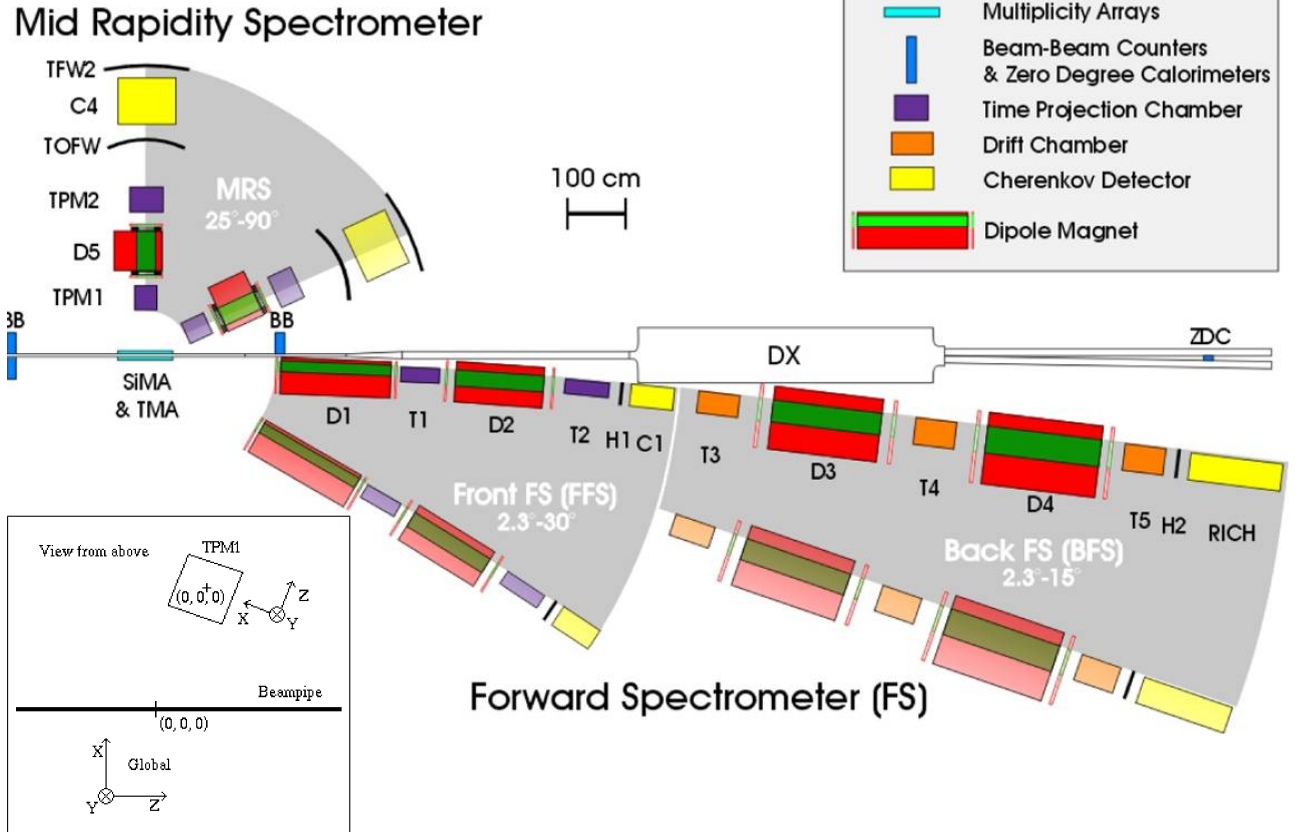
Figure 5.2: Schematic layout of the detectors in BRAHMS. The C1 and C4 are threshold Čherenkov detectors, while RICH is a ring imaging detector and can therefore do direct particle identification. The RICH detector can identify particles at very high p_{T}. The global and the local coordinate systems are shown in the insert. The global system has origo at nominal vertex position, while the local has its origo at the center of the detector. The Y-axis points vertically. The XZ-plane is always in the horizontal plane. Local coordinates have the Z-axis pointing away from the nominal vertex, through the center point on the front and back of the opening to the detectors active volume.

5.2 Global detectors

The global detectors consist of 2 multiplicity arrays: SiMA (Silicon Multiplicity Array) and TMA (Tile Multiplicity Array), 2 BBCs (Beam Beam counters), 3 CC counters ("Chellis Chasman" counters[1]) and 2 ZDC (Zero Degree Calorimeters). The ZDC, BBC and CC are used to determine the location of the collision, also called interaction point and vertex position, which is not fixed in a collider. The

---

[1]The CC counters were designed by BRAHMS collaborator Chellis Chasman.
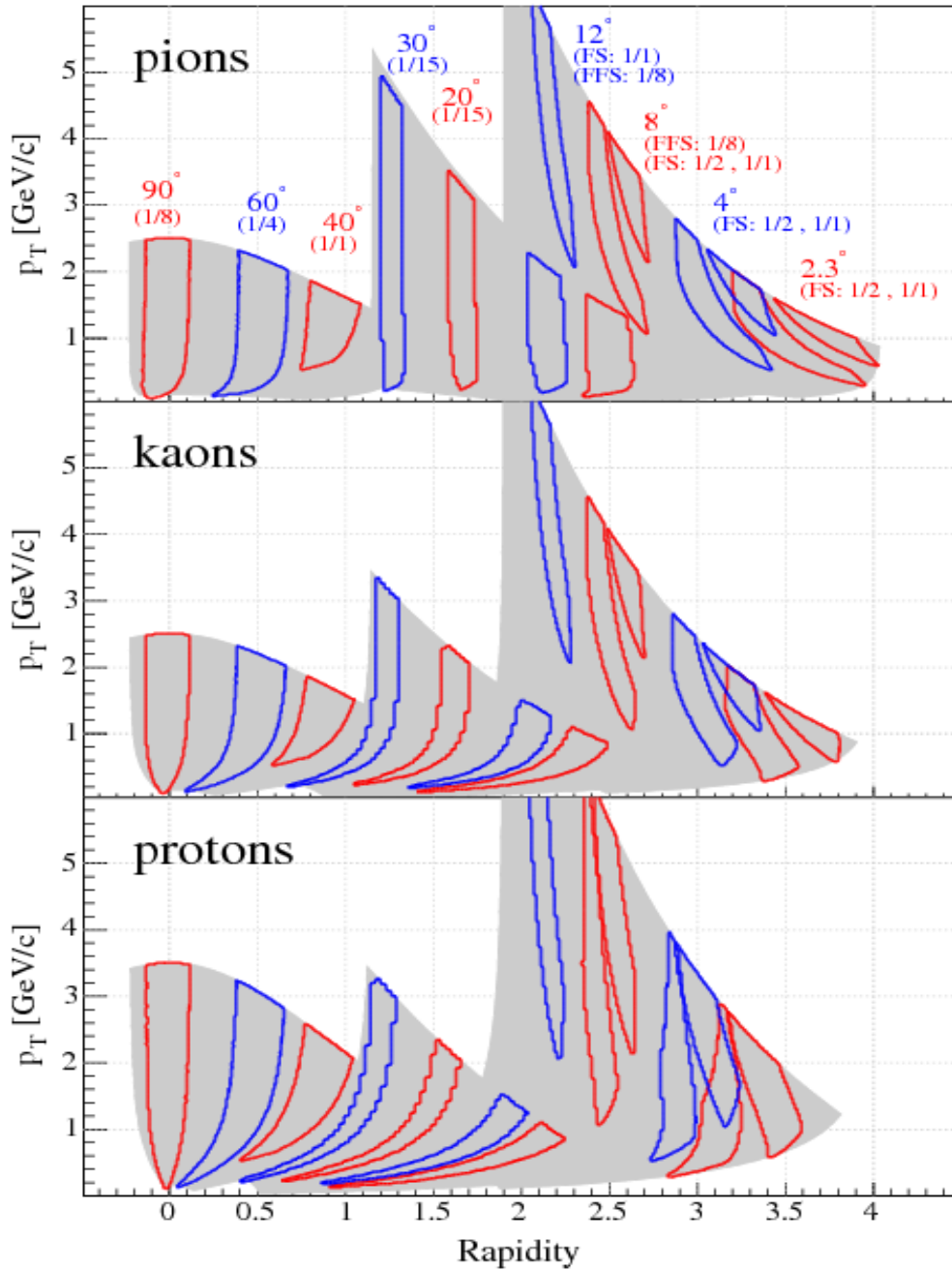
Figure 5.3: By varying the the angle and the magnetic field strength, BRAHMS has the $p_\mathrm{T}y$ phase space coverage shown above in gray. The red and blue encircled areas show examples of specific settings of the spectrometer angle and for different values of the magnetic field (actually fractions of the maximum magnetic field). The figure is from [3].
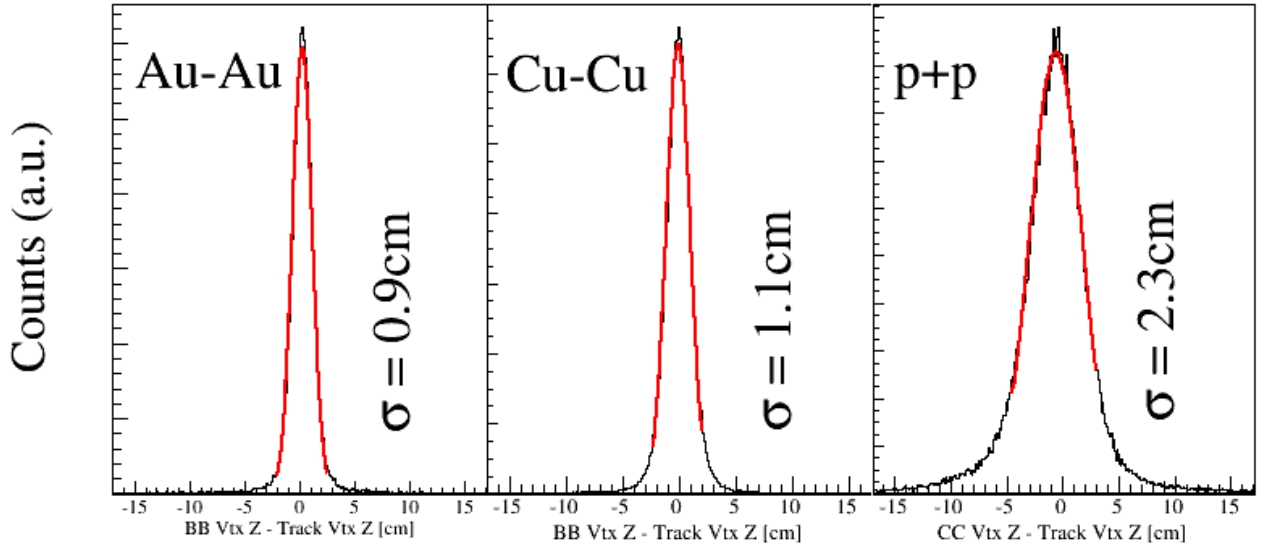
Figure 5.4: The figure shows the vertex resolution for the BBC and CC in $\sqrt{s_{\mathrm{NN}}} = 62.4$ GeV Au+Au (left panel), Cu+Cu (middle panel) and $p + p$ collisions (right panel). The global vertex is subtracted from the vertex obtained from tracks in TPM1. The distribution is then fitted to a gaussian. The fit is not extended to the tails, because very few particles here should originate from the primary vertex.

position of these detectors is indicated in figure 5.2.

The two layer multiplicity array is used to measure the centrality of a heavy ion collision. 5.3 cm outside the beam pipe is the SiMA, which is a six sided coaxial barrel, with the active detector volume made out of silicon. It was rearranged before the 2004 Au+Au run, to enable measurements of the reaction plane. All slats were rotated 90°, from perpendicular to parallel relative to the beam axis. This gives the azimuthal angle resolution necessary to determine the reaction plane. The array measures the energy deposition of the particles that fly through it. The total energy deposition can then be associated to the number of charged particles via a GEANT simulation of the detector response. The outer barrel is the six sided coaxial TMA, with the active part of the detector made out of scintillating slats. A detailed description of the TMA can be found in [100]. It is used in the same way as the SiMA. A detailed description of the centrality determination method can be found in BRAHMS first publication [101].

The BBCs (Beam Beam Counters) are used for measuring the primary vertex position in heavy ion collisions. They consist of arrays of Čherenkov tubes, positioned around the beam pipe 2.2 meters away from the nominal interaction point on each side. The time difference between the arrival of the participants on each side determines the position of the interaction point. The timing resolution enables vertex determination with an accuracy of about $\sim 9mm$ for the Au+Au collisions at $\sqrt{s_{\mathrm{NN}}} = 62.4$ GeV, and $\sim 10mm$ for Cu+Cu collisions. Figure 5.4 shows the vertex resolution achieved by the BBCs.

For the 2006 $p + p$ collisions, additional detectors were installed, called the CC counters(Chellis Chasman counters), with the active part of the detector volume made of Čherenkov radiating material. Four sets were installed around the beam pipe. They were symmetrically positioned at ± 1.9 m and
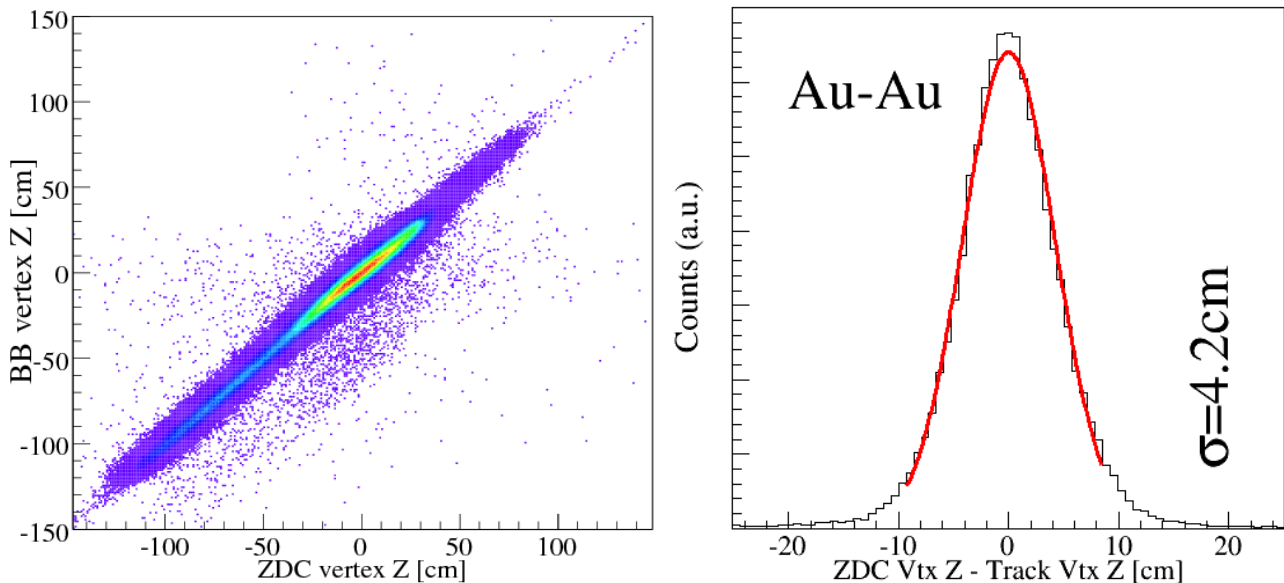
Figure 5.5: The left figure shows the correlation between the ZDC and the BBC vertex. On the right panel is the ZDC vertex correlation with the tracks from MRS. As can be seen the resolution is $7-8$ times bigger than for the BBCs.

± 6.4 m. They were used as the minimum bias detector and for determining the nominal interaction point, in the same fashion as described for the ZDC and BBC. They covered $\sim 70\%$ of the $p+p$ inelastic cross–section of 41 mb.

The ZDCs (Zero Degree Calorimeters) are positioned 18m away from the nominal interaction point, one on each side. They sit between the two beam pipes (at zero degrees), with one of the accelerator bending magnets, market "DX" in figure 5.2, between the detector and the interaction point. They measure spectator neutrons, as all other particles are swept away by the bending magnet. The calorimeter's absorber is made out of tungsten and use quartz optical fibers to only sample high energy neutrons that produce Čherenkov light. The relative timing between the arrival of the neutrons on each side determines the vertex. During the heavy ion runs the ZDC was also used as a minimum bias trigger. The left panel in figure 5.5 shows the performance of the ZDC as a vertex detector relative to the BBC vertex detector. The resolution is much worse than the BBCs, as seen in the right hand panel, and is therefore not used for determining the primary vertex. After 2002 the ZDC was only used as a trigger detector by BRAHMS. But it enables consistency checks of the BBC vertex. All four experiments had identical ZDCs, which alone enabled the beam developers to diagnose the beam quality and collision rate. The line labeled "trigger 4" in figure 5.8, show the quality of the ZDC as a minimum bias detector.

5.3 The Mid Rapidity Spectrometer

The MRS consists, starting closest to the beam pipe, of a TPC (Time Projection Chamber) (named TPM1), a dipole magnet, another TPC (TPM2), a TOF (TOFW), a threshold Čherenkov detector and another TOF (TFW2). All the detectors are mounted on a platform that can rotate from $40°^2$ to $90°$, around a center of rotation which is the nominal vertex. Angles are relative to the beam pipe. When the MRS is positioned $45°$ or less, the TFW2 can be pulled back an additional 1.5 meters away from the nominal vertex. A schematic view of the MRS is seen in figure 5.2. As can be seen from the figure, the solid angle coverage is modest, ~ 6 msr at $90°$.

The TPCs measure straight tracks since they are not inside any magnet. They have been described in detail in [93, 97, 102, 103, 104]. By matching up local tracks from TPM1 and TPM2, the momentum can be derived from the calculated curvature of the track in the magnet and the field strength. The matching is is done as described in section 6.2.

The vertex information can also be used when matching track segments for improved accuracy in momentum resolution and secondary particle suppression. PID (Particle IDentification) is achieved, by matching these tracks to hits in the TOF walls, and has been described in detail in [96]. With the TOF information of the track's relativistic velocity ($\beta = v/c$), the particles mass, $m = p\sqrt{\beta^{-2} - 1}$, can be calculated. An example of m^2 and β^{-1} distribution is shown in figure 5.6. To extend the PID to higher $p_{\rm T}$ one can use C4 and TFW2. Using TFW2 in combination with C4 vetoing, one can extend the pion and kaon identification with ~ 0.5 GeV, and protons with ~ 1 GeV, ~ 2.5 GeV and ~ 4.3 GeV respectively.

5.4 The Forward Spectrometer

The FS (Forward Spectrometer) consist of two individual spectrometers, the FFS and the BFS. These are mounted on individual platforms that can rotate between $2.3°$ to $30°$, and $2.3°$ to $15°$, respectively. Angles are relative to the beam pipe. The FS covers a solid angle of 0.8 msr. All the detectors in the FS are mounted along an arc of circle, when the FFS and BFS are lined up. By correlating the magnetic field of all four magnets, a particle with a specific momentum, flying through the center of the first magnet will fly through the center of each of the following detectors and magnets. This momentum is called the reference momentum for a given magnetic field setting, This configuration also means that the full spectrometer always has an upper and lower momentum limit, related to the magnetic field. The forward part has no upper momentum limit, as a straight line can be drawn through both D1 and D2, though for high momenta the determination would be very uncertain. This momentum determination "limit" depends on the magnetic field strength. At maximum magnetic field strength, the limit is above 60 GeV/c. A schematic view of the FS is seen in figure 5.2. The 2 spectrometers are described in detail below.

The Front Forward Spectrometer
Starting closest to the beam pipe, the FFS (Front Forward Spectrometer) consists of a dipole magnet (D1), a TPC (T1), another dipole magnet (D2), the second TPC (T2), a TOF (H1) and a threshold

---

[2]Originally it could rotate down to $25°$, but the installation of a shield wall in 2003, to reduce the background noise in the TPCs, changed this to $40°$.
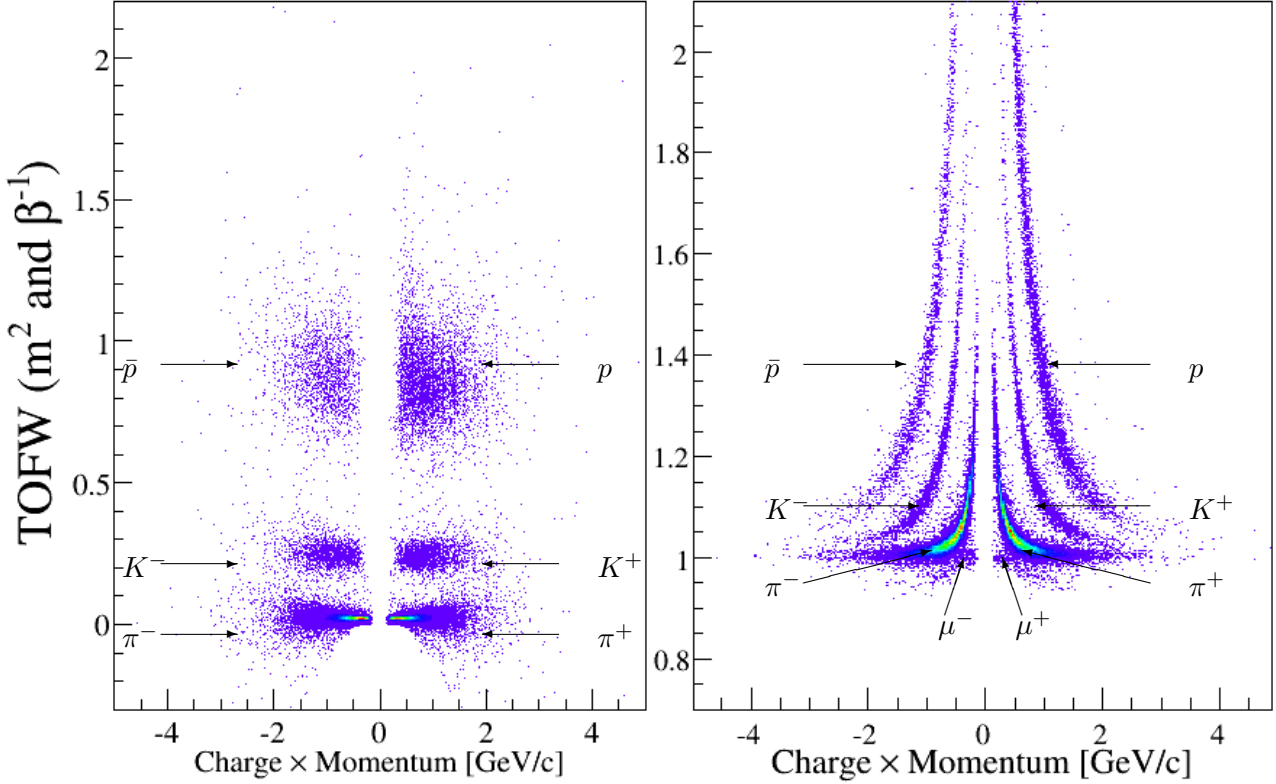
Figure 5.6: The panel on the right shows the m^2 calculation from the time measurements of the TOFW. The right panel shows the β^{-1} calculation. Negatively charged particles are plotted with negative momentum. The PIDs are indicated in the figure. The muons are visible as blobs at $\beta^{-1} = 1$ and $p \simeq \pm 0.2$.

Čherenkov detector. Since the spectrometer is rather short, compared to the momentum of the particles at forward angles, it does not enable particle identification at high p_{T}. Particle identification with the H1 is used in the BRAHMS soft physics program. Typically the PID extents to $\sim 1\,\mathrm{GeV}/c$ in p_{T} for pions and kaons and $\sim 2\,\mathrm{GeV}/c$ in p_{T} for protons. A m^2 and β^{-1} particle distribution vs momentum would look like 5.6, though it extends a little further in momentum as H1is further away from the nominal vertex than TOFW.

The Back Forward Spectrometer

The first detector in the back part of the forward spectrometer is a DC (Drift Chamber) (T3), then a dipole magnet (D3), another DC (T4), another dipole magnet (D4), the last DC (T5), a TOF (H2) and then last ring imaging Čherenkov detector (RICH). Using both H2 and RICH, enables particle identification from intermediate to really high momentum, as seen in figure 5.7. The RICH can easily do PID above the kinematic limit, in $p+p$ collisions at $\sqrt{s_{\mathrm{NN}}} = 62.4\,\mathrm{GeV}$ (limit is then $p = 31.2\,\mathrm{GeV}/c$). Technical details about the RICH detector can be found in [99], and a thorough description of the analysis algorithm can be found in [3].
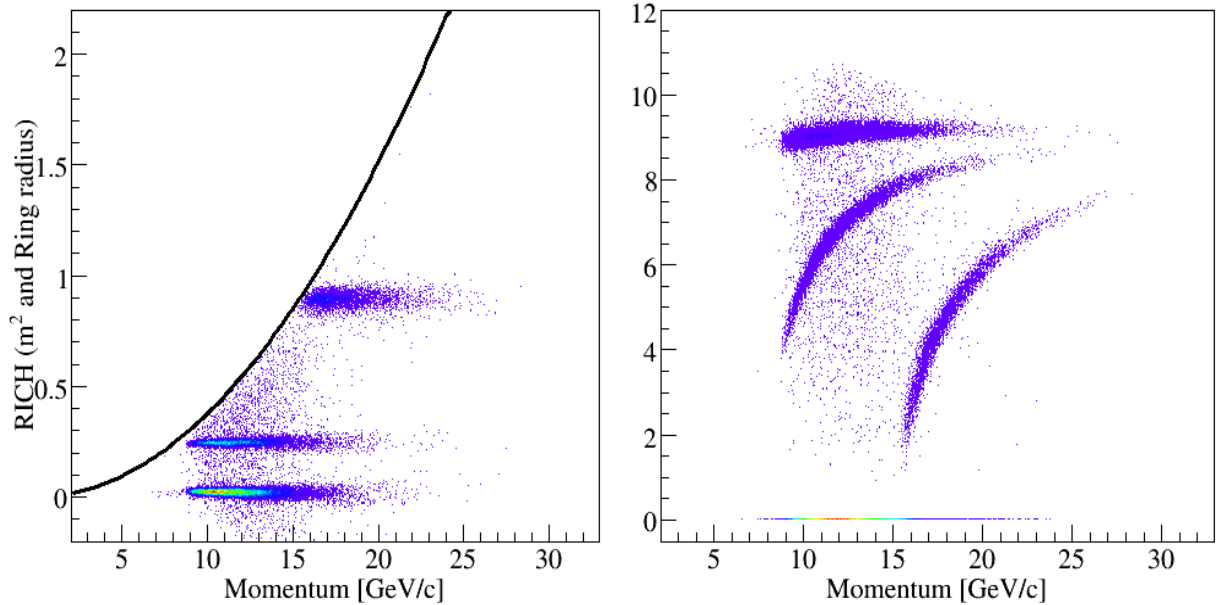
Figure 5.7: The radius of the ring created by particles passing through the RICH vs their momentum is shown in the right panel. The left panel shows the m^2 vs momentum distribution of the RICH, calculated from the ring radius: $m^2 = p^2(n^2 \cdot \cos^2(\tan^{-1}(r/L)) - 1)$, where n is the refractive index of the gas inside the RICH detector, r the ring radius and L the focal length of the RICH detector. The magnetic fields are set to half of maximum field strength, which corresponds to 0.63 T. Particles moving slower than the speed of light in the RICH gas, end up with a ring radius of 0, as can be seen in the right panel, which corresponds to the area above the solid black line drawn in m^2 distribution. Between $9 - 19$ GeV/c these particles are protons. π/K separation can be done up to ~ 25 GeV, and protons > 40 GeV.

5.5 Triggers

The basic trigger in BRAHMS is a timing coincidence of signals from the BBC or the ZDC. These provide the number of minimum bias collisions from $0 - 60\%$ in 62.4GeV collisions, as seen in figure 5.8. This information is used for normalisation of particle spectra.

Since BRAHMS is a small solid angle experiment collecting high statistics can take time. To improve this process, so called track triggers were developed just before the 2003 run to select specific events of interest. Seven plastic slats, of the same type as the ones in the TOF only wider, were positioned in front of TPM1, called TrMRS, and in front of D1, called TrFS. Then a timing coincidence between a vertex detector, one of these slats and a TOF was put into the experiment as track triggers. Three of these were developed and used, as described in detail in table 5.2.

Since the collision rate was very high, and trigger 1 or 4 were required by all other triggers, not all minimum bias triggers were recorded. Most of these events had no tracks in the spectrometer, and therefore only every Nth minimum bias event was recorded, were N was of the order 100–1000. Instead most of the events recorded were events that fired the track triggers. Depending on the beam quality and species these would be scaled down with a factor of 1–10, due to limitations in the speed
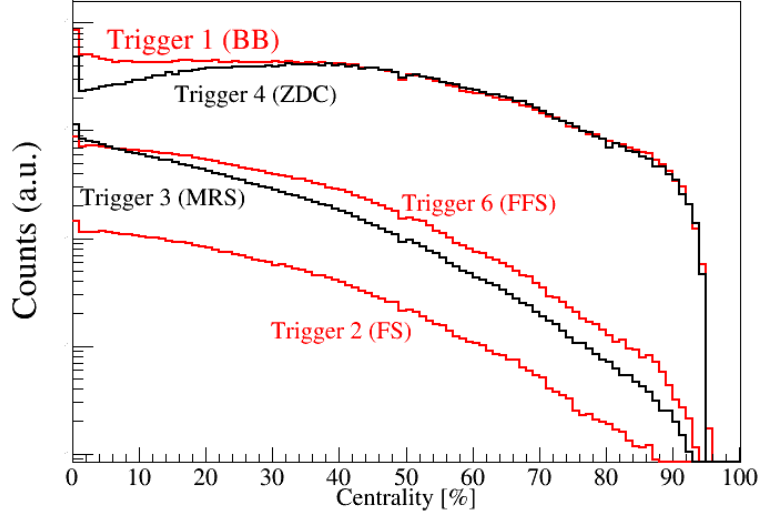
Figure 5.8: Distribution of scaled triggers vs centrality in heavy ion collisions. The figure also shows that the ZDCs are not 100% efficient for heavy ion central collisions at $\sqrt{s_{NN}} = 62.4$ GeV, as it drops below the BBC trigger at collisions more central the $\sim 30\%$. Therefore trigger 1 must be used as a minimum bias trigger for collisions with centrality $< 30\%$ at this energy. Notice that the y–axis has a logarithmic scale.

Trigger	Detectors	Description
1	BBC	Minimum bias trigger for central collisions ($> 55\%$).
2	BBC–TrFS–H1–H2	The forward trigger. Require timing coincidence between all 4 detectors. During the Au+Au $\sqrt{s_{NN}} = 62.4$ GeV run in 2004, the H2 signal was not in the trigger.
3	BBC–TrMRS–TOFW	The mid rapidity trigger. Require timing coincidence between all 3 detectors.
4	ZDC	Minimum bias trigger. Decreasing coverage with decreasing particle size. Gets slightly inefficient for very central collisions.
5	CC(ZDC CDF)	Minimum bias trigger in $p + p$ collisions. (In heavy ion collisions, when the CC is not installed, it is used as a special minimum bias trigger for diagnostics.)
6	BBC–TrFS–H1	The front forward trigger. Require timing coincidence between all 3 detectors. During the Au+Au $\sqrt{s_{NN}} = 62.4$ GeV run in 2004, the BBC was replaced with the ZDC signal.

Table 5.2: The table lists the triggers used in the BRAHMS experiment. An example of the event distribution recorded with these triggers is shown in figure 5.8.

of the DAQ (Data Acquisition) system.

An example of the centrality distribution of events recorded by the various triggers can be seen in figure 5.8. The figure shows that trigger 1 and trigger 4 can both be used for normalisation purposes. The fall off seen at $\sim 60\%$ centrality, indicates the beginning of an inefficiency of these triggers. Consequently no analysis is performed below 60% centrality, i.e. 60–100%.

Chapter 6

Data reconstruction

BRAHMS recorded so–called raw digital signals from all its detectors, corresponding to the energy deposition related to the passage of charged particles through individual detector segments. The typical primary information is position, deposited energy and time. To track and identify the actual particles flying through and interacting with the detectors, a complicated and time consuming data analysis has to be performed. The details of all analysis steps are described here and in the appendix A. This chapter will focus on the performance of the spectrometers, how particle spectra are build and what corrections went into construction of the invariant transverse momentum spectra that will presented in chapter 7. These spectra form the basis for the analysis of the nuclear modification factors.

6.1 Global event characteristics

The vertex position, the event plane and the collision centrality are used by BRAHMS for global event characterisation, though the event plane is not used in this analysis. The vertex position is calculated from the timing signals from either the BBCs, ZDCs or CCs. From the left and right position the vertex is calculated from the following formula:

$$z_{vtx} = 0.5 \cdot c \cdot (t_L - t_R) \qquad (6.1)$$

where the detected particles are assumed to travel with the speed of light c and arrive at times t_L and t_R at the left and right side detector, respectively. The timing resolution of these detectors is shown in figure 5.4 and 5.5.
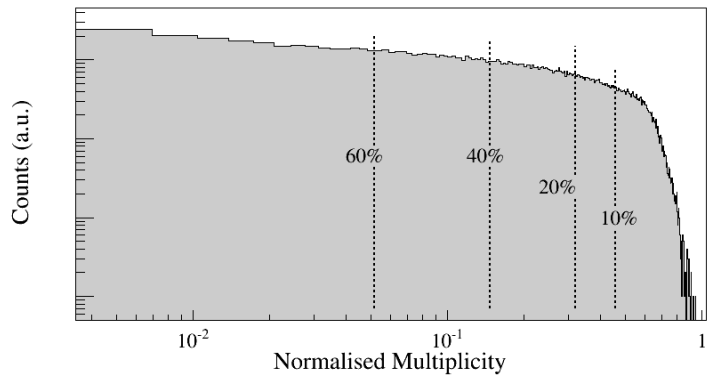
Figure 6.1: The figure shows a measurements multiplicity distribution. The black vertical dotted lines show the relation between centrality in the multiplicity, i.e. collisions with 40-60% centrality produce a multiplicity between the corresponding dotted lines.

Centrality	0–10%	10–20%	20–40%	40–60%	30–45%	38–50%
$\langle N_{\text{part}}\rangle$Cu+Cu	92^{+2}_{-2}	71^{+3}_{-3}	43^{+3}_{-3}	20^{+2}_{-2}	Not Used	Not Used
$\langle N_{\text{part}}\rangle$Au+Au	315^{+5}_{-7}	222^{+8}_{-9}	129^{+9}_{-9}	56^{+8}_{-6}	95^{+9}_{-8}	72^{+8}_{-7}
$\langle b_{\text{CuCu}}\rangle$ [fm]	$2.6^{+0.1}_{-0.1}$	$4.1^{+0.2}_{-0.2}$	$5.9^{+0.3}_{-0.3}$	$7.6^{+0.3}_{-0.3}$	Not Used	Not Used
$\langle b_{\text{AuAu}}\rangle$ [fm]	$3.5^{+0.2}_{-0.1}$	$6.0^{+0.3}_{-0.3}$	$8.4^{+0.5}_{-0.4}$	$10.7^{+0.6}_{-0.5}$	$9.4^{+0.5}_{-0.4}$	$10.1^{+0.6}_{-0.5}$

Table 6.1: The table contains the average impact parameter and the average number of participants for each centrality bin used in this work. The numbers are calculated as stated in section 3.2.

The multiplicity is determined from the energy deposits in the multiplicity barrel (the TMA and SiMA). The energy is found through a comparison of the detector response and a GEANT [105] simulation of the detector, thus including the simulation of background. The TMA and SiMA cover $-2.2 < \eta < 2.2$. The detectors are calibrated using peripheral events, so that the energy deposits from a single particle can be determined. In more central events this information is used to determine the actual number of particles going through each detector segment. The accuracy of the multiplicity measurements using the single particle energy deposit has been estimated through simulations, using HIJING, to be better than 3%. To determine the centrality, the multiplicity distribution shown in figure 6.1 is integrated. This is then corrected for the total cross–section coverage, which is done through a GEANT simulation of the minimum bias trigger using HIJING events. Relative centralities, C, are found from the multiplicity distribution, M, shown in figure 6.1, by making the ratio:

$$C = \frac{\int_x^1 M}{\int_0^1 M} \tag{6.2}$$

where x is the normalised measured multiplicity, $0 < x < 1$.

To relate the the impact parameter to the experimental centrality bin, BRAHMS has done a Monte Carlo simulation using the HIJING event generator and the formalism in section 3.2. The centrality measurement is related to an average impact parameter, $< b >$, and an average number of participants $\langle N_{\text{part}}\rangle$, as shown in table 6.1.

6.2   Particle reconstruction and identification

Getting global tracks

The local tracking in the TPCs and DCs has been well described in [3, 96, 102], and is done by a "swimming" algorithm. This means it starts at a hit in the front of the tracking detector and looks into the detector and tries to follow hits that lie along a straight line. The matching of tracks is done by projecting local tracks to the xy-plane in the middle of the magnet, between two tracking chambers, as shown in figure 6.2. The tracks with good matching parameters in Y-position Δy, Y-slope $\Delta\alpha_y$ and bending angle $\Delta\Psi$ are kept and the others are rejected, as seen in figure 6.3. The selection is done on the sum of the three parameters:

$$\left(\frac{\Delta y - \Delta y_{offset}}{\sigma_{\Delta y}}\right)^2 + \left(\frac{\Delta\alpha_y - \Delta\alpha_{y,offset}}{\sigma_{\Delta_{\sigma_y}}}\right)^2 + \left(\frac{\Delta\Psi - \Delta\Psi_{offset}}{\sigma_\Psi}\right)^2 < n_\sigma^2 \tag{6.3}$$
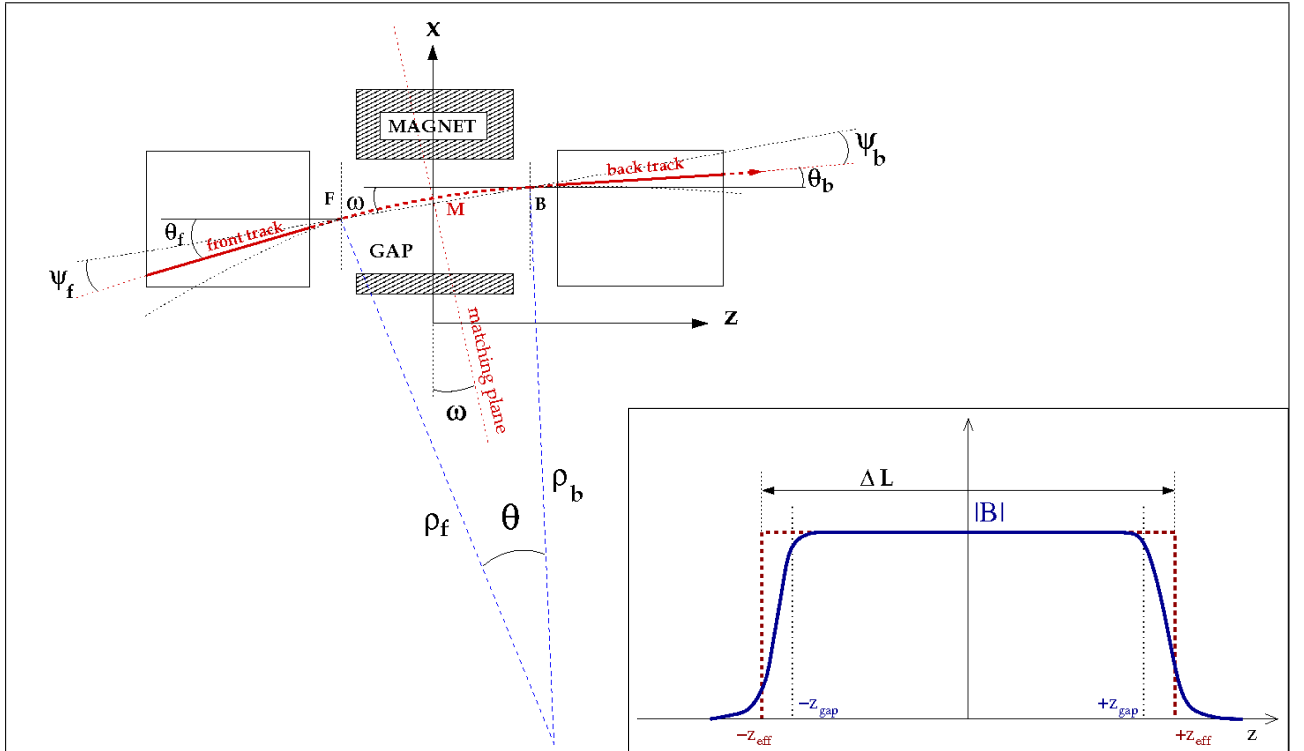
Figure 6.2: The figure show how local straight line tracks in the tracking chambers are paired to make global tracks. From the curvature of the track inside the magnet, the particle momentum can be calculated. Using the relation $\vec{p} = q\vec{B} \times \vec{\rho}$ and trigonometry on the figure gives: $p = (qB\Delta L)/((\sin\theta_f - \sin\theta_b)\sqrt{1 - \alpha_y^2})$, where q is the particle's charge $(-e)$, B the magnetic field strength, ΔL the length between the "effective edges" of the magnetic field (point F to point B) and α_y is the angle of the track in the YZ-plane. The angles θ_f and θ_b are shown in the figure. The effective edges of the magnetic field (z_{eff}) and the physical opening of the magnet (z_{gap}) can be seen in the insert. The area under each curve, the square box and the measured field strength, is the same. The figures are taken from [96].

where n_σ it set to be 4 in BRAHMS analysis. This corresponds to 4 standard deviations.

Track quality

For hadron analysis, the matching criterium in eq. 6.3 is set to 4 standard deviations. To make sure that the track is a primary particle that originates from the vertex point, the track is projected back to the vertex plane. For MRS tracks the vertex plane is the YZ-plane at $X = 0$, and for the FS/FFS tracks it is the XY-plane at $z = z_{vtx}$. Figure 6.4 shows the distribution of tracks projected back to the vertex plane.

In the same fashion as for the track matching, a 2 dimensional elliptical cut is made on tracks
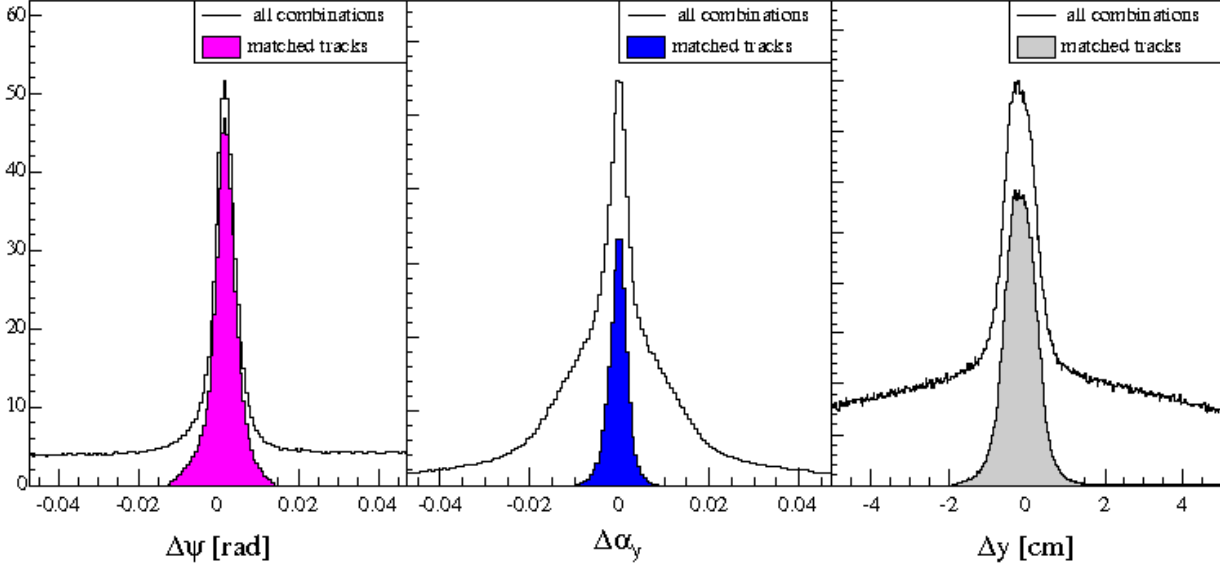
Figure 6.3: The black solid line shows all combinations of matching tracks. The selection of tracks that have good matching parameters are shown in the coloured areas. The $\Delta\Psi$ in the left panel is defined as $\Delta\Psi = \Psi_f - \Psi_b$. Ψ_f and Ψ_b are shown in figure 6.2.

projected back to the vertex plane:

$$\left(\frac{y - y_{offset}}{\sigma_y}\right)^2 + \left(\frac{t - t_{offset}}{\sigma_t}\right)^2 < n_\sigma^2 \tag{6.4}$$

where $t = z_{track} - z_{global}$ for the MRS and $t = x$ for the FS/FFS.

PID track quality

When the global tracks have been reconstructed, their PID information is added from the appropriate detector(s). Selecting particles with good PID in TOFs are done as described in appendix A.2. Plotting the $\beta_{reco}^{-1} - \beta_{calc}^{-1}$ gives gaussian distributions, seen in figure 6.5. The distributions are fitted and particles within 2 standard deviations are selected as particles with proper PID. All final identified particle spectra are corrected with a factor corresponding to this 2 standard deviation selection. This method is applied for all particles above 0.85 GeV/c. As can be seen in figure 5.6, separation of pions and kaons in TOFW can be done up to 2 GeV/c and protons from kaons up to about 3.3 GeV/c. These upper limits of separation depends on the calibration of the detector, and how far it is from the detector is from the interaction point.

Lower momentum particles are identified through their calculated m^2, $-0.0805, < m_{\pi^\pm}^2 < 0.1195$ (GeV/c^2)^2, $0.1237 < m_{K^\pm} < 0.3637$ (GeV/c^2)^2 and $0.6804 < m_{p,\bar{p}} < 1.4804$ (GeV/c^2)^2. As can be seen in left panel of figure 5.6, selecting identified particles using their β^{-1} value becomes difficult when the $\beta^{-1}(p)$ distribution is too steep. The distributions narrows which makes a selection via m^2 ideal. The method used in [97, 96, 83] calculated the m^2 resolution, which gives the best PID selection
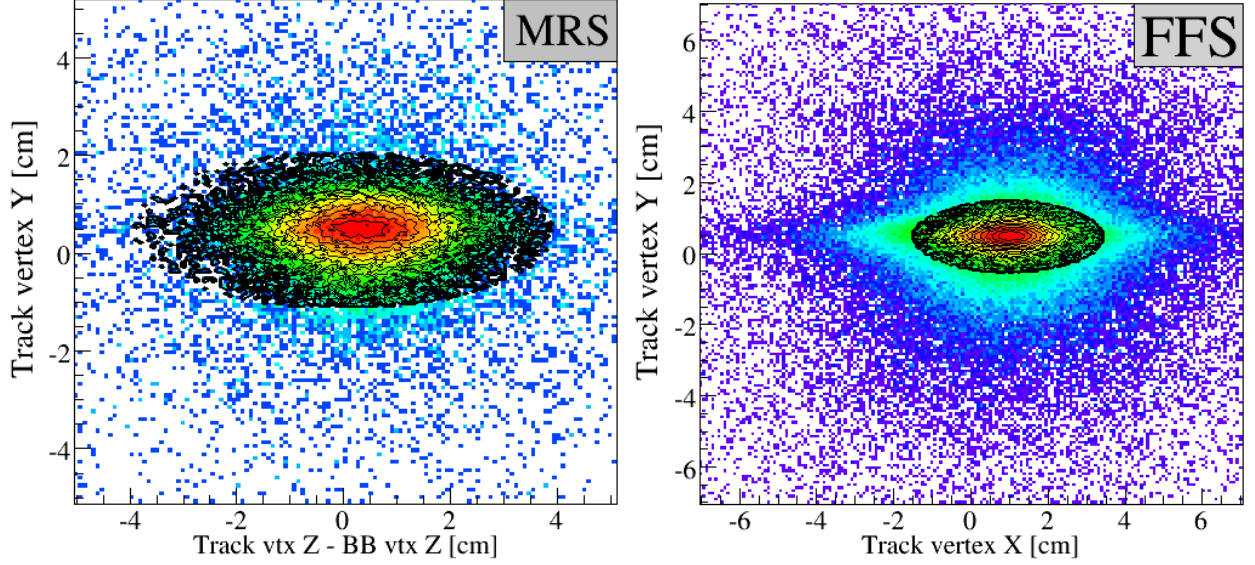
Figure 6.4: The figure shows the distribution of particles projected back to the primary vertex plane. The left panel shows the MRS and the right shows the FS/FFS track projection. The contour levels are logarithmic. The coloured scatter are all matched tracks. The black area are the tracks that satisfies the condition in eq. 6.4 with a 4 standard deviations cut off. These are then treated as primary particles.

for all momenta, but requires high statistics. This could not be done in the analysis presented in chapter 7 as the statistics was not high enough.

Identified particles then go through a "refitting" algorithm, which calculates a χ^2 value for the global track. It starts with projecting the track in the first tracking chamber back to the vertex and to the next tracking chamber. The deviation between the projected track position and direction and the measured one is calculated. The widths, σ_{value}, of these distributions are found, see example in middle panel of figure 6.3, and a χ^2 value can be calculated. It is calculated as follows:

$$\chi^2 = \frac{(z_{vtx}^{global} - z_{vtx}^{proj})^2}{\sigma_{z_{vtx}^2}} +$$
$$\sum_{TN} \left(\frac{(x_{track} - x_{proj})^2}{\sigma_x^2} + \frac{(y_{track} - y_{proj})^2}{\sigma_y^2} + \frac{(\alpha_{y_{track}} - \alpha_{y_{proj}})^2}{\sigma_{\alpha_y}^2} + \frac{(\theta_{track} - \theta_{proj})^2}{\sigma_\theta^2} \right) \tag{6.5}$$

where z_{vtx}^{global} is the vertex position found by global detectors, z_{vtx}^{proj} is the projection of the track back to the beam axis YZ-plane, the sum TN is over all the tracking chambers, x and y is the coordinates of the track in tracking chamber TN, α_y is the slope parameter in the Y-direction and θ is the angle in the local XZ-plane relative to the Z-axis.

This χ^2 value can now be used to remove poorly matched particles, as shown in figure 6.7. By propagating pions, kaons and protons (and their anti particles) through the middle of the spectrometer
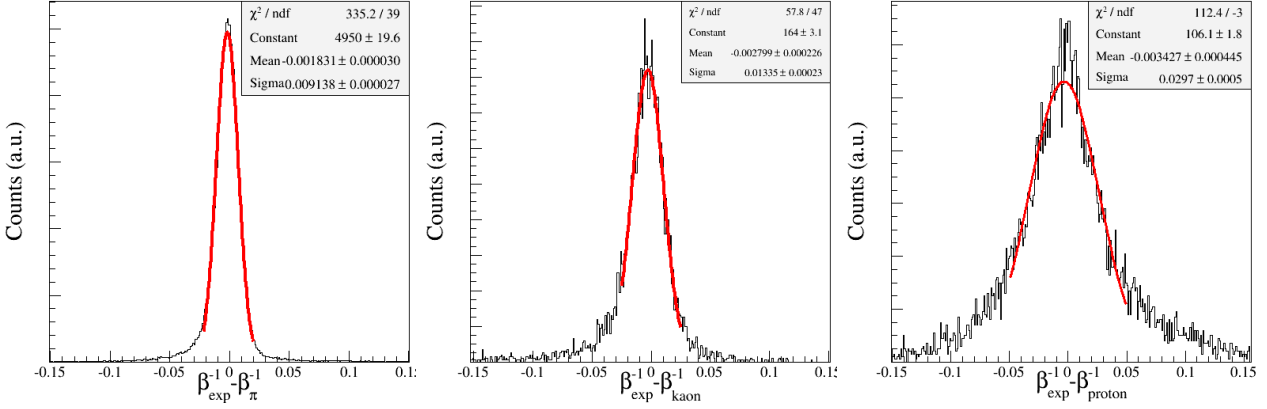
Figure 6.5: The figure shows the $\beta_{reco}^{-1} - \beta_{calc}^{-1}$ distribution for pions, kaons, and (anti-) protons. The distributions are fitted with a gaussian function. Particles within 2 standard deviation of the mean, and a momentum above 0 GeV/c.85 are accepted as identified particles.

using GEANT with multiple scattering, absorption and decay processes turned on, and reconstruction them using the same programs that analyse data, a χ^2 distribution is found. An example for the FS is shown in figure 6.6. This distribution is then sliced into momentum regions. Each region's root mean square (RMS) value is then plotted vs momentum. The FS and MRS RMS points are then fitted with: $\chi^2 = a + b/p$ and $\chi^2 = a + b \cdot p^{-2} + c \cdot p^{-4}$, respectively.

6.3   Data corrections

Following the philosophy from the reconstruction process of the data, the correction is divided into as many steps as possible. It is assumed that these corrections factorise. Pure geometric acceptance correction (see section 6.3.2) and tracking efficiency are applied to all types of particle spectra. In addition to these corrections, identified particle spectra are applied a PID efficiency, multiple scattering, absorption and feed down correction. The PID and tracking efficiency corrections are obtained from the data itself and is discussed in section 6.3.1. The later three ("GEANT corrections") do not factorise and are estimated through a Monte Carlo simulation of the BRAHMS detector, using GEANT. These corrections are discussed in section 6.3.3. One special correction must be used when dealing with $p + p$ collisions. There is no centrality or impact parameter in $p + p$ collisions, which mean that only minimum bias data can be collected. All data therefore need to be corrected for the cross–section coverage of the minimum bias trigger in $p + p$ collisions (the CC detector). The heavy ion results presented in chapter 7 will not show minimum bias spectra, only selected centrality bins, so no cross–section coverage correction is needed, as the trigger is $\gg 99\%$ effective in these centrality ranges.

    The following sections describe in detail how these various correction factor are calculated, and how they are applied to the data.
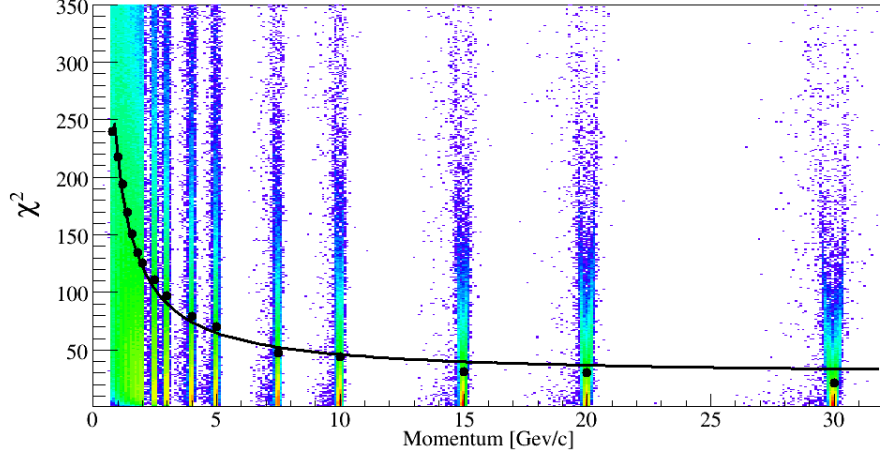
Figure 6.6: The figure shows the distribution of the track χ^2 vs momentum for a GEANT simulation of pions. The RMS root–mean–square) values are shown as black circles. These points are then fitted with $A + B/p$ where p is the momentum. All particles above $4 * (A + B/p)$ are rejected as poorly matched tracks.

Angle	Pions	Kaons	Protons
40°	$0.950 - 9.8 \cdot 10^{-5} \cdot H$	$0.958 - 9.0 \cdot 10^{-5} \cdot H$	$0.976 - 9.5 \cdot 10^{-5} \cdot H$
52.5°	$0.956 - 11.0 \cdot 10^{-5} \cdot H$	$0.966 - 11.0 \cdot 10^{-5} \cdot H$	$0.956 - 7.0 \cdot 10^{-5} \cdot H$
60°	$0.947 - 11.0 \cdot 10^{-5} \cdot H$	$0.953 - 10.0 \cdot 10^{-5} \cdot H$	$0.949 - 6.8 \cdot 10^{-5} \cdot H$
90°	$0.945 - 7.4 \cdot 10^{-5} \cdot H$	$0.952 - 7.2 \cdot 10^{-5} \cdot H$	$0.956 - 6.0 \cdot 10^{-5} \cdot H$
W.Av.	$0.948 - 9.6 \cdot 10^{-5} \cdot H$	$0.955 - 9.0 \cdot 10^{-5} \cdot H$	$0.959 - 7.2 \cdot 10^{-5} \cdot H$

Table 6.2: The table shows the tracking efficiency function for the MRS at various angles. It is taken from [103]. The main difference between the species is in the slopes. A total average can be made: $0.954 - 8.6 \cdot 10^{-5}$.

6.3.1 Tracking and PID efficiency

The tracking chambers do not detect 100% of the tracks. There are two different types of tracking detectors in BRAHMS: TPCs and DCs. Calculation of tracking efficiencies for the TPCs were done using a track embedding method, where simulated tracks are embedded into real events and then attempted to be reconstructed, see [103]. This study concluded that the tracking efficiency depended strongest on the occupancy of the TPCs, i.e. the number of hits in the TPC. Table 6.2 shows the main results for the tracking efficiency of global tracks in the MRS as a function of the number of hits in the TPCs. For data analysis without PID, it is not straight forward to use the numbers in table 6.2, as one should make a weighted average for the 3 types of particles corresponding to the actual distribution of species. The constants found in table 6.2 are very similar, only differing $\sim 3\%$. The slopes on the other hand range from $(6 - 11) \cdot 10^{-5}$. Inserting a low and high occupancy, say 10 and 100, see figure 6.10, will give pions a tracking efficiency correction of 94.7% and 93.8%. Correspondingly, kaons will get 95.4% and 94.6% and protons will get 95.8% and 95.2%. Making a simple average from these 1. degree polynomials should have a systematic uncertainty $\lesssim 1\%$.
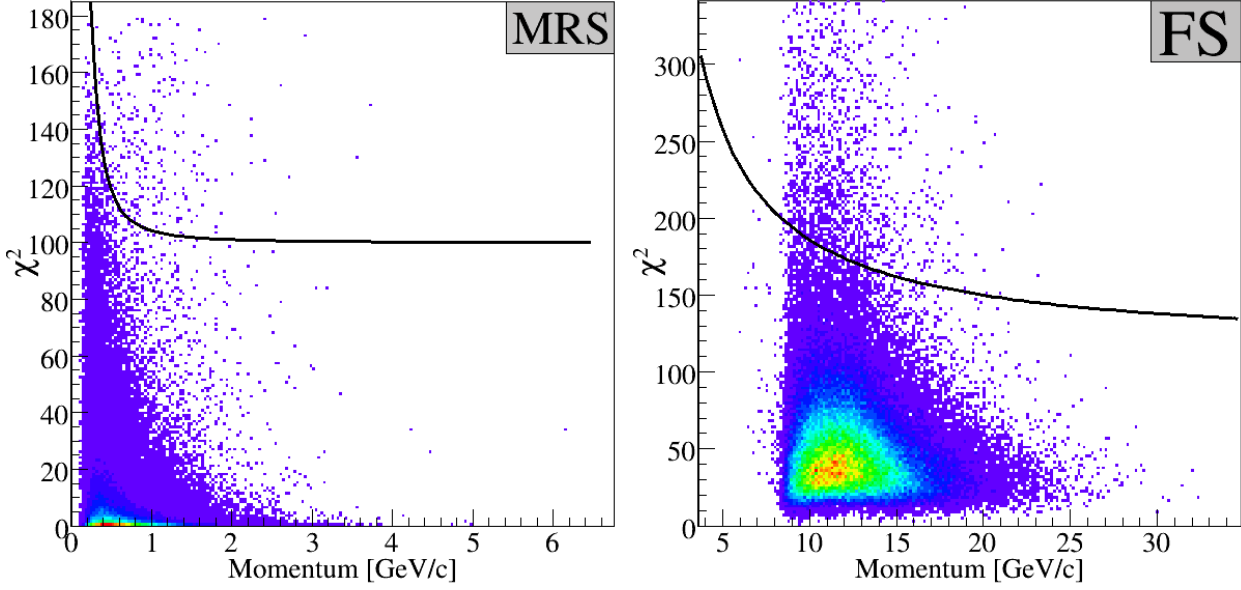
Figure 6.7: The figure shows the χ^2 vs momentum distribution. All particles above the solid lines are discarded from the analysis. These lines originate from fits of empirical functions to distributions such as the one shown in figure 6.6. The solid line in the FS figure is: $\chi^2 = n_\sigma(a + b/p)$, where $n_\sigma = 4$, $a = 28.5$, and $b = 180$. The solid line in the MRS figure is: $\chi^2 = n_\sigma(a + (m^2 + p^2) \cdot b/p^4)$, where $n_\sigma = 10$, $a = 10$, $b = 0.42$, m is the mass of the particle. he FS function was found to be independent of the particle's mass. Many of these particles are identified as muons or electrons. An example of the impact on the RICH PID is shown in figure 6.8.

The PID efficiency depends on the PID detector used. It can either be a TOF wall or the RICH detector. The PID efficiency for the TOFs are calculated as the ratio of hits to extrapolated tracks to each individual slat in the TOF wall. They typically have an efficiency of ~ 0.94, as shown in figure 6.9.

In addition to this, the RICH suffers from contamination of pions and kaons in the proton distribution with the RICH in veto mode. These are the particles with ring radius 0 and momentum between 9-19 GeV/c. This contamination is estimated to be $\sim 3\%$ from studies of pions and kaons identified by H2, see [97]. This means that a sum of π^+ and K^+ spectra must be made in this momentum region. 3% of this spectra must then be subtracted from theproton spectrum made by using the RICH in veto mode. Corresponding the sum of the π^- and K^- spectra must be subtracted from the anti–proton spectrum.

6.3.2   Geometric acceptance correction

As seen in figure 5.2, the opening of the spectrometers in BRAHMS does not cover 2π in azimuthal angle, so this has to be corrected for when constructing any spectra for a given (pseudo-)rapidity interval. The correction is done using the physical invariant quantities p_{T} and y (or η). Through a simple Monte Carlo simulation particles are propagated from a given vertex point towards the
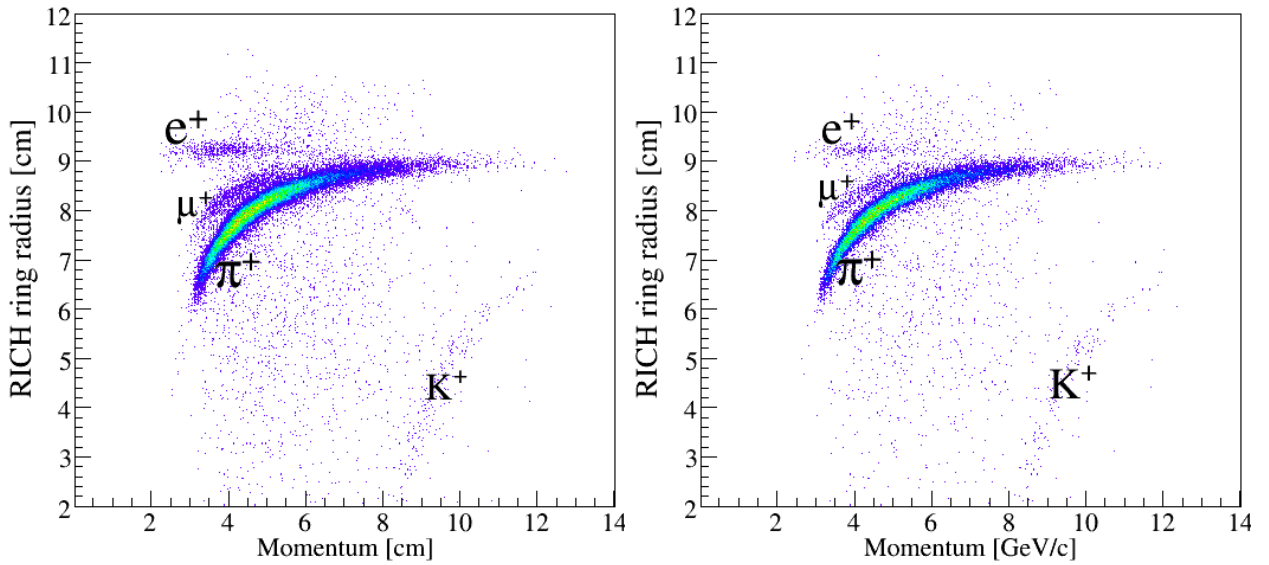
Figure 6.8: The left panel shows the RICH ring radius as a function of momentum, for a low field setting. A fiducial cut is imposed on the tracks intercepting the image plane, to avoid rings extending outside the RICH image plane. In the right panel a χ^2 cut is applied to the tracks. The χ^2 is calculated from matching the individual detectors information. Poorly matched tracks gets high χ^2, and are therefore removed. The right panel shows a lower density in the scatter plot in general, and in particular a cleaner sample of electrons an muons. Many of the muons originate from a decayed pion.

spectrometers, choosing angular regions in the spherical coordinates α and ϕ slightly bigger than the opening of the spectrometer. The opening of the MRS is the D5 magnet and the opening of the FFS/FSis the D1 magnet.

Furthermore a set of vertex ranges are selected. These are chosen to be bins of 5cm. Particles are then thrown from each vertex bin as a flat distribution with $\phi_{min} < \phi < \phi_{max}$, $\theta_{min} < \theta_{max}$ and $p_{min} < p < p_{max}$. The ranges in ϕ and θ are found by calculating the angles between the upper and lower side of the vertex and the respective corners of the opening of the first magnet in the spectrometer, then choosing the smallest and biggest angle. The momentum range must be chosen equal or slightly larger than what is found in the data.

In the simulation the actual geometry and magnetic field of the BRAHMS experiment is used. Additional fiducial cuts may also be introduced as needed. Each particle thrown is then tested if it can fly inside the spectrometer and passes any fiducial cuts. If it is not outside any detector or fiducial cuts, it is accepted. Two distributions in p_{T} vs y (or η) are made during this simulation, one for all thrown particles and one for the accepted particles. This two distribution are illustrated in figure 6.11. The ratio of the accepted to thrown distribution is called the acceptance map, and can be seen in figure 6.12. The accuracy of the acceptance map is in this analysis calculated to $< 1\%$.
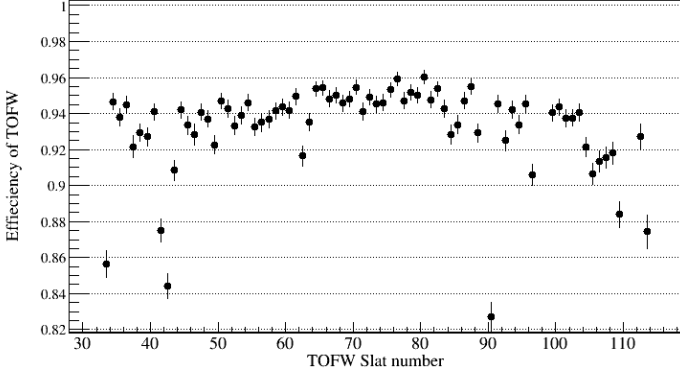
Figure 6.9: The figure shows the PID efficiency for the TOFW. The ratio is constructed from the number of good hits in a slat divided by the number of tracks that were extrapolated back to that slat.
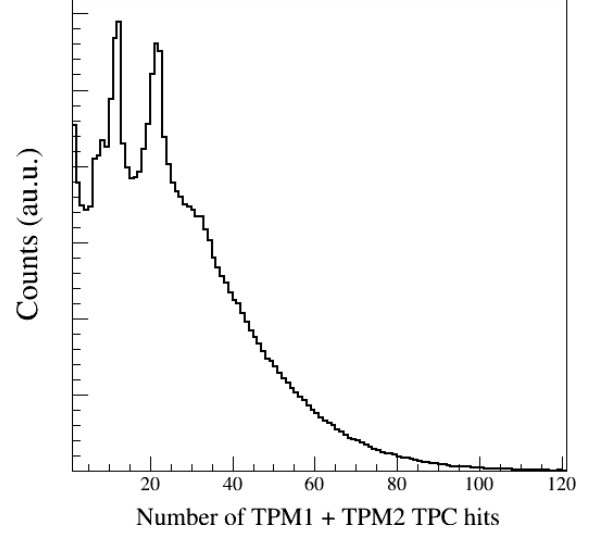
Figure 6.10: The figure shows a sample distribution of hits Cu+Cu collisions in the MRS from events with at least 1 track, TPM1 and TPM2 combined. This information can be used to properly correct for the tracking inefficiency.

6.3.3   Multiple scattering, decay and absorption correction

Identified particle distributions can be corrected for multiple scattering, decay and absorption. Pions, kaons and protons (and their anti–particles) are propagated through the middle of each detector (using the reference momentum) to avoid other detector and magnet edge effects that might affect the particle and its trajectory. By reconstructing the simulated tracks with the BRAT software, see appendix A, a χ^2 distribution with good statistics for all p_{T} is found. The particles are thrown with a flat p_{T} distribution. For each particle thrown, the magnetic field is changes so the spectrometer reference momentum becomes that of the particle. The track χ^2 cut described in the paragraph about the track quality in section 6.2 arises from this simulation. The simulated tracks and the data are have a very similar distribution.

The χ^2 cut–off is the RMS value of the χ^2 distribution for a given p_{T} range, making the cut p_{T} dependent. These RMS values are then plotted vs p_{T} and fitted with a function:

$$C_{MRS} = \sigma_N \left(a + \frac{b \cdot (m^2 + p^2)}{p^4} \right) \tag{6.6}$$

$$C_{FS} = \sigma_N \left(a + \frac{b}{p} \right) \tag{6.7}$$

where p is the momentum and a and b are free variables. σ_N was chosen to be 10 for the MRS and 4 for the FS.
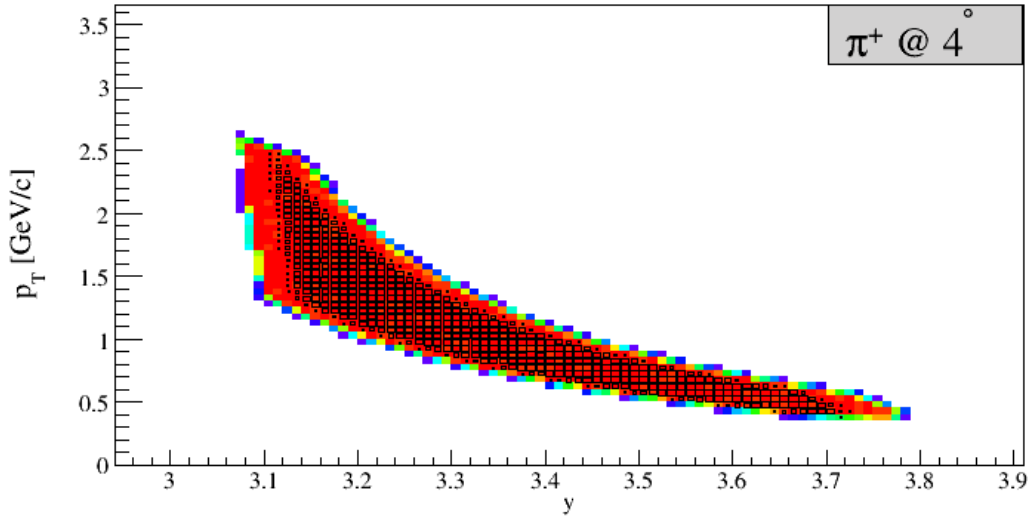
Figure 6.11: The figure shows the thrown and accepted π^+s at a 3° setting for the RICH, for one specific vertex bin. The colour contour is all thrown particles, while those who flew through the entire FS spectrometer and through the active volume in the RICH are shown as black boxes.

The correction factor for each p_{T} range is then found as the ratio of the number of good reconstructed tracks after the χ^2 cut is applied, to the number of thrown tracks. The correction factors for the MRS and the FS are shown in figure 6.13. The point to point ratio is not fitted with any function and the correction factor for a particle with momentum p is an extrapolation of the neighbouring points.

6.3.4 Minimum bias correction for $p + p$

The experience from collisions of d+Au and later $p + p$ at $\sqrt{s_{\mathrm{NN}}} = 200$ GeV, had lead to the implementation of an extra set of vertex detectors which also constituted the minimum bias trigger. These are the CC counters, described in section 5.2. This addition was needed because d+Au and $p + p$ collisions do not generate high multiplicity events, thus leading to a trigger inefficiency. The CC enlarged BRAHMS capability to detect as many events as possible. Minimum bias spectra therefore needs to be corrected for this trigger inefficiency.

A very important measurement performed by the beam developers during the $p + p$ collisions, were so–called "Vernier Scans" . The "Vernier Scans" were performed during special dedicated runs, where the beam profile was measured. Widths, σ_x and σ_y, assuming the beam bunches have gaussian profiles, are obtained. These calculations enabled the experiments to determine the cross section coverage for their minimum bias trigger. With the luminosity and the widths of the beam known, BRAHMS could then use the CC counters trigger rate to calculate the cross section coverage, σ_{CC}:

$$\sigma_{CC} = \frac{f_{CC} \cdot 4\pi \cdot \sigma_x \cdot \sigma_y}{f_{RHIC} \cdot n_1 \cdot n_2 \cdot} \tag{6.8}$$

where f_{CC} is the trigger frequency of the CC detector, $\sigma_x = 0.51$ cm and $\sigma_y = 0.66$ cm the width
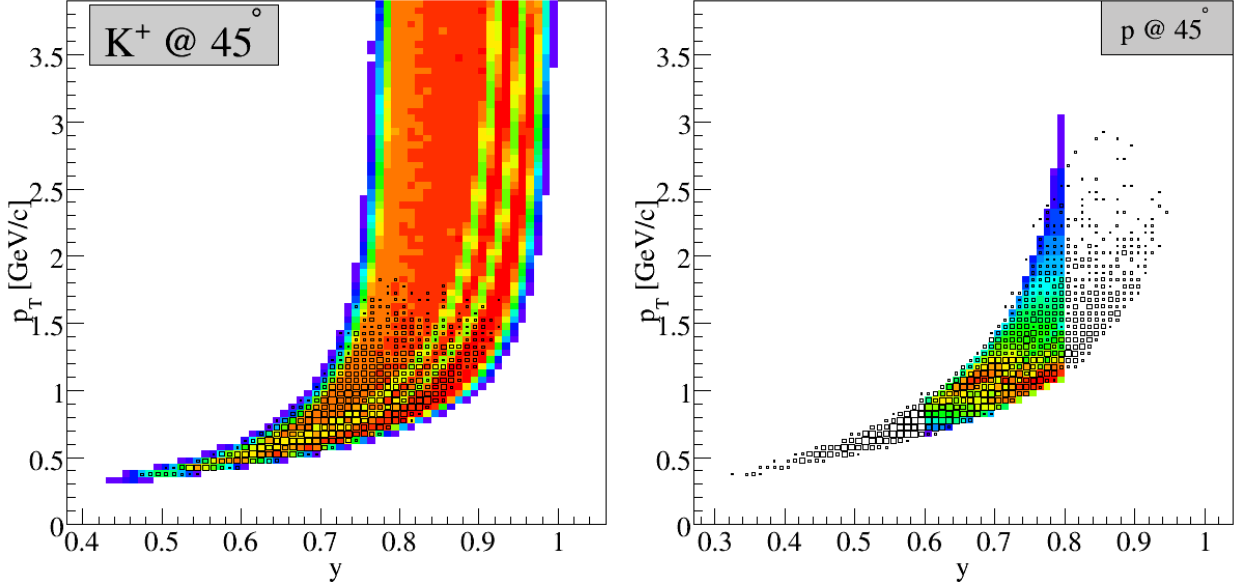
Figure 6.12: The left panel shows recorded data, black squares, on top of the geometrical acceptance map for K^+s identified by the TOFW. The two bands with reduced acceptance, seen in the middle of the distribution, are due to two dead slats in TOFW, 89 and 97. The right panel shows protons on top of a processed acceptance map. This map has been cut off between $0.6 < y < 0.8$ and is normalised for the its rapidity width for each p_{T} bin, which can be used to make a proton spectrum for this rapidity interval. The two dead slats are also visible underneath the black boxes.

of the beam, n_1 and n_2 the number of ions in the 2 crossing bunches and f_{RHIC} the RHIC bunch crossing frequency, which is 9.6 MHz.

The Vernier Scans were done twice during the run period and gave $\sigma_{CC} = (11.6 + 12.5)/2 = 12.1$ mb. The total inelastic cross section for $p + p$ collisions at $\sqrt{s_{\mathrm{NN}}} = 62.4$ GeV is 36 mb. The relative coverage, or trigger efficiency for the CC detector was 33%±.

As the CC detector is also part of the track trigger, the cross section coverage for the track trigger also needs to be determined. The probability for a track in a specific (p_{T}, y) (or (p_{T}, η)) in the spectrometer to have a CC vertex associated with it is given as:

$$P_{track,cc} = \frac{N(y, p_{\mathrm{T}})}{L \cdot E_{acc} \cdot \sigma_{y, p_{\mathrm{T}}}} \tag{6.9}$$

where $N(y, p_{\mathrm{T}})$ is the number of counts in a (y, p_{T}) bin, L the luminosity, $\sigma_{y, p_{\mathrm{T}}}$ the cross section at (p_{T}, y) and E_{acc} is the geometric acceptance. Correspondingly, one can make the same formula for the probability of recording an event, for a given $p + p$ interaction, with the CC detector:

$$P_{\mathrm{CC}} = \frac{N_{\mathrm{CC}}}{L \cdot \sigma_{\mathrm{inel}}} \tag{6.10}$$
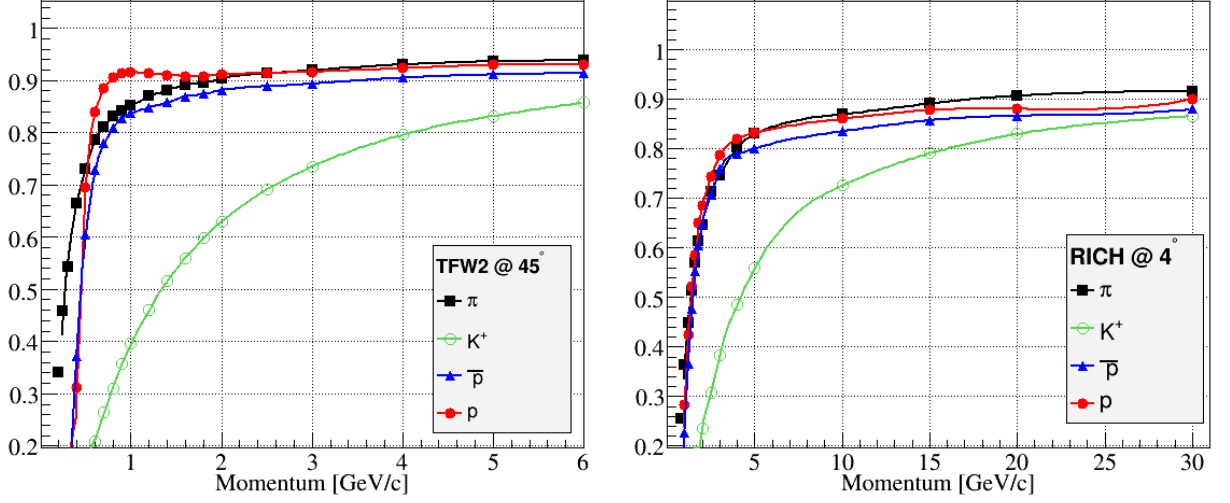
Figure 6.13: The figure shows the correction factors due to multiple scattering, decay and absorption for various particles types. The K^- corrections is equal to the K^+ to $< 1\%$ and is omitted from the figure for clarity.

where N_{CC} is the number of events recorded by the CC detector and σ_{inel} is the total inelastic cross section[1].

To get the correct normalisation for $p + p$ collisions at $\sqrt{s_{\mathrm{NN}}} = 62.4$ GeV, the spectra must be multiplied by a factor of:

$$C = \frac{P_{CC}}{P_{track,cc}} \tag{6.11}$$

The probability for detecting a track with a CC trigger can actually be determined from the data in the following way:

1. Count the number of good tracks in an event sample regardless of whether the inclusive trigger contains the minimum bias trigger CC is trigger 5), and regardless of whether the event is with or without a vertex calculated by the CC. Build a p_{T} spectrum of the particles.

2. From the same event sample as above count the number of tracks but this time require an inclusive trigger with trigger 5 in it, and a good CC vertex for the track. Build a p_{T} spectrum of the accepted particles.

3. The ratio of the spectra from condition 2 to condition 1 gives a p_{T} dependent efficiency of the track trigger. An example is shown in figure 6.14.

---

[1]Eq. 6.8 is related to eq. 6.10 through $\sigma_{\mathrm{CC}} = \sigma_{\mathrm{inel}} \cdot P_{\mathrm{CC}}$
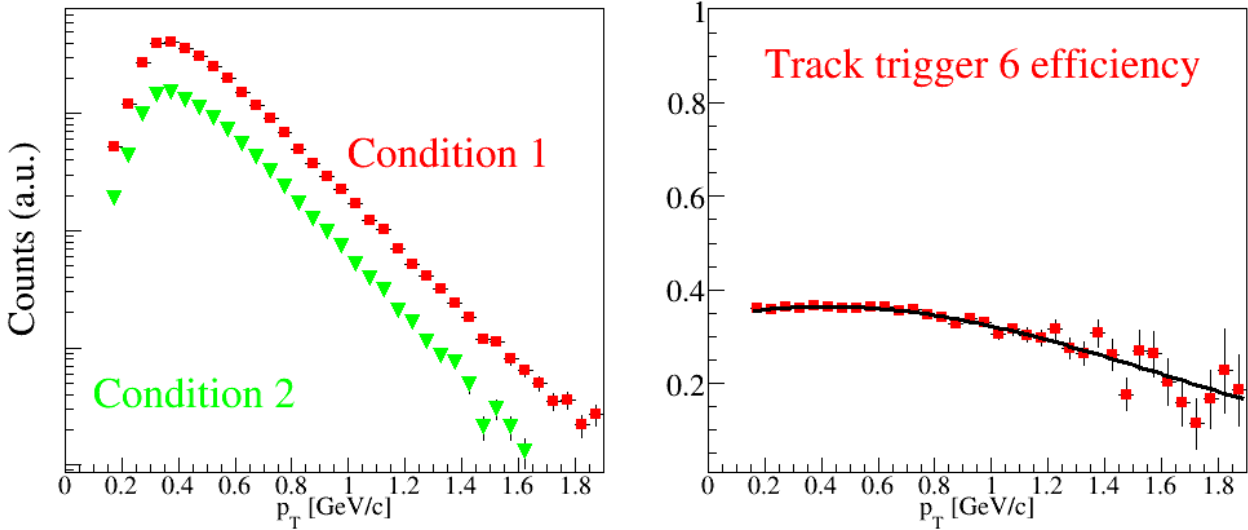
Figure 6.14: The left panel shows the distribution of condition 1 and 2 described in the text. The right panel shows the ratio of the two p_{T} distributions, which is the efficiency of trigger 6, the FFS track trigger. The distribution is fitted a gaussian function: $0.365e^{(\frac{p_{\mathrm{T}}-0.420}{1.176})^2}$

6.4   From raw data to physics data

This section will describe in detail how the data reduction is done, from raw recorded data to the final tree structured files containing particle identified tracks.

The first ~ 3 years of BRAHMS running was used to gather experience on how to analyse the BRAHMS data. During that period there was no official policy, on how it should be done or on how to store the data. From this experience BRAHMS decided to do the data reduction in steps, which was implemented in 2004. This had many benefits. The usage of the two BRAHMS computer farms, *crs* and *cas*, was better utilised, as many small jobs could be spread over all the CPUs. These small jobs would not require long running time. Fixing analysis mistakes or problems was not time consuming as one did not always have to start the analysis from scratch. With many small steps in the analysis procedure, that storage of files needed to be effective as the data volume was increasing beyond the capability of the hard drives. Therefore a file catalogue database was set up in the same fashion as the BRAHMS calibration data base. This data base keeps records of where all versions of any files are at any time. A specific user account called *bramreco* was set up with all the necessary programs and scripts to submit the data reduction/analysis jobs to the computer farms. All jobs are submitted to the CONDOR queues, see [106]. At RHIC all analysis jobs submitted to the *crs* farms go through the RHIC CRS software [107], which enables access to the BRAHMS tape drives.

The data files are kept in two places: either on the HPSS tape drives or on hard drives. The HPSS tape drives are only accessible from one of BRAHMS two computer farms. The hard drives are accessible from all farm machines. When any data is analysed it is assigned a version number. Any reanalysis of data gets a new version number. This way comparison with the previous results

is possible. There is also a "production number" used on all types of official reconstruction. The production number should only be increased if there is any new detector calibration added to the analysis.

There are 3 official analysis steps in BRAHMS, which generates files called LTR, GTR and DST. Section 6.4.4 in this chapter, describes two ways to analyse the DST files, to get final physics results. All final analysis of the DSTs are done using method 1 (*hadronAnalyse*) or 2 (*tree2datamap*) in section 6.4.4.

6.4.1 Local TRacking

All BRAHMS raw data are recorded to the BRAHMS HPSS tape drives. The files are divided into runs and each runs is divided into a necessary number of sequences, so as not to exceed the computer system maximum allowed file size. They have names:

```
runXXXXXXseqYYY.dat
```

where XXXXXX is the run number and YYY is the sequence number. The biggest bulk of data comes from the BRAHMS 4 TPCs. The first data size reduction is therefore to do the local tracking, i.e. reconstruct straight tracks in each individual TPC and DC, and replace the raw data signals with these tracks. In short, the tracking is done by combing ADC signals into clusters/hits and the combining the hits into tracks, see [103, 102] for a full description on how the TPC tracking is done. Furthermore the LTR program copies all the raw data from the other detectors: ZDC, BBC (and CC for $p + p$collisions), TMA, SiMA, TOFW, TFW2, H1, H2, C1, C4and RICH. The data is stored as a chain of events in a file on a hard drive in the ROOT standard format [108]. The files have a typical file size of $\sim 350 - 400$ Mb and are called:

```
ltrXXXXXXseqYYYvApB.root
```

where B is the production number and A is the version number for this production. To perform this analysis in BRAHMS, one logs into the *bramreco* account, enters the directory designated a run period, specie and energy. The program to execute is called *submitLtr.perl*. The default options tells on which disk the LTR file will be stored. Making sure there is enough disk space left, is crucial. The large statistics data sets, like the Au+Au $\sqrt{s_{\mathrm{NN}}} = 200$ GeV from 2004, needs to have the LTR files on several different disks. Executing the following commands:

```
$ cd DataProduction/run[YEAR]/[SPECIE]/[ENERGY]/ltr/
$ ./submitLtr.perl [STARTRUNNUMBER] [ENDRUNNUMBER]}
```

performs local tracking on all data runs, including all their sequences, between the 2 given run numbers.

6.4.2 Global TRacking

The second stage of the reconstruction connects the local tracks, from the TPCs and the DCs, into "global tracks" that span from the first tracking chamber in the spectrometer to the last one. These tracks are also matched to raw hits in the time–of–flight walls. The BBC vertex, ZDC vertex and, if present, the CC vertex are reconstructed, which also provide the start time for the event. The start time is a very important calculation for the particle identification process. It comes from either the

BBC of the CC. The other detectors that also get a data reduction are the multiplicity detectors, SiMA and TMA, and the Čherenkov detectors. The multiplicity array can after this analysis step provide the centrality of the collision, and the RICH can provide a particle identification, through a calculated ring radius and mass of the particle.

The steps for doing the reconstruction is the same as for the local tracking. From the *bramreco* account one executes the commands:

```
$ cd DataProduction/run[YEAR]/[SPECIE]/[ENERGY]/gtr/
$ ./submitGtr.perl
```

This generates another set of files in the ROOT format, which are stored on disk. The files is still kept on run–sequence basis which means that they still require a large amount of disk space, so care has to be taken when deciding where to put the data. It is also smart not to write to the same disk as the one is reading from, as this will speed up the reconstruction time, as this step is quite i/o intensive. The files have a typical size of $\sim 350 - 400$ Mb and are called:

```
gtrXXXXXXseqYYYvApB.root
```

6.4.3 "Data Summary Tree"

The last official step in the BRAHMS analysis, is the DST generation. The DSTs are not pure "data summary trees". There are still some numbers in these trees that are very detector specific. The first part of the analysis on the GTR files is a global refitting of the spectrometer tracks. The a full analysis of the TOF data is done, and each track that had a TOF hit associated with it gets a calculated β^{-1} and m^2 using the start time. Finally the event is extracted from each individual detector/segment, and the data is put into a tree structure. The reconstruction procedure is the same as the one for LTR and GTR production. From the *bramreco* account one executes:

```
$ cd DataProduction/run[YEAR]/[SPECIE]/[ENERGY]/gtr/
$ ./submitGtr.perl
```

This step reduces the data size by a factor of about $5 - 10$, which means that the sequences in a run are merged into one single file. They now have a reasonable size, which depends on the number of sequences in the run, which is suitable for the final step of the analysis. This final step is typically repeated many times, as one checks the quality of the data, performs preliminary analysis, includes or improves calibration etc. The DSTs are also kept on disk, but after they are generated, the LTR and the GTR files are often moved to HPSS storage. One needs to consider disk space and i/o bottle–necks when generating DSTs, the same way as for the GTR files. Once generated the files are called:

```
dstXXXXXXvApB.root
```

6.4.4 Brahms ANalysis APPlications

To acquire a copy of BANAPP you need to be a member of the BRAHMS collaboration. You get the package from CVS [109], though also needed are the libraries from ROOT, BRAT and BDST. These are also available from CVS.
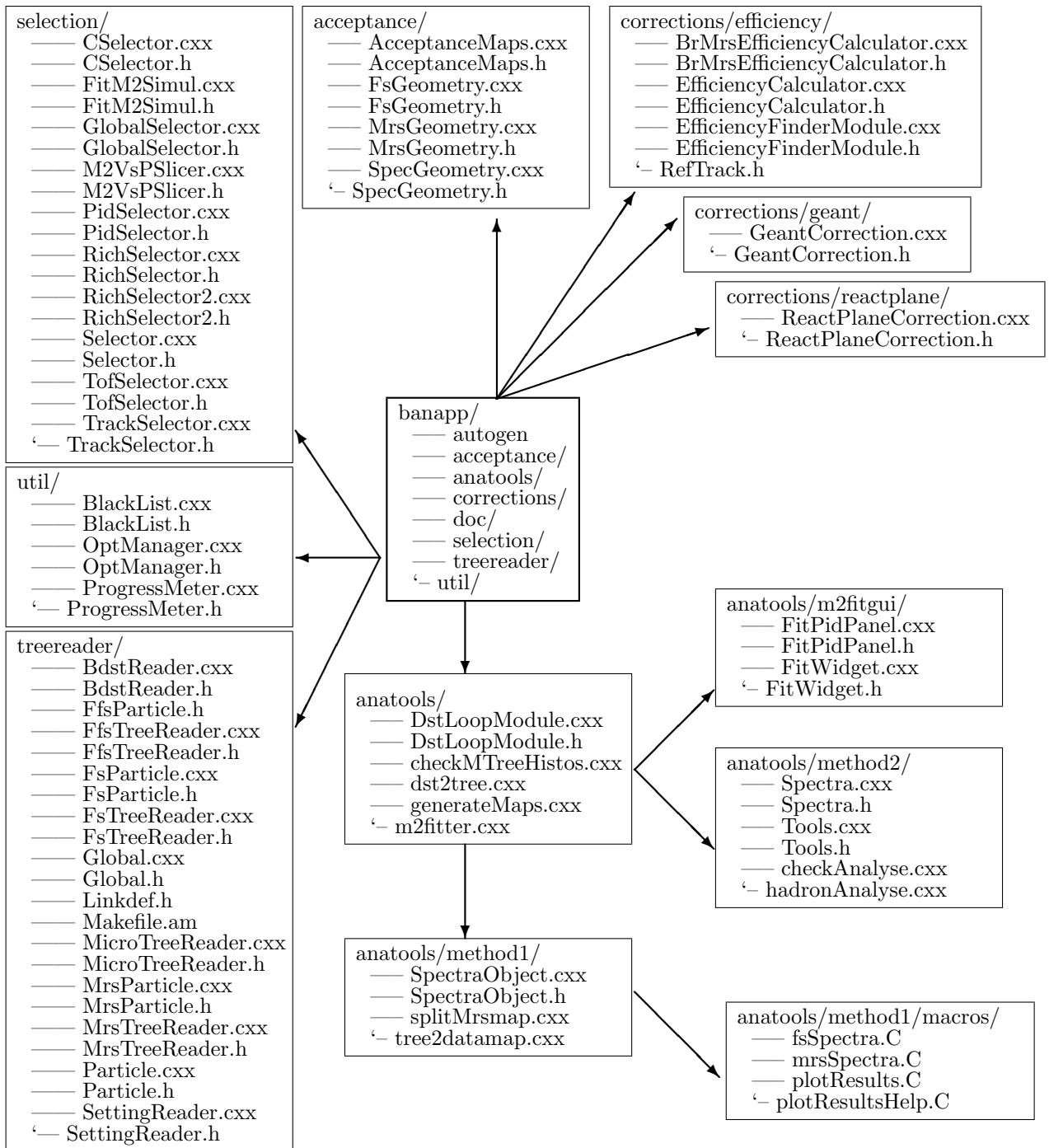
Figure 6.15: The figure shows the files in the BANAPP package. Only the **c++** code files are shown. To compile and install BANAPP: `./autogen && ./configure --with-bdst=[BDST-installation-dir] && make && make install.`

The BANAPP package's purpose is to make invariant p_T spectra. It has two different methods for doing this. The idea for these methods developed by Peter Christiansen [97] and Djamel Ouerdane [96], called *method 1*, and by Claus E. Jørgensen [3], called *method 2*. It is also a placeholder for other small, but important analysis applications, like generating correction factors: tracking efficiencies, pure geometrical acceptance, feed down-, multiple scattering- and decay corrections and event plane correction. A list of all the files in BANAPP is listed in 6.15. They are all written in c++. Section 6.4.5 will give a short description of each directory/file, emphasising on their purpose, and the programs will be described in section 6.4.6.

6.4.5   BANAPP files

The base directory contains the the files: `Makefile.am`, `acinclude.m4`, `configure.in` and `autogen`. The first 3 files are needed for the package to compile with the AUTOMAKE [110] tools. `autogen` contains some simple simple commands for maintainers of the package to use. All the **c++** code is placed in the subdirectories. These contains in most cases a library where all the classes of that sub directory are available. Each directory also contains a `Makefile.am` and possibly a `Linkdef.h`. They are for compiling purposes and will not be documented.

The acceptance directory contains the headers and sources of `AcceptanceMaps`, `FsGeometry`, `MrsGeometry` and `SpecGeometry`. These classes are available through the *libAcceptance* library. The three geometry classes contains the geometries of all the detectors in the corresponding spectrometer at its current setting. They can "swim" a particle through the spectrometer, with a specific momentum, direction and origin, and determine if it is possible. **TFW2** and **C4** can be switched off in `MrsGeometry`. `FsGeometry` is defined either as the FFS spectrometer without **C1**, or as the FS spectrometer with or without the **RICH**.

The `AcceptanceMaps` class is responsible for building the 2D histograms, saving and writing them too file. This class is used by `generateMaps`, described in a paragraph in section 6.4.6, to make the geometric acceptance maps, and is also used by `tree2datamap` and `hadronAnalyse` to get the acceptance correction factor for a reconstructed particle. The class handles unidentified particles, pions, kaons, protons and deuterons.

The anatools directory contains the header and source of `DstLoopModule` and the programs `checkMTreeHistos`, `dst2tree`, `generateMaps` and `m2fitter` which are described in section 6.4.6. The `DstLoopModule` class is available through the *libDstLoop* library. `DstLoopModule` is used by `dst2tree`, and contains the main loop over the events in the DSTs. As the class iterates over the events, the information is passed on to the selection classes that builds diagnostics histograms and other distribution needed to do proper particle selection in "method 1" and "method 2". Events and particles that does not satisfy the criterias given to the options in the `dst2tree`, will not be saved in the output tree. `DstLoopModule` reads the DSTs using `BdstReader`, and writes a *micro–tree* containing arrays of `treereader/Particle` and `treereader/Global`.

The anatools/m2fitgui directory contains the headers and sources of `FitPidPanel` and `FitWidget`. These *GUI* classes are available though the *libM2FitGui* library, and are used by the graphical `anatools/m2fitter` program. They are responsible for reading and updating the

histograms and functions in the *micro–tree* file and provide the graphical interface through which the simultaneous fitting of PID histograms can be done. For a full description see the paragraph on the `m2fitter` in section A.1.3.

📁 **The anatools/method1 directory** contains the header and source of `SpectraObject`. This class is available though the *libSpectraObject* library and is used by the program `tree2datamap`, see section 6.4.6. This "method 1" is optimised for low p_T physics. The `splitMrsmap` programs is a utility to split the geometrical acceptance maps for the MRS into 2 maps, one for negative particles and one for positive particles. The default map has both charges, but plotted as $q \cdot p_\mathrm{T}$.

📁 **The anatools/method1/macros directory** contains a set of ROOT macros for plotting and merging the results which are stored in the `SpectraObject`. They are called: `fsSpectra.C`, `mrsSpectra.C`, `plotResults.C` and `plotResultsHelp.C`. Inside each macro is a set of functions for drawing and inspecting the final invariant p_T spectra.

📁 **The anatools/method2 directory** contains the header and source of `Spectra`. A set of useful functions are stored in a *namespace* called `Tools`. This class and *namespace* are available though the *libSpectra* library. The `Spectra` class is responsible for building the invariant p_T spectra through the use of `Tools`. The "Method 2" program is called `hadronAnalyse` and uses the `Spectra` class and the `Tools` *namespace*. `hadronAnalyse` is described further in a paragraph in section 6.4.6

📁 **The corrections/efficiency directory** contains the headers and sources of `RefTrack`, `BrMrs-EfficiencyCalculator`, `EfficiencyFinderModule` and `EfficiencyCalculator`. These classes are available though the *libEfficiency* library. The directory also contains the main ROOT macro, `fsRecEff.C`, for running the tracking efficiency calculation. 3 utility sub directories contain additional macros for making efficiency–maps, merging files and submitting analysis jobs through the CONDOR queue to the computer farms.

The `EfficiencyCalculator` can read the produced tracking efficiency histograms and return tracking efficiencies track by track in an event analysis loop. The tracking efficiency can be set to depend on a number of different physical quantities of the track, like position and momentum. The class is used by the `hadronAnalyse` and `tree2datamap` programs.

📁 **The corrections/geant directory** contains the header and source of `GeantCorrection`. This class is available though the *libGeant* library. The class is used to read files that contains correction factors for multiple scattering, feed–down and decay. The subdirectories contain ROOT scripts that generate the corrections factor for particles identified by **H1**, **H2**, **RICH**, **TOFW** and **TFW2**. There are also ROOT scripts for testing of the produced output.

📁 **The corrections/reactplane directory** contains the header and source of `ReactPlaneCorrection`. This class is available though the *libReactPlane* library. This class is not used in by any other class or program in BANAPP. Its purpose is to determine the correction factor for determining the proper reaction plane.

📁 **The selection directory** contains the headers and sources of `Selector`, `GlobalSelector`, `TrackSelector`, `CSelector`, `PidSelector`, `TofSelector`, `RichSelector`, `M2VsPSlicer` and
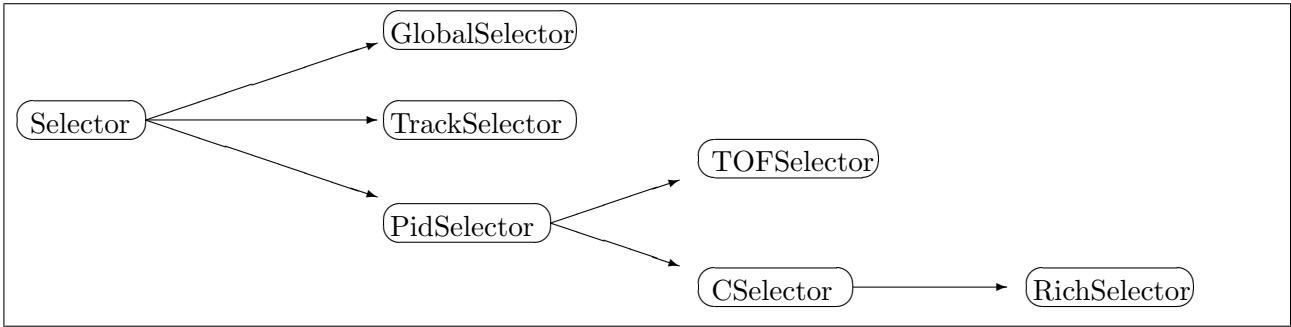
Figure 6.16: The figure shows the inheritance tree for the "selector" classes in the **selection** directory.

Fit- M2Simul. These classes are available though the *libSelection* library. Figure 6.16 shows the inheritance tree. These selection classes are first used by `DstLoopModule` to build distributions for proper particle selection, when this is needed. They also do other cuts that does not need any prior distribution, like the minimum and maximum allowed vertex position and centrality cuts, implemented in `GlobalSelector`. The `CSelector`, "Čherenkov" selector is for the **C1** and **C4** detector. The `PidSelector` handles many of the typical cuts/distributions done by all PID capable detectors and also uses the utility classes `M2VsPSlicer` and `FitM2Simul`. The first makes slices of the m^2 vs p histograms into "momentum–bins", and the other one does a simultaneous fit of the 3 PID delimiter functions to the data obtained from the `M2VsPSlicer`.

This algorithm for slicing the m^2 vs p histogram works in the following way. There is individual slicing of each particle species, to get even statistics in each of the N_{Sl} momentum–bins. This is done by counting the number of particles, N_{tot}^{pid}, between $m_{pid}^2 \pm \Delta m_{pid}^2$, where m_{pid}^2 is the nominal mass for a pion, kaon or (anti–) proton. Then the algorithm makes a m^2 distribution between the $m_{nom}^2 \pm \Delta m^2$ values, from p_{high} down to p_{low}, such that the number of particles in this part of the phase space is N_{tot}^{pid}/N_{Sl}. The process starts at the highest $|p|$ value of the histogram and continues down to $p = 0$. This is to ensure that the highest momentum slice has good statistics. The biggest momentum slice, $(p_{high} - p_{low})$, will be the one with $p_{high} = p_{max}$, and the smallest momentum slice will be the one containing that particle's $\langle p_{\mathrm{T}} \rangle$ value.

Another method for PID in the TOFs is determining its β^{-1} resolution. Figure A.18, A.19 and A.20 explains how this information is extracted from the data for pions, kaons and protons, respectively.

Other examples of diagnostic histograms are shown in section A.2.2 on page 120 and A.2.3.

The treereader directory contains the headers and sources of `BdstReader`, `MicroTreeReader`, `MrsTreeReader`, `FfsTreeReader` and `FsTreeReader`, `Global`, `Particle`, `MrsParticle`, `FfsParticle` and `FsParticle`. These classes are available though the *libTreeReader* library. The `BdstReader` is used to read the BRAHMS DSTs. To speed up the analysis, all the branched in the DST can be switched on or off for reading. The branches are called: *R (Run), G (Global), FL (Flow), MRS, TPM1, FFS, FS*. The other three "tree–readers" reads the *micro–tree* that is produced by the dst2tree program. The reading is done through the last five classes.

The five last classes are data objects. The `Particle` object is an abstract base class for the other particle objects. The *micro–tree* consists of these objects. `Global` is in all the three *micro–tree* types, and only one of the other objects, which determines the tree type. The leafs produced by `Global` and `MrsParticle` when saved in a tree structure are illustrated in figure 6.17.

The util directory contains the headers and sources of `BlackList`, `OptManager`, `ProgressMeter`. These classes are available though the *libAnaUtil* library. The `BlackList` can read a text file that contains run number, and can thereafter be asked whether or a given run number was in the file. Useful for removing runs that are bad, i.e. due to detector high voltage trips, and other malfunctions that happened during the data taking. The `OptManager` is a wrapper utility around the `BrAppOptionManager` in the BRAT library and the `ProgressMeter` is a small utility to estimate the running time of some of the programs in BANAPP.

There is also a sub directory with an executable called `banapp--config`, that gives information of the installation of the BANAPP package, which is useful for other packages and/or programs that are built upon BANAPP.

6.4.6 BANAPP programs

BANAPP has 3 sets of programs. The first is a single programs that merges DSTs together, and reducing tree size. This new tree is called a *micro–tree*. The *micro–tree* contains data for one spectrometer: MRS, FFS or FS. In addition it contains a set of histograms for each detector, which are used for final step data quality checks. Some of the histograms are fitted with functions, enabling proper event and particle selection in the second loop over the data, i.e. global vertex to particle vertex correlation for removing secondary and background particles, as shown in figure 5.4.

The *dst2tree* program
The main purpose of *dst2tree* is to merge together DSTs for a single setting, thus producing a single *micro–tree* for each spectrometer setting. *dst2tree* produces a file with a tree structure. The branches and leaves of a *MrsTree* is shown in figure 6.17.

The `generateMaps` program
`generateMaps` implements a simple Monte Carlo simulation, making pure geometrical acceptance maps in p_{T}-y or η space. It is done throwing particles with charge $+1e$ through the spectrometer. The particles have a flat distribution in p, vertex Z-position, θ and ϕ, making sure that they cover more than the actual "opening" of the spectrometer. The geometry of the detectors in the spectrometer are read from the BRAHMS geometry database, for a particular specified run number. Two set of histograms are generated, one containing the accepted particles and one containing all the thrown particles. Dividing the first with the second and normalising for azimuthal ϕ width, gives an acceptance histogram suitable for analysis. The histogram is not normalised for its width in y or *eta*, which must be done before applying the map to an analysis. These maps can therefor be used in analysis with different widths in y or η. This list of options on how to generate a map is found in table A.2. This program was used to generate the acceptance maps used in the analysis presented in chapter 7. The acceptance maps used in the analysis in chapter 7 used `generateMaps`.

global	**particle**.fTheta	**particle**.fTofdy
TObject	**particle**.fPhi	**particle**.fTofMulti
fBbVtx	**particle**.fVtxX	**particle**.fTofSlat
fZdcVtx	**particle**.fVtxY	**particle**.fTofPslat
fInelVtx	**particle**.fVtxZ	**particle**.fTofBeta
fCCVtx	**particle**.ffChiSq	**particle**.fTofMass2
fCent	**particle**.fTpc1LineOrigin[]	**particle**.fCEnergy
fMult	**particle**.fTpc2LineDirection[]	**particle**.fTfw2dy
fRunno	**particle**.fTpc1LineOrigin[]	**particle**.fTfw2Multi
fTriggers[]	**particle**.fTpc2LineDirection[]	**particle**.fTfw2Slat
fScaleDown[]	**particle**.fMagdy	**particle**.fTfw2Pslat
fNTpcHits	**particle**.fMagdaly	**particle**.fTfw2Beta
fNTracks[]	**particle**.fMagdang	**particle**.fTfw2Mass2
particle	**particle**.fMagEdgeDistX	
particle.fP	**particle**.fMagEdgeDistY	

Figure 6.17: The figure shows the branches and leaves in the tree that is generated by the *dst2tree* program, nick named *micro–tree*, when doing an MRS analysis. The tree has 2 main branches: *global* and *particle*. The global branch has single leave entries, while the the particle branch could be an array of branches, one entry for every reconstructed particle in the event.

The `hadronAnalyse` program

`hadronAnalyse` analyses *micro–trees* with a specific setting, producing invariant p_{T} spectra. Acceptance maps generated by `generateMaps` is mandatory with this analysis. The spectra are built on a particle by particle basis, using the `Spectra` class. When a track is accepted, within the specified cut, the track is added to the histograms. It is weighted with a product of the acceptance correction and tracking efficiency if it is used as a unidentified hadron. If the hadrons are assumed to be pions, multiple scattering, absorption and feed down corrections are also multiplied to the weight. Tracks in PID analysis always get correction from multiple scattering, absorption, decay and PID efficiency multiplied to the weight. All fiducial cuts in the acceptance map will also be applied to the particles. Several other cuts, specified by the options in table A.3, will also be applied. This method performs well for high p_{T} analysis, where occupancy is low, since variable p_{T} bin sizes can be used. The list of options for this program is found in table A.3. The analysis presented in chapter 7 used

`hadronAnalyse`. The spectrum is build according to:

$$Spectrum(p_{\mathrm{T}}; \Delta y) = \left(\sum_{d, \Delta y} track_d(y, p_{\mathrm{T}}) \cdot Weight(y, p_{\mathrm{T}}) \right) / N_{\mathrm{events}} \tag{6.12}$$

where the sum over d is all the reconstructed tracks, for tracks in the rapidity interval Δy.

The `Tools` *namespace* has functions to merge the spectra from the different magnetic field setting in a proper way. The individual spectra are weighted by using the statistics in each spectra and the information from the acceptance maps of its high or low p_{T} boundary.

Usage of `tree2datamap`

`tree2datamap` is optimised for low p_{T} physics with PID. Acceptance maps generated by `generateMaps` and *micro–trees* from `dst2tree` is mandatory with this analysis. The program builds two sets of histograms. The first histograms are data maps in p_{T}-y space, one for each particle specie and vertex bin. Correspondingly histograms with weights are built. The weights are the product of the acceptance map, multiple scattering, feed down, decay, tracking efficiency and PID efficiency corrections. The maps are all made with the same binning as the one found in the acceptance maps. The ROOT macros in the sub directories are used to build the spectra, through the `SpectraObject`. The cuts and normalisation in (pseudo-) rapidity is done at this stage. The macros also handles merging of different magnetic field settings. This method applies the right correction for low p_{T} particles (< 0.5 GeV/c), as it merges particles and corrections from different vertex bins. The spectra is build according to:

$$Spectrum(p_{\mathrm{T}}; \Delta y) = \left(\sum_{i} Data_i(p_{\mathrm{T}}; \Delta y) \right) \cdot \sum_{i} Weight_i(p_{\mathrm{T}}; \Delta y) \tag{6.13}$$

where the sum over i is the different vertex bins and settings, for data in the rapidity interval Δy.

6.5 Building p_{T} spectra

The p_{T} spectra are built particle by particle, for each vertex bin and centrality bin. As described in section 6.4.6, `hadronAnalyse` calculates the weight for each track and adds that weight at the track's p_{T} to a histogram. The collision's centrality and the vertex Z coordinate, the particle originated from, determined which histogram is filled. Along the process of histogramming, `tree2datamap` also counts the total number of collisions occuring in each vertex and centrality bin. At the end of the analysis each histogram is divided by the total number of collisions that happened in it's bin, the normalisation.

The analysis will only use tracks from collisions with a specific trigger, described in table 5.2. MRS analysis always uses trigger 3, both for charged hadrons and for PID analysis. Trigger 2 or 6 is used when the data is recorded with the FS or FFS. The normalisation number is counted with the trigger 1 or 5 in heavy ion or $p+p$ collisions, respectively. The spectra histograms from each vertex bin contains an invariant p_{T} spectra. The average of all of them needs to be calculated. Each of the histograms get a weight according to the number of entries that was put into it. When the weighted average of these histograms are calculated, each vertex bin's acceptance in p_{T} must be taken into account. Only
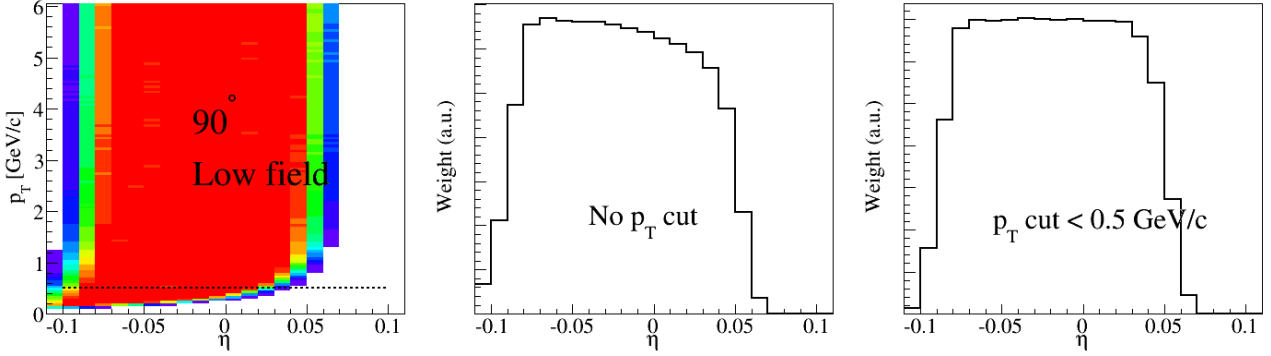
Figure 6.19: The figure shows the effect on the sum of acceptance weights when a cut off in p_T is applied to the map. The acceptance map shown is for the MRS at $90°$ with low magnetic field, with vertices from $0 - 5$ cm.

histograms from vertex bins that have acceptance for a specific p_T bin, are used in calculating the weighted average for that p_T bin.

The next step is finding the weighted average of different spectrometer settings, i.e. those that have acceptance overlap: MRS at $90°$ with all different magnetic field settings. Another example from the FS with two different settings can be seen in figure 6.18. The weight used for each setting is the number of entries[2]. PID p_T spectra for a specific spectrometer settings always has a upper p_T limit depending upon the resolution of the detector used to identify the tracks. This always sets the upper limit in PID p_T spectra.

Due to the analysis method, with separate vertex bins and settings, a lower momentum cut off has to be applied to the acceptance maps, which is then transfered onto the data. This is due to the decreasing (pseudo)rapidity coverage and acceptance edges at low p_T values. Figure 6.19 illustrates this. The cut off values are dependent on the magnetic field strength and angle. The absolute lowest p_T value that should be used is determined from the lowest magnetic field used when recording the collisions.
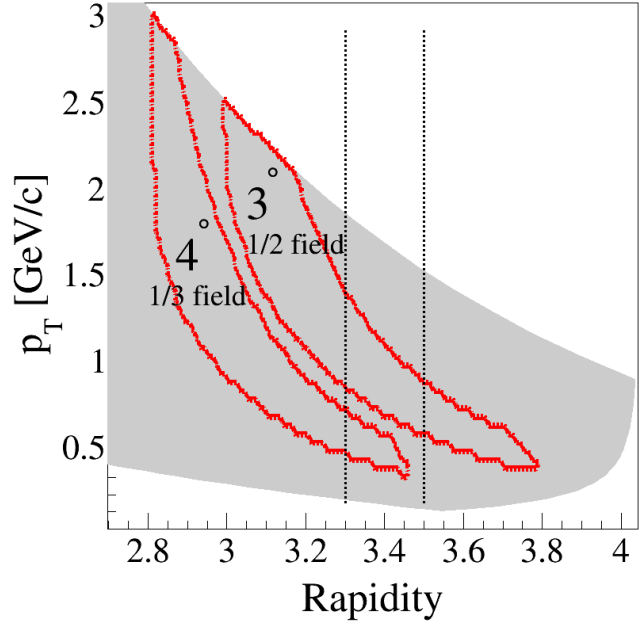
Figure 6.18: The figure shows the theoretical geometric acceptance for two different FS settings. A p_T spectra at $y = 3.3 \pm 0.1$ can utilise tracks from both settings to get a larger p_T coverage than a single setting could.

---

[2]The FS only accepts one charge sign determined by the polarity. Weighted average for inclusive charges hadrons are therefor a simple average between the two magnetic polarities.

Chapter 7

Particle spectra at $\sqrt{s_{\text{NN}}} = 62.4$ GeV

Several experiments have measured p_{T} spectra in $p + p$ collisions at $\sqrt{s_{\text{NN}}} = 62$–63 GeV at the ISR. The top panel of figure 7.1 shows all the pion (pi^0 and $\pi^{\pm}$) p_{T} spectra and 3 scaled charged hadron spectra. There is a wide spread in the spectra, and it is not obvious how to find a spectrum as the baseline for R_{AA} measurements. The $p + p$ p_{T} spectra used by the RHIC experiments, in the first presentations of the R_{AA} in Au+Au collisions at $\sqrt{s_{\text{NN}}} = 62.4$ GeV, were all different. The different data samples were fitted with:

$$E\frac{d^3\sigma^{pp \to h+X}}{d^3p} = A\left(1 + \frac{p_{\text{T}}}{p_0}\right)^{-n} \tag{7.1}$$

$$E\frac{d^3\sigma^{pp \to h+X}}{d^3p} = A\left(e^{a \cdot p_{\text{T}}} + \frac{p_{\text{T}}}{p_0}\right)^{-n} \tag{7.2}$$

PHOBOS and STAR used equation 7.1 and fitted it to data from [111]. Their parameters were: $A = 244.5$ and 292.48, $p_0 = 2.188$ and 1.75, and $n = 15.37$ and 13.23, respectively. PHENIX made an interpolation of data at lower and higher energies, which they then fitted with equation 7.2: $A = 196.4$, $a = 0.0226$, $p_0 = 2.301$, and $n = 14.86$. All three experiments assigned an uncertainty of $\pm 25\%$ to the reference spectrum.

To get a better understanding of the differences between the measurements at $\sqrt{s_{\text{NN}}} = 62.4$ GeV, D. d'Enterria combined all available measurements [112], as shown in figure 7.1. Most of the measured spectra in figure 7.1 are of π^0s, 4 are $\pi^{\pm}$s, and 3 charged hadrons. The experiments did not measure their spectra in the same way and did not either do the same corrections to their data. D. d'Enterria therefore made the following corrections to the spectra: Charged hadrons were scaled by $1/1.6$, in order to have data points at $p_{\text{T}} < 2$ GeV/c. Most of the experiments did not properly reconstruct invariant m^2 values from γ pairs, which resulted in contamination from η decays. The early experiments did not correct for direct γs either. The center of mass collision energy also varied between the experiments, ranging from $\sqrt{s_{\text{NN}}} = 62$–63 GeV. This was due to a non–zero angle between the colliding protons depending on the experimental setups. D. d'Enterria corrected all the spectra as needed and compiled
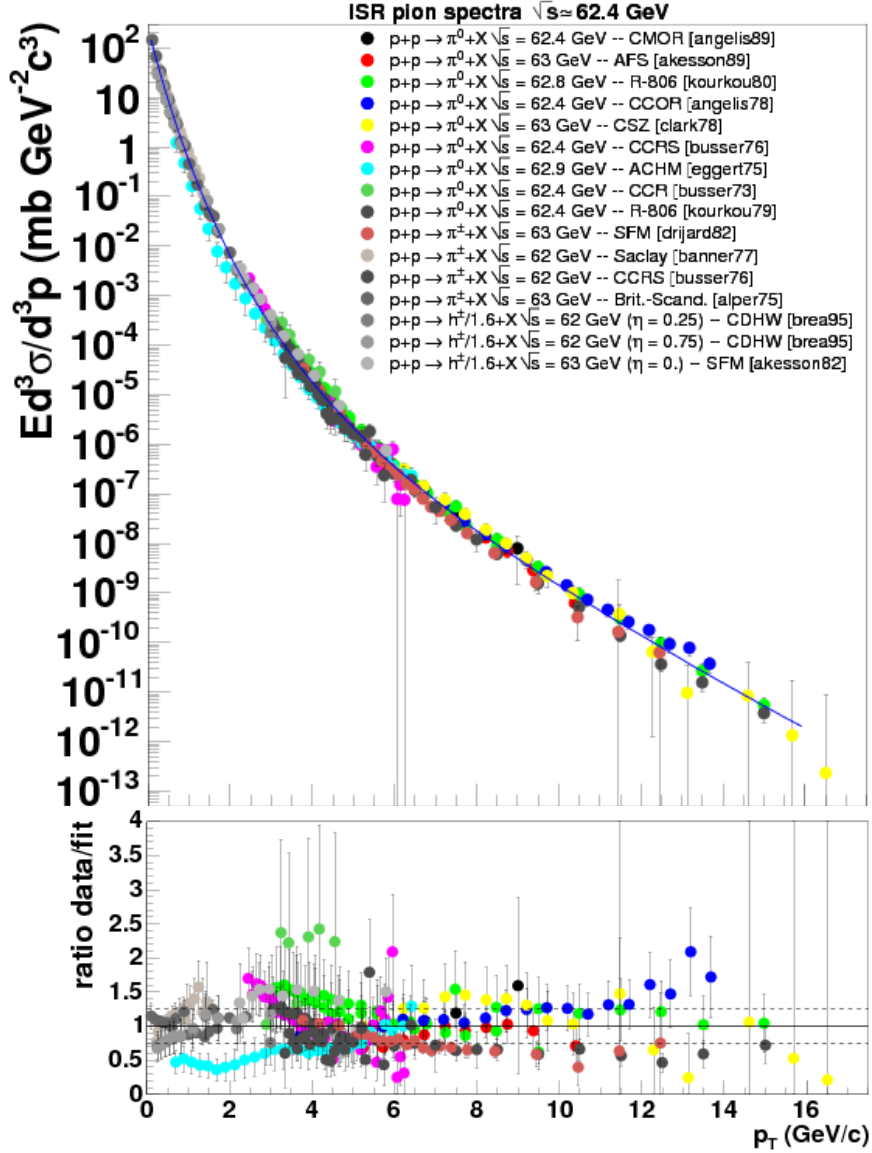
Figure 7.1: The figure shows a compilation of all available $p + p$ data at $\sqrt{s_{\mathrm{NN}}} = 62$–63 GeV. Most of the experiments measured pions but three measured charged hadrons. The charged hadron spectra are scaled by $1/1.6$. There were different corrections applied to the original data in [112], which gave the results shown in the figure. The bottom panel shows the ratio between the solid line in the top panel and the data points. The solid line is a fit to all the p_{T} spectra shown in the top panel using equation 7.3. The uncertainties reflect both the statistical and the systematic added in quadrature.

the spectra shown in figure 7.1. The combined data were fitted to an empirical function:

$$E\frac{d^3\sigma^{pp\to\pi+X}}{d^3p} = A\left(e^{ap_{\mathrm{T}}+bp_{\mathrm{T}}^2} + \frac{p_{\mathrm{T}}}{p_0}\right)^{-n} \tag{7.3}$$

where the parameters were found to be $A = 265.1$, $a = 0.04975$, $b = 0.0129$, $p_0 = 2.639$, and $n = 17.95$. The function is only valid for $0 < p_{\mathrm{T}} < 16$ GeV/c. The bottom panel has been divided by this function. Systematic differences exists making it evident that, to reduce the uncertainty of the reference spectra in the R_{AA}, it is necessary to measure reference spectra with the same experiment as the heavy ion spectra are measured from. To this end $\sqrt{s_{\mathrm{NN}}} = 62.4$ GeV $p + p$ collisions at RHIC were produced early in the summer of 2006.

7.1 $\quad p + p$ collision

The $p+p$ p_{T} spectra were produced from the last data BRAHMS collected. BRAHMS was designed for a high multiplicity environment. $p + p$ collisions have very low multiplicity compared to Au+Au or Cu+Cu collisions, but using the CC detector as an efficient trigger, as described in section 5.2, sufficient statistics were collected. The data analysis was performed using the procedure, cuts, and programs described in chapter 6. Since the BRAHMS experiment does not have full differential cross section coverage in $p + p$ collisions, the p_{T} spectra were corrected for the CC trigger inefficiency, as described in section 6.3.4.

Figure 7.2 shows the inclusive charged hadron p_{T} spectra at three pseudorapidities. Multiple scattering, decay and absorption corrections were applied assuming the tracks were pions. The spectrum at $\eta = 0$ is not as steep as the spectrum at $\eta = 0.9$. The forward rapidity measurements also show a different slope between the positive and negative particles. These spectra show reasonable agreement with the spectra obtained at the CERN ISR(see the discussion in section 7.3). A particle with p_{T} = 2 GeV/c at $\eta = 3.1$ has $\sim 65\%$ of the maximum available momentum (kinematic limit), taking momentum conservation in the $p + p$ collision into consideration. The forward spectra reach these p_{T} values, as can be seen in the two, top, right panels, where the solid line is the kinematic limit.

Figure 7.3 shows the identified particle spectra from the same data set. PID was accomplished using TFW2 at midrapidity and the RICH detector at forward rapidity. The data was analysed as described in chapter 6. The particles were not corrected for feed–down. This correction is not done since BRAHMS can not identify hyperons, see discussion in section 7.2 and 7.3.

As seen in figure 7.3, most of the particles produced at midrapidity are pions. This is also true for π^- at forward rapidity for negative charged particles. A clear difference in slope is visible between the p and π^+ spectra at forward rapidity. This rapidity corresponds to that of the fragmentation region in Au+Au [113] and $p + p$ collisions, as shown in figure 7.7. The physics in the fragmentation region should be very different from midrapidity. The inclusive unidentified and identified p_{T} spectra constitute the reference for the the nuclear modification factors presented in chapter 8.

7.2 Cu+Cu and Au+Au collisions

^{63}Cu particles were collided at the RHIC to explore the scaling behaviour of the observables measured in ^{197}Au+^{197}Au collisions. The number of participants and incoherent binary collisions in Au+Au collisions is about 2-5 times larger than in Cu+Cu collisions, as shown in table 6.1 and 8.1. If the suppression or enhancement of high p_{T} particles depends on the volume of the matter created it should be evident when comparing Cu+Cu collisions to Au+Au collisions at the same center of mass energy, per participant or incoherent binary collisions.
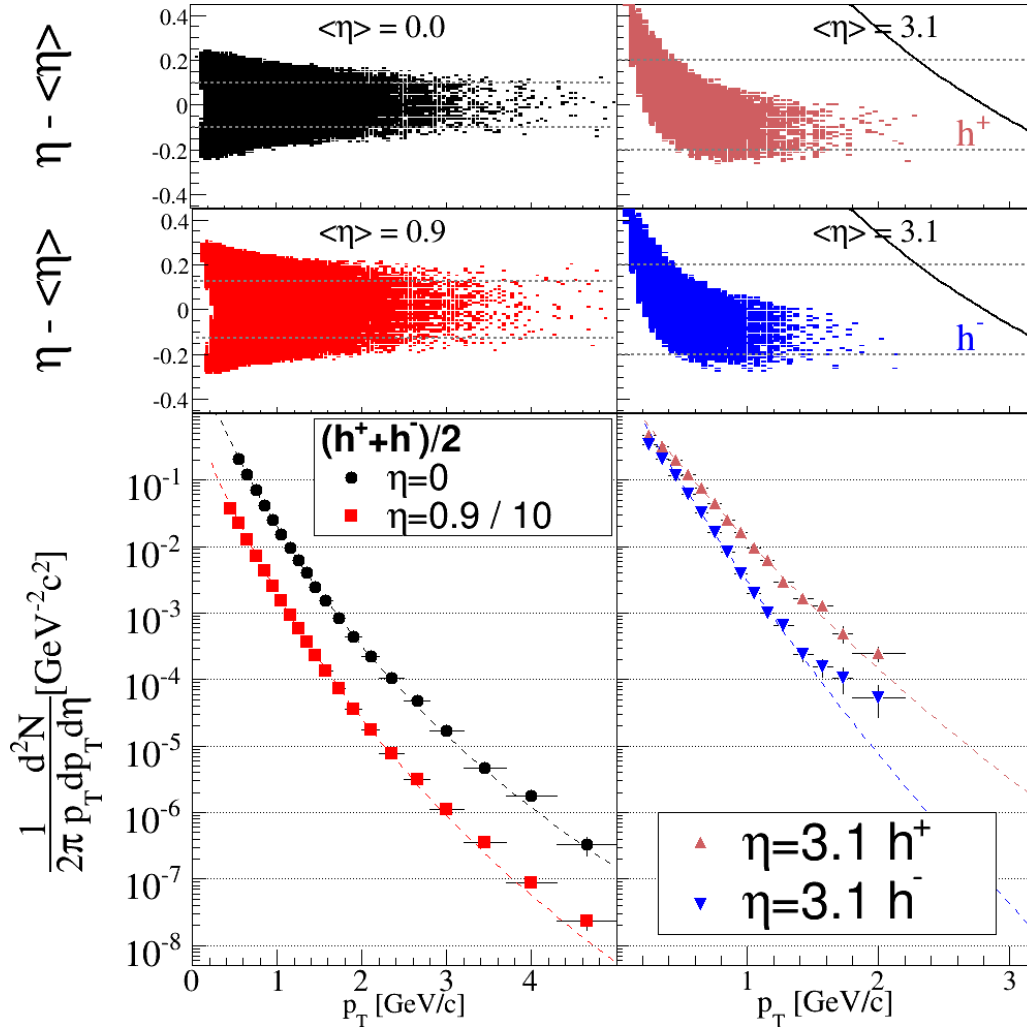
Figure 7.2: The figure shows the minimum bias charged hadron $p + p$ p_{T} spectra measured by the BRAHMS experiment. $\langle\eta\rangle$ is the center value in the pseudorapidity bin. The $\langle\eta\rangle = 0.9$ spectrum is scaled by a factor of 10 for clarity. The rapidity bins are: $-0.1 < \eta < 0.1$, $0.75 < \eta < 1.0$ and $2.9 < \eta < 3.3$. The solid line in the $\langle\eta\rangle = 3.1$ plots, shows the kinematic limit at this pseudorapidity. The kinematic limit is the maximum momentum a particle can get from a $p + p$ collision using momentum conservation, i.e. assuming the collision only produces 2 particles emitted back–to–back at $+\eta$ and $-\eta$. The dashed lines are powerlaw fits (as defined in equation 7.4) to the spectra. The systematic uncertainty, which is $\sim 10\%$ point–to–point, is not shown.

In figure 7.4 and 7.5 the Cu+Cu and Au+Au p_{T} spectra of inclusive charged hadrons are shown from mid to forward rapidity. The same spectrometer settings, analysis cuts, and corrections used in the $p + p$ analysis were also used on the Cu+Cu, Au+Au data. Multiple scattering, decay and absorption corrections were applied assuming all tracks were pions. The data was divided into 4 centrality bins: 0–10%, 10–20%, 20–40% and 40–60%, where the three last bins have been scaled for
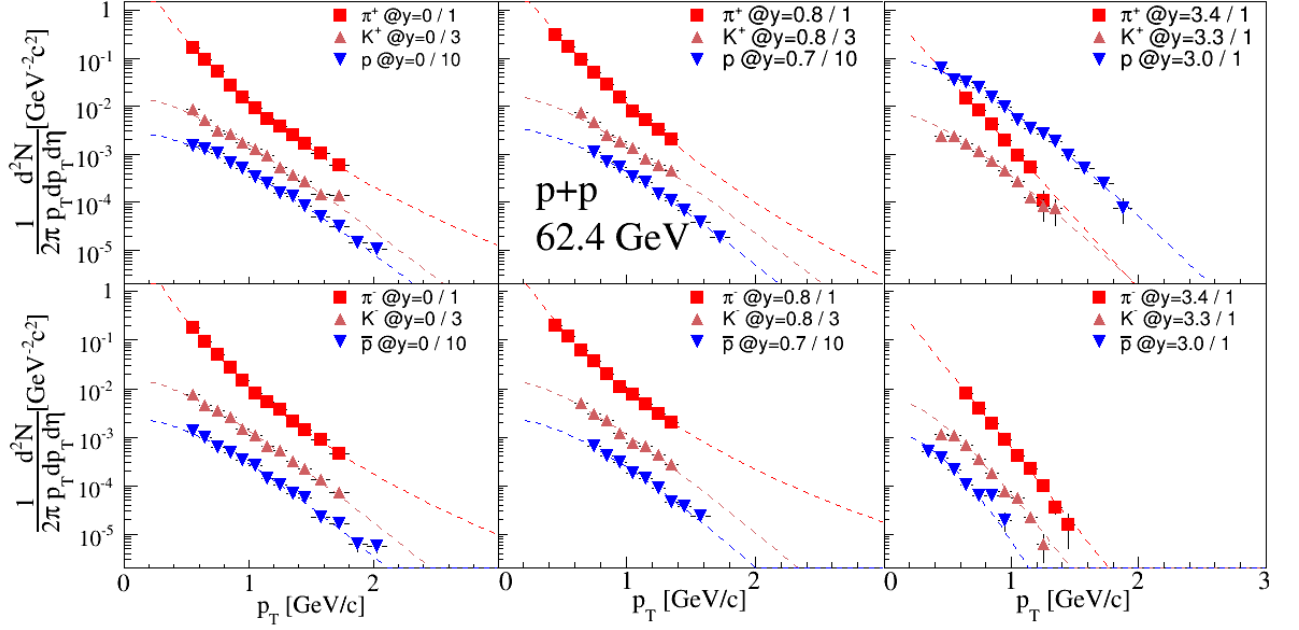
Figure 7.3: The figure shows minimum bias $p + p$ identified particle p_T spectra measured by the BRAHMS experiment. The kaons and (anti-) protons are scaled down by a factor of 3 and 10, respectively for clarity. The two left and the two right panels have rapidity bin widths of 0.2. The two middle panels are 0.15 wide in rapidity for pions and kaons, while the (anti–) proton spectra have rapidity bin widths of 0.2. The rapidities listed in the legends are the centers of the selected rapidity bins. Notice that the forward spectra have not been scaled. The particle species have different p_T coverage, which is due to different acceptances as seen in figure 5.3. The dashed lines are powerlaw fits to the pion spectra, and Boltzmann fits to the kaon and (anti–) proton spectra. The systematic uncertainty, which is $\sim 15\%$ point–to–point, is not shown.

clarity in the figures. The rapidity bins are the same as shown for $p + p$ collisions.

The identified particle p_T spectra for Cu+Cu and Au+Au collisions are shown in the top and bottom panel of figure 7.6, respectively. PID was performed using the TOFW when analysing the Cu+Cu midrapidity data and TFW2 when analysing the Au+Au data. The RICH detector was used for PID at forward rapidity for both collision systems. Tracks were identified the same way as in the $p + p$ data analysis. None of the identified particles have been corrected for feed down from heavier particles. There are no weak processes which produce kaons as the final state. Λ and Σ decays are responsible for the majority of feed–down to pions and (anti-) protons. K_S^0's also contribute to the feed down to pions. The BRAHMS experiment cannot measure these heavier particles, but they have been measured at midrapidity by PHENIX in Au+Au at $\sqrt{s_{NN}} = 130$ GeV [114]. In central $\sqrt{s_{NN}} = 130$ GeV Au+Au collisions $\Lambda/p = 0.89$ and $\bar{\Lambda}/\bar{p} = 0.95$. In [72] PHOBOS assumed $\Lambda/p = 0.9$ and $\bar{\Sigma}^+/\bar{p} = 0.3$ for the proton correction, and the $\bar{p}$ correction should be 1.18 times the correction for p.

Λ decay would contribute to both the proton and pion spectra. The proton trajectories would have very small differences between their trajectories and the Λ trajectories and would be considered as coming from the primary vertex. The pion trajectories would differ more from the Λ trajectories and
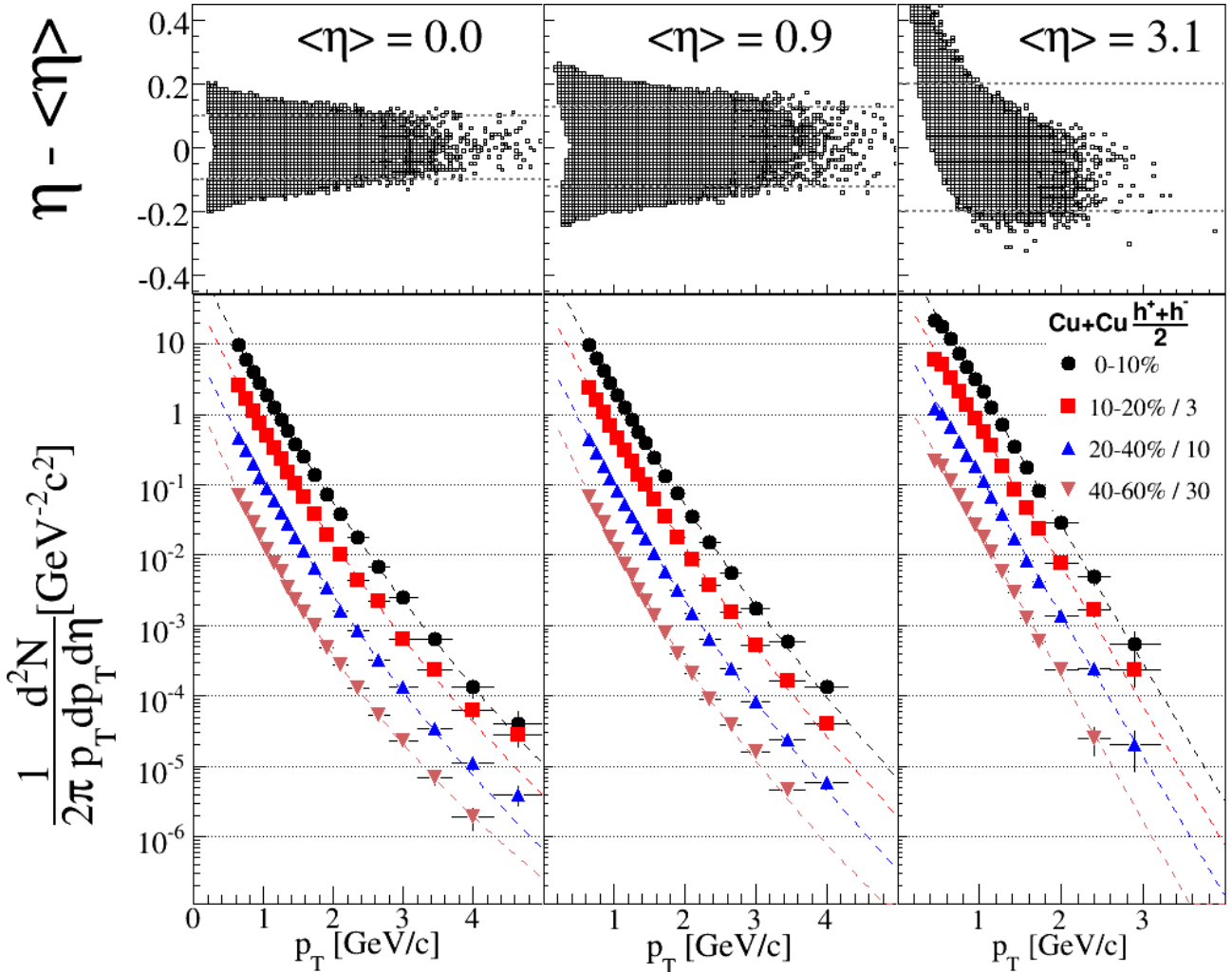
Figure 7.4: The figure shows Cu+Cu inclusive charged hadron p_{T} spectra measured by the BRAHMS experiment. The top row shows the all reconstructed hadrons. The p_{T} spectra shown in the bottom row are the particles between the dashed lines in the top row, respectively. The dashed lines are powerlaw fits, using equation 7.4, to the spectra. The systematic uncertainty, which is $\sim 10\%$ point–to–point, is not shown.

the trajectories less likely to project back to the primary vertex. Λ decays will therefore contribute more to the proton spectrum than the pion spectrum. The likelihood of projecting these tracks to the primary vertex depends on the vertex resolution. Since Λ measurements do not exist in the forward region in Cu+Cu or $p + p$ collisions, this correction has been omitted.

Pions are the most abundant particles at midrapidity. At forward rapidity this is also true for π^- compared to K^- and $\bar{p}$. The particles at forward rapidity are produced in the fragmentation region, as shown in figure 7.7. There are very few anti–protons produced at forward angles in both collision systems. The top and bottom panel of figure 7.6 show that the production of protons is ~ 100 times
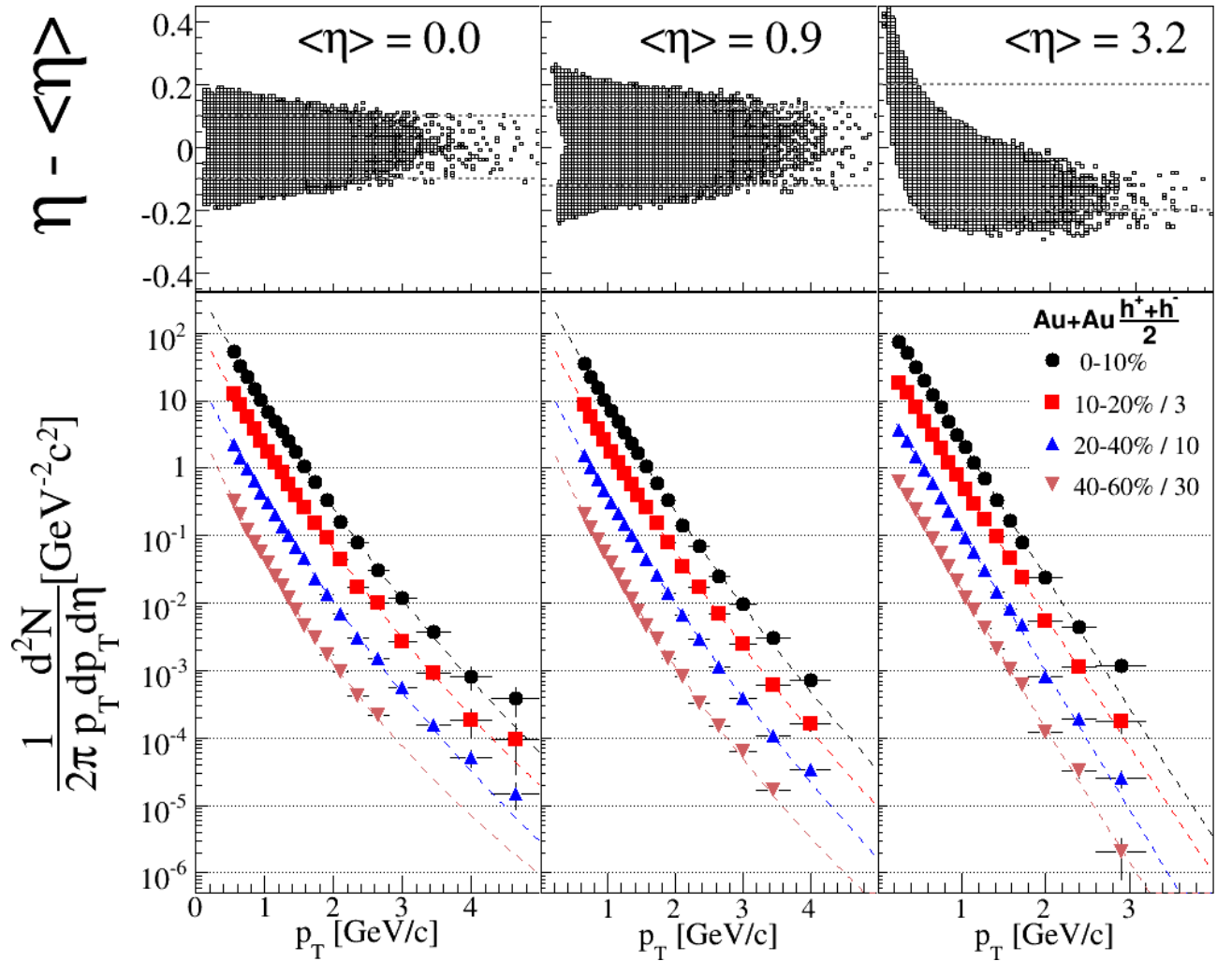
Figure 7.5: The figure shows Au+Au inclusive charged hadron p_T spectra measured by the BRAHMS experiment. The top row shows the all reconstructed hadrons. The p_T spectra shown in the bottom row are the particles between the dashed lines in the top row, respectively. The dashed lines are powerlaw fits, using equation 7.4, to the spectra. The systematic uncertainty, which is $\sim 10\%$ point–to–point, is not shown.

bigger than the production of anti–protons at forward rapidity. The narrow acceptance of the FS did not allow for the collection of sufficient statistics to produce proper anti–proton p_T spectra, but they are included in figure 7.6 for reference.
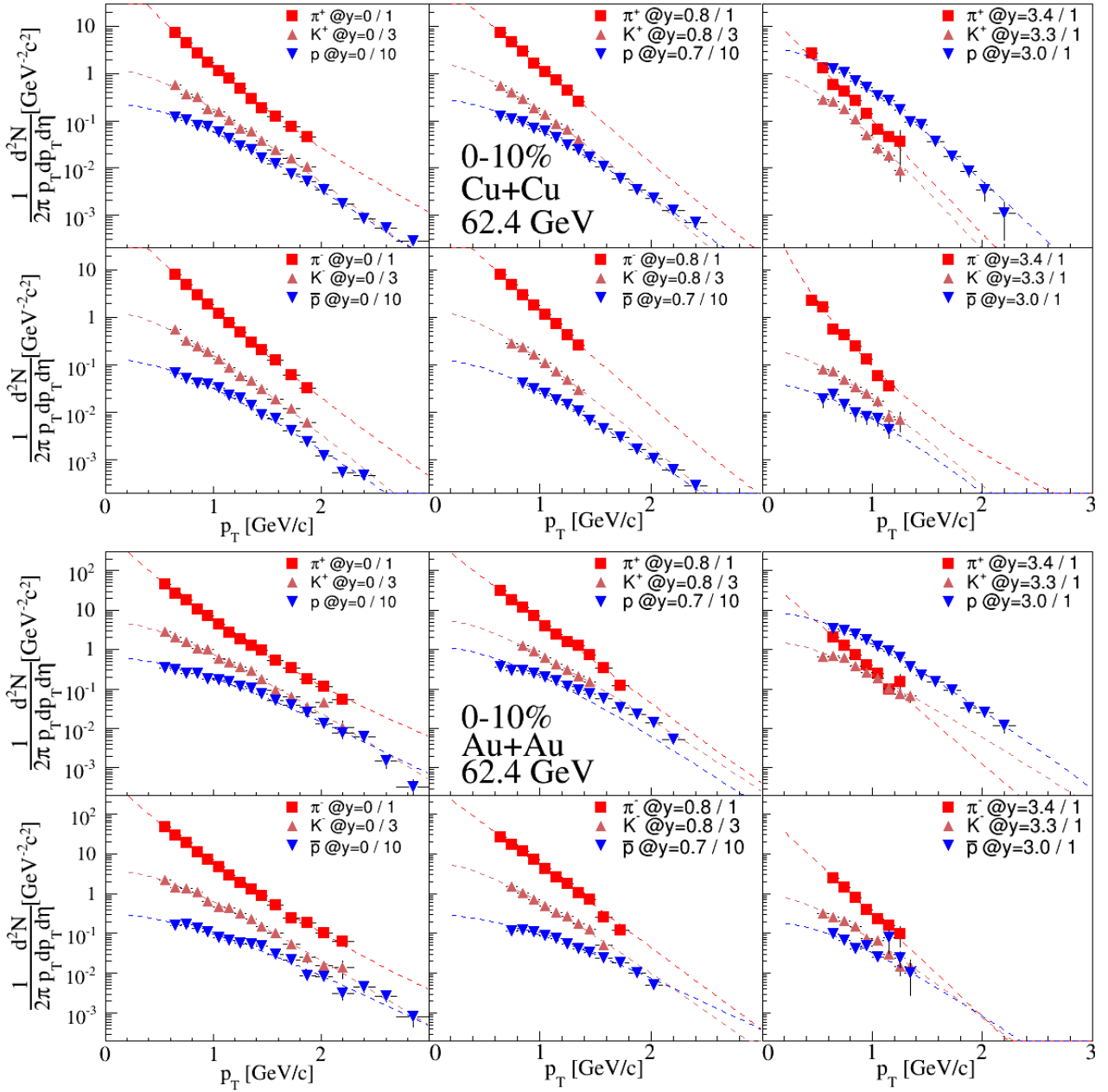
Figure 7.6: The figure shows identified particle p_{T} spectra for 0–10% central Cu+Cu collisions measured by the BRAHMS experiment. The top row of panels shows positively charged hadrons, while the bottom row shows the negatively charged hadrons. The rapidity increases from the left panels to the right panels.The kaon and (anti–) proton spectra have been scaled for clarity as shown in the legends, except at forward rapidity. The included rapidities in the left panels are $-0.1 < y < 0.1$, while the included rapidities in the middle panels are $0.75 < y < 0.9$ ($0.6 < y < 0.8$ for (anti–) protons). The forward rapidity bins are 0.2 wide with the center of the bin as stated in the legend. The dashed lines are powerlaw fits to the pion spectra, and Boltzmann fits to the kaon and (anti–) proton spectra. The systematic uncertainty, which is $\sim 15\%$ point–to–point, is not shown.
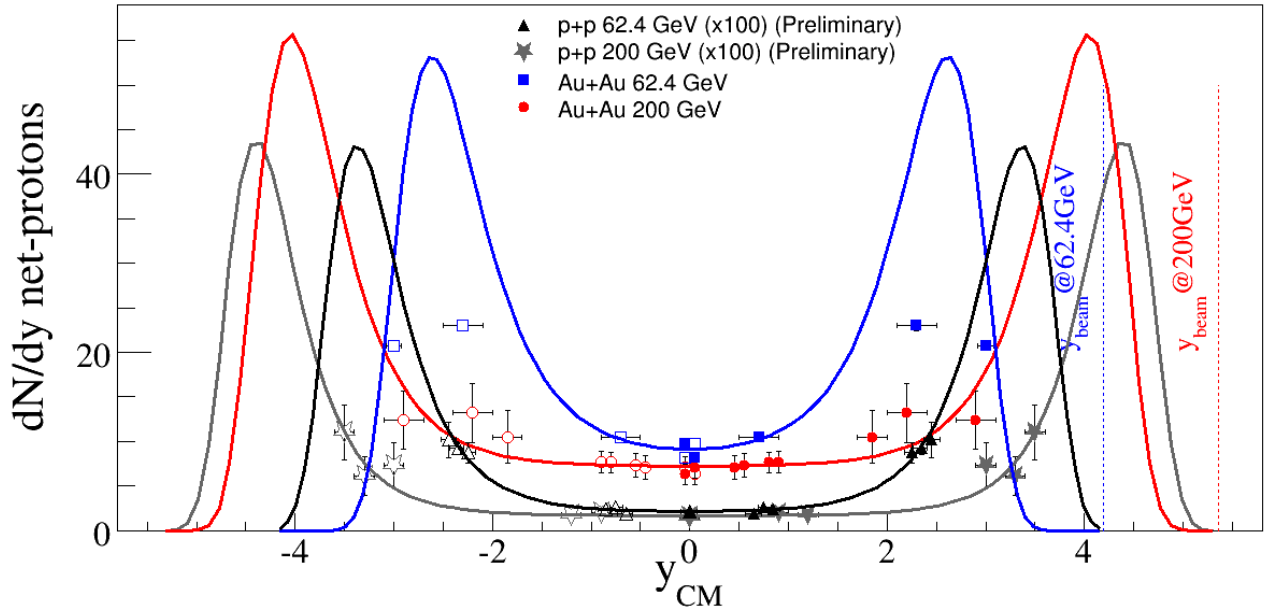
Figure 7.7: The figure shows the net proton distribution $(dN_p/dy - dN_{\bar{p}}/dy)$ at $\sqrt{s_{\mathrm{NN}}} = 62.4$ GeV and 200 GeV for 0–10% central collisions, and is taken from [113, 11]. The $p + p$ net proton distributions are scaled with a factor of 100, and are preliminary BRAHMS results. The $\sqrt{s_{\mathrm{NN}}} = 200$ GeV results can be found in [115]. The open symbols are reflections around $y = 0$. The solid lines are double gaussian momentum fits in $p_{\mathrm{L}} = p \cdot \cos\theta$. The fragmentation peaks for the $p + p$ collisions is closer to the beam rapidity than the heavy ion collisions, at both collision energies.

7.3 Systematic uncertainties and cross experiment comparison

A comparison of inclusive charged hadron spectra from $p + p$ collisions measured at ISR, and Cu+Cu and Au+Au measured by PHOBOS will be discussed in the following sections. PHOBOS has also published results on identified particles in Au+Au collisions. The following section compares the spectra they have measured with the spectra presented in this chapter and discusses differences and similarities between the measured spectra and the experiments. It is important to understand any systematic differences between the results and the experiments.

7.3.1 The fit functions

All the p_{T} spectra presented in this chapter have been fitted with a powerlaw function in p_{T}, as defined in equation 7.4, a Boltzmann function in m_{T}, as defined in equation 7.5, or a Gaussian in p_{T}, as described in equation 7.6. The parameters from the fits are given in table 7.1 for the inclusive charged hadron spectra, and in table 7.2, 7.3 and 7.4 for the identified particle spectra.

$p + p$ Min. Bias	K_P [GeV$^{-2}c^2$]	p_0 [GeV]	n	χ / NDF
$\eta = 0 \ (h^+ + h^-)/2$	8.57 ± 0.28	1.630 ± 0.046	12.74 ± 0.22	63.5 / 17
$\eta = 1 \ (h^+ + h^-)/2$	7.18 ± 0.13	2.410 ± 0.055	16.99 ± 0.28	245 / 18
$\eta = 3 \ h^+$	2.75 ± 0.40	4.2 ± 1.7	25.5 ± 8.7	19.7 / 9
$\eta = 3 \ h^-$	3.68 ± 0.80	4.7 ± 2.7	37 ± 18	18.3 / 9
Cu+Cu $(h^+ + h^-)/2$	K_P [GeV$^{-2}c^2$]	p_0 [GeV]	n	χ / NDF
$\eta = 0$ 0–10%	181.8 ± 7.0	4.88 ± 0.37	23.6 ± 1.4	31.2 / 16
$\eta = 0$ 10–20%	158.6 ± 7.3	4.16 ± 0.34	20.8 ± 1.3	29.8 / 16
$\eta = 0$ 20–40%	98.8 ± 4.1	4.07 ± 0.29	20.6 ± 1.1	34.9 / 16
$\eta = 0$ 40–60%	74.2 ± 6.3	2.14 ± 0.19	13.34 ± 0.76	21.6 / 15
$\eta = 1$ 0–10%	180.9 ± 3.5	5.71 ± 0.25	27.17 ± 0.97	32.7 / 15
$\eta = 1$ 10–20%	141.4 ± 3.4	5.24 ± 0.27	25.3 ± 1.0	39.4 / 15
$\eta = 1$ 20–40%	90.9 ± 2.3	4.78 ± 0.22	23.84 ± 0.85	24.8 / 15
$\eta = 1$ 40–60%	60.3 ± 2.8	3.19 ± 0.21	18.13 ± 0.89	36.6 / 14
$\eta = 3$ 0–10%	224.9 ± 5.7	$(3.37 \pm 0.29) \cdot 10^5$	$(1.53 \pm 0.13) \cdot 10^6$	21.1 / 10
$\eta = 3$ 10–20%	198.5 ± 5.5	$(2.81 \pm 0.16) \cdot 10^5$	$(1.287 \pm 0.072) \cdot 10^6$	21.3 / 10
$\eta = 3$ 20–40%	132.2 ± 3.2	$(2.702 \pm 0.052) \cdot 10^5$	$(1.242 \pm 0.025) \cdot 10^6$	36.5 / 10
$\eta = 3$ 40–60%	75.1 ± 3.0	$(1.214 \pm 0.017) \cdot 10^6$	$(5.764 \pm 0.099) \cdot 10^6$	6.06 / 9
Au+Au	K_P [GeV$^{-2}c^2$]	p_0 [GeV]	n	χ / NDF
$\eta = 0$ 0–10%	541 ± 24	5.47 ± 0.57	24.6 ± 2.1	36.6 / 17
$\eta = 0$ 10–20%	434 ± 22	4.65 ± 0.47	21.7 ± 1.8	20.8 / 17
$\eta = 0$ 20–40%	248 ± 12	4.76 ± 0.50	22.2 ± 1.9	44.1 / 17
$\eta = 0$ 40–60%	162 ± 18	2.43 ± 0.36	13.9 ± 1.4	23.2 / 13
$\eta = 1$ 0–10%	525 ± 14	6.86 ± 0.49	30.2 ± 1.8	65.6 / 15
$\eta = 1$ 10–20%	424 ± 13	6.06 ± 0.44	27.4 ± 1.7	36.9 / 15
$\eta = 1$ 20–40%	254.6 ± 7.3	5.92 ± 0.39	27.0 ± 1.5	25.5 / 15
$\eta = 1$ 40–60%	136.8 ± 7.5	3.69 ± 0.33	19.2 ± 1.3	30.2 / 14
$\eta = 3$ 0–10%	253.8 ± 2.8	$(9.660 \pm 0.037) \cdot 10^5$	$(4.483 \pm 0.023) \cdot 10^6$	27.9 / 12
$\eta = 3$ 10–20%	200.6 ± 5.8	25 ± 11	122 ± 50	25 / 12
$\eta = 3$ 20–40%	124.5 ± 1.4	$(2.999 \pm 0.074) \cdot 10^5$	$1.415 \pm 0.035) \cdot 10^6$	49.4 / 12
$\eta = 3$ 40–60%	65.7 ± 2.7	34 ± 29	168 ± 140	12.3 / 12

Table 7.1: The table shows the fit parameters of the powerlaw function in equation 7.4 to the inclusive charged hadron spectra shown in figures 7.2, 7.4, and 7.5. All functions are fitted to all points in the given spectra. Due to high χ^2/NDF values, the functions should not be trusted outside the fit ranges.

$$\frac{d^2N}{2\pi p_{\mathrm{T}} dp_{\mathrm{T}} dy} = K_P \left(1 + \frac{p_{\mathrm{T}}}{p_0}\right)^{-n} \tag{7.4}$$

$$\frac{d^2N}{2\pi p_{\mathrm{T}} dp_{\mathrm{T}} dy} = K_B \cdot m_{\mathrm{T}} \cdot e^{-m_{\mathrm{T}}/T_B} \tag{7.5}$$

$$\frac{d^2N}{2\pi p_{\mathrm{T}} dp_{\mathrm{T}} dy} = K_G \cdot e^{-p_{\mathrm{T}}^2/2\sigma_G^2} \tag{7.6}$$

$p + p$ **Minimum bias central collisions**				
Powerlaw	K_P [GeV$^{-2}c^2$]	p_0 [GeV]	n	χ / NDF
$y = 0.0\ \pi^+$	19.8 ± 4.1	0.82 ± 0.11	9.2459 ± 0.61	37.0 / 9
$y = 0.0\ \pi^-$	27.3 ± 5.8	0.8 ± 0.1	9.4 ± 0.6	22.2 / 9
$y = 0.8\ \pi^+$	6.82 ± 0.53	3.59 ± 0.64	25.936 ± 3.8	61.6 / 7
$y = 0.8\ \pi^-$	7.1 ± 1.4	1.10 ± 0.21	10.235 ± 1.2	20.7 / 7
$y = 3.4\ \pi^+$	1.23 ± 0.09	$(2.95 \pm 0.11 \cdot 10^5$	$2.000 \pm 0.081) \cdot 10^6$	23.7 / 4
$y = 3.4\ \pi^-$	1.006 ± 0.063	$(1.7888 \pm 0.19) \cdot 10^4$	$(1.326 \pm 0.15) \cdot 10^5$	8.75 / 6
Boltzmann	K_B [GeV$^{-3}c^4$]	T_B [GeV]		χ / NDF
$y = 0.0\ K^+$	1.10 ± 0.14	0.1995 ± 0.0045		18.4 / 10
$y = 0.0\ K^-$	1.28 ± 0.19	0.1902 ± 0.0047		8.7 / 10
$y = 0.8\ K^+$	1.33 ± 0.29	0.1944 ± 0.0072		12 / 6
$y = 0.8\ K^-$	1.49 ± 0.27	0.1796 ± 0.0055		17.2 / 6
$y = 3.3\ K^+$	0.251 ± 0.027	0.1683 ± 0.0035		28.4 / 8
$y = 3.3\ K^-$	0.596 ± 0.086	0.1217 ± 0.0025		39.7 / 7
$y = 0.0\ p$	4.25 ± 0.52	0.1897 ± 0.0031		16.5 / 12
$y = 0.0\ \bar{p}$	6.3 ± 1.1	0.1711 ± 0.0037		16.2 / 12
$y = 0.7\ p$	9.5 ± 1.3	0.1708 ± 0.0028		6.7 / 8
$y = 0.7\ \bar{p}$	9.2 ± 2.3	0.1603 ± 0.0047		9.4 / 7
$y = 3.0\ p$	54.5 ± 2.0	0.1496 ± 0.0007		681 / 12
$y = 3.0\ \bar{p}$	25 ± 22	0.0927 ± 0.0069		6.0 / 5
Gaussian	K_G [GeV$^{-2}c^2$]	σ_G [GeV]		χ / NDF
$y = 0.0\ p$	0.02031 ± 0.00084	0.5715 ± 0.0061		58.2 / 12
$y = 0.0\ \bar{p}$	0.0175 ± 0.0010	0.5324 ± 0.0076		38.7 / 12
$y = 0.7\ p$	0.0236 ± 0.0012	0.5417 ± 0.0060		15.6 / 8
$y = 0.7\ \bar{p}$	0.0173 ± 0.0012	0.5085 ± 0.0084		15.8 / 7
$y = 3.0\ p$	0.08194 ± 0.00076	0.4622 ± 0.0015		644 / 12
$y = 3.0\ \bar{p}$	0.00084 ± 0.00010	0.337 ± 0.014		7.3 / 5

Table 7.2: The table shows the fit parameters of a powerlaw function fitted to the pion spectra, and a Boltzmann function in m_T fitted to the (anti-) proton and kaon spectra in figure 7.3 for $p+p$ collisions. The (anti–) proton spectra were also fitted with a Gaussian function in p_T. The powerlaw function, Boltzmann function, and Gaussian function are given in equations 7.4, 7.5, and 7.6, respectively. The (anti–) proton spectra are slightly better described by a Boltzmann function. The functions should not be trusted outside the fit ranges due to the high χ^2/NDF values. Neither the Boltzmann function nor the Gaussian could describe the proton spectrum at $y = 3.0$.

where K_p, K_B, K_G, p_0, n, T_B, and σ_G are free parameters. The rapidity density, dN/dy, can be extracted from these formulas through integration:

$$\frac{dN}{dy} = 2\pi \int_0^{\mathrm{inf}} p_\mathrm{T} S(p_\mathrm{T}) \tag{7.7}$$

where $S(p_\mathrm{T})$ is one of the formulas defined in equation 7.4, 7.5, or 7.6. This calculation involves extrapolations in p_T. The dN/dy depends strongly on the low–p_T part of the spectrum, thus leading to uncertainties in the dN/dy which is discussed in section 7.3.3.

Cu+Cu 0–10% central collisions				
Powerlaw	K_P [GeV$^{-2}c^2$]	p_0 [GeV]	n	χ / NDF
$y = 0.0$ π^+	285 ± 50	2.42 ± 0.55	15.386 ± 2.5	16.4 / 9
$y = 0.0$ π^-	219 ± 25	5.7 ± 1.7	30.831 ± 7.9	5.78 / 9
$y = 0.8$ π^+	161 ± 5	$(5.793 \pm 0.063) \cdot 10^5$	$(2.761 \pm 0.035) \cdot 10^4$	29.4 / 5
$y = 0.8$ π^-	205 ± 5	14.34 ± 0.24	73.7 ± 1.1	7.61 / 5
$y = 3.4$ π^+	103 ± 96	1.0 ± 1.0	10.2 ± 5.9	28.6 / 6
$y = 3.4$ π^-	34.7 ± 2.1	$(4.241 \pm 0.084) \cdot 10^5$	$(2.511 \pm 0.063) \cdot 10^6$	76 / 5
Boltzmann	K_B [GeV$^{-3}c^4$]	T_B [GeV]		χ / NDF
$y = 0.0$ K^+	66.4 ± 6.1	0.2258 ± 0.0039		31.2 / 10
$y = 0.0$ K^-	80.5 ± 7.4	0.2126 ± 0.0035		16.5 / 10
$y = 0.8$ K^+	132.4 ± 9.1	0.1950 ± 0.0024		11.5 / 6
$y = 0.8$ K^-	102 ± 11	0.1963 ± 0.0035		12.7 / 5
$y = 3.3$ K^+	53 ± 10	0.1550 ± 0.0053		25.5 / 6
$y = 3.3$ K^-	5.3 ± 1.6	0.196 ± 0.013		3.5 / 6
$y = 0.0$ p	105.1 ± 6.7	0.2491 ± 0.0025		24.4 / 16
$y = 0.0$ $\bar{p}$	68.7 ± 5.4	0.2417 ± 0.0030		39.9 / 16
$y = 0.7$ p	203.9 ± 8.5	0.2243 ± 0.0014		93.8 / 14
$y = 0.7$ $\bar{p}$	90.5 ± 6.9	0.2250 ± 0.0025		13.5 / 12
$y = 3.0$ p	868 ± 75	0.1724 ± 0.0020		25.6 / 12
$y = 3.0$ $\bar{p}$	4.0 ± 4.4	0.207 ± 0.037		2.13 / 5
Gaussian	K_G [GeV$^{-2}c^2$]	σ_G [GeV]		χ / NDF
$y = 0.0$ p	1.610 ± 0.045	0.7058 ± 0.0056		109 / 16
$y = 0.0$ $\bar{p}$	0.950 ± 0.034	0.6912 ± 0.0069		35.7 / 16
$y = 0.7$ p	2.071 ± 0.037	0.6488 ± 0.0034		88.6 / 14
$y = 0.7$ $\bar{p}$	0.861 ± 0.027	0.6609 ± 0.0056		41.5 / 12
$y = 3.0$ p	2.616 ± 0.067	0.5321 ± 0.0042		40.7 / 12
$y = 3.0$ $\bar{p}$	0.0358 ± 0.0095	0.563 ± 0.061		2.14 / 5

Table 7.3: The table shows the fit parameters of a powerlaw function fitted to the pion spectra, and a Boltsmann function in m_T fitted to the (anti-) proton and kaon spectra in figure 7.6 for Cu+Cu collisions. The (anti–) proton spectra were also fitted with a Gaussian function in p_T. The power-law function, Boltzmann function, and Gaussian function are given in equations 7.4, 7.5, and 7.6, respectively. The (anti–) proton spectra are slightly better described by a Boltzmann function. The functions should not be trusted outside the fit ranges due to the χ^2/NDF values. Neither the Boltzmann function nor the Gaussian could describe the proton spectrum at $y = 0.7$.

The functions were fitted to the full p_T range in the data samples. As can be seen in table 7.1 most of the spectra give $1.5 \lesssim \chi^2/NDF \lesssim 3$, though some have even higher values, e.g. the midrapidity $p + p$ spectra. The same is seen for the identified particle spectra. Fitting the (anti-) proton spectra with a gaussian in p_T gives a slightly worse χ^2/NDF than a Boltzmann function in m_T. Therefore the latter was chosen. These fit functions have been used to compare BRAHMS data with other experiments, as will be discussed below. Due to the χ^2/NDF values, the fit functions should not be trusted outside of the fit ranges.

Au+Au 0–10% central collisions					
Powerlaw	K_P [GeV$^{-2}c^2$]	p_0 [GeV]	n	χ^2 /	NDF
$y = 0.0\ \pi^+$	1089 ± 180	2.06 ± 0.44	13.412 ± 1.9	14.9 /	12
$y = 0.0\ \pi^-$	909 ± 120	3.22 ± 0.81	18.755 ± 3.6	11.7 /	12
$y = 0.8\ \pi^+$	774 ± 30	31.69 ± 13	159.68 ± 63	54.6 /	8
$y = 0.8\ \pi^-$	606 ± 20	(5.40 ± 0.17)·10^5	(2.569 ± 0.084)·10^6	62.1 /	8
$y = 3.4\ \pi^+$	77 ± 10	(2.81 ± 0.11)·10^5	(1.551 ± 0.072)·10^6	9.83 /	4
$y = 3.4\ \pi^-$	118 ± 13	(1.424 ± 0.087)·10^5	(8.4 ± 0.55)·10^5	5.67 /	4
Boltzmann	K_B [GeV$^{-3}c^4$]	T_B [GeV]		χ^2 /	NDF
$y = 0.0\ K^+$	257 ± 32	0.2312 ± 0.0054		14.5 /	13
$y = 0.0\ K^-$	187 ± 25	0.2363 ± 0.0059		11.7 /	13
$y = 0.8\ K^+$	363 ± 56	0.2143 ± 0.0058		1.48 /	5
$y = 0.8\ K^-$	421 ± 47	0.2008 ± 0.0037		20.4 /	7
$y = 3.3\ K^+$	31.1 ± 3.9	0.2218 ± 0.0066		50.2 /	7
$y = 3.3\ K^-$	26.6 ± 5.0	0.1844 ± 0.0070		15.3 /	7
$y = 0.0\ p$	198 ± 16	0.27599 ± 0.0038		63.4 /	16
$y = 0.0\ \bar{p}$	82 ± 13	0.28904 ± 0.008		26.7 /	15
$y = 0.7\ p$	1159 ± 55	0.20786 ± 0.0013		759 /	13
$y = 0.7\ \bar{p}$	91 ± 11	0.28017 ± 0.0063		21.9 /	10
$y = 3.0\ p$	1297 ± 75	0.19135 ± 0.0016		102 /	12
$y = 3.0\ \bar{p}$	21 ± 21	0.20176 ± 0.031		5.98 /	6
Gaussian	K_G [GeV$^{-2}c^2$]	σ_G [GeV]		χ^2 /	NDF
$y = 0.0\ p$	4.25 ± 0.17	0.7799 ± 0.0089		11.8 /	16
$y = 0.0\ \bar{p}$	2.20 ± 0.16	0.781 ± 0.016		28.8 /	15
$y = 0.7\ p$	7.20 ± 0.15	0.6568 ± 0.0032		328 /	13
$y = 0.7\ \bar{p}$	2.30 ± 0.10	0.746 ± 0.011		14.2 /	10
$y = 3.0\ p$	6.97 ± 0.12	0.5666 ± 0.0032		65.4 /	12
$y = 3.0\ \bar{p}$	0.168 ± 0.038	0.560 ± 0.052		6.46 /	6

Table 7.4: The table shows the fit parameters of a powerlaw function fitted to the pion spectra, and a Boltsmann function in m_T fitted to the (anti-) proton and kaon spectra in figure 7.6 for Au+Au collisions. The (anti–) proton spectra were also fitted with a Gaussian function in p_T. The powerlaw function, Boltzmann function, and Gaussian function are given in equations 7.4, 7.5, and 7.6, respectively. The (anti–) proton spectra are slightly better described by a Gaussian function. The functions should not be trusted outside the fit ranges due to the χ^2/NDF values. Neither the Boltzmann function nor the Gaussian could describe the proton spectrum at $y = 0.7$.
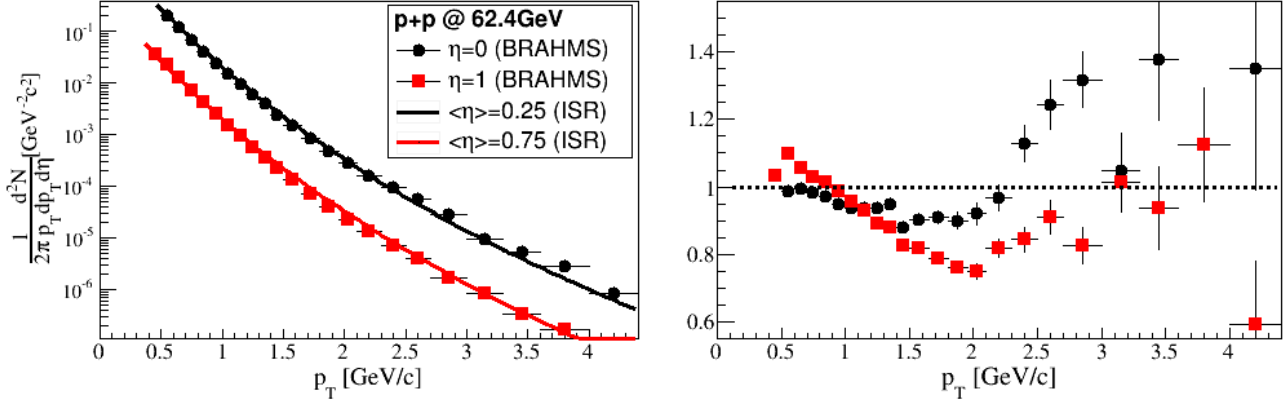
Figure 7.8: The figure shows the $p + p$ data measured by BRAHMS (points) compared to powerlaw fits to similar data from ISR. The parametrisation of ISR data is from the BRAHMS publication [116]. The solid lines are the powerlaw functions from [116]. The right panel shows the ratio of the BRAHMS spectra to the respective ISR fit. The BRAHMS spectrum is 5–10% lower than the parametrisation on average. For $p_{\mathrm{T}} < 2.5~GeV/c$, there are $\pm 10\%$ deviations from the average. Above $p_{\mathrm{T}} > 2.5~GeV/c$, the $\eta = 0$ spectrum is less steep than the parametrisaton and deviates by $\sim 40\%$. These spectra will be used as the reference spectrum for the R_{AA} in chapter 8.

7.3.2 $\sqrt{s_{\mathrm{NN}}} = $ **62.4 GeV results from ISR and PHOBOS**

Unidentified hadrons

Figure 7.8 shows a comparison of $p + p$ p_{T} spectra with a parametrisation of ISR spectra BRAHMS has previously used [116]. This special parametrisation was obtained by combining hadron spectra from [111, 117, 118]. The spectra shows different slopes compared to the parametrisation. For $p_{\mathrm{T}} > 2.5$ GeV/c, the spectra are $\sim 10\%$ lower than the parametrisation. The spectra agree within the $\pm 25\%$ uncertainty quoted [116] on the parametrisation though. These spectra constitute the denominater in the midrapidity R_{AA} presented in chapter 8 and should provide a lower uncertainty in the R_{AA}, since the spectra are obtained with the same aperature and data analysis.

The 0–6% central inclusive charged hadron spectra from Cu+Cu and Au+Au collisions are compared to the PHOBOS results in [119, 120]. The PHOBOS p_{T} binning was also used in this comparison. Since the PHOBOS acceptance was $0.2 < \eta < 1.4$, an average of the spectra obtained obtained in BRAHMS at $\eta = 0$ and at $\eta = 0.9$ was made for comparison to PHOBOS. These spectra are shown in the left panels of figure 7.9, together with the parameters of the powerlaw fits shown in the legends. The ratio of PHOBOS to BRAHMS are shown in the right panels. The PHOBOS spectra were divided by both the powerlaw fit to the BRAHMS spectra as well as the BRAHMS spectra themselves. Reasonable agreement is found for both spectra. The ratios show agreement within $\pm 10\%$, except that the BRAHMS Cu+Cu spectrum is on averge lower by $\sim 10\%$. The fit function for the Cu+Cu spectrum does not reproduce the high p_{T} part, and the ratio with the fit function (solid points) deviate from the ratio of with the spectrum. The BRAHMS and PHOBOS Au+Au data shows very good agreement for $p_{\mathrm{T}} < 2.5$ GeV/c, but for $p_{\mathrm{T}} > 2.5$ GeV/c it is on average
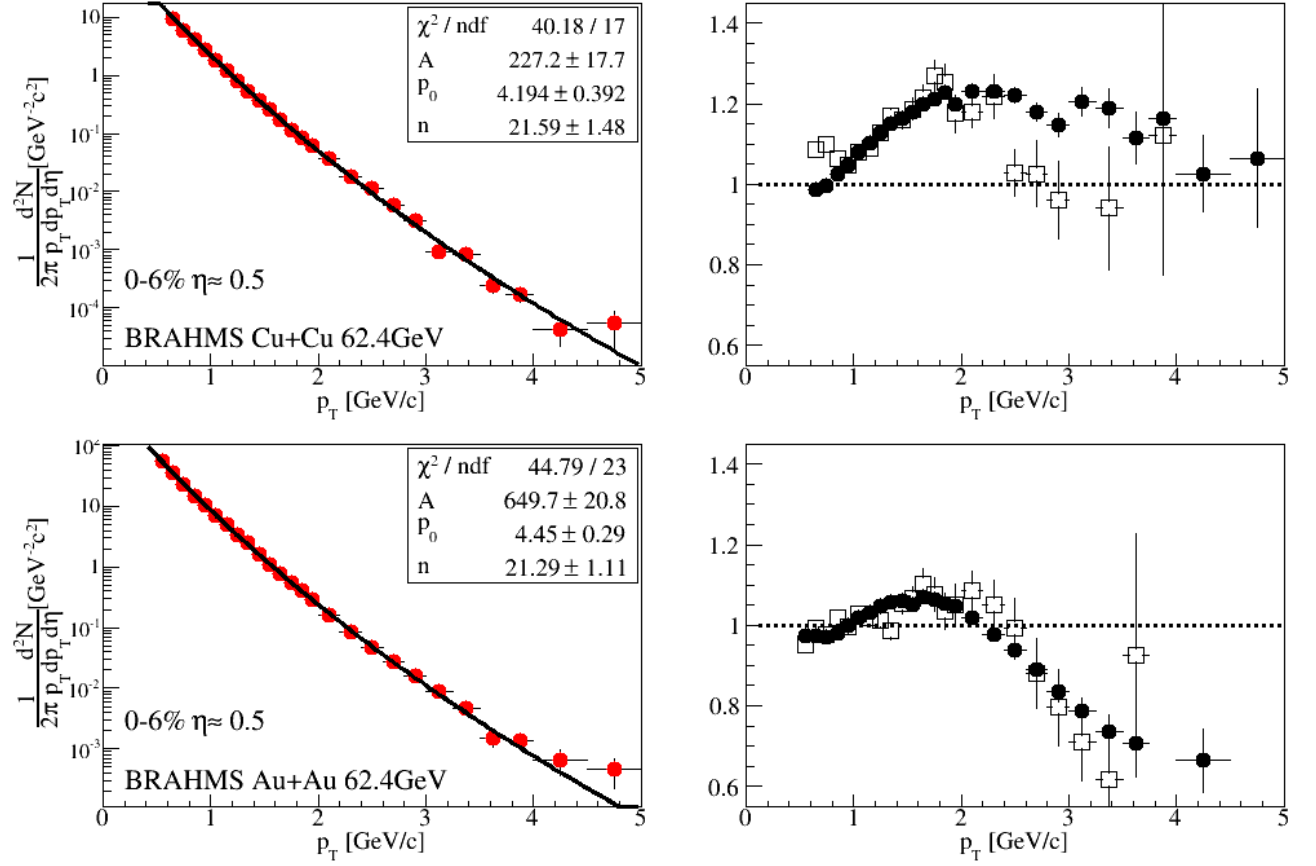
Figure 7.9: The figure shows PHOBOS's 0–6% central inclusive charged hadron spectra [119, 120] in the left panels along with these spectra divided by powerlaw fits to the p_T spectra from the BRAHMS data. The top row shows the Cu+Cu data and the bottom row the Au+Au data. The PHOBOS data were collected in the pseudorapity interval $0.2 < \eta < 1.4$. For comparison the BRAHMS data was made as an average of the $\eta = 0.0$ and $\eta = 0.9$ spectra. As can be seen in the top right panel the powerlaw fit does not accurately describe the BRAHMS Cu+Cu data $p_T > 2.5$ GeV/c. The open symbols are the ratios of the PHOBOS spectra by the BRAHMS spectra, while the solid points are the PHOBOS spectrum divided by the fit function. The BRAHMS Cu+Cu spectra are lower than the PHOBOSdata. The agreement is within $\pm 10\%$, with an offset of 10%. The Au+Au data comparison in the bottom panels show a better agreement. For $p_T < 2.5$ GeV/c, no bigger deviations than $\pm 5\%$ are seen in the ratios. The ratios with solid symbols only reflect the PHOBOS statitical uncertainties.

higher by $\sim 15\%$. Both the ratio using the fit function and the ratio using the spectrum for $p_T < 2.5$ GeV/c show that, within $\pm 5\%$, the spectra are the same. Comparison between the experiments are not easy, as triggering on a track is not done in the same way. The BRAHMS MRS trigger (trigger 3) requires that there is a hit in the TOFW, while PHOBOS requires that there is a track in their spectrometer which is $\sim$ 1m long.
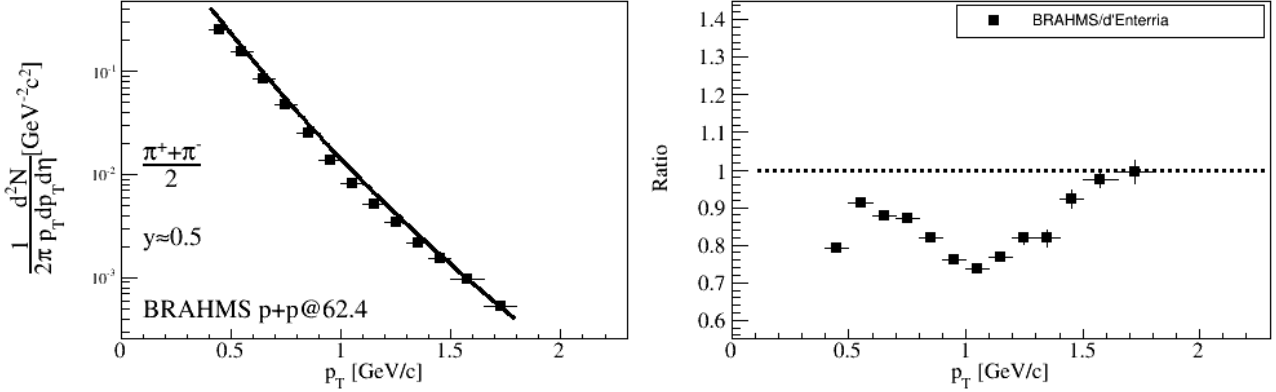
Figure 7.10: The figure show the charged pions measured in $p+p$ collisions compared to the ISR global fit, presented by D. d'Enterria in [112]. The left panel shows the $(\pi^+ + \pi^-)/2$ transverse momentum spectra (the average of those measured at $y = 0.0$ and $y = 0.8$) The solid line is the D. d'Enterria function. The right panel shows ratio of the combined pion spectra to the function. The BRAHMS data show an overall lower spectrum of about 10%. The spectra agree, around this offset, within $\pm 15\%$.

Identified particles

The pion spectra in $p + p$ collisions, discussed in the introduction of this chapter can be compared to the empirical function in equation 7.3, proposed by D. d'Enterria in [112]. The results for 0–10% centrality is shown in figure 7.10. Since many of the experiments had wide rapidity bins, and equation 7.3 was fitted to data from many different experiments, the average of the $(\pi^+ + \pi^-)/2$ spectra at $y = 0.0$ and $y = 0.8$ was used. The p_{T} spectrum can be seen in the left panel of figure 7.10. The D. d'Enterria function is drawn together with the spectrum. The right panel shows this spectrum divided by the function. The BRAHMS data are $\sim 15\%$ lower than the parametrisation, but, apart from that, show agreement with parametrisation, within $\pm 10\%$.

PHOBOS has also measured identified particles in Au+Au collisions. Comparisons with the BRAHMS spectra are shown in figure 7.11. The comparison is for 0–15% central collisions, against the average of spectra at $y = 0.0$ and $y = 0.8$ ($y = 0.7$ for (anti-) protons). PHOBOS has corrected their (anti-) proton spectra for feed down from Λ ($\bar{\Lambda}$) decay, with the numbers discussed in section 7.2. They state in [72] that the correction for pions in their analysis is $< 1\%$ and was therefore not applied. The kaon spectra need no such corrections, and also show good agreement, within $\sim \pm 10\%$, with the results presented in this chapter.

The pion ratio in figure 7.11, is ~ 0.8, indicating that the BRAHMS pion spectra are contaminated with pions from Λ, Σ and K_0^S decays. PHOBOS reject these pions through a more precise vertex resolution, "distance–of–closest–approach" ≈ 0.35 cm [72]. As shown in figure 5.4, the BRAHMS vertex resolution is ~ 1.1 cm, making it difficult to reject pion decay products. BRAHMS has

estimated this to be $\sim 1\%$ from Λ decay and $\leq 4\%$ from K_0^S in Au+Au collisions at $\sqrt{s_{NN}} = 200$ GeV in [121]. Au+Au collisions at $\sqrt{s_{NN}} = 200$ GeV have a better vertex resolution that the results presented here. The contamination should thus be higher for $p+p$, Cu+Cu, and Au+Au at $\sqrt{s_{NN}} = 62.4$ GeV, thereby accounting for the 20% difference in the pion spectra. Protons from Λ and Σ decays contribute to about half the (anti–) protons spectrum, which is visible in the (anti–) proton ratio in the right panel of figure 7.11.
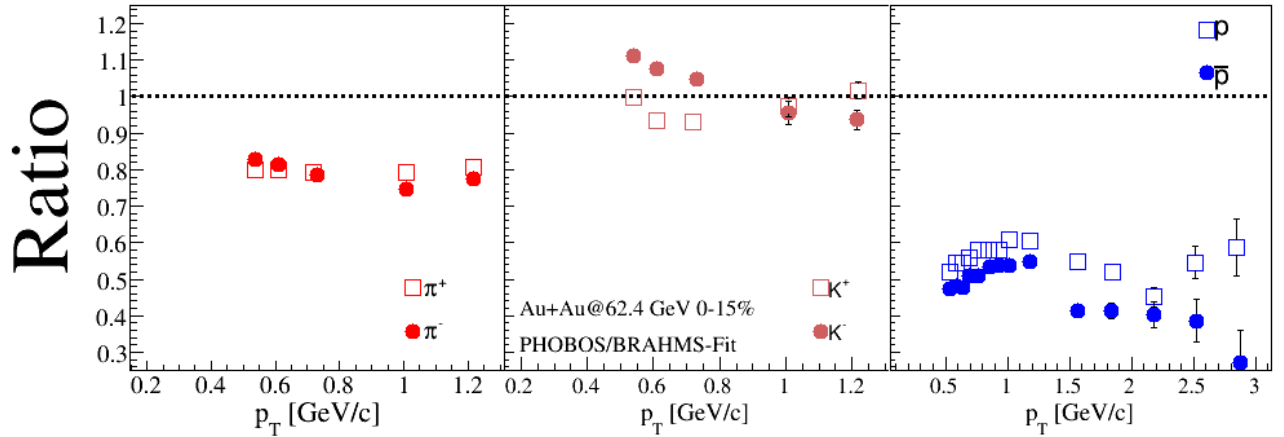
Figure 7.11: The figure shows the ratio of the 0–15% central identified particle PHOBOS spectra to a powerlaw fit to the BRAHMS data. The BRAHMS data was made as an average of the $y = 0$ and the $y = 0.8$ spectra ($y = 0.7$ for (anti-) protons). The PHOBOS data [72] is shown with statistical uncertainties. The PHOBOS data points outside the fit range are not shown. Kaon spectra show agreement within $\pm 10\%$. The pion and (anti–) proton spectra are not comparable, since feed–down correction has not been applied to the BRAHMS spectra. The Λ/p ratio is about 0.9. The proton ratio in the left panel is about 0.55, and the anti–proton ratio is about 0.6. The difference between the spectra is accounted for by the feed–down correction to the PHOBOS data.

The STAR experiment has also published pion and (anti–) proton spectra in Au+Au collisions at $\sqrt{s_{NN}} = 62.4$ GeV, but the data points are not yet available. A systematic comparison could therefore not be performed.

7.3.3 Systematic uncertainties

The systematic uncertainties on the p_T spectra shown in this chapter arise from the cuts and corrections which are applied to the data. The charged hadron spectra are subject to the following cuts which determine the systematic uncertainties:

- event–by–event centrality determination

- matching of local tracks between the TPCs

- comparing track vertices to the primary vertex (where the Z-direction is obtained from the BBCs or the CCs),

- tracking efficiency

- matching tracks with hits in the PID detector and selection β^{-1} values

- PID efficiency

- correction for multiple scattering, absorption and decay

- trigger inefficiency for the $p + p$ collisions

- spectrum construction method

By varying cut parameter values in the analysis, some of the systematic uncertainties can be estimated. The uncertainty in the centrality determination arises from the design of the minimum bias trigger detectors (see table 5.2). They are less efficient at very low multiplicities. The 0–10%, 10–20%, and 20–40% centrality selections are not affected in Cu+Cu or Au+Au collisions, but the 40–60% centrality selection in Cu+Cu collisions is affected at centralities $> 55\%$. Preliminary investigation of the inefficiency, for the centrality selection 55–60%, has shown it to not be bigger than 10%. Further investigation, through a full simulation of the trigger detectors will be needed to correct for trigger inefficiency in 40–60% Cu+Cu collisions. No trigger inefficiency has been found in Au+Au collisions, in the centrality selections presented in this chapter.

All of the p_{T} spectra shown in this chapter have been treated identically. It was found that they behave identically when varying the cut parameters, and that they have approximately the same uncertainties. All the inclusive charged hadron transverse momentum spectra are assigned a systematic uncertainty of $\pm 10\%$ point–to–point. Many of the systematic uncertainties should cancel out in the ratios of spectra which are presented in chapter 8.

The identified particle spectra has additional cuts for the PID determination. This introduces a slightly larger uncertainty in the identified particle spectra. Varying the PID cuts were, again, seen to have an identical effect on the spectra for all three collision systems. The PID spectra are assigned a systematic uncertainty of $\pm 15\%$ point–to–point.

It should be noted that the systematic uncertainties are bigger for $p_{\mathrm{T}} \lesssim 0.6$ GeV/c. This was found when comparing the different analysis methods, `tree2datamap` and `hadronAnalyse`, described in section 6.4.6. The chosen method was used because it could utilise sparse statistics at high p_{T}. The `hadronAnalyse` method produced systematically low values in the spectra at low p_{T}, but were removed through the low–p_{T} cut discussed in section 6.4.6. The same effect were seen for all collision systems. The two different methods treat the pure geometric acceptance maps differently, as discussed in section 6.5. The p_{T} spectra presented here should not be used for calculating the rapidity densities, which is done by integrating the p_{T} spectra. Such an analysis depends strongly on the low p_{T} region of the spectra. Since the lowest p_{T} data of the spectra are removed through the low–p_{T} cut, the extrapolation becomes large. This will produce large uncertainties on the particle yields.

Chapter 8

The nuclear modification factor at $\sqrt{s_{\mathrm{NN}}} = 62.4$ GeV

After the the first Au+Au run at maximum energy at the RHIC, all four experiments reported observations of suppression of high p_{T} hadrons relative to nucleon–nucleon collisions. Many more measurements have later been done, discussed in chapter 4, and it is now established that at $\sqrt{s_{\mathrm{NN}}} = 200$ GeV the suppression saturates at ~ 4 GeV/c, and stays constant up to at least $p_{\mathrm{T}} \sim 20$ GeV/c as shown in figure 4.9. Additionally, BRAHMS measurements have also shown suppression to be independent of rapidity, as seen in figure 4.5.

Since no suppression was seen in the lower energy experiments, the RHIC experiments requested collisions at an intermediate energy. The choice of $\sqrt{s_{\mathrm{NN}}} = 62.4$ GeV was made because the CERN ISR experiments had measured $p + p$ collisions at this energy, and could be used as a reference. This would give an opportunity to investigate the onset of suppression as a function of collision energy.

Au+Au, Cu+Cu, and $p+p$ collisions at $\sqrt{s_{\mathrm{NN}}} = 62.4$ GeV have been produced at RHIC from 2004 to 2006. With the much smaller Cu ions, one can look for scaling behaviour as a function of system size. Colliding $p+p$, meant that systematic uncertainties arising from using a $p+p$ p_{T} spectrum from experiments at ISR can be eliminated. The following sections will present the nuclear modification factor for Cu+Cu and Au+Au collisions.

Centrality	0–10%	10–20%	20–40%	40–60%	30–45%	38–50%
$\langle b_{\mathrm{CuCu}}\rangle$ [fm]	$2.6\ ^{+\ 0.1}_{-\ 0.1}$	$4.1\ ^{+\ 0.2}_{-\ 0.2}$	$5.9\ ^{+\ 0.3}_{-\ 0.3}$	$7.6\ ^{+\ 0.3}_{-\ 0.3}$	(Not Used)	(Not Used)
$\langle b_{\mathrm{AuAu}}\rangle$ [fm]	$3.5\ ^{+\ 0.2}_{-\ 0.1}$	$6.0\ ^{+\ 0.3}_{-\ 0.3}$	$8.4\ ^{+\ 0.5}_{-\ 0.4}$	$10.7\ ^{+\ 0.6}_{-\ 0.5}$	$9.4\ ^{+\ 0.5}_{-\ 0.4}$	$10.1\ ^{+\ 0.6}_{-\ 0.5}$
$\langle N_{\mathrm{part}}^{\mathrm{CuCu}}\rangle$	$92\ ^{+\ 2}_{-\ 2}$	$71\ ^{+\ 3}_{-\ 3}$	$43\ ^{+\ 3}_{-\ 3}$	$20\ ^{+\ 2}_{-\ 2}$	(Not Used)	(Not Used)
$\langle N_{\mathrm{part}}^{\mathrm{AuAu}}\rangle$	$315\ ^{+\ 5}_{-\ 7}$	$222\ ^{+\ 8}_{-\ 9}$	$129\ ^{+\ 9}_{-\ 9}$	$56\ ^{+\ 8}_{-\ 6}$	$95\ ^{+\ 9}_{-\ 8}$	$72\ ^{+\ 8}_{-\ 7}$
$\langle N_{\mathrm{coll}}^{\mathrm{CuCu}}\rangle$	$142\ ^{+\ 15}_{-\ 14}$	$97.8\ ^{+\ 12}_{-\ 11}$	$49.4\ ^{+\ 8}_{-\ 7}$	$18.6\ ^{+\ 4}_{-\ 3}$	(Not used)	(Not used)
$\langle N_{\mathrm{coll}}^{\mathrm{AuAu}}\rangle$	$752\ ^{+\ 90}_{-\ 113}$	$459\ ^{+\ 66}_{-\ 77}$	$217\ ^{+\ 40}_{-\ 43}$	$70\ ^{+\ 18}_{-\ 16}$	$142\ ^{+\ 30}_{-\ 31}$	$96.9\ ^{+\ 23}_{-\ 22}$

Table 8.1: The table contains the average number of incoherent binary collisions for each centrality bin used in this chapter. The number of participants and the average impact parameter is also quoted. The numbers are calculated as explained in section 3.2. The uncertainties from the Glauber calculations are given in the sub– and superscripts.
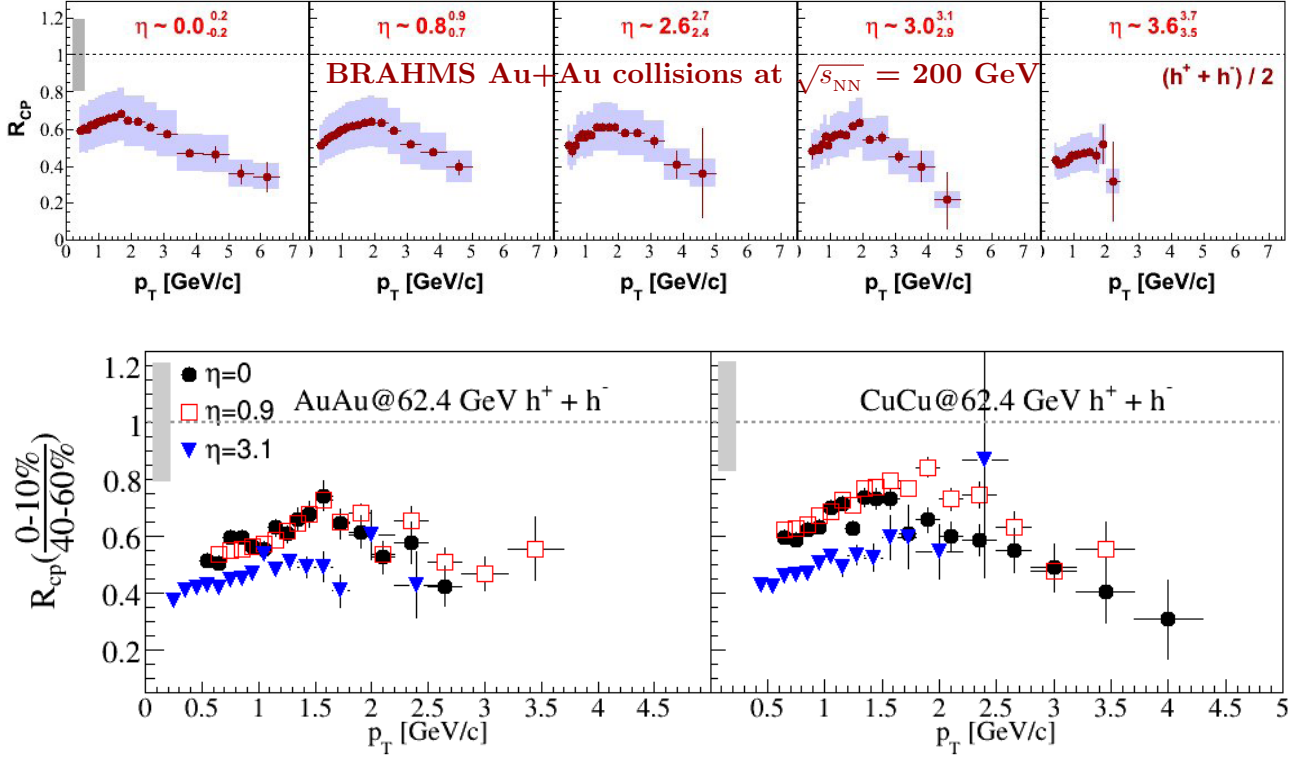
Figure 8.1: The top panels show the R_{cp} in $\sqrt{s_{\mathrm{NN}}} = 200$ GeV Au+Au collisions, measured by BRAHMS [83]. The bottom panel shows the central to peripheral ratio for Cu+Cu and Au+Au collisions at $\sqrt{s_{\mathrm{NN}}} = 62.4$ GeV. The central spectra are 0–10% and the peripheral spectra are 40–60%. The central and the peripheral p_{T} spectra are scaled with their respective average number of binary collisions, which can be found in table 8.1. The shaded band at 1 is the uncertainty on the normalisation arising from the numbers in table 8.1. The R_{cp} in $\sqrt{s_{\mathrm{NN}}} = 200$ GeV has the same shape and absolute value for for $\eta \leq 3.0$. The ratio at $\eta = 3.6$ slightly lower. In $\sqrt{s_{\mathrm{NN}}} = 62.4$ GeV collisions, the R_{cp} at $\eta = 3.1$ have a lower absolute value than at midrapidity, for both collision systems. The Au+Au R_{cp} is lower compared to Cu+Cu collisions.

8.1 R_{cp} and R_{AA} for charged hadrons

Figure 8.1 shows the ratio of central to peripheral spectra for Au+Au collisions at $\sqrt{s_{\mathrm{NN}}} = 200$ GeV (top panel) and Cu+Cu and Au+Au collisions at $\sqrt{s_{\mathrm{NN}}} = 62.4$ GeV (bottom panel). The ratio is between the spectra in the 0–10% and 40–60% centrality bins, scaled by the average number of binary collisions in the given centrality classes found in table 8.1 for $\sqrt{s_{\mathrm{NN}}} = 62.4$ GeV collisions. In both collisions systems, very weak dependency on p_{T} is seen. The only difference between mid– and forward rapidity is the absolute value of the R_{cp}. The ratio is lower in Au+Au compared to Cu+Cu collisions. There is an indication that more suppression exist at forward rapidity than at midrapidity. $\sqrt{s_{\mathrm{NN}}} = 200$ GeV collisions also show the same behaviour in the R_{cp}, but with no difference between the absolute value at midrapidity and at forward rapidity, as shown in the top panel of figure 8.1, though

there is an indication that this happens at $\eta \sim 3.6$. The R_{cp} shows that the particle production in central collisions is suppressed relative to peripheral collisions, but the amount of suppression does not change between $\sqrt{s_{\text{NN}}} = 62.4$ GeV and 200 GeV.

The nuclear modification factors for inclusive charged hadrons are shown in figure 8.2 for Cu+Cu (top panel) and Au+Au (bottom panel) collisions. The midrapidity ratios increase from low p_{T} up to $p_{\text{T}} \sim 2$ GeV/c, where it either saturates or decrease again. The forward R_{AA} has it's highest value at $p_{\text{T}} \sim 1 - 1.5$ GeV/c before it decreases again. The most central Cu+Cu collisions show very little enhancement at midrapidity, and the $\eta = 0.0$ and $\eta = 0.9$ ratios are identical. The forward results show suppression as one approaches 2 GeV/c, for the 0–10% and 10–20%, and 20–40% centrality bins. The enhancement of high p_{T} particles grows strongly for more peripheral collisions. For all centralities, at forward rapidity, the R_{AA} shows no dependence on the charge.

The R_{AA} for Au+Au collisions (bottom panel of figure 8.2) show the same behaviour as the Cu+Cu collisions, though for all centralities less enhancement is seen. The ratio does not exceed 1 for the the most central collisions at midrapidity, while the forward results show a clear suppression. As the collisions become more peripheral, the enhancement of high p_{T} particles becomes stronger. The suppression weakens at forward rapidity in peripheral collisions. The R_{AA} in $\sqrt{s_{\text{NN}}} = 62.4$ GeV collisions are qualitatively very different compared to $\sqrt{s_{\text{NN}}} = 200$ GeV (see also figure 4.5), as the R_{AA} depends on the pseudorapidity. By comparing the centrality bins in Cu+Cu with Au+Au collisions, a larger fireball imposes a stronger suppression on the high p_{T} particles. There is an indication that there is also a charge dependence at forward rapidity for the most peripheral collisions.

8.2 R_{AA} for identified particles

The top panel of figure 8.3 shows the R_{AA} for identified particles in Cu+Cu collisions. All the particle species show a different shape. R_{AA} for kaons and (anti–) protons does not show any dependence on the charge. The kaon ratio has a flat shape in all three rapidity bins, while the (anti–) protons has the shape seen in the unidentified R_{AA}. The R_{AA} for π^-s does not seem to depend on the rapidity, while π^+ does, showing strong suppression at forward rapidity. The kaons does neither depend on the rapidity, and show no suppression or enhancement. Protons show a different behaviour than the mesons. At midrapidity, a clear Cronin enhancement is seen for the (anti–) protons, while at forward rapidity they are suppressed by a factor of ~ 2. There was not enough statistics to make the R_{AA} for $\bar{p}$ at $y = 3.0$. The protons at $y = 3.0$ are fragmentation protons, as indicated in figure 7.7. The R_{AA} for π^+ and protons are comparable at forward rapidity.

The R_{AA} in Au+Au collisions in figure 8.3 show, again, a similar behaviour to Cu+Cu collisions in figure 8.3. There is, in general, more suppression for all particle species in the Au+Au collisions compared to Cu+Cu collisions. The relative differences between the particles species is the same in Au+Au collisions compared to Cu+Cu collisions. In both collision systems, the R_{AA} for protons and π^+ clearly shows that the physics is different inside the fragmentation region compared to the midrapidity region at this collision energy. This is further discussed in chapter 9.
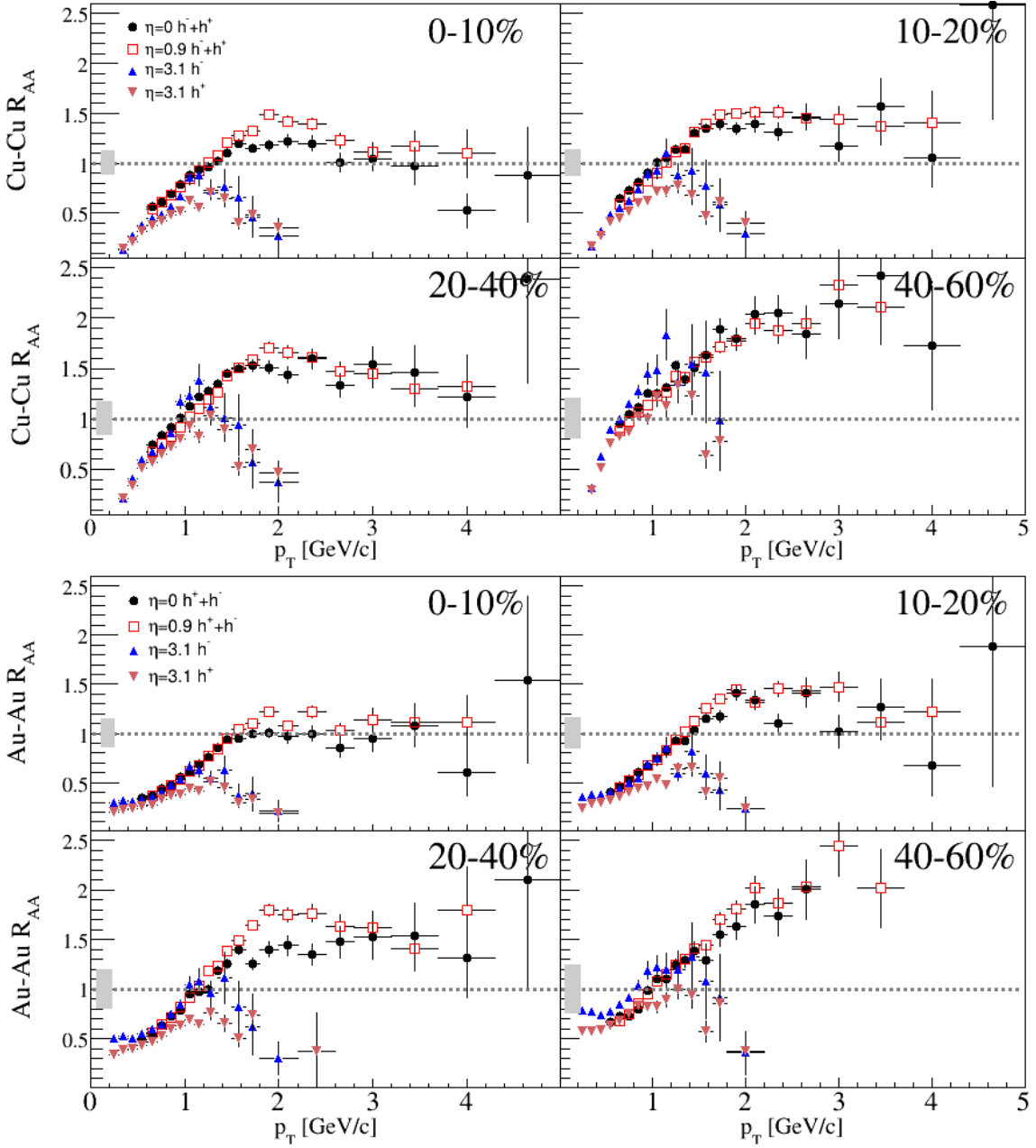
Figure 8.2: The figure shows the inclusive charged hadron nuclear modification factor for Cu+Cu (top panel) and Au+Au collisions (bottom panel) at $\sqrt{s_{\mathrm{NN}}} = 62.4$ GeV. The midrapidity results have both positive and negative charges combined, while the forward rapidity results show the positive hadrons as downward triangle and the negative hadrons as upward triangle. The shaded band at $R_{AA} = 1$ is the uncertainty on the normalisation arising from the numbers in table 8.1. At midrapidity an increasing suppression is seen with more peripheral collisions. Forward rapidity is most suppressed in the central collisions, though the suppression persist to the peripheral collisions.
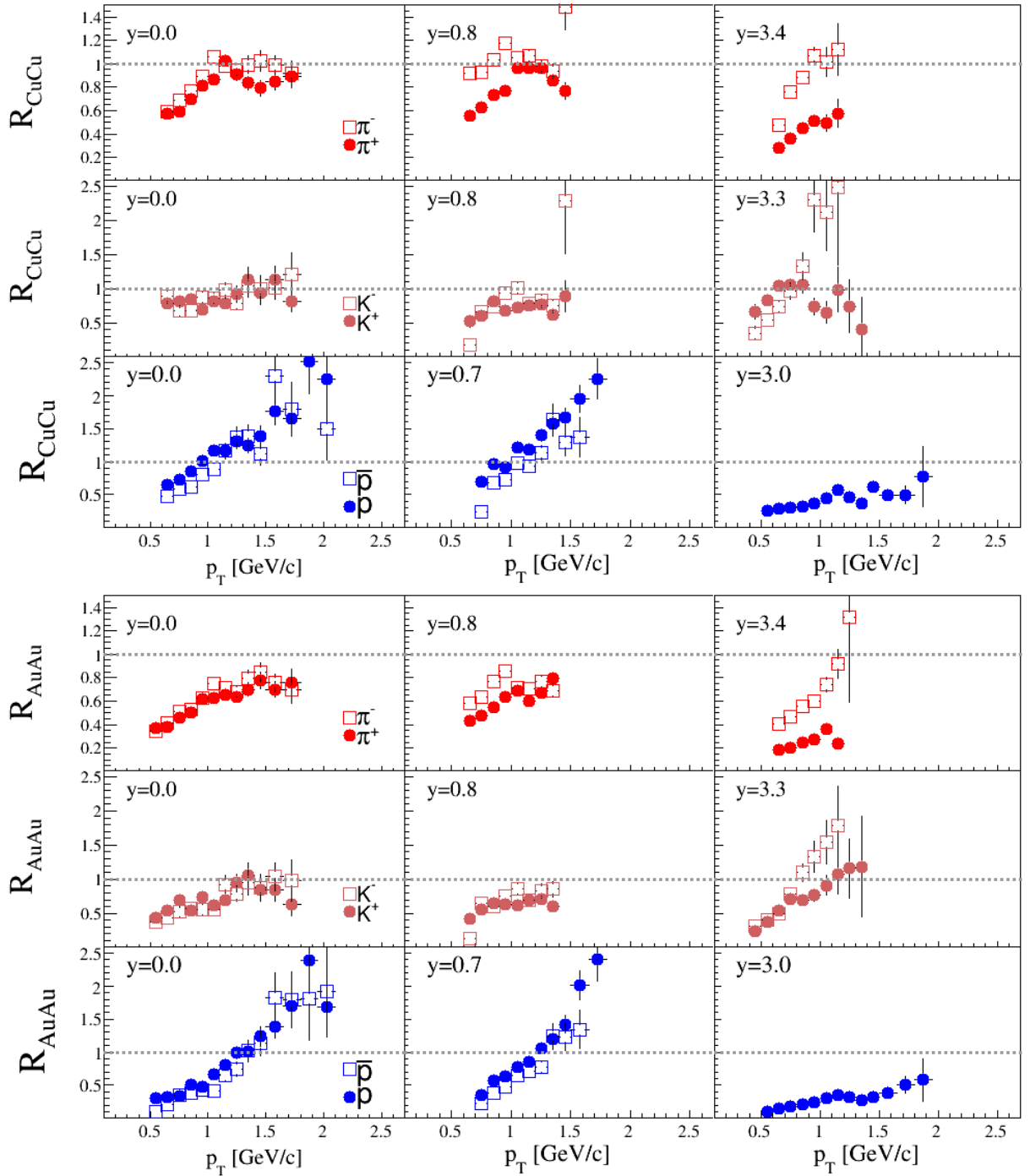
Figure 8.3: The figure shows the nuclear modification factor for $\pi^{\pm}$, $K^{\pm}$, p and $\bar{p}$ in 0–10% central Cu+Cu collisions (to panel) and Au+Au collisions (bottom panel) at $\sqrt{s_{NN}} = 62.4$ GeV. The suppression of π^{+} in Cu+Cu collisions increases with rapidity. π^{-} and the kaons show no rapidity dependence. The (anti–) proton production is enhanced at midrapidity, but strongly suppressed at forward rapidity. The uncertainty in the normalisation the from the Cu+Cu $\langle N_{coll} \rangle$ scaling is ±0.12. At midrapidity in Au+Au collisions pions are suppressed, kaons are neither suppressed nor enhanced, and the (anti–) protons are enhanced. At forward rapidity the π^{+} and the protons are severly suppressed, while the kaons and π^{-} are unchanged from midrapidity.
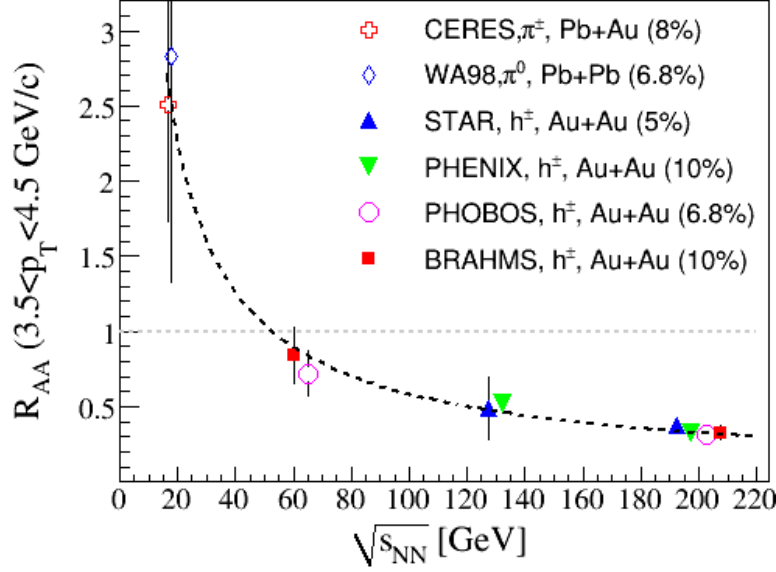
Figure 8.4: The figure shows R_{AA} as a function of collision energy. The 4 collision energies are $\sqrt{s_{\mathrm{NN}}} = 17.3$ GeV 62.4 GeV, 130 GeV, and 200 GeV. The points are offset around the collision energies for clarity. The dashed line is a fit to the average R_{AA} at each of the 4 collision energies. The function is purely empirical: $R_{AA}(\sqrt{s_{\mathrm{NN}}}) = k/(\sqrt{s_{\mathrm{NN}}})^n$, with $k = 28 \pm 13$ and $n = 0.84 \pm 0.09$. This determines the onset of suppression at $\sqrt{s_{\mathrm{NN}}} = 53 \pm 28$ GeV. Extrapolating to LHC energies gives an $R_{AA} = 0.02^{+0.04}_{-0.01}$. The numbers are taken from [122, 123, 120, 124, 125, 37, 126, 127, 128]. The $p + p$ reference spectrum at $\sqrt{s_{\mathrm{NN}}} = 17.3$ GeV [75] is given as $Ed^3N/dp^3 = C \cdot (p_0/(p_{\mathrm{T}} + p_0))^n$, with parameters $C = 4.125$, $p_0 = 9.02$ and $n = 55.77$.

8.3   Size and energy scaling of the R_{AA}

As seen in the previous section, the nuclear modification factor at midrapidity in $\sqrt{s_{\mathrm{NN}}} = 62.4$ GeV is in the vicinity of the onset of suppression. To investigate the onset in a more qualitative way, the R_{AA} for $3.5 < p_{\mathrm{T}} < 4.5$ as a function of collision energy is shown in figure 8.4. The solid line is a fit to all the data points. The formula is given as: k/p_{T}^n. The fit yields $k = 28 \pm 13$ and $n = 0.84 \pm 0.09$. With this formula the suppression starts to dominate at $\sqrt{s_{\mathrm{NN}}} = \sim 53$ GeV. Extrapolating this to higher energies would determine the suppression at to LHC energies to be $R_{AA} = 0.02^{+0.04}_{-0.01}$ at $p_{\mathrm{T}} \approx 4$ GeV/c.

The ^{63}Cu and ^{197}Au nuclei are very different in size, but one can make comparison of the two different collision systems be making a ratio of Au+Au p_{T} spectra and Cu+Cu p_{T} spectra, R_{AuCu}. Two reasonable choices are available for comparing the system sizes: A ratio where the centrality class is the same for both collisions systems, and a ratio of spectra where the $\langle N_{\mathrm{coll}} \rangle$ and $\langle N_{\mathrm{part}} \rangle$ are the same.

The first ratio is shown in figure 8.5 for the 0–10% and the 40–60% centrality bin. The charged hadron spectrum at $\eta = 0.0$ and the spectrum at $\eta = 0.9$ were combined. The forward spectra are $h^+ + h^-$. All spectra were scaled with the corresponding $\langle N_{\mathrm{coll}} \rangle$. The ratio for the central collisions
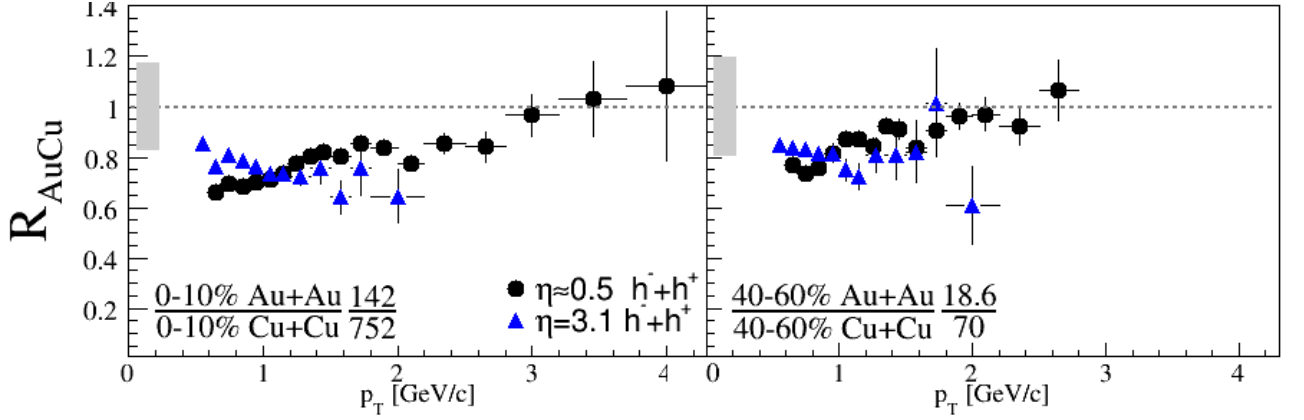
Figure 8.5: The figure shows two ratios of Au+Au and Cu+Cu collisions with the same centrality class. The figure shows inclusive charged hadrons, and the average of the $\eta = 0$ and $\eta = 0.9$ spectra. The forward ratio is $h^+ + h^-$. The central collisions show that particle production at midrapidity is suppressed in Au+Au collisions relative to Cu+Cu collisions for $p_{\rm T} < 3$ GeV/c, while there is binary scaling above. The semi–peripheral collisions indicate that binary scaling at midrapidity from $p_{\rm T} > 2$ GeV/c. The ratio for forward rapidity do not change from central to peripheral collisions.

shows that both at mid– and at forward rapidity the Au+Au collisions are more suppressed for $p_{\rm T}$ < 3 GeV/c. The midrapidity results show that there is binary scaling for $p_{\rm T} > 3$ GeV/c. The ratios for peripheral collisions are closer to 1, showing that suppression or enhancement in both system are comparable, when the created matter is small. The ratio for the forward rapidity is ~ 0.8 and does not change, as much as the midrapidity ratio, from central to semi–peripheral collisions.

The second way to compare the two collision system, where the $\langle N_{\rm coll} \rangle$ and $\langle N_{\rm part} \rangle$ are the same, is shown in figure 8.6. Three values for the average number of binary collisions were chosen: $\langle N_{\rm coll} \rangle =$ 142, 97 and 70, left, middle and right panels, respectively. The nuclear modification factor for these centrality classes are shown for both systems, in the top and the middle panels. The charged hadron spectrum at $\eta = 0.0$ and at $\eta = 0.9$ were combined. The forward spectra are also $h^+ + h^-$. The bottom panels show the Au+Au to Cu+Cu spectra ratio, $R_{\rm AuCu}$. These ratios reveal that there are more particles produced at mid rapidity for $p_{\rm T} > 2$ GeV/c in the semi peripheral Au+Au collisions compared to Cu+Cu collisions for the three $\langle N_{\rm coll} \rangle$ selections. For $p_{\rm T} < 2$ GeV/c the ratio is flat at a value of 1.1 for $\langle N_{\rm coll} \rangle = 142$ collisions and 1 for the other two. The ratio at forward rapidity show decrease with $p_{\rm T}$ from a value of about 1.5 down to 1. The shape is the same in the all the forward rations, but with a slightly higher overall, absolute value in the 30–45% to 0–10% spectra ratio. The $\langle N_{\rm coll} \rangle = 97$ and 70 ratios for forward rapidity are identical in shape and absolute value.

Though the $\langle N_{\rm coll} \rangle$ value is the same for both collision systems, there is more enhancement, probably originating from the initial state, in Au+Au collisions. Figure 8.7 shows a schematic view of the collision geometry with the impact parameters found in table 8.1. The figure shows, in combination with the results presented in figure 8.6, that the enhancement is stronger when the overlap region between the colliding nuclei is almond shaped, than for a more circular geometry. Also visible in the figure is that the actual collision geometry, for Au+Au collisions, changes very slowly with centrality for the semi-peripheral collisions. The change in $\overline{R}(\theta)$ is much bigger for the smaller Cu+Cu collision between the 0–10% and the 15–30% centrality bin.
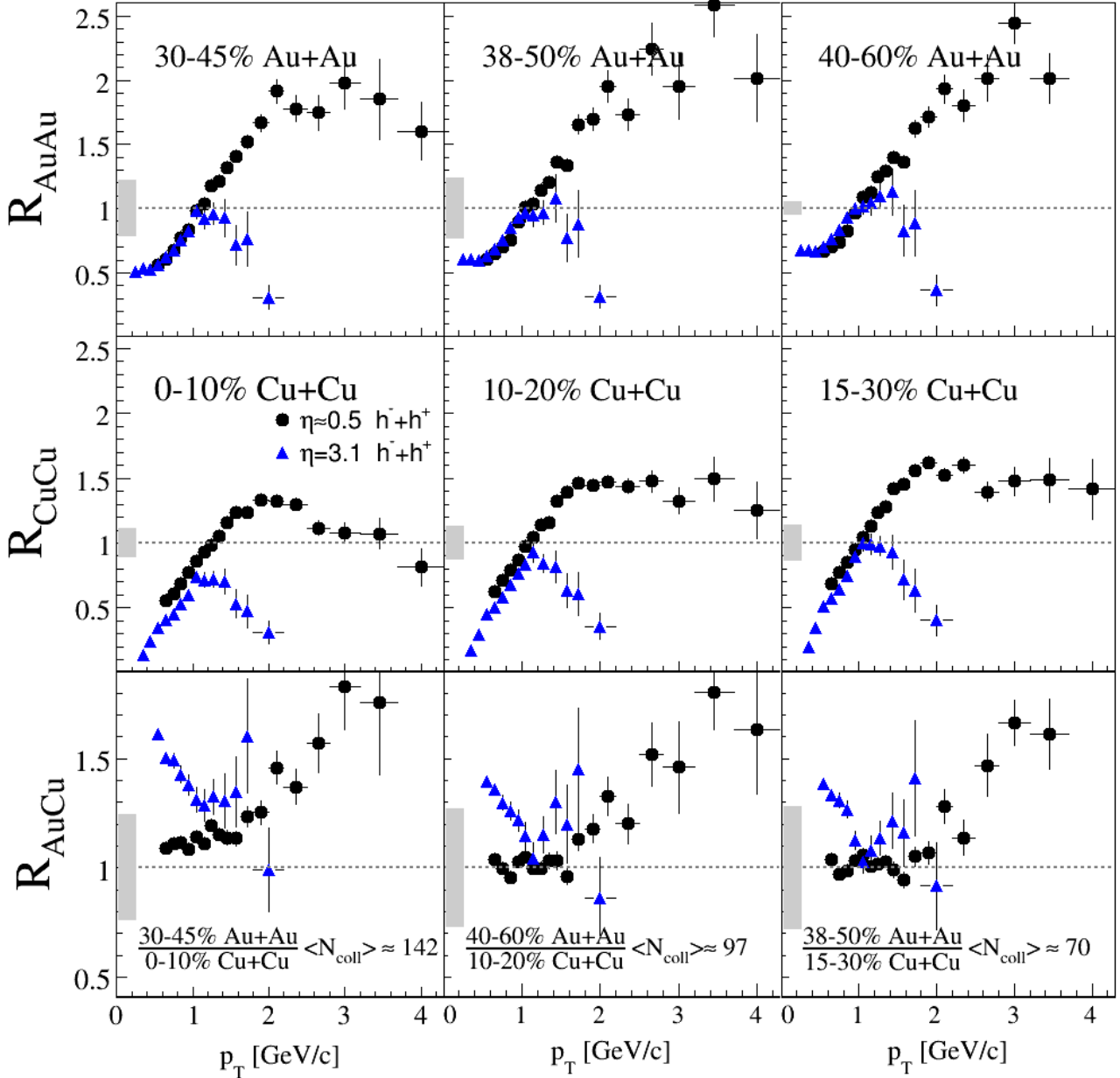
Figure 8.6: The figure shows R_{AA} for Au+Au and Cu+Cu collisions with the same average number of binary collisions in the top and middle row, respectively. The bottom row shows the ratio of Au+Au spectra to Cu+Cu spectra, R_{AuCu}, used in the R_{AA} in the panel directly above. The gray band around $R_{AA} = 1$ shows the uncertainty on the normalisation originating from the numbers found in table 8.1. The gray band around $R_{AuCu} = 1$, does not explicitly reflect the uncertainty on the normalisation, as the spectra are not scaled with $\langle N_{coll} \rangle$. But the $\langle N_{coll} \rangle$calculation was used to determine the centrality selections containing the same $\langle N_{coll} \rangle$. For $\langle N_{coll} \rangle = 142$, the midrapidity ratio is constant at 1.1 for $p_T < 2 \, GeV/c$. The ratio with the other two $\langle N_{coll} \rangle$ values is constant at 1 in the same p_T range. The Au+Au collisions shows enhancement above 2 GeV/c relative to Cu+Cu collisions.
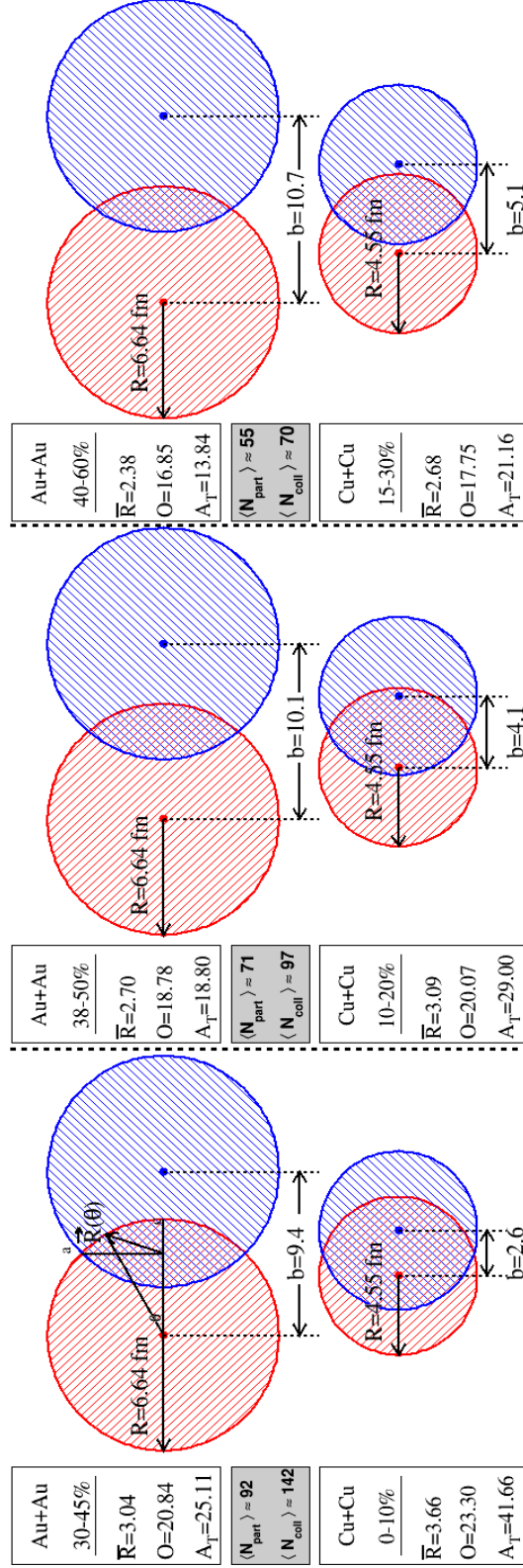
Figure 8.7: The figure shows the collisions geometry in Au+Au and Cu+Cu collisions for equal number of participants. The two collision systems are shown in pairs where they have the same $\langle N_{\text{coll}} \rangle$ and $\langle N_{\text{part}} \rangle$. The impact parameters b are taken from table 8.1. The average length of $R(\theta)$ between point a and point c, shown in the left panel, gives the average distance to the surface from the center point of the overlapping region: $\bar{R}_\theta = \theta_m^{-1} \int_0^{\theta_m} R(\theta) d\theta$, where $R(\theta) = \sqrt{R^2 + (b/2)^2} - Rb\cos\theta$, and $\theta_m = \cos^{-1}(\frac{b}{2R})$. The circumference of the overlap region is $O = 4R \cdot \theta_m$ and the transverse area is $A_T = 4 \cdot (\pi R^2 \cdot \theta_m/2\pi - b/2 \cdot \sqrt{R^2 - (b/2)^2}/2)$. The biggest change in the $\bar{R}(\theta)$ variables occurs for Cu+Cu collisions between 0–10% and 15–30%.
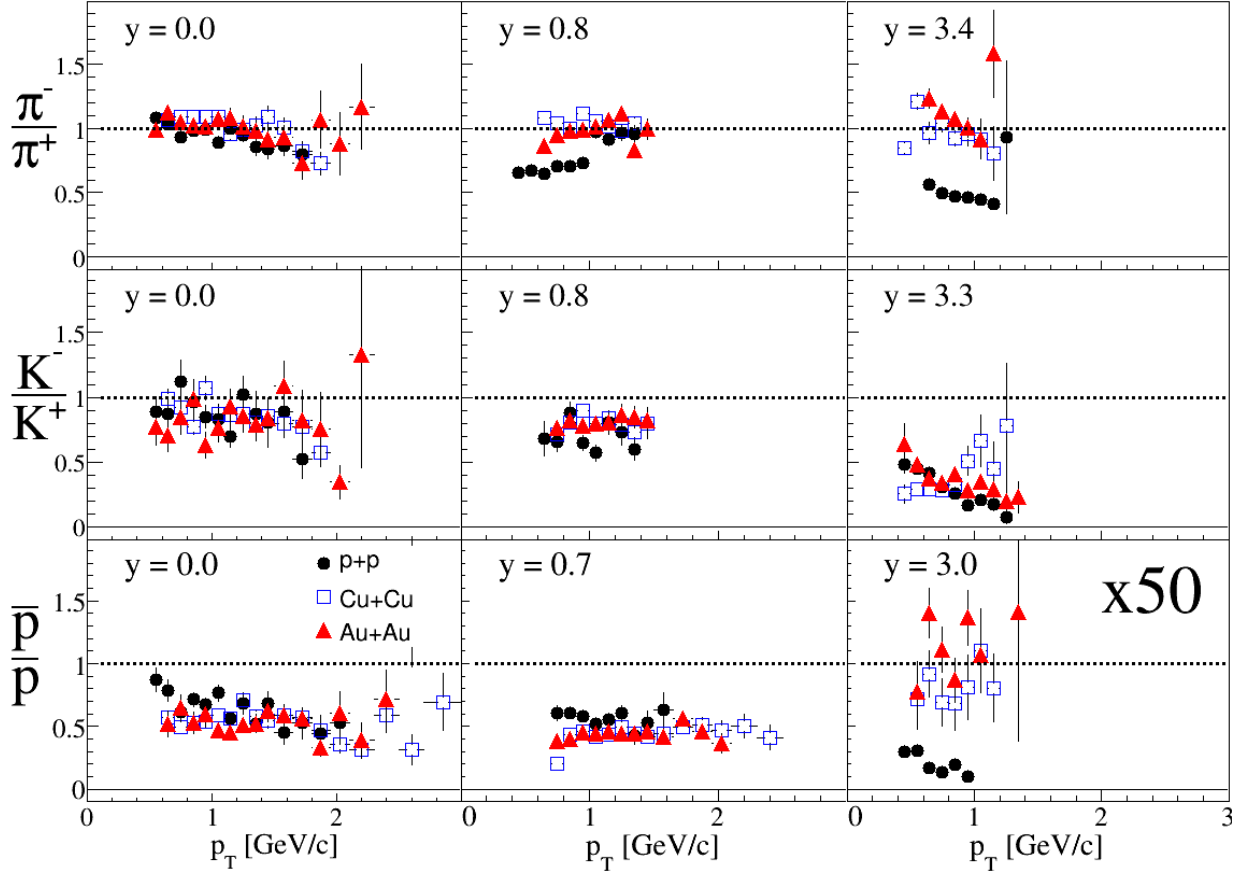
Figure 8.8: The figure shows the like particle ratios in Au+Au, Cu+Cu, and $p+p$ collisions at $\sqrt{s_{\mathrm{NN}}} = 62.4$ GeV. The figure shows that the K^-/K^+ ratios are the same for all three collision systems, from mid to forward rapidity. The same is seen in the $\bar{p}/p$ ratio. The π^-/π^+ is ~ 1 for Au+Au and Cu+Cu collisions from mid to forward rapidity. The $p+p$ collisions does not show this. The ratio is decreasing with rapidity. It is ~ 1 at $y = 0.0$, ~ 0.7 at $y = 0.8$, and ~ 0.5 at $y = 3.4$. The $\bar{p}/p$ ratio at $y = 3.0$ has been scaled up by 50 for clarity.

8.4   Particle ratios

The like–particle ratios are given in figure 8.8. The particle ratios, for all particle species and at all rapidities, as the same in both Cu+Cu and in Au+Au collisions. The kaon ratio in Cu+Cu collisions is equal to that in heavy ion collisions. The same is true for (anti–) protons at mid rapidity. The $p + p$ pion ratio deviates from the heavy ion collisions at $y = 0.8$ and at $y = 3.4$. The pion ratio in the heavy ion collisions is 1 at the three rapidities, while it drops from 1 at $y = 0.0$ to ~ 0.4 at $y = 3.4$ in $p+p$ collisions. The $\bar{p}/p$ ratio has the approximate same value for all three collision system at midrapidity, while the differ at forward rapidity. For $p + p$ collisions the ratio is ~ 0.004 and for Cu+Cu and Au+Au collisions it is about 5 times higher ~ 0.02.
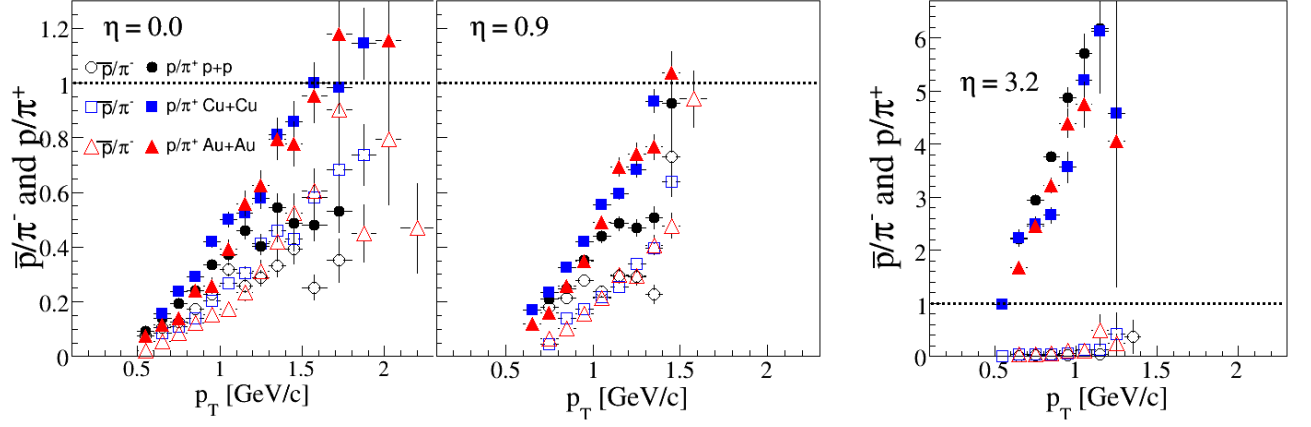
Figure 8.9: The figure shows the 0–10% central p/π^+ (solid symbols) and $\bar{p}/\pi^-$ (open symbols) ratios. At midrapidity, the p/π^+ ratio in Cu+Cu and Au+Au collisions (squares and triangles, respectively) are steeper than the ratio in $p + p$ collisions. The particle ratio is steeper at all three rapidities than the antiparticle ratio. At $\eta = 3.2$, $\bar{p}/\pi^- = 0.03$.

8.5 Unlike particle ratios

The parton recombination model proposed by R. C. Hwa and C. B. Yang in [65, 66] makes a prediction for the p/π^+ ratio at $\eta = 3.2$. This is peculiar, as the appropriate invariant quantity to use is rapidity. The p/π^+ ratio is shown in figure 8.9, at $\eta = 3.2$, which corresponds to $y = 3.0$ for the protons and $y = 3.4$ for the pions. The particle ratio (solid symbols) at midrapidity is steeper than the antiparticle ratio (open symbols). The particle ratio for Cu+Cu and Au+Au collisions (squares and triangles, respectively) is steeper than the particle ratio for $p + p$ collisions (circles). The ratios for $p + p$ collisions saturates as p_{T} approaches 1.5 GeV/c, while the heavy ions does not indicate such a saturation.

The forward results are very different compared to the midrapidity results. Here the protons dominate the particle production, for the three collision systems. The antiparticle ratio is ~ 0.03 in the covered p_{T} range. The p/π^+ ratio slope is linear in the p_{T} range covered by the statistics, but is much steeper than predicted by R. C. Hwa and C. B. Yang in [66]. At $p_{\mathrm{T}} \sim 1$ GeV/c, the ratio is $\sim 3 - 4$, where the prediction was ~ 1.

Chapter 9

Conclusion

The inclusive charged hadron nuclear modification factor, R_{AA}, at midrapidity in central Au+Au collisions at $\sqrt{s_{\mathrm{NN}}} = 62.4$ GeV (figure 8.2) shows that the competing effects of enhancement and suppression cancel. From the evolution of the R_{AA} from SPS to RHIC top energy, it is evident that the onset of suppression happens in the vicinity of $\sqrt{s_{\mathrm{NN}}} = 62.4$ GeV collision energy. The interpolation in figure 8.4 indicates that it happens at $\sqrt{s_{\mathrm{NN}}} \sim 50$ GeV. The partons produced in Cu+Cu collisions at $\sqrt{s_{\mathrm{NN}}} = 62.4$ GeV experience less suppression compared to Au+Au collisions at the same energy. Except for the most central collisions, high p_{T} "Cronin" enhancement was observed in both Cu+Cu and Au+Au collisions. The suppression/enhancement pattern is very different at SPS and RHIC top energy, $\sqrt{s_{\mathrm{NN}}} = 17.3$ GeV and $\sqrt{s_{\mathrm{NN}}} = 200$ GeV, respectively. The R_{AA} at SPS showed a stronger "Cronin" enhancement than seen in $\sqrt{s_{\mathrm{NN}}} = 62.4$ GeV. At RHIC top energy, high p_{T} suppression was observed for charged particles at all rapidities.

The behaviour of the inclusive charged hadron R_{AA} for both Cu+Cu and Au+Au collisions shows binary and participant scaling for p_{T} below 2 GeV/c, when comparing Cu+Cu and Au+Au collisions with the same $\langle N_{\mathrm{coll}} \rangle$ and $\langle N_{\mathrm{part}} \rangle$ (figure 8.6). Thus the created matter in Cu+Cu and Au+Au is the same at this energy. The high p_{T} particles, $p_{\mathrm{T}} > 2$ GeV/c, originating from initial hard parton–parton scattering, are less suppressed when the parton travels a shorter distance in the created matter. This was demonstrated in the illustration shown in figure 8.7.

The most peripheral collisions shows show a large "Cronin" enhancement at midrapidity, with a value close to that seen at the SPS energies. This is seen in both collisions system. Thus created matter has properties similar to the matter created at SPS, and that it is not a QGP. Alternatively, the size of the QGP matter is too small to affect the high p_{T} particles, even if it has the properties to quench high p_{T} partons. The enhancement in the peripheral collisions is larger than that seen in asymmetric d+Au collisions at $\sqrt{s_{\mathrm{NN}}} = 200$ GeV, shown in figure 4.4.

The forward rapidity results are the most remarkable and unique results. The forward rapidity has previously been scanned by the BRAHMS experiment at RHIC top energy, as shown in figure 4.5. These results shows no dependence on pseudorapidity for central collisions. A pseudorapidity dependence emerge when the collisions become more peripheral. The peripheral collisions show less suppression and more enhancement. In $\sqrt{s_{\mathrm{NN}}} = 62.4$ GeV collisions a strong pseudorapidity dependence is seen for all centralities. The forward rapidity high p_{T} particles are strongly suppressed while at midrapidity they are slightly to strongly enhanced. This big difference between the $\sqrt{s_{\mathrm{NN}}} = 62.4$

GeV and 200 GeV forward rapidity results is related to the rapidity shift in the fragmentation region between these two collision energies. The forward results at $y = 3.1$ is within 1 unit from beam rapidity. Figure 7.7 shows that this is inside the fragmentation region in $p + p$ and Au+Au collisions at $\sqrt{s_{\mathrm{NN}}} = 62.4$ GeV, but not in $\sqrt{s_{\mathrm{NN}}} = 200$ GeV collisions. The created matter in the fragmentation region is very different from the created at midrapidity in $\sqrt{s_{\mathrm{NN}}} = 62.4$ GeV collisions.

The identified particle spectra provide an incite into the chemistry of the created matter. 6 particle species where identified in both collision systems. The PID R_{AA} shows that the mesons and baryons contribute differently to the unidentified particle R_{AA}. A Au+Au collision creates a larger volume of matter than a Cu+Cu collision. The larger Au+Au collision system equally increases the suppression of all the particle species, compared to Cu+Cu collisions. The identified baryons, p and $\bar{p}$, shows "Cronin" enhancement in both Cu+Cu and Au+Au collisions at midrapidity. The R_{AA} for kaons shows a balance of the enhancement and the suppression. The lighter pions shows the same behaviour as the kaons at mid rapidity but were more suppressed.

Again, remarkable results were seen when comparing the forward rapidity to midrapidity. The kaon R_{AA} did not change, showing that production of kaons in heavy ion collisions scales with the production of kaons in $p + p$ collisions. The pions shows charge dependence at forward rapidity, π^+ being suppressed while π^- showing binary scaling or enhancement. The protons also show strong suppression at forward rapidity in both collision systems. The fragmentation region for the $p + p$ collisions at $\sqrt{s_{\mathrm{NN}}} = 62.4$ GeV and 200 GeV is shown in figure 7.7. The fragmentation peak for $p + p$ collisions at $\sqrt{s_{\mathrm{NN}}} = 200$ GeV is at $y \approx 4.5$, close to the Au+Au fragmentation peak. The fragmentation region in $p + p$ collisions at $\sqrt{s_{\mathrm{NN}}} = 62.4$ GeV is at $y \approx 3.5$, very different from Au+Au collisions at the same energy. This shows that relatively more of the net–protons in $p + p$ collisions are transfered into the fragmentation region compared to heavy ion collisions. They suffer a higher rapidity loss compared to heavy ion collisions at the same energy, thus creating a suppressed proton R_{AA}. The suppression is therefore not a final state effect at forward rapidity.

This picture, with no final state effects at forward rapidity, is also consistent with the observation of R_{AA} for pions an kaons. The kaons must be produced in the collision, i.e. s and $\bar{s}$ quarks must both be produced. $\langle N_{\mathrm{coll}} \rangle$ scaling is seen for the high p_{T} kaons in both collision systems, thus there are no final state effects in the fragmentation region. The R_{AA} for the π^+ show suppression and the π^- show no suppression. This could come from the valence quark flavour abundance in the initial state. A proton is made of uud quarks, which are fermions. Thus it is more energy efficient to produce a $d\,\bar{d}$ pair than a $u\,\bar{u}$ pair in a $p + p$ collision, as there are more low energy quantum number states available for the d quark in such a Fermi gas. This makes π^+ $(u\bar{d})$ production higher than π^- $(\bar{u}d)$. This is seen in the top, right panel of figure 8.8 where the π^-/π^+ ratio is ~ 0.5. The ^{63}Cu and ^{197}Au also contains a large number of neutrons (udd), 34 and 118, respectively, which results in roughly equal amounts of u and d valence quarks $(u/d = 0.95$ and 0.88 in Cu and Au, respectively). This makes the production of $d\,\bar{d}$ and $u\,\bar{u}$ equally energy efficient. This is consistent with the π^-/π^+ ratios in Cu+Cu and Au+Au collisions seen in figure 8.8.

The $\sqrt{s_{\mathrm{NN}}} = 62.4$ GeV results presented points towards a created matter at midrapidity. The matter not as strongly interacting as the matter created in $\sqrt{s_{\mathrm{NN}}} = 200$ GeV collisions. The created matter at $\sqrt{s_{\mathrm{NN}}} = 62.4$ GeV imposes a higher degree of suppression than the matter created in heavy ion collisions at the SPS. Furthermore, the observation at forward rapidity show that the matter created in this part of phase space is dramatically different from the matter observed at mid rapidity. The created matter in Au+Au and Cu+Cu collisions also show geometric scaling behaviour when

$\langle N_{\mathrm{part}} \rangle$ and $\langle N_{\mathrm{coll}} \rangle$ are the same in the low p_{T} part of the spectra. This is not seen in the high p_{T} region and is due to a lower average distance the parton has to travel in the created matter from the Au+Au collision compared to the Cu+Cu collision (see numbers in figure 8.7). To get a complete picture and understanding of collisions at $\sqrt{s_{\mathrm{NN}}} = 62.4$ GeV the rapidity densities must be calculated for all particle species in the three collision systems.

Appendix A

Manual for BRAHMS data reconstruction and analysis

A.1 BANAPP program options

In the following paragraphs the programs are described and their list of options shown. In addition to the options shown, `--version` and `--verbose` is available. Options written with bold are mandatory. Default value -1111 is the BRAHMS definition of an unphysical value.

A.1.1 Options in *dst2tree*

Available options are listed in table A.1 below.

	Option	Description	Default
-a	**–add-run**	Add this run to analysis	-1
	–batch	Run in batch mode	false
-b	**–begin-run**	Begin run range	0
-d	**–dst-prod**	DST production number	-1
	–dst-vers	DST version no, -1111 means latest available	-1111
-e	**–end-run**	End run range	0
	–event	Number of events pr setting	2147483647
	–file	Force analysis of file (no checking and wild cards allowed)	
	–fstrk-vtx	Recalculate FS track vtx X,Y at BBC vtx Z	false
-h	–help	Show this help	
	–inel-cc	Get Inel and CC vertex in tree	false
-i	–input-dir	DST input directory	
	–mass2	# slices in PID m^2 histo (0 is NO slicing/fitting)	10
		table A.1 continued on next page...	

111

...table A.1 continued from previous page			
	Option	Description	Default
-C	–max-cent	Select maximum centrality in %	100
-c	–min-cent	Select minimum centrality in %	0
-O	–output-base	BASIS for output filenames	tree
-o	–output-dir	Output directory for all files	
	–raw-mult	Get the "raw" multiplicity	false
-r	–remove-run	Remove this run from run range	
-s	**–spec-set**	Magnetic field current (e.g. 40A1050, or FFS8A427 or FS8A427)	
-t	**–trigger**	Trigger num (1→6) (Remember min bias). 0 is all	0
-l	**–vtxlimit**	Select BBC vtx from -X→+X (in cm)	

Table A.1: Available options for `dst2tree`.

To run the program, the `--spec-set`, `--trigger`, `--vtxlimit` and `--dst-prod` options must be specified. Then either `--begin-run` and `--end-run` or `--add-run` must be specified. All these options are written with bold characters in table A.1. The `--dst-prod` ensures that all the DSTs are from the same production with the highest version number (if `--dst-vers=-1111`). Using `--begin-run` and `--end-run` to set a run range will add all runs within that range, with the requirement that they have the specified spectrometer setting, all the required triggers and their status field set to "Good", to the *micro-tree*. The *micro-tree* is either a *MrsTree*, a *FfsTree* or *FsTree*, defined by the `--spec-set` option.

The event loop is done by the `DstLoopModule`. The module accepts all events that have:

1. at least one of the specified triggers.

2. **BBC** vertex within the specified limits. The `--inel-cc` option must be given for $p + p$ analysis, to ensure usage of the **CC** vertex. This vertex will then also get saved in the micro-tree.

3. centrality within specified centrality range. For $p + p$ analysis, the `--raw-mult` options has to be given, to turn this checking off.

All tracks in the accepted event, in the specified spectrometer, are saved if the have a their "magnet status" flag set to "good". This means that the track did not have a trajectory that intersected the walls inside the magnet.

A.1.2   Options in *generateMaps*

Available options are listed in table A.2 below.

	Option	Description	Default
	–D1-fidX	Closest acceptable distance to D1 magnet walls in X	0
	–D1-fidY	Closest acceptable distance to D1 magnet walls in Y [The above D1 options are also available for D2, D3, D4, and D5]	0
	–T1-fidbhiX	Highest acceptable X on back of T1	-1111
	–T1-fidbhiY	Highest acceptable Y on back of T1	-1111
	–T1-fidblowX	Lowest acceptable X on back of T1	-1111
	–T1-fidblowY	Lowest acceptable Y on back of T1	-1111
	–T1-fidfhiX	Highest acceptable X on front of T1	-1111
	–T1-fidfhiY	Highest acceptable Y on front of T1	-1111
	–T1-fidflowX	Lowest acceptable X on front of T1	-1111
	–T1-fidflowY	Lowest acceptable Y on front of T1 [The above T1 options are also available for T2, T3, T4, T5, TPM1 and TPM2]	-1111
	–TOFW-hislat	Last acceptable slat in TOFW	-1
	–TOFW-loslat	First acceptable slat in TOFW [The above TOFW options are also available for TFW2, H1 and H2]	-1
	–MRST0-fidfhiX	Highest acceptable X on front of MRST0	-1111
	–MRST0-fidfhiY	Highest acceptable Y on front of MRST0	-1111
	–MRST0-fidflowX	Lowest acceptable X on front of MRST0	-1111
	–MRST0-fidflowY	Lowest acceptable Y on front of MRST0	-1111
	–Rich-fidhighX	Highest acceptable X on front of Rich	-1111
	–Rich-fidhighY	Highest acceptable Y on front of Rich	-1111
	–Rich-fidlowX	Lowest acceptable X on front of Rich	-1111
	–Rich-fidlowY	Lowest acceptable Y on front of Rich	-1111
	–batch	Running in batch mode	false
	–dpt	Transverse momentum bin width	0.05
	–dy	Rapidity bin width	0.01
-h	–help	Show this help	1.5
-e	–maxError	Maximum relative average error on pion map	
-o	**–outputfile**	Output file name	
	–pbeam	Beam momentum for Xf calculation	100
-I	–pidmap	Generate Pid maps	true
	–pmax	Maximum P in calculation	40
	–ptmax	Maximum Pt in calculation	7
-R	–rich	Require Rich in the acceptance map	false
-r	**–run**	Run number	-1
-s	**–spectrometer**	Spectrometer (FFS,FS,MRS,MRS2,Run3MRS)	
-d	–vtxbinwidth	Width of vertex bins	5

	Option	Description	Default
. . . table A.2 continued from previous page			
	Option	Description	Default
-Z	–vtxzmax	Max. vertex z	20
-z	–vtxzmin	Min. vertex z	-20
-X	–xfptmap	Generate xf vs Pt map	false
	–ymax	maximum rapidity	4
	–ymin	Minimum rapidity	-0.5

Table A.2: Available options for `generateMaps`.

The option given with bold text in table A.2 are mandatory: `--run --spectrometer` and `--output-file`. The `--spectrometer` option only takes the predefined values shown. `MRS2` means including the **TFW2** and `run3MRS` means including a track trigger slat for the MRS spectrometer. The default values for the other options are usually set to reasonable values, but should always be reviewed for any analysis. It is therefore common to specify more options: a fiducial cut on the last and/or first detector in the spectrometer, a fiducial cut in the magnet(s), minimum and maximum vertex position, a vertex bin width and/or the binning and the axis limits of the histograms. Making too fine binning in the histograms will consume a lot of computer memory.

A.1.3   Usage of *m2fitter*

The `m2fitter` program requires only one argument, a *micro-tree* file generated by `dst2tree`. The program uses the *GUI* classes `FitWidget` and `FitPidPanel`. The simultaneous fitting of 3 functions, and acquiring the points to fit the functions to, is done by the classes `FitM2Simul` and `M2VsPSlicer`, respectively. *dst2tree* will not make simultaneous fits, as these usually need fine tuning of the fit parameter seeds. Running *m2fitter* will extract the m^2 vs p histograms from the input *micro-tree*, for each of the TOFs. The number of slices can then be tuned to utilise the statistics, as described in the paragraph about `M2VsPSlicer` in section 6.4.5. One standard deviation points to the mean m^2 for each particle specie can then be fitted. Starting with individual fits, one can extract good seeds for the simultaneous fitting of the pion, kaon, and (anti–) proton functions.

A.1.4   Options in *hadronAnalyse*

Available options are listed in table A.3 below.

	Option	Description	Default
	–acc-trk-vtxZ	Track vertex Z for acceptance map, no global vtx required for track	false
	–cent-bins	String with centrality bins	0-10,. . .
-D	–dy-sigma	# sigmas in TOF-track dy	3
	–effic	Name of directory with efficiency files or file	
		table A.3 continued on next page. . .	

	Option	Description	Default
	...table A.3 continued from previous page		
	Option	Description	Default
	–effic-bn	Base name of histogram in the efficiency file	
	–track-eff	Custom tracking efficiency formula, momentum dependent	
-G	–geant-chi	Chi square cut used on global matching of tracks (integer)	4
-C	–track-chi	Chi Square Formula for FS track cut (it's multipiled by -G option)	
-g	–geant-sim	Directory with the geant simulation correction files	
	–hadron-cor	Assume all hadrons are pions and apply pion geantcorrection	false
-h	–help	Show this help	
-i	**–input-tree**	Input tree	
-m	**–map-file**	Map file name	
	–mb-trig	The minumim bias trigger is BBC (1) for cent< 30 and ZDC (4) elsewhere if this option is not set	-1
-A	**–min-acc**	Relative Minimum acc value (remove acc edges)	-1
-e	**–min-eta**	Minimum hadron eta cut	-1
-E	**–max-eta**	Maximum hadron eta cut	-1
	–min-pi-rap	Minimum pion rapidity cut	-1
	–max-pi-rap	Maximum pion rapidity cut. [The above options are also available for kaon (k), proton (p) and deuteron (d).]	-1
	–min-vtx	Minimum value for the BBC vertex (-1 means use accmap)	-1
	–max-vtx	Maximum value for the BBC vertex (-1 means use accmap)	-1
-n	–nevents	Number of events	2147483647
	–no-ds	Do not check for dead slats in the TOF when doing PID	false
-o	**–output-file**	Output file name	spectra.root
-p	–pid	PID with detector (TOFW, TFW2 or MRS) (H1, H2, RICH, or FS)	
-P	–pid-sigma	# sigmas in PID functions/cuts	3
	–pt-bins	String with p_{T} bin limits, or on form $p_{\text{T}}^{min} : p_{\text{T}}^{max} : dp_{\text{T}}$	0:7:0.1
-r	–remove	Don't analyse runs listed in this text file	
	–rich-pi-cut	Max offset from pion RICH radius cut function (in cm)	0.5
	–rich-pi-func	Custom pion RICH radius cut function vs p [The above RICH options are also available for tof1 (TOFW/H1) and tof2 (TFW2/H2), with PIDs equal to kaon (k), proton (p) and deuteron (d).]	
-s	**–spec**	Spectrometer setting (eg: 90A1050 or FFS8B861 or FS8B861)	
-t	**–trk-trig**	Trigger for the tracks	-1
-L	–vtx-sigma	# sigmas for eliptic cut on vertex (or single variable: add X, Y or Z after)	4
		table A.3 continued on next page...	

...*table A.3 continued from previous page*		
Option	Description	Default
–vtxZ-method	Which detector to use for vtxZ (BBC, ZDC, INEL, CC)	BBC

Table A.3: Available options for `hadronAnalyse`.

There are a number of options that must be specified to run this program. These options are written in bold. The following list of options are required in a hadron analysis: `--spec`, `--input-tree`, `--map-file`, `--output-file`, `--min-acc`, `--trk-trig`, `--mb-trig`, `--min-eta` and `--max-eta`. In addition `--geant-sim`, `--geant-chi`, `--track-chi`, `--min-pi/k/p-rap`, `--max-pi/k/p-rap`, and `--pid` must be specified when doing PID analysis. These options are indicated in cursive.

If hadrons should be corrected with a pion multiple scattering, feed down and decay correction, the `--hadron-cor`, `--no-ds`, `--geant-sim`, `--geant-chi`, `--track-chi`, `--min-pi-rap` and `--max-pi-rap` also need to be turned on. Also a common option is to "black list" unusable runs with the `--remove` option. Custom PID functions can also be used in a PID analysis, which will override the function stored in the histograms in the *micro-tree*.

Setting `--cent-bins="0-1200"` is necessary for $p + p$ analysis, as a centrality cut is not used. Another special option that can be used in $p + p$ analysis is `--acc-trk-vtxZ` which turns off checking of the global vertex and use all tracks if the track vertex Z position is inside the required limits. This also disables any elliptical cut on the track vertex relative to the global vertex in the MRS, so `--vtx-sigma` should be set to e.g. "3Y".

A.1.5   Options in *tree2datamap*

Available options are listed in table A.4 below.

	Option	Description	Default
-C	–cent-max	Centrality high cut	20
-c	–cent-min	Centrality low cut	0
-D	–dy-sigma	# sigmas in TOF-track dy	3
-E	**–eff-path**	efficiency db (path name)	
-S	**–eff-suffix**	efficiency db file name suffix (e.g. PSv1 or SJSv1 or NKv1)	PSv1
-e	–event	Number of events	2147483647
-h	–help	Show this help	
-i	**–input-tree**	ROOT input filename	
-m	**–map-file**	Acceptance map file name	
	–max-vtx	Maximum value for the BB vertex (-1 means use accmap)	-1
	–min-vtx	Minimum value for the BB vertex (-1 means use accmap)	-1
	–mb-trig	The minumim bias trigger is BB (1) for cent¡30 and ZDC (4) elsewhere if this option is not set	-1
		table A.4 continued on next page...	

	Option	Description	Default
	...*table A.4 continued from previous page*		
	Option	Description	Default
-o	**–output-base**	ROOT output filename	
-p	**–pid**	PID with detector (TOFW, TFW2 or MRS) (H1, H2, RICH, or FS)	FS
-P	–pid-sigma	# sigmas in PID functions/cuts	3
-r	–remove	Don't analyse runs listed in this text file	
-s	**–spec**	Spectrometer setting (eg: 90A1050 or FFS8B861 or FS8B861)	
-t	**–trk-trig**	Use this trigger in analysis	2
-v	–var-requ	variable to use for efficiency (use CX for AA and XA for pp)	CX
-L	**–vtx-sigma**	# sigmas in 2D vtx cut	3
	–vtxZ-method	Which detector to use for vtxZ (BB, ZDC, INEL, CC)	BB

Table A.4: Available options for `tree2datamap`.

tree2datamap is optimised for low p_{T} physics with PID. The program builds two sets of histograms. The first histograms are data maps in p_{T}–y space, one for each particle specie and vertex bin. Correspondingly histogram with weights are built. The weights are the product of the acceptance map, multiple scattering, feed down, decay, tracking efficiency and PID efficiency corrections. The maps are all made with the same binning as defined by the acceptance maps. The ROOT macros in the sub directories are used to build the spectra, through the `SpectraObject`. The cuts and normalisation in (pseudo-) rapidity in done at this stage. The macros also handles merging of different magnetic field settings. Since the acceptance maps are made with constant bin sizes, this method does not support variable size p_{T} bins.

The mandatory options for *tree2datamap* are `--spec`, `--input-tree`, `--map-file`, `--trk-trig`, `--vtx- sigma`, `--eff-path`, `--eff-suffix` and `--output-base`. The fiducial cuts found in the acceptance map file is applied to all particles in addition to the cuts specified by the options.

A.2 Diagnostic histograms in the *micro-trees*

Each *micro-tree* has a set of histograms saved in the same file. These are summary histograms for the entire setting/*micro-tree* and run by run histograms. The histograms are made by the selector classes. The histograms are stored in subdirectories in the *micro-tree* ROOT file.

- The Global directory is created by the `GlobalSelector` class and contains 2 subdirectories: `/Global/Vertex/` and `Global/Centrality/`.

- The Tracks is created by the `TrackSelector` class and contains 4 subdirectories: `/Tracks/AvgTracks/`, `/Tracks/Magnets/`, `/Tracks/TrackChambers/` and `/Tracks/TrackToVtx/`.

- The TOFW, TFW2, H1 and/or H2 directory are created by the `TofSelector` class and contains 4 subdirectories: `/TOF/InverseBeta/`, `/TOF/Mass2/`, `/TOF/SlatHits/` and `/TOF/TrackHits/`.

- The `/C1/`, `C4` directory is created by the `CSelector` class.

- The `/RICH/` directory is created by the `RichSelector` class.

A.2.1   Global event characteristic diagnostic histograms

Inside the `/Global/Vertex/` and the `/Global/Centrality/` directories the histograms shown in figure A.1, A.2 and 5.8 are found. These are the most important ones and should be examined carefully when doing an analysis. In additions thee is a `Run/` directory in each of the subdirectories that contains the same histogram on a run by run basis.
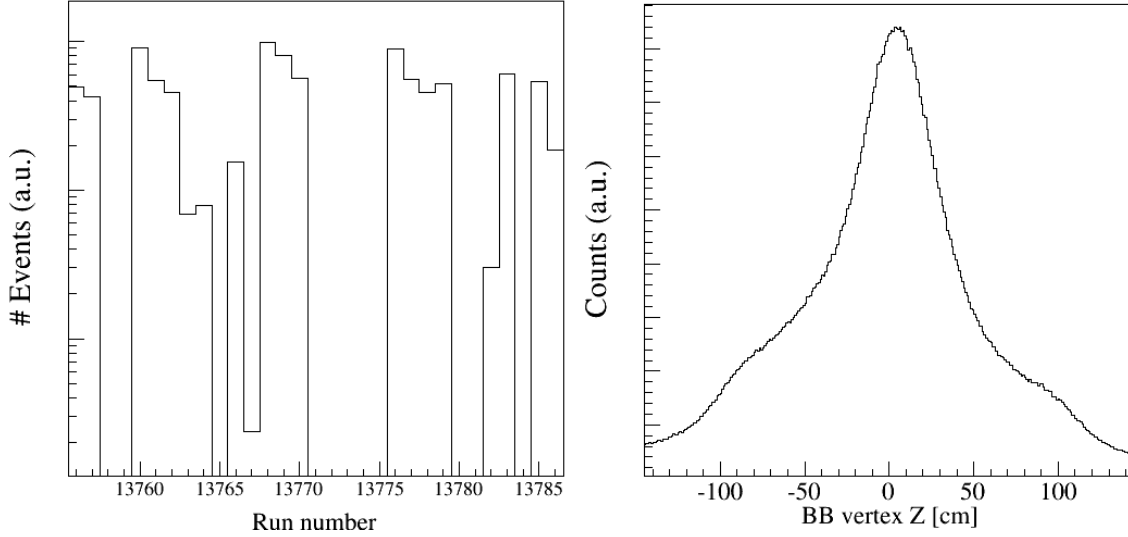
Figure A.1: The left panel shows the number of minimum bias events in each run analysed in this *micro-tree*. Notice the logarithmic scale. The right panel shows the vertex distribution of these events. The beam quality is fairly consistent for all these runs, with most collisions occurring between ±50 cm. The distribution for each individual run is also saved in the *micro-tree*. The data is taken from Cu+Cu collisions at 90°, B-polarity 1/3 magnetic field.

A.2.2   Global track diagnostic histograms

The `/Tracks/AvgTracks/`, `/Tracks/Magnets/`, `/Tracks/TrackChambers/` and `/Tracks/TrackToVtx/` contains the histograms shown in 6.4, A.3, A.4, A.5, A.6, A.7, A.8, A.9, A.10, A.11, and A.12. They also contain subdirectories called `Run/`, which contains the same histograms on a run by run basis. The histograms shown can reveal important information on the status of the detectors during the data taking and the quality of the data. All histogram show that the quality of the data stored in the *micro-tree* is good.
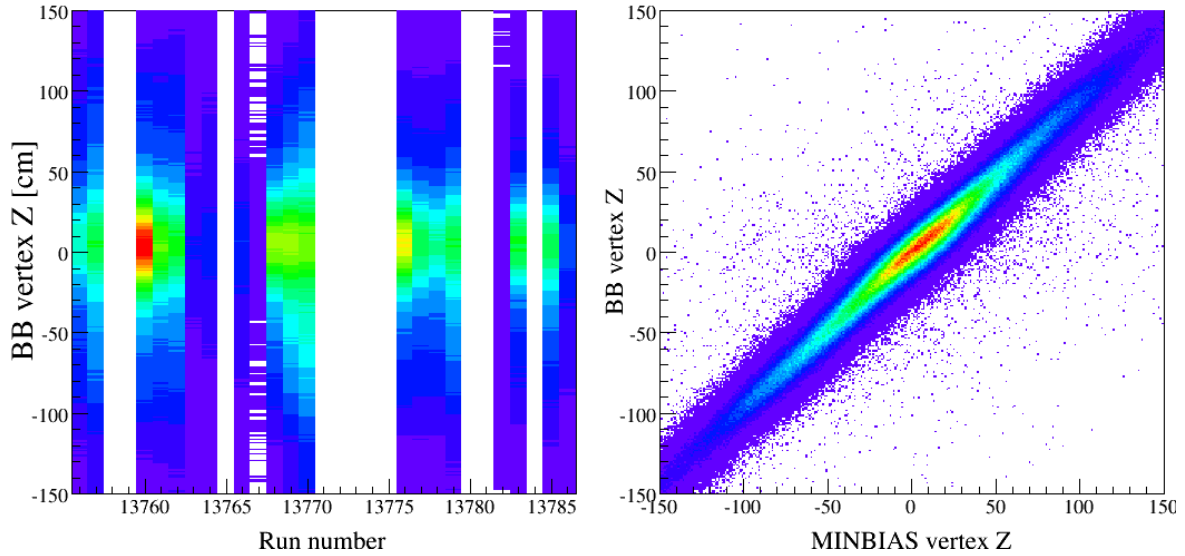
Figure A.2: The left panel shows the BB vertex distribution for each run in this *micro-tree*. The distributions are centered on zero. In runs with offsets larger than 30 cm, most event will be rejected in a particle spectrum analysis, giving runs with poor statistics. The right panel shows the vertex correlation between the BBC and the minimum bias detector, which in this case is the ZDC. All the statistics are shown in this distribution. The same distribution for each individual run is also saved in the *micro-tree*. The data is taken from Cu+Cu collisions at 90°, B-polarity 1/3 magnetic field.
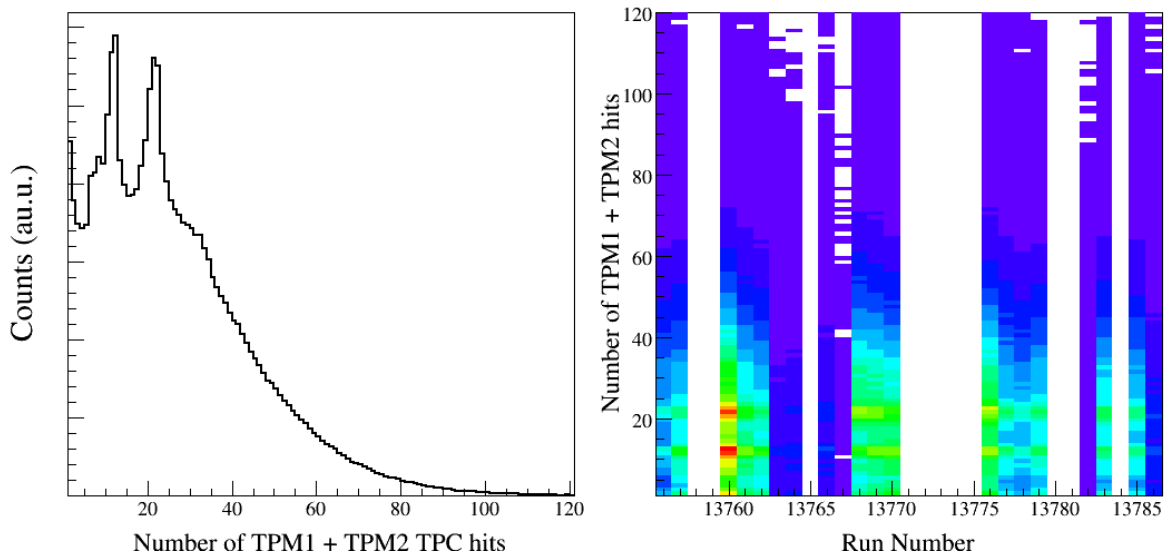
Figure A.3: The two panels show the number of hits/clusters, called the occupancy, in TPM1 and TPM2 combined, for events with at least 1 track. The left panel shows all the events, with a clear 1 track and 2 track peak. The stability of these peaks, run by run is seen the right panel. This indicates that the TPCs had a stable performance during these runs. The data is taken from Cu+Cu collisions at 90°, B-polarity 1/3 magnetic field.
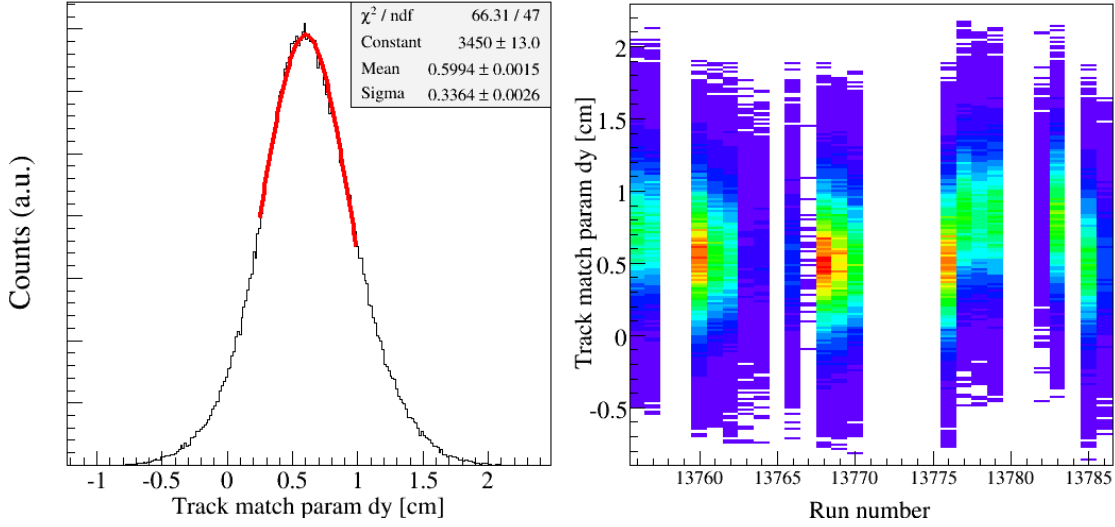
Figure A.4: The left panel shows the difference in the Y position of the projection of the front and back track to the middle of the magnet (see also figure 6.2). The distribution on a run by run basis is shown in the right panel. The centroid moves back and forth with ~ 0.4 cm. The centroid and the width of this distribution is used to determine if a front and back track match up. The figure reveals that the dy distribution must be done on a run by run basis. The data is taken from Cu+Cu collisions at $90°$, B-polarity 1/3 magnetic field.
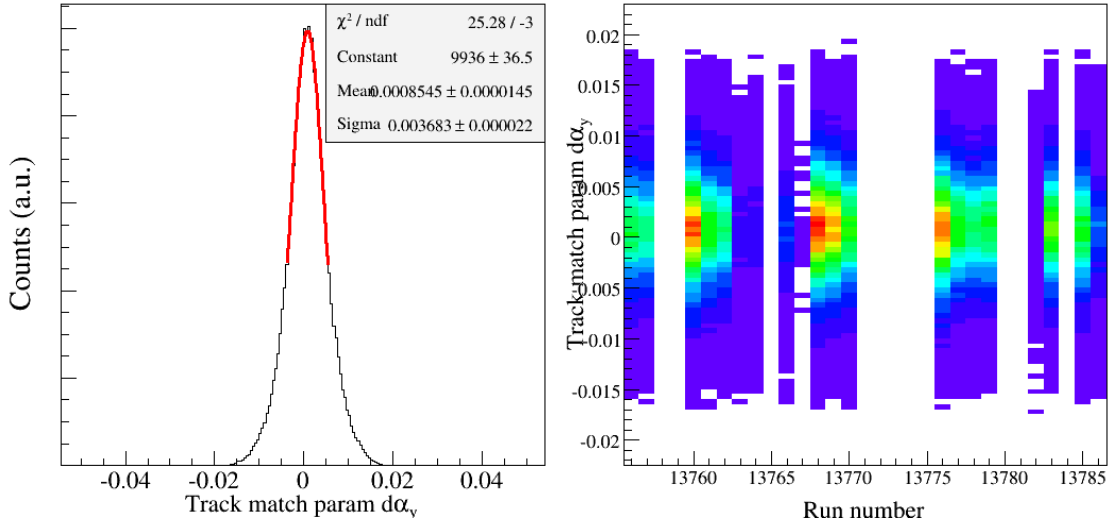
Figure A.5: The left panel shows the difference in the α_y, the difference in angle in the local YZ-plane of the projection of the front and back track to the middle of the magnet, see figure 6.2. The distribution on a run by run basis as shown in the right panel. The width of the distribution changes from run to run. Since the centroid and the width of this distribution is used to determine if a front and back track match up, the $d\alpha_y$ centroid and width must be used on a run by run basis. The data is taken from Cu+Cu $90°$, B-polarity 1/3 magnetic field.
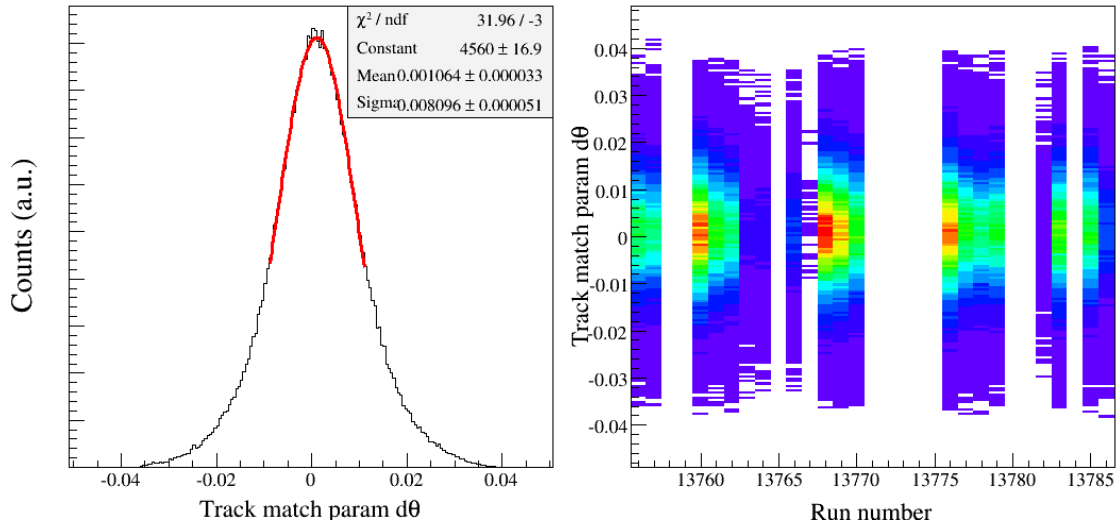
Figure A.6: The left panel shows the difference in the θ, see definition in figure 6.2, of the projection of the front and back track to the middle of the magnet. The distribution on a run by run basis is shown in the right panel. The width and centroid of the distribution could change from run to run. Since the centroid and the width of this distribution is used to determine if a front and back track match up, the $d\theta$ centroid and width must be used on a run by run basis. The data is taken from Cu+Cu collisions at 90°, B-polarity 1/3 magnetic field.
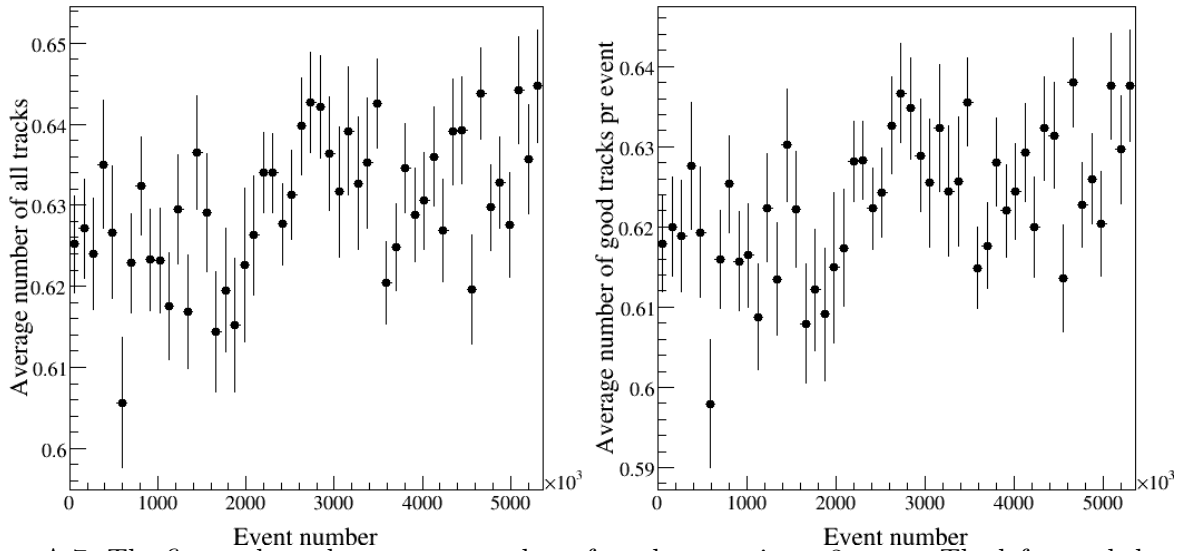
Figure A.7: The figure show the average number of tracks per trigger 3 event. The left panel shows all tracks that were matched after applying the condition in eq. 6.3. The right panel has the additional requirement that the track must not intersect the magnet walls. This changes the average number down by about 0.01. The data is taken from Cu+Cu collisions at 90°, B-polarity 1/3 magnetic field.
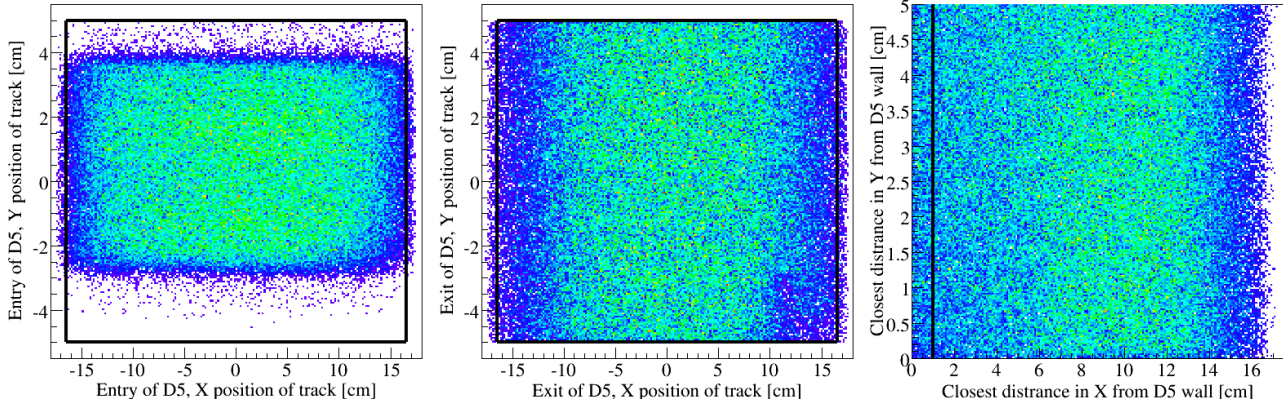
Figure A.8: The left and middle panel of the figure shows the distribution of matched tracks intersecting the entry and exit plane in D5. The solid lines are the fiducial cuts in the magnet. The right panel shows the distribution of the tracks closest distance to the magnet walls. The 1 cm fiducial cut in the X direction in D5 is used to make sure particles does not scatter off the magnet wall. In the FS one can easily detect this through the χ^2 track quality cut, since the χ^2 is calculated from the track vertex position, 5 tracking chambers and the PID detector. The χ^2 in the MRS is only calculated from the track vertex, 2 tracking chambers and the PID detector. The data is taken from Cu+Cu collisions at 90°, B-polarity 1/3 magnetic field.
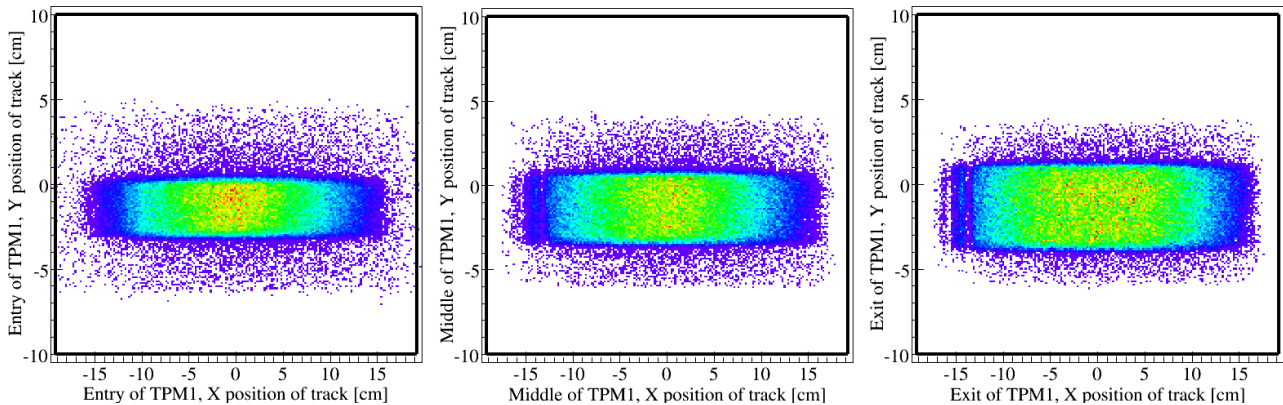
Figure A.9: The figure shows, from left to right, the distribution of matched tracks intersecting the entry, middle and exit plane in TPM1. The solid lines are the physical active volume (which is also the fiducial cuts) of the tracking detector. The data is taken from Cu+Cu collisions at 90°, B-polarity 1/3 magnetic field.
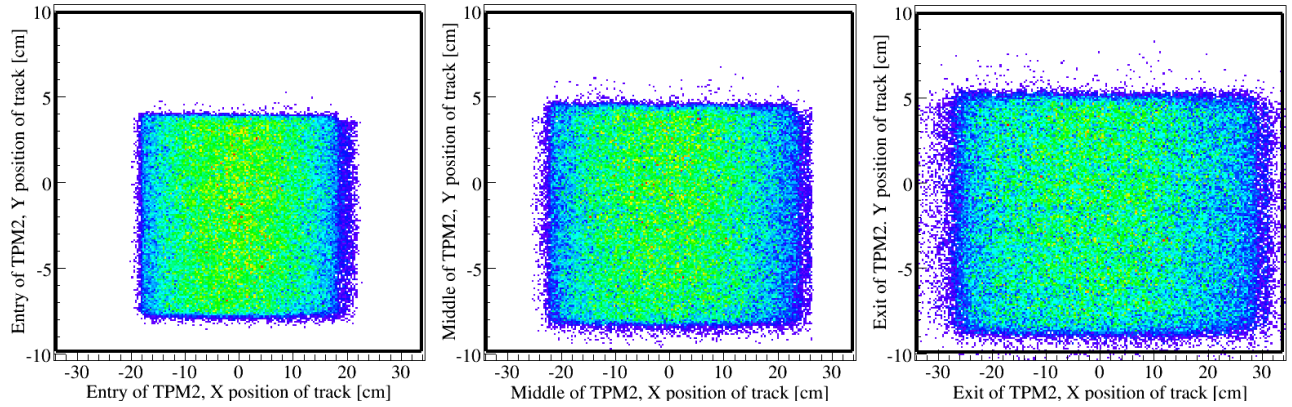
Figure A.10: The figure shows, from left to right, the distribution of matched tracks intersecting the entry, middle and exit plane in TPM2. The solid lines are the physical active volume (which is also the fiducial cuts) of the tracking detector. The data is taken from Cu+Cu collisions at 90°, B-polarity 1/3 magnetic field.
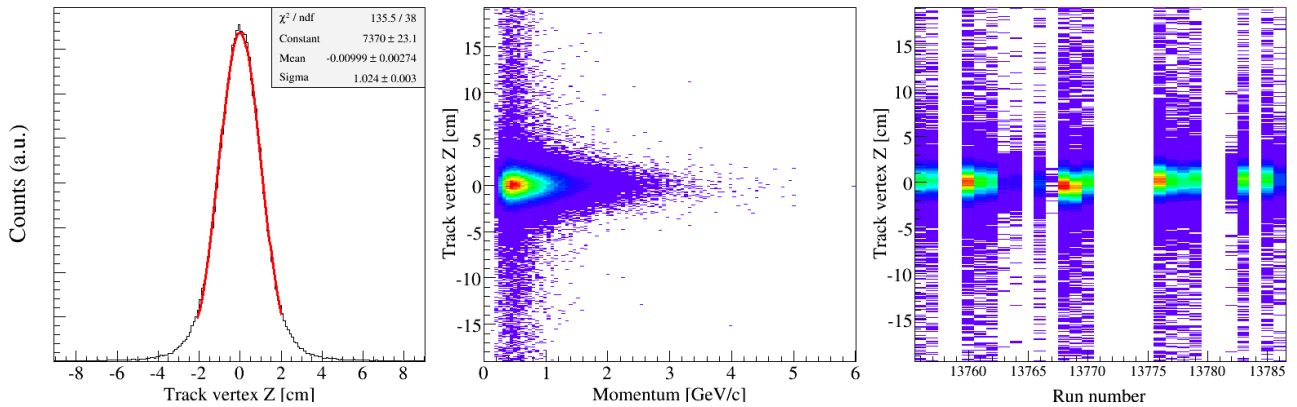
Figure A.11: The panels show the Z position of the intersection of MRS tracks at the MRS vertex plane, global YZ-plane. The left panel shows the difference relative to the BBC vertex Z position, and shows that the vertex resolution has small fluctuations. The middle panel clearly shows that the vertex correlation with the BBC is momentum dependent. The proper way to determine if a track is a primary track, is to include a momentum dependence in eq. 6.3. The right panel shows that in this data sample the centroid and possibly the width of the distribution changes from run to run. The data is taken from Cu+Cu collisions at 90°, B-polarity 1/3 magnetic field.
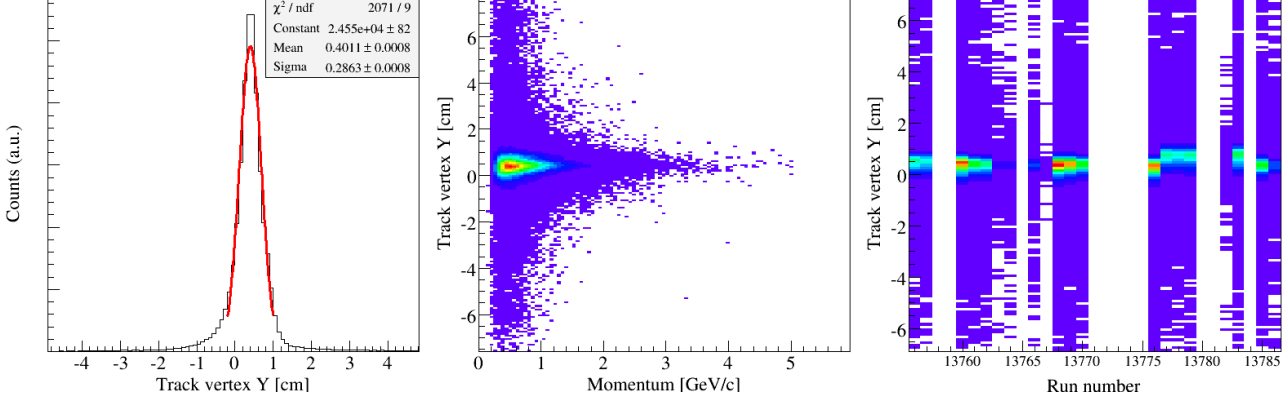
Figure A.12: The panels shows the Y-position of the intersection of MRS tracks at the MRS vertex plane, global YZ-plane. The left panel shows a centroid offset of 0.4 cm, which is due to an offset in the TPM1 drift velocity calibration. The middle panel shows that the width of the distribution is momentum dependent, and that this should be incorporated into the selection of primary tracks, described by eq. 6.3. The right panel shows that the centroid of the distribution changes from run to run. The data is taken from Cu+Cu collisions at 90°, B-polarity 1/3 magnetic field.
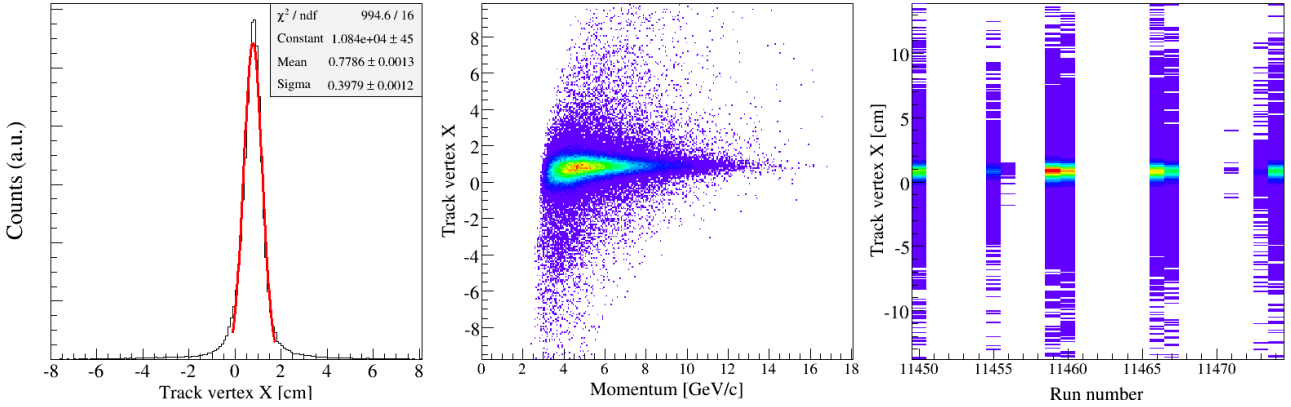
Figure A.13: The panels shows the X-position of the intersection of FS tracks at the FS vertex plane, global XY-plane at the BBC vertex Z position. The left panel shows the X distribution. The middle panel shows that the width of the distribution is momentum dependent, and that this should be incorporated into the selection of primary tracks as described by eq. 6.3. The $X < 0$ side of the distribution has acceptance for higher momentum tracks than the $X > 0$ side. This is a pure geometric effect. The right panel shows that the centroid of the distribution changes from run to run. The data is taken from Au+Au collisions at 4°, B-polarity 1/6 magnetic field.

A.2.3 PID diagnostic histograms

The PID histograms are all highly sensitive to the calibration of the detector, see [96]. There are many steps going into the calibration and small imperfections in the calibration can easily be seen in the following histogram. The Time of flight histogram are all found in the subdirectories `/TOF/InverseBeta/`, `/TOF/Mass2/`, `/TOF/SlatHits/` and `/TOF/TrackHits/`. Each of these also have a subdirectory call `Run/`, where run by run histograms are found. The Čherenkocv detector, only contain a single diagnostics histogram in addition to the PID histogram. C1 and C4 has a energy distribution histogram and the RICH has a distribution of the number of hits per reconstructed ring.
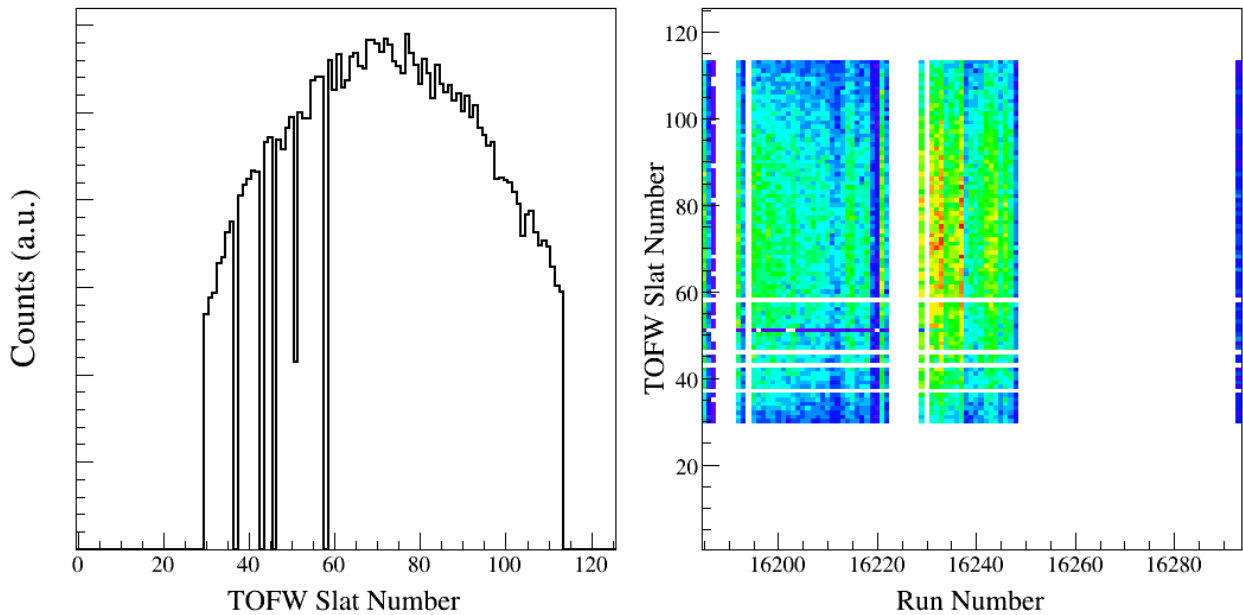
Figure A.14: The left panel in the figure shows the distribution of reconstructed hits in the TOFW slats. The slats without any hits are dead slats. Which means they cannot be used for PID. These slats worked only for triggering. The distribution above is for a low magnetic field setting. A high magnetic field setting will have a flatter distribution, maybe even U-shaped. The right panel shows the same distribution vs the run number. The same dead slats are seen as white stripes. In addition, the figure shows that slat 52 is not working for the first half of runs. This means that this set of runs needs a different geometrical acceptance map that the last half. The data is taken from $p+p$ collisions at $90°$, A-polarity 1/3 magnetic field.
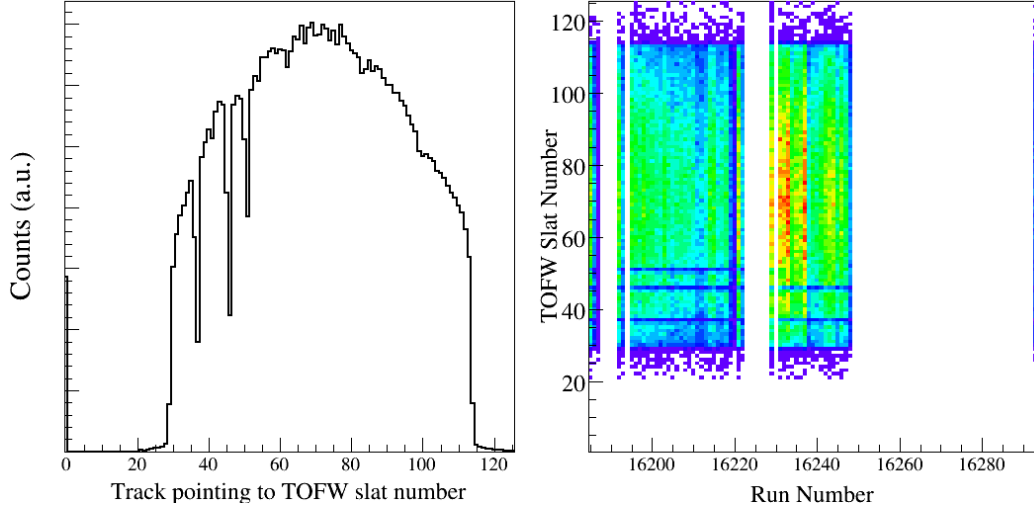
Figure A.15: The figures shows the distribution of projecting global track onto the TOFW. All the data are shown in the left panel, while the right panel shows the the same distribution run by run. The bumps in the distribution indicates a trigger inefficiency for 3 of the slats. These slats appear as dead in figure A.14. These slats must be removed from the geometry when making geometrical acceptance maps. The data is taken from $p + p$ collisions at $90°$, A-polarity 1/3 magnetic field.
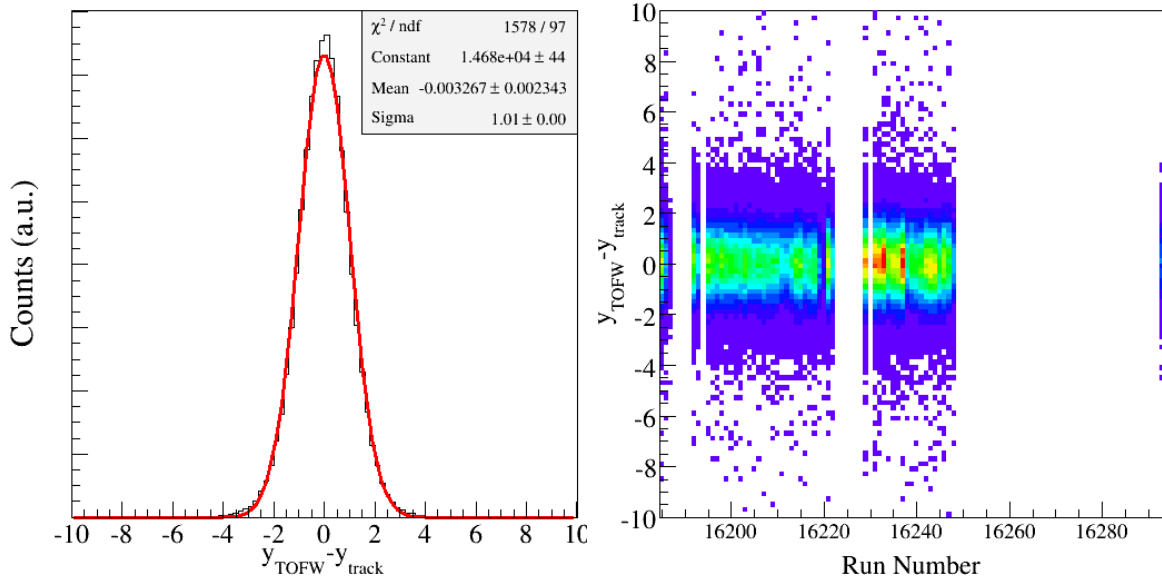
Figure A.16: The figures shows the difference between the reconstructed y_{TOFW} position of the hit on the slat and y_{track} position of the projection of the track on the TOFW. Left right panel shows the $dy = y_{\mathrm{TOFW}} - y_{\mathrm{track}}$. The width and the centroid of the distribution is used to select tracks for PID. BRAHMS uses a 3 standard deviation cut on this distribution. The width and centroid of the distribution can vary so the cut is best made on a run by run basis. The data is taken from $p + p$ collisions at $90°$, A-polarity 1/3 magnetic field.
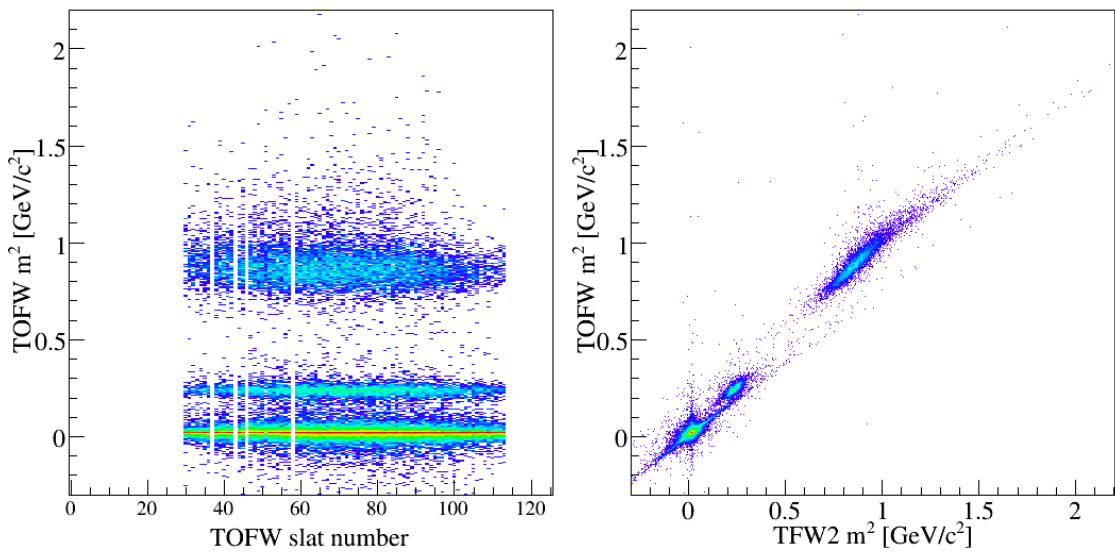
Figure A.17: The left panel of the figure shows the m^2 vs the slat number distribution. The three flat ridges in the contour are from top to bottom: (anti–) protons, kaons and pions. The straight horizontal ridges shoes that all the individual slats are equally well calibrated. The right panel shows the correspondence between the m^2 in TOFW and TFW2. The 3 peaks in the contour does not have an circular/elliptical shape, indicating that one can clean up the PID by utilising both walls. This will extend the PID to higher p_{T}, but involves a more complicated PID efficiency calculation. Both of the distributions have logarithmic contours. are The data is taken from $p + p$ collisions at $90°$, A-polarity $1/3$ magnetic field.
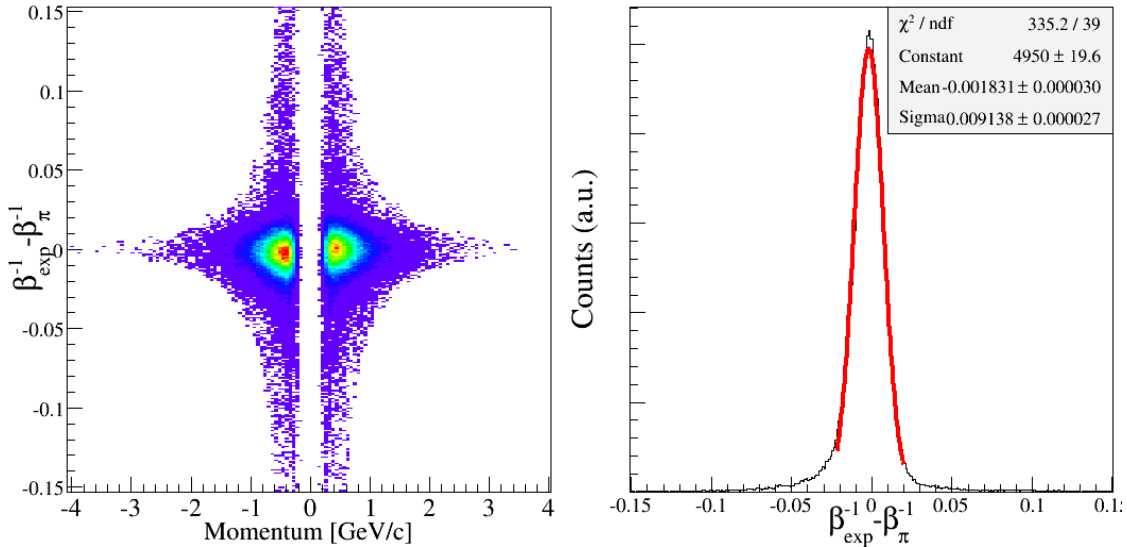
Figure A.18: The figures shows the pion track candidates in the TOFW. The candidates have $-0.08052 < m^2 < 0.1195$ and $|p| < 2$ GeV/c. Candidates are selected for building the histogram and finding the β^{-1} resolution. On the second iteration over the data one can identify pions using this resolution. The right panel shows the projection of the $d\beta$ distribution and the resolution parameters. The data is taken from $p + p$ collisions at $90°$, A-polarity 1/3 magnetic field.
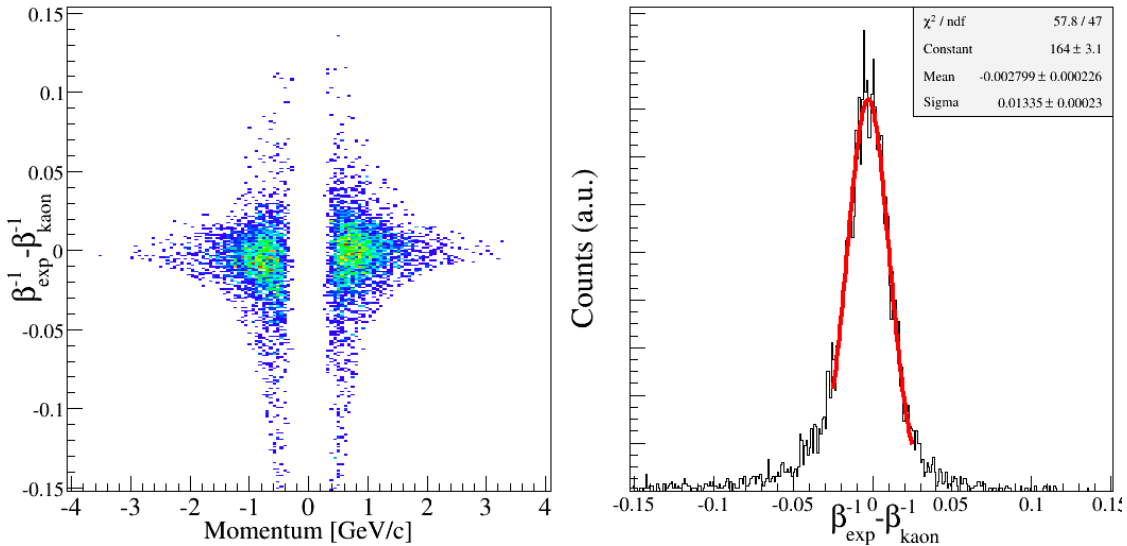
Figure A.19: The figures shows the kaon track candidates in TOFW. The candidates have $.1237 < m^2 < 0.3637$ and $|p| < 2$ GeV/c. Candidates are selected for building the histogram and finding the β^{-1} resolution. On the second iteration over the data one can identify kaons using this resolution. The right panel shows the projection of the $d\beta$ distribution and the resolution parameters. The data is taken from $p + p$ collisions at $90°$, A-polarity 1/3 magnetic field.
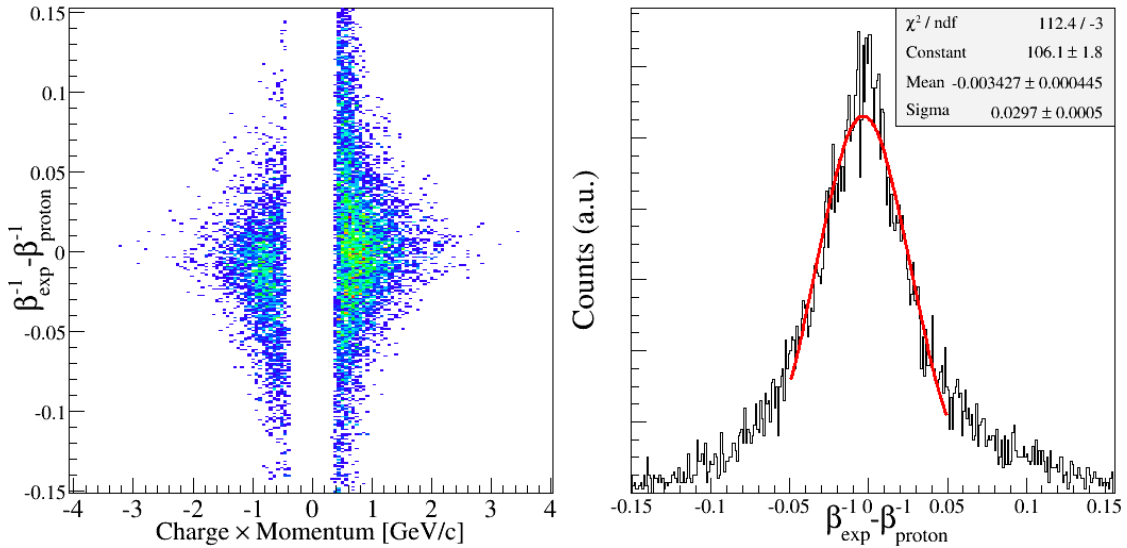
Figure A.20: The figures shows the proton track candidates in TOFW. The candidates have $.6804 < m^2 < 1.080$ and $|p| < 3.3$ GeV/c. Candidates are selected for building the histogram and finding the β^{-1} resolution. On the second iteration over the data one can identify protons using this resolution. The right panel shows the projection of the $d\beta$ distribution and the resolution parameters. The data is taken from $p + p$ collisions at $90°$, A-polarity 1/3 magnetic field.
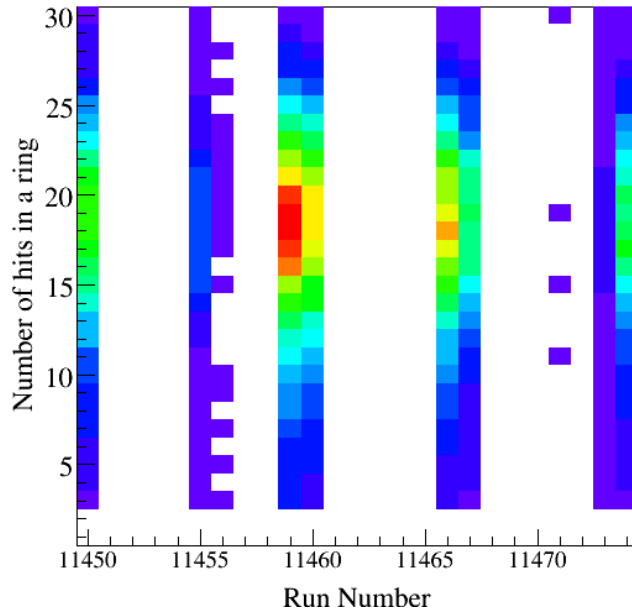
Figure A.21: The data shows the number of hits that went into reconstructing the RICH rings on a run by run basis. The plot shows a steady performance of the RICH during all runs used in the analysis. The data is taken from Au+Au collisions at $4°$, B-polarity 1/6 magnetic field.

Appendix B

The BRAHMS collaboration

I. Arsene[10], I. G. Bearden[7], D. Beavis[1], C. Besliu[10], B. Budick[6], H. Bøggild[7], C. Chasman[1], C. H. Christensen[7], P. Christiansen[7], J. Cibor[3], R. Debbe[1], E. Enger[12], J. J. Gaardhøje[7], M. Germinario[7], K. Hagel[8], H. Ito[1], A. Jipa10, F. Jundt[2], J. I. Jørdre[9], C. E. Jørgensen[7], R. Karabowicz[4], E. J. Kim[1,11], T. Kozik[4], T. M. Larsen[7], J. H. Lee[1], Y. K. Lee[5], S. Lindal[12], R. Lystad[9], G. Løvhøiden[12], Z. Majka[4], A. Makeev[8], M. Mikelsen[12], M. Murray[8,11], J. Natowitz[8], B. Neumann[11], B. S. Nielsen[7], D. Ouerdane[7], R. Planeta[4], F. Rami[2], C. Ristea[7], O. Ristea[10], D. Röhrich[9], B. H. Samset[12], D. Sandberg[7], S. J. Sanders[11], R. A. Scheetz[1], P. Staszel[7], T. S. Tveter[12], F. Videbæk[1], R. Wada[8], Z. Yin[9], and I. S. Zgura[10]

1 Brookhaven National Laboratory, Upton, New York 11973
2 Institut de Recherches Subatomiques and Université Louis Pasteur, Strasbourg, France
3 Institute of Nuclear Physics, Krakow, Poland
4 Smoluchkowski Inst. of Physics, Jagiellonian University, Krakow, Poland
5 Johns Hopkins University, Baltimore 21218
6 New York University, New York 10003
7 Niels Bohr Institute, Blegdamsvej 17, University of Copenhagen, Copenhagen 2100, Denmark
8 Texas A&M University, College Station, Texas, 17843
9 University of Bergen, Department of Physics, Bergen, Norway
10 University of Bucharest, Romania
11 University of Kansas, Lawerence, Kansas 66049
12 University of Oslo, Department of Physics, Oslo, Norway

Index

List of Figures

List of Tables

Bibliography

[1] T. D. Lee and G. C. Wick. Vacuum stability and vacuum excitation in a spin-0 field theory. *Phys. Rev. D*, 9:2291, 1974. 3

[2] G. Baym. Report of the workshop on BeV/nucleon collisions of heavy ions–how and why. *Bear Mountain, New York, 29 November-1 December*, 1975. 3

[3] Claus O. E. Jørgensen. *High p_{T} Charged Hadron Production at RHIC*. PhD thesis, Niels Bohr Institute, 2004. http://www4.rcf.bnl.gov/brahms/WWW/thesis/ekman_phd_thesis.pdf. 6, 7, 46, 48, 52, 56, 72

[4] I. G. Bearden et al. BRAHMS Collaboration. Quark–gluon plasma and color glass condensate at RHIC? the perspective from the BRAHMS experiment. *Nucl. Phys. A*, 757:1–27, 2005. 8

[5] S. S. Adler et al. PHENIX collaboration. Formation of dense partonic matter in relativistic nucleus–nucleus collisions at RHIC: Experimental evaluation by the PHENIX Collaboration. *Nucl. Phys. A*, 757:184–283, 2005. 8, 19

[6] B. B. Back et al. PHOBOS collaboration. The PHOBOS perspective on discoveries at RHIC. *Nucl. Phys. A*, 757:28–101, 2005. 8

[7] J. Adams et al. STAR collaboration. Experimental and theoretical challenges in the search for the quark–gluon plasma: The STAR Collaboration's critical assessment of the evidence from RHIC collisions. *Nucl. Phys. A*, 757:102–183, 2005. 8, 10, 13

[8] J. D. Bjorken. Highly relativistic nucleus–nucleus collisions: The central rapidity region. *Phys. Rev. D*, 27:140, 1983. 8

[9] J. Bächler et al NA35 Collaboration. Study of the energy flow in sulphur- and oxygen–nucleus collisions at 60 and 200 GeV/nucleon. *Z. Phys. C*, 52:239–263, 1991. 8

[10] T. Alber et al NA49 Experiment. Transverse Energy Production in ^{208}Pb+^{208}Pb Collisions at 158 GeV per Nucleon. *Phys. Rev. Lett*, 75:3814, 1995. 8

[11] I. G. Bearden et al. BRAHMS Collaboration. Nuclear stopping in Au+Au collisions at $\sqrt{s_{NN}} = $ 200 GeV. *Phys. Rev. Lett.*, 93:102301, 2004. 9, 35, 87

[12] Ulrich Heinz Ekkard Schnedermann, Josef Sollfrank. Thermal phenomenology of hadrons from 200A GeV S+S collisions. *Phys. Rev. C*, 48:2462–2475, 1993. 9

[13] O. Barannikova for the STAR Collboration. Probing collision dynamics at RHIC. 2004. arXiv:nucl-ex/0403014v1. 9, 10

[14] J. Stachel P. Braun-Munzinger, I. Heppe. Chemical equilibration in Pb+Pb collisions at the SPS. *Phys. Lett. B*, 465:15–20, 1999. 9, 10

[15] R. Hanburry-Brown and R. Q. Twiss. *Philos. Mag. Ser.*, 7(45 (366)):663, 1954. 10

[16] R. Hanburry-Brown and R. Q. Twiss. *Nature*, 178:1046, 1956. 10

[17] S. Pratt. Pion interferometry of quark–gluon plasma. *Phys. Rev. D 33, 1314*, 33:1314, 1986. 10

[18] G. Bertsch. Pion interferometryas a probe of the plasma. *Nucl. Phys A*, 498:173, 1989. 10

[19] B. B. Back et al PHOBOS Collaboration. Transverse momentum and rapidity dependence on hanbury–brown–twiss correlation in Au+Au collisions at $sqrts_{NN} = 62.4$ and 200 GeV. *Phys. Rev. C*, 73:031901, 2006. 11

[20] B. I. Abelev et al STAR Collaboration. Mass, quark–number, and $\sqrt{s_{NN}}$ dependence of the second and fourth flow harmonics in ultra–relativistic nucleus–nucleus collisions. *Phys. Rev. C*, 75(054906), 2007. 11

[21] D. Teaney J. Casalderrey-Solana, E. V. Shuryak. Hydrodynamic flow from fast particles. *Phys. Conf. Ser.*, 27:22, 2005. arXiv:hep-ph/0602183v1. 13

[22] A. Adare et al PHENIX Collaboration. Transverse momentum and centrality dependence of dihadron correlations in Au+Au collisions at $\sqrt{s_{NN}} = 200$ GeV: Jet–quenching and the response of partonic matter. 2007. arXiv:http://arxiv.org/abs/0705.3238v10705.3238v1. 13, 14

[23] A. Adare et al PHENIX Collaboration. System Size and Energy Dependence of Jet-Induced Hadron Pair Correlation Shapes in Cu+Cu and Au+Au Collisions at $\sqrt{s_{NN}} = 200$ and 62.4 GeV. 2006. arXiv:nucl-ex/0611019. 13, 14

[24] J. Ruppert and B. Müller. Waking the colored plasma. *Phys. Lett. B*, 618:123–130, 2005. 13

[25] J. F. Owens. Large–momentum–transfer production of direct photons, jets, and particles. *Rev. Mod. Phys.*, 59:465, 1987. 15, 18, 19

[26] R. P. Feynman. *Photon–hadron interactions*. Benjamin, New York, 1972. 15

[27] J. Kogut and L. Susskind. The parton picture of elementary particles. *Physics Reports*, 8:75, 1973. 15, 16

[28] Zhongbao Yin. *High p_{T} Physics in Heavy Ion Collisions at $\sqrt{s_{NN}} = 200$ GeV*. PhD thesis, University of Bergen, Norway, 2005. http://www4.rcf.bnl.gov/brahms/WWW/thesis/thesis_zhongbao.pdf. 16

[29] G. Altarelli and G. Parisi. Asymptotic freedom in parton language. *Nucl. Phys. B*, 126:298, 1977. 16, 18, 26

[30] C. Collins-Tooth. Structure functions and parton densities at HERA. *Nucl. Phys. B*, 152:71–74, 2006. In color: http://ppewww.physics.gla.ac.uk/~chrisc/webpagedocs/qcd04-ccollins.ps. 17

[31] Alessandro Bacchetta et al. Collins fragmentation function for pions and kaons in a spectator model. 2007. arXiv:0707.3372v1. 18

[32] R. J. Glauber and G. Matthiae. High–energy scattering of protons by nuclei. *Nucl. Phys. B*, 21:135–157, 1970. 20

[33] Xin-Nian Wang. HIJING, Heavy Ion Jet INteraction Generator. Web page. http://www-nsdth.lbl.gov/~xnwang/hijing/. 20

[34] H. deVries C.W. deJager and C. deVries. *Atomic data and nuclear data tables*, 14:485, 1974. 21

[35] K. Hagiwara et al. Review of particle properties. *Phys. Rev. D*, 66:010001, 2002. 21

[36] J. Adams et al STAR collaboration. Production of charged pions and hadrons in Au+Au collisions at $\sqrt{s_{NN}} = 130$ GeV. *Submitted to Phys. Rev. C*, 2003. arXiv:nucl-ex/0311017. 21

[37] I. G. Bearden et al. BRAHMS Collaboration. Transverse momentum spectra in Au+Au and d+Au collisions at $\sqrt{s_{NN}} = 200$ GeV and the pseudorapidity dependence of high–p_{T} suppression. *Phys. Rev. Lett.*, 91:072305, 2003. 22, 35, 102

[38] J. Cronin et al. roduction of hadrons at large transverse momentum at 200, 300, and 400 GeV. *Phys. Rev. D*, 11:3105, 1975. 21, 31, 33

[39] D. Antreasyan et al CP Collaboration. Production of hadrons at large transverse momentum in 200–, 300–, and 400–GeV $p - p$ and $p-$nucleus collisions. *Phys. Rev. D*, 19:764, 1979. 21, 31, 33

[40] X.-N. Wang. A pqcd–based approach to parton production and equilibration in high–energy nuclear collisions. *Phys. Rept.*, 280:287, 1997. 22

[41] R. C. Hwa and C. B. Yang. Final state effect as the origin of the Cronin effect. *Phys. Rev. Lett.*, 93:082302, 2004. 22, 33

[42] I. Arsene et al. BRAHMS Collaboration. Evolution of the nuclear modification factors with rapidity and centrality in d+Au collisions at $\sqrt{s_{NN}} = 200$ GeV. *Phys. Rev. Lett.*, 93:242303, 2004. 22

[43] J. J. Aubert et al EMC collaboration. The ratio of the nucleon structure functions f_2^n for iron and deuterium. *Phys. Lett. B*, 123:275–278, 1983. 23

[44] Dasu et al. E140 Collaboration. Measurement of the difference in $r = \sigma l/\sigma t$ and of $\sigma a/\sigma d$ in deep–inelastic $e-$d, $e-$fe, and $e-$au scattering. *Phys. Rev. Lett.*, 60:2591, 1988. 23

[45] E Amaudruz et al. NA37/NMC Collaboration. Measurements of $r^d - r^p$ and $r^{Ca} - r^c$ in deep inelastic muon scattering. *Phys. Lett. B*, 294:120, 1992. 23

[46] M. Arneodo et al. The structure function ratios f_c^2/f_d^2 and f_c^2/f_d^2 at small x. *Nucl. Phys. B*, 441:12–30, 1995. 24

[47] M. Arneodo. Nuclear effects in structure functions. *Phys. Rep.*, 240:301–393, 1994. 23

[48] D. Kharzeev and M. Nardi. Hadron production in nuclear collisions at RHIC and high–density QCD. *Phys. Lett. B*, 507:121–128, 2001. 23

[49] K. Golec-Biernat and M. Wüsthoff. Saturation effects in deep inelastic scattering at low q^2 and its implications on diffraction. *Phys. Rev. D*, 59:014017, 1998. 25

[50] R. Baier et al. Induced gluon radiation in a QCD medium. *Phys. Lett. B*, 345:277, 1995. 25

[51] R. Baier et al. Radiative energy loss of high energy quarks and gluons in a finite–volume quark–gluon plasma. *Nucl. Phys. B*, 483:291, 1997. 25

[52] R. Baier et al. Radiative energy loss and $p_\perp$–broadening of high energy partons in nuclei. *Phys. Lett. B*, 484:265, 1997. 25

[53] P. Levai M. Gyulassy and I. Vitev. Jet quenching in thin quark–gluon plasmas I: formalism. *Nucl. Phys. B*, page 197, 2000. arXiv:hep-ph/9907461. 25

[54] P. Levai M. Gyulassy and I. Vitev. Reaction operator approach to non–abelian energy loss. *Nucl. Phys. B*, 594:371, 2001. arXiv:nucl-th/0006010. 25

[55] U. A Wiedemann. Gluon radiation off hard quarks in a nuclear environment: opacity expansion. *Nucl. Phys. B*, 588:303, 2000. 25

[56] Miklos Gyulassy Ivan Vitev. High–p_T Tomography of d+Au and Au+Au at SPS, RHIC, and LHC. *Phys. Rev. Lett.*, 89:252301, 2002. 26, 28

[57] M. Guylassy and L. McLerren. New forms of QCD matter discovered at RHIC. *Nucl.Phys. A*, 750:30–63, 2005. 26, 27

[58] I. I. Balitsky and L. N. Lipatov. The Pomeranchuk singularity in quantum chromodynamics. *Sov. J. Nucl. Phys.*, 28:822, 1978. 26

[59] E. A. Kuraev, L. N. Lipatov, and Victor S. Fadin. The Pomeranchuk singularity in nonabelian gauge theories. *Sov. Phys. JETP*, 45:199, 1977. 26

[60] V. N. Gribov and L. N. Lipatov. Deep inelastic $e - p$ scattering in perturbation theory. *Sov. J. Nucl. Phys.*, 15:438 and 675, 1972. 26

[61] Y. L. Dokshitzer. Calculation of the structure functions for deep inelastic scattering and $e^+ - e^-$ annihilation by perturbation theory in quantum chromodynamics. (in Russian). *Sov. Phys. JETP*, 46:641, 1977. 26

[62] E. Shuryak. What RHIC experiments and theory tell us about properties of quark–gluon plasma? *Nucl. Phys. A*, 750:64–83, 2005. 27

[63] J. L. Nagle. The letter "s" (and the sQGP). *Eur. Phys. J. C*, 49:275, 2007. arXiv:nucl-th/0608070. 28

[64] M. H. Thoma. The Quark-Gluon-Plasma Liquid. *J. Phys. G: Nucl. Part. Phys*, 31:L7, 2005. Erratum arXiv:hep-ph/0503154. 28

[65] R. C. Hwa and C. B. Yang. Hadron production in the transfragmentation region in heavy–ion collisions. *Phys. Rev. C*, 73:044913, 2006. 28, 29, 107

[66] R. C. Hwa and C. B. Yang. Forward production with large p/π ratio and without jet structure at any p_{T}. *To be published in Phys. Rev. C.*, 2007. arXiv:nucl-th/0605037v4. 28, 30, 107

[67] B. B. Back et al PHOBOS collaboration. Significance of the fragmentation region in ultrarelativistic heavy ion collisions. *Phys. Rev. Lett.*, 91:052303, 2003. 28, 29

[68] R. C. Hwa. Evidence for valence–quark clusters in nucleon structure functions. *Phys. Rev. D*, 22:759, 1980. 29

[69] R. C. Hwa. Clustering and hadronization of quarks: A treatment of the low–p_{T} problem. *Phys. Rev. D*, 22:1593, 1980. 29

[70] R. C. Hwa and C. B. Yang. Parton distributions in the valon model. *Phys. Rev. C*, 66:025204, 2002. 29

[71] R. C. Hwa and C. B. Yang. Scaling behavior at high p_{T} and the p/π ratio. *Phys. Rev. C.*, 67:034902, 2004. 29

[72] B. B. Back et al PHOBOS collaboration. Identified hadron transverse momentum spectra in Au+Au collisions at $\sqrt{s_{NN}} = 62.4$ GeV. *Phys. Rev. C*, 75:024910, 2007. 31, 83, 94, 95

[73] B. I. Abelev et al STAR Collaboration. Enegy dependence of $\pi^{\pm}$, p, and $\bar{p}$ transverse momentum spectra for au+au collisions at $\sqrt{s_{NN}} = 62.4$ GeV and 200 GeV. *Submitted for publication*, 2007. arXiv:nucl-ex/0703040. 31

[74] D. d'Enterria. Indications of suppressed high p_{T} hadron production in nucleus–nucleus collisions at cern–sps. *Phys. Lett. B*, 596:32–43, 2004. 31, 33

[75] M. M. Aggarwal et al WA98 Collaboration. Transverse mass distributions of neutral pions from ^{208}Pb–induced reactions at 158≤AGeV. *Eur. Phys. J. C*, 23:225, 2002. 32, 102

[76] J. Slivova. PhD thesis, Charles University, Prague, 2003. From the CERES experiment. 32

[77] R. Albrecht et al WA80 Collaboration. Transverse momentum distribution of neutral pions from nuclear collisions at 200 AGeV. *Eur. Phys. J. C*, 5:255, 1998. 32

[78] F. Antinori et al NA57 collaboratation. Central–to–peripheral nuclear modification factors in Pb-Pb collisions at $\sqrt{s_{NN}} = 17.3$ GeV. *Phys. Lett. B*, 623:17, 2005. 32

[79] K. Reygers for the WA98 collaboration. Are high-p_{T} pions suppressed in Pb+Pb collisions at $\sqrt{s_{NN}} = 17.4$ GeV? *J. Phys. G: Nucl. Part. Phys*, 34:S797–S800, 2007. 33, 34

[80] J. Adams et al STAR collaboration. Evidence from d+Au measurements for final–state suppression of high-p_{T} hadrons in Au+Au collisions at RHIC. *Phys. Rev. Lett.*, 91:072304, 2003. 35

[81] S. S. Adler et al PHENIX Collaboration. Absence of suppression in particle production at large transverse momentum in $\sqrt{s_{NN}} = 200$ GeV d+Au collisions. *Phys. Rev. Lett.*, 91:072303, 2003. 35

[82] B. B. Back et al PHOBOS collaboration. Pseudorapidity dependence of charged hadron transverse momentum spectra in d+Au collisions at $\sqrt{s_{NN}} = 200$ GeV. *Phys. Rev. C*, 70:061901, 2004. 35

[83] Catalin Ristea. *The Rapidity Dependence of High p_{T} Suppression in Au+Au Collisions at BRAHMS Experiment.* PhD thesis, Niels Bohr Institute, 2007. http://www4.rcf.bnl.gov/brahms/WWW/publications.html. 36, 37, 42, 58, 98

[84] S. S. Adler et al PHENIX Collaboration. A Detailed Study of High-p_{T} Neutral Pion Suppression and Azimuthal Anisotropy in Au+Au Collisions at $\sqrt{s_{NN}} = 200$ GeV. *Submitted to Phys. Rev. C*, 2006. arXiv:nucl-ex/0611007v1. 39, 40

[85] J. Adams et al STAR Collaboration. ϕ meson production in Au+Au and $p + p$ collisions at $\sqrt{s_{NN}} = 200$ GeV. *Phys. Lett. B*, 612:181, 2005. 41

[86] A. Adare et al PHENIX Collaboration. High transverse momentum η meson production in $p+p$, d+Au, and Au+Au collisions at $\sqrt{s_{NN}} = 200$ GeV. *Phys. Rev. C*, 75:024909, 2007. 41

[87] J. Adams et al STAR Collaboration. $k(892)^*$ Resonance Production in Au+Au and $p + p$ Collisions at $\sqrt{s_{NN}} = 200$ GeV at STAR. *Phys. Rev. C*, 71(064902), 2005. 42

[88] J. Adams et al STAR Collaboration. Scaling properties of hyperon production in Au+Au collisions at $\sqrt{s_{NN}} = 200$ GeV. *Phys. Rev. Lett.*, 98(062301), 2007. 42

[89] A. Adare et al PHENIX Collaboration. j/ψ Production in Au+Au Collisions at $\sqrt{s_{NN}} = 200$ GeV. *Submitted to Phys. Rev. Lett.*, 2006. arXiv:nucl-ex/0611020v1. 42, 43

[90] B. I. Abelev et al STAR Collaboration. Transverse momentum and centrality dependence of high-p_{T} non–photonic electron suppression in Au+Au collisions at $\sqrt{s_{NN}} = 200$ GeV. *Phys. Rev. Lett.*, 98:192301, 2007. arXiv:nucl-ex/0607012v1. 42, 43

[91] P. Thieberger et al. Tandem injected relativistic heavy ion facility at Brookhaven, present and future. *Nucl. Instr. Meth.*, A268:513, 1988. 45

[92] Tandem Van de Graaff, LINAC, Booster and AGS at BNL:. Web page. http://www.bnl.gov/bnlweb/facilities/TVdG.asp http://www.bnl.gov/bnlweb/facilities/LINAC.asp http://www.bnl.gov/bnlweb/facilities/booster.asp http://www.bnl.gov/bnlweb/facilities/AGS.asp. 46

[93] I. G. Bearden et al. BRAHMS Collaboration. The BRAHMS Experiment at RHIC. *Nucl. Instr. Meth. A*, 499:437, 2003. 46, 51

[94] T. Abbott et al. A single arm spectrometer detector system for high–energy heavy–ion experiments. *Nucl. Instr. Meth. A*, 290:41–60, 1990. 46

[95] P. Vincent et al. The E802 aerogel čherenkov detector. *Nucl. Instr. Meth. A*, 272:660–668, 1988. 46

[96] Djamel Ouerdane. *Charged Pion and Kaon Production in Central Au+Au Collisions at $\sqrt{s_{NN}} = 200$ GeV*. PhD thesis, Niels Bohr Institute, 2003. http://www4.rcf.bnl.gov/brahms/WWW/thesis/djam_thesis.pdf. 46, 51, 56, 57, 58, 72, 127

[97] Peter Christensen. *Stopping in central $\sqrt{s_{NN}} = 200$ GeV Au+Au collisions at RHIC*. PhD thesis, Niels Bohr Institute, 2003. http://www4.rcf.bnl.gov/brahms/WWW/thesis/pchristi_thesis.pdf. 46, 51, 58, 62, 72

[98] Bjørn H. Samset. *Charged particle production in $p + p$ collisions at $\sqrt{s_{NN}} = 200$ GeV*. PhD thesis, Physics Institute, University of Oslo, 2005. http://www4.rcf.bnl.gov/brahms/WWW/thesis/bjornhs_phd_thesis.pdf. 46

[99] R. Debbe et al. The BRAHMS Ring Imaging čherenkov Detector. *Nucl. Instr. Meth. A*, 499:Submitted, 2006. 46, 52

[100] R. Debbe et al. Plastic Scintilator Centrality Detector for BRAHMS. *Nucl. Instr. Meth. A*, 516:281, 2004. 49

[101] I. G. Bearden et al. BRAHMS Collaboration. Charged Particle Densities from Au+Au Collisions at $\sqrt{s_{NN}} = 130$ GeV. *Phys. Lett.*, B523:227, 2001. 49

[102] Jens Ivar Jørdre. *Rapidity and transverse momentum spectra and the reaction dynamics in Au+Au collisions at RHIC*. PhD thesis, University of Bergen, Norway, 2005. http://www4.rcf.bnl.gov/brahms/WWW/thesis/jens_thesis.pdf. 51, 56, 69

[103] Truls Martin Larsen. Efficiency calculations for the Time Projection Chambers in the BRAHMS experiment at the RHIC accelerator. Master's thesis, University of Oslo, Norway, 2003. http://www4.rcf.bnl.gov/brahms/WWW/thesis/brahms_tpc_eff.pdf. 51, 61, 69

[104] Bjørn H. Samset. Vertex Determination in the BRAHMS and Measurements of Centrality Depedent Charged Particle Production in Au-Au Collisions at $\sqrt{s_{NN}} = 130$AGeV. Master's thesis, University of Oslo, Norway, 2001. http://www4.rcf.bnl.gov/brahms/WWW/thesis/BHS_master_thesis.ps. 51

[105] GEANT, GEometry ANd Tracking. Web page. http://geant4.web.cern.ch/geant4. 56

[106] Condor. Web page. http://www.cs.wisc.edu/condor/. 68

[107] CRS Software. Web page. https://www.racf.bnl.gov/docs/sw/crs. 68

[108] Rene Brun and Fons Rademakers. Root - an object oriented data analysis framework. *Nucl. Inst. Meth.*, A389:81–86, 1997. http://root.cern.ch/. 69

[109] Concurrent Versions System. Web page. http://www.nongnu.org/cvs/. 70

[110] GNU Automake and GNU Autoconf. Web page. http://sources.redhat.com/automake/ http://www.gnu.org/software/autoconf/. 72

[111] A. Breakstone et al. Inclusive charges particle cross sections in full phase space from proton proton interactions at isr energies. *Z. Phys. C*, 69:55–65, 1995. 79, 92

[112] D. d'Enterria. Relevance of baseline hard proton–proton spectra for high–energy nucleus–nucleus physics. *J. Phys. G: Nucl. Part. Phys*, 31:S491, 2005. 79, 80, 94

[113] H. H. Dalsgaard for the BRAHMS collaboration. Nuclear Stopping: Paving the way from RHIC to LHC. *To be published in J. Modern. Phys. E*, 2007. http://www4.rcf.bnl.gov/brahms/WWW/pubs/2006/QM06proceedingHHD-v2-3.pdf. 81, 87

[114] K. Adcox et al. PEHNIX Collaboration. Measurement of Λ and Λ^- particles in Au+Au collisions at $\sqrt{s_{NN}} = 130$ GeV. *Phys. Rev. Lett.*, 89:092302, 2002. 83

[115] H. Yang for the BRAHMS collaboration. Identified particle production in $p + p$ and d+au collisions at RHIC. *J. Phys. G: Nucl. Part. Phys*, 34:S619–S622, 2007. 87

[116] I. G. Bearden et al. BRAHMS Collaboration. Rapidity dependence of high p_T suppression at $\sqrt{s_{NN}} = 62.4$ GeV. *Submitted to Phys. Lett. B*, 2006. arXiv:nucl-ex/0602018. 92

[117] T. Åkeson et al. AFS Collaboration. Large transverse momentum particle production in $\alpha\alpha$ and pp collisions at the CERN ISR. *Nucl. Phys. B*, 209:309, 1982. 92

[118] B. Alper et al. BSC Collaboration. Production spectra of $\pi^\pm$, $k^\pm$, $p^\pm$ at large angles in proton–proton collisions in the cern intersecting storage rings. *Nucl. Phys. B*, 100:2237, 1975. 92

[119] B. Alver et al PHOBOS collaboration. System size and centrality dependence of charged hadron transverse momentum spectra in Au+Au and Cu+Cu collisions at $\sqrt{s_{NN}} = 62.4$ and 200 GeV. *Phys. Rev. Lett.*, 96:212301, 2006. 92, 93

[120] B. B. Back et al PHOBOS collaboration. Centrality dependence of charged hadron transverse momentum spectra in Au+Au collisions from $\sqrt{s_{NN}} = 62.4$ to 200 GeV. *Phys. Rev. Lett.*, 94:082304, 2005. 92, 93, 102

[121] I. G. Bearden et al. BRAHMS Collaboration. Charged meson rapidity distributions in central Au+Au collisions at $\sqrt{s_{NN}} = 200$ GeV. *Phys. Rev. Lett.*, 94:162301, 2005. 95

[122] G. Agakashin et al CERES Collaboration. High p_T charged–pion production in Pb-Au collisions at 158AGeV/c. 2000. arxiv.org:hep-ex/0003012. 102

[123] M. M. Aggarwal et al WA98 Collaboration. Centrality dependence of neutral pion production in 158A GeV ^{208}Pb+ ^{208}Pb collisions. *Phys. Rev. Lett.*, 81:4087, 1998. 102

[124] J. Adams et al STAR Collaboration. Centrality dependence of high p_{T} hadron suppression in Au + Au collisions at $\sqrt{s_{nn}} = 130$ GeV. *Phys. Rev. Lett.*, 89:202301, 2002. 102

[125] K. Adcox et al PHENIX Collaboration. Centrality dependence of the high p_{T} charged hadron suppression in Au+Au collisions at $\sqrt{(s_{NN})} = 130$ GeV. *Phys. Lett. B*, 561:82–92, 2003. 102

[126] J. Adams et al STAR Collaboration. Transverse momentum and collision energy dependence of high pt hadron suppression in Au+Au collisions at ultrarelativistic energies. *Phys. Rev. Lett.*, 91:172302, 2003. 102

[127] S. S. Adler et al PHENIX Collaboration. High–p_{T} charged hadron suppression in Au+Au collisions at $\sqrt{s_{NN}} = 200$ GeV. *Phys. Rev. C*, 69:034910, 2004. 102

[128] B. B. Back et al PHOBOS collaboration. Charged hadron transverse momentum distributions in au+au collisions at $\sqrt{s_{NN}} = 200$ GeV. *Phys. Lett. B*, 578:297, 2004. 102